Immunomodulation of Influenza A Virus Infection by Fibroblast-Derived Versican

Jourdan E. Brune

A dissertation
submitted in partial fulfillment of the
requirements for the degree of

Doctor of Philosophy

University of Washington
2023

Reading Committee:
Charles W. Frevert, Chair
William A. Altemeier
W. Conrad Liles
Kristina M. Adams Waldorf

Program Authorized to Offer Degree:
Molecular Medicine and Mechanisms of Disease

University of Washington

Abstract

Immunomodulation of Influenza A Virus Infection by Fibroblast-Derived Versican

Jourdan E. Brune

Chair of the Supervisory Committee:
Charles W. Frevert
Department of Comparative Medicine

Viral and bacterial lung infections place a significant burden on public health. Versican, an extracellular matrix (ECM) chondroitin sulfate proteoglycan, is a critical coordinator of the innate immune response. Versican's potential as an immunomodulatory molecule makes it a promising therapeutic target for controlling the host's immune response to lung infection. However, versican's contribution to lung inflammation, injury, and immune cell activity during influenza A virus (IAV) infection represents a critical knowledge gap. In the following work, we characterized the spatiotemporal accumulation of versican in the lungs of wild-type (C57BL/6J, WT) mice in response to IAV and found that versican accumulation correlates with mouse acute lung injury scores and pulmonary inflammatory cell infiltration. We found that versican expression is increased in both mononuclear phagocytic cells and stromal cells in the lungs in response to IAV in WT mice and discovered that the expression of versican in stromal cells is partially mediated by type I interferon receptor signaling. These data from WT mice raised intriguing questions about the role of versican in the early host response to IAV.

To rigorously investigate the potential of versican to modulate lung inflammation, we developed a complete protocol combining spectral flow cytometry with *in vivo* compartmental analysis, for the precise localization of multiple immune cell populations participating in the pulmonary host response to IAV. The lungs have high autofluorescence (AF) compared to other tissues, which complicates the analysis of pulmonary leukocytes by flow cytometry. In the following work, we described changes in the AF characteristics of control and IAV-infected lungs during the transition from innate to adaptive immunity. We meticulously assembled a

broad panel of 20 antibody-fluorophore conjugates compatible with these AF characteristics and spectral flow cytometry. Additionally, our studies validated that incorporating multiple heterogeneous AF signatures from the lungs improves the resolution and identification of fluorescence signals, particularly when alveolar macrophages are a component of the immune response. The methodology presented includes a robust gating strategy for the identification of B cells, T cells (cytotoxic T, T helper, and γδ T cells), NK cells, macrophages (alveolar, recruited and monocyte-macrophages), monocytes (Ly6C^{lo} and Ly6C^{hi}), dendritic cells (CD103^{+} and CD11b^{+}), neutrophils, and eosinophils in combination with dual *in vivo* CD45 labeling to facilitate identification of these immune cell populations in four pulmonary compartments. Finally, our studies implemented informed gating and dimensionality reduction algorithms to visualize the recruitment and migration of leukocytes from the vasculature, across the lung interstitium, and into the alveolar airways at 9 days post-infection with IAV.

Our robust spectral flow cytometry panel and *in vivo* intravascular CD45 labeling technique were applied to studies investigating the role of versican in lung inflammation, injury, and immune cell activity during IAV infection. To address our central hypothesis that fibroblast-derived versican is pro-inflammatory and enhances the innate immune response to IAV infection, we generated a tamoxifen-inducible mouse strain that is deficient in fibroblast-derived versican (B6. Col1a2-Cre$^{ERT+/-}$/Vcan$^{tm1.1Cwf}$, Col1a2/Vcan$^{-/-}$). We reported that fibroblast-derived versican plays a critical role in neutrophil, monocyte, mono-macrophage, dendritic cell, and eosinophil migration into the lungs and airways early in IAV infection. Intriguingly, fibroblast-derived versican deficiency had the most substantial impact on neutrophil emigration into the lungs. We found that Col1a2/Vcan$^{-/-}$ mouse lung fibroblasts (mLFs) have reduced cell-associated hyaluronan (HA) and that neutrophils were less adhesive to the versican/HA ECM of Col1a2/Vcan$^{-/-}$ mLFs compared to WT controls. These findings suggest that fibroblast-derived versican and associated HA are necessary for the adhesion of neutrophils to the lung fibroblasts as they transit into the lung interstitium and airways from the pulmonary vasculature. Our findings demonstrate that fibroblast-derived versican is a key integrator of the early host immune response to IAV.

Acknowledgements

First and foremost, I would like to thank my research mentor, Chuck Frevert, for all of his guidance and support for the past six years. I joined the Frevert lab when I started my veterinary specialty training in 2017, before I knew that I wanted to pursue PhD training, and have learned so much from him and everyone in his lab. Thank you, Chuck, for encouraging me to pursue a career as a veterinary scientist and for making it possible for me to receive a PhD in Laboratory Medicine and Pathology. Many Frevert laboratory members have been instrumental in my training. Thank you to Jessica Felgenhauer for recruiting me to the Frevert lab and for being a wonderful friend. I miss listening to you think out loud from the other side of our lab bench. Thank you to Mary Chang for your patience, your careful review of my proposals and manuscripts, and for pointing me in the right direction when I've gotten stuck. Sally Tang, thank you for your friendship and mentorship on the adhesion assay that proved to be the crux of this work. Thank you to Peter Waldron for your friendship and for all the long hours you've spent collecting tissues for my thesis project. Thank you to Christina Chan for your assistance and expertise on hyaluronan ELISAs and versican Western blots.

Thank you to all the members of my thesis committee, Dr. Bill Altemeier, Dr. W. Conrad Liles, and Dr. Kristina Adams Waldorf. Your mentorship and support have improved my critical thinking, elevated the caliber of my scientific inquiry, and made my dream of becoming a veterinary scientist possible. Additionally, I want to thank Bill Mahoney for his encouragement, support, and guidance throughout my time in the M3D PhD program. Megan Barker's coordination of student activities and scientific retreats has also been instrumental to my experience in the M3D program. Thank you, Megan, for everything you do for M3D graduate students and faculty.

I want to thank everyone in the Department of Comparative Medicine (DCM) at UW who has had a profound impact on my veterinary career and professional development. Before I became connected to DCM, my priorities were horseback riding and the minimum prerequisite classes for admittance to veterinary school. Thank you to UW DCM veterinary technicians Gary Fye, Sara Kerner, and Amy Martinson for training me as an undergraduate student assistant and exposing me to many facets of laboratory animal medicine. Thank you to Lillian Maggio-Price and Thea Brabb for giving me the opportunity to gain invaluable experience in laboratory animal anesthesia after I graduated from undergrad. Thank you to Jessica Snyder for writing me a letter of recommendation for my veterinary school application and for connecting me with Dr. Annie Chen at Washington State University College of Veterinary Medicine. Dr. Chen, thank you for friendship, encouragement, patience, and grace. I learned so much while working in your lab and ultimately decided to pursue a laboratory animal medicine residency that emphasized basic research training due to your mentorship. An additional special thanks goes to Thea Brabb, who at this point has hired me to work for DCM multiple times over. Thea, you've been such an important mentor me to at so many stages of my personal and professional development. Thank you for graciously putting up my antics, for encouraging me to pursue PhD training, and for entertaining all the Star Wars references. You really are Yoda.

Thank you to all of my family for your love and support not only throughout my life but especially as I've pursued a PhD while simultaneously becoming a mom. Thank you to my parents, Richard and Cindy Brune, for all of your encouragement and the many hours you've spent watching Olive. Thank you to my brother, Erik, and sister-in-law Courtney for watching Olive when she was home sick from daycare so that I could still go into the lab and complete experiments. Thank you to my in-laws, Jon and Kristin Collins, for helping Ryan with Olive on the long weekends I spent completing this thesis. Thank you, Olive, for being an especially cute and relatively easy baby. Thank you to my close friends, Jenna Klug and Dimitra Lotakis, for the emotional support and for laughing at my silly jokes.

Finally, thank you to my wonderful husband, Ryan Collins, for all of your support and satirical words of encouragement throughout my residency and PhD training. You've kept me laughing, even when I've lapsed into thinking that I'm not up for the challenges of a career as a veterinary scientist. Thanks for always reminding me that by comparison I wouldn't enjoy companion animal medicine practice and that no matter how many advanced degrees I earn, you'll always be a buffer scientist.

Dedication

To Ryan Collins, a wonderful husband and father,
and buff scientist

Table of Contents

List of Figures

List of Tables

Chapter 1. Introduction

This chapter will introduce the motivation for investigating the role of fibroblast-derived versican during influenza A virus infection.

1.1 Influenza A Viral Infections and Human Health

Viral respiratory disease places a significant burden on global health, with an estimated 145,000 to 645,000 annual deaths attributed to influenza A virus (IAV) lower respiratory tract infections alone.[2,3] Although recently overshadowed by the SARS-CoV-2 pandemic, seasonal influenza virus infection is a top cause of hospitalization among patients with community-acquired pneumonia in the United States.[4,5] Severe disease outcomes such as hospitalization, pneumonia, acute respiratory distress syndrome (ARDS), and death are more common in high-risk patient populations.[6] These high-risk populations include very young (< 2 years old), elderly (> 65 years old), pregnant, immune-compromised, and obese patients, as well as those that have been exposed to cigarette smoke, and have chronic illnesses, such as heart disease, chronic obstructive pulmonary disease, and asthma.[6] Additionally, pandemic influenza virus strains can cause severe disease in patients that lack these high-risk factors.[7] An estimated 62-85% of the influenza-related deaths during the 2009 H1N1 influenza A pandemic occurred in patients under 65 years old.[8] The disease burden from seasonal and pandemic influenza A viruses, and the growth of high-risk patient populations, underscores the need for continued influenza A research and the development of therapies for influenza A virus infection.

Influenza viruses belong to the Orthomyxoviridae family and are enveloped viruses that have zoonotic potential.[7,9] They are classified into four types, A, B, C, and D.[7,9] Influenza A viruses are responsible for the majority of seasonal influenza illnesses and have caused all influenza pandemics.[7,10] They have a segmented genome consisting of eight negative-sense, single-stranded RNAs.[6,7] IAVs are subtyped according to two surface viral glycoproteins, haemagglutinin and neuraminidase.[7] There are 18 and 11 different haemagglutinin (H1-H18) and neuraminidase (N1-N11) subtypes respectively.[9] In addition to humans, many species are infected with influenza A viruses including pigs, dogs, cats, ferrets, horses, bats, and marine mammals.[9] Spillover events have resulted in zoonotic IAV strains becoming the predominant circulating seasonal influenza strains and being the causative agents of influenza pandemics.[10]

The broad host range and segmented genome of IAV allow for genetic rearrangement in co-infected cells, enabling potential zoonotic spread.[6,7,9] Birds are the primary reservoir for IAVs.[6] Nearly all influenza A subtype combinations have been identified in avian species, except for H17N10 and H18N11, which have only been identified in bats.[6,9] It is increasingly common for spillover events of IAVs that originate from animals to impact human health.[10] In 2013, avian influenza H7N9 caused hundreds of human infections due to multiple spillover events in China.[11] Additionally, pandemic strains of IAV have been determined to be of avian or swine origin.[10] With the potential to develop antigenically novel viruses of zoonotic origin, influenza A viruses pose a significant threat to human health.

IAV infection is challenging to treat as it can undermine conventional prophylaxis and therapies. Through its ability to rapidly mutate and undergo genetic drift via the activity of its error-prone RNA-dependent RNA polymerase, IAV requires that influenza A vaccines be seasonally redesigned.[7] Antigenic drift that occurs between vaccine design and administration has the potential to reduce vaccine efficacy further.[12] Meanwhile, antigenically novel pandemic IAV strains are typically not covered by seasonal vaccines and therefore can potentially place large populations at risk of severe infection.[6,10] Taken together, vaccination alone cannot effectively control influenza, emphasizing the need for efficacious therapeutics. Currently, neuraminidase inhibitors, which block the release of new virions from infected cells, are the most common type of antiviral medication used to treat influenza infection. Neuraminidase inhibitors are particularly effective when given early in the clinical disease course and have demonstrated some efficacy against severe infections.[13,14] However, viral resistance to neuraminidase inhibitors has been reported.[15] Other available therapies include antivirals against viral RNA-dependent RNA polymerase and monoclonal antibody therapy against haemagglutinin.[16,17] While it has not been observed, there is potential for viral resistance to develop against these therapeutics.[18] Additionally, not all of these therapeutics are widely available and their performance beyond the treatment of acute, uncomplicated influenza infection is poorly characterized.[7] The limitations of currently available antiviral treatments emphasize the need to develop additional therapeutics for severe influenza infections and influenza disease-associated lung injury.

Both the intrinsic viral pathogenicity of IAV and the host immune response to IAV infection contribute to patient morbidity and mortality.[7,9] A comparison of severe influenza disease with the clinical syndromes of other respiratory viruses such as SARS-CoV-1, SARS-CoV-2, and MERS-CoV, revealed shared deleterious clinical and pathological sequelae, including respiratory failure from acute respiratory distress syndrome (ARDS) and diffuse alveolar damage, the histopathological hallmark of ARDS.[19] These viruses are intrinsically diverse with unique virion structures, genomic material, host cell receptor targets, and replication methods.[6,19] The fact that they have shared clinical syndromes suggests that the host inflammatory response to viral lung infection is principally responsible for patient morbidity and mortality.[19] Several additional observations support immunopathology as the principal driver of severe influenza illness. In both clinical patients and in studies investigating influenza infection using animal models, there is a poor correlation between viral load, disease severity, and disease outcome.[20-24] Additionally, in cases of fatal influenza infections, death typically occurs long after viral clearance.[22,25] Antiviral therapies are also less efficacious in these patients, particularly when given late in the clinical disease course.[25,26] The specific mechanisms by which host immunopathology is initiated and regulated are incompletely understood. Therefore, modulation of the host immune response is an important target for therapeutic interventions and has the potential to improve patient outcomes in cases of severe influenza pneumonia.[19,27-29]

The host immune response to influenza pneumonia is carried out in the tissue microenvironment of the lung. The host extracellular matrix (ECM) is a key contributor to defining the pulmonary microenvironment by conferring mechanical and biological characteristics which impact cellular phenotype.[30,31] The pulmonary ECM is dynamic and is remodeled considerably during lung development, infection, and injury to support select microenvironments required for specific biological activities.[32-34] Increasingly, the ECM is recognized for being inextricably linked to the host immune response and for its potential as a target for host-directed therapies of pulmonary disease.[30,33,35] However, how the ECM regulates and modulates pulmonary innate immunity is not well understood. Investigation of the mechanisms by which the ECM alters the host innate immune response to pulmonary pathogens, such as influenza A virus, could lead to the development of novel host-directed therapies that limit immunopathology during influenza infection.

1.2 The Pulmonary Extracellular Matrix

The extracellular matrix is the non-cellular portion of a tissue, has a dynamic composition, and is made up of diverse components.[36] The two major tissue structures comprised of ECM are the basement membrane and the interstitial matrix.[36] Basement membranes are thin, dense sheets of ECM that are in immediate proximity to the basal aspect of airway epithelium, alveolar epithelium, and vascular endothelial cells.[36] The interstitial matrix is a porous lattice which forms in the pulmonary interstitium.[36] In mammals, approximately 300 proteins have been identified as making up the core matrisome.[37] The core matrisome includes collagens, proteoglycans, and ECM glycoproteins.[37] Additionally, there are matrisome-associated proteins which include ECM-affiliated proteins, ECM-regulators, and secreted factors.[37] ECM-affiliated proteins are those that are affiliated structurally or functionally with core ECM proteins.[37] ECM-regulators include proteins that cross-link the ECM, enzymes that modify the ECM, and ECM-associated proteases and their inhibitors.[37] Finally, secreted factors are soluble proteins that may interact with ECM components, and include chemokines, cytokines, and growth factors.[37]

The extracellular matrix is continually turned over and renewed during both homeostasis and disease progression, requiring the proteolysis of matrix proteins.[32,34] Fragmentation of matrix proteins by proteases generates peptides known as matrikines, which have biological properties that may differ from those of their intact parent protein.[38] Predominant ECM proteins such as collagen, elastin, and fibronectin, all have associated matrikine peptides.[38] Matrikines have been shown to modify cell growth, proliferation, migration, and survival.[38] The relative abundance and activity of matrikines is challenging to capture by transcriptomic approaches as intact parent proteins may yield a variety of matrikines via sequential or differential cleavage by proteases.[39,40] For this reason, proteomic approaches are especially important for understanding the contribution of matrikines to ECM composition and function.[30]

In addition to proteins and peptides, glycosaminoglycans (GAGs) are crucial components of the ECM.[41,42] GAGs are linear polysaccharides made up of repeating disaccharide units in which one of the saccharides has a hydroxyl replaced by an amine.[36,42] The majority of GAGs are present in the ECM as part of a proteoglycan (PG).[36] PGs are complex proteins that consist of a core protein with one or more GAG side chains that are covalently attached to a GAG-binding domain in the core protein.[36] PGs are classified by the contents of their GAG side chains into three groups, heparan sulfate/heparin PGs, chondroitin sulfate/dermatan sulfate PGs, and keratan sulfate PGs.[36,42,43] Proteoglycans are additionally classified by their cellular location as intracellular, cell-surface, pericellular, and extracellular.[43] Hyaluronan is another important ECM GAG but is distinguished from GAGs of proteoglycans as it is not associated with a core protein and is not sulfated.[42,44]

The physical properties of GAGs impact the structure and biological activity of the ECM. They are highly negatively charged due to the sulfate and carboxyl groups present on their repeating disaccharides.[45] Osmotically active cations are drawn to these negative charges and bring large amounts of water along with them.[36] GAGs are able to form gels at low concentrations and their expansive conformations result in the formation of porous hydrated gels which provide both structural support to the ECM and a specialized microenvironment for biological activities.[45]

GAGs interact with a wide array of molecules, including growth factors, morphogens, chemokines, ECM proteins, and their bioactive fragments, receptors, lipoproteins, and pathogens.[42] This extensive collection of binding partners mediates diverse GAG functions from ECM assembly to immunomodulation in various contexts, including embryonic development, homeostasis, angiogenesis, cancer, neurodegenerative diseases, and infection.[42] The GAG interactome detailing GAG-protein interaction and interaction networks has recently been published.[42] Additional versatility is conferred to GAG interactions with molecules through various processes that alter GAG structure. These include hyperelongation of GAG chains, epimerization of acids, and changes in the sulfation patterns.[46,47] Regarding secreted factors, GAGs can impact the availability and mobilization of secreted factors for receptors, control the development of secreted factor gradients, and sequester factors from proteolytic degradation.[48-50] The model by which chemokines are presented to leukocytes by GAGs has recently been refined by evidence that chemokines are presented in solution while sequestered within the glycocalyx, instead of being exclusively GAG-bound.[48] The versatility of GAG structure and function and their predominance within the ECM, underscores the need to further understand the contributions of PGs and hyaluronan to the host immune response to pulmonary pathogens, such as influenza A virus.

1.3 Versican, An Extracellular Matrix Proteoglycan

Versican is a large extracellular chondroitin sulfate PG that is an important component of the extracellular matrix during health and disease. Versican is known to interact with hyaluronan and lectins; therefore, it is classified as being part of the hyalectan family of proteoglycans.[43,51] Chondroitin sulfate GAG chains comprise of repeating disaccharides made up of glucuronic acid and N-acetyl-galactosamine. Glucuronic acid can be converted to iduronic acid by epimerases and when this occurs, PGs are classified as chondroitin sulfate/dermatan sulfate PGs due to the heterogenous content of disaccharide units. Versican GAG side chains contain up to 10% iduronic acid.[27]

Versican is the largest member of the hyalectan proteoglycans and alternative splicing of versican mRNA produces five versican isoforms that are different in size and chondroitin sulfate GAG content (**Figure 1.1**). The versican gene has 15 exons that correspond to the N-terminal G1 domain (exons 2-6), the α-GAG binding domain (exon 7), the β-GAG binding domain (exon 8), and the C-terminal G3 domain (exons 9-15). The G1 domain contains an immunoglobular (Ig)-like motif and link module structure which are known to bind hyaluronan and hyaluronan proteoglycan link protein 1 (HAPLN1).[52,53] The G3 domain contains two epidermal growth factor (EGF)-like repeats, a carbohydrate recognition domain (CRD) or lectin-like domain, and a complement binding protein (CBP)-like motif. Alternative splicing occurs at exons 7 and 8 impacting the two GAG-binding domains. V0 possesses both the α-GAG and β-GAG binding domains and is the largest isoform (~370 kDa).[54-56] V1 (~263 kDa) contains only the β-GAG domain, while V2 (~180 kDa) only has the α-GAG domain.[52,54,56] V3 (~74 kDa) is unique in that is lacks both GAG-binding domains. Finally, V4 (~135 kDa) contains only the first 1194 base-pairs of the N-terminal of the β-GAG domain.[52,57,58] All versican isoforms, with the exception of V3, have chondroitin sulfate attachment sites located on the GAG binding domains. The consensus sequence sites for GAG attachment on human versican suggest that the number of GAG chains is 17-23 for V0, 12-15 for V1, 5-8 for V2, and none for V3.[59]

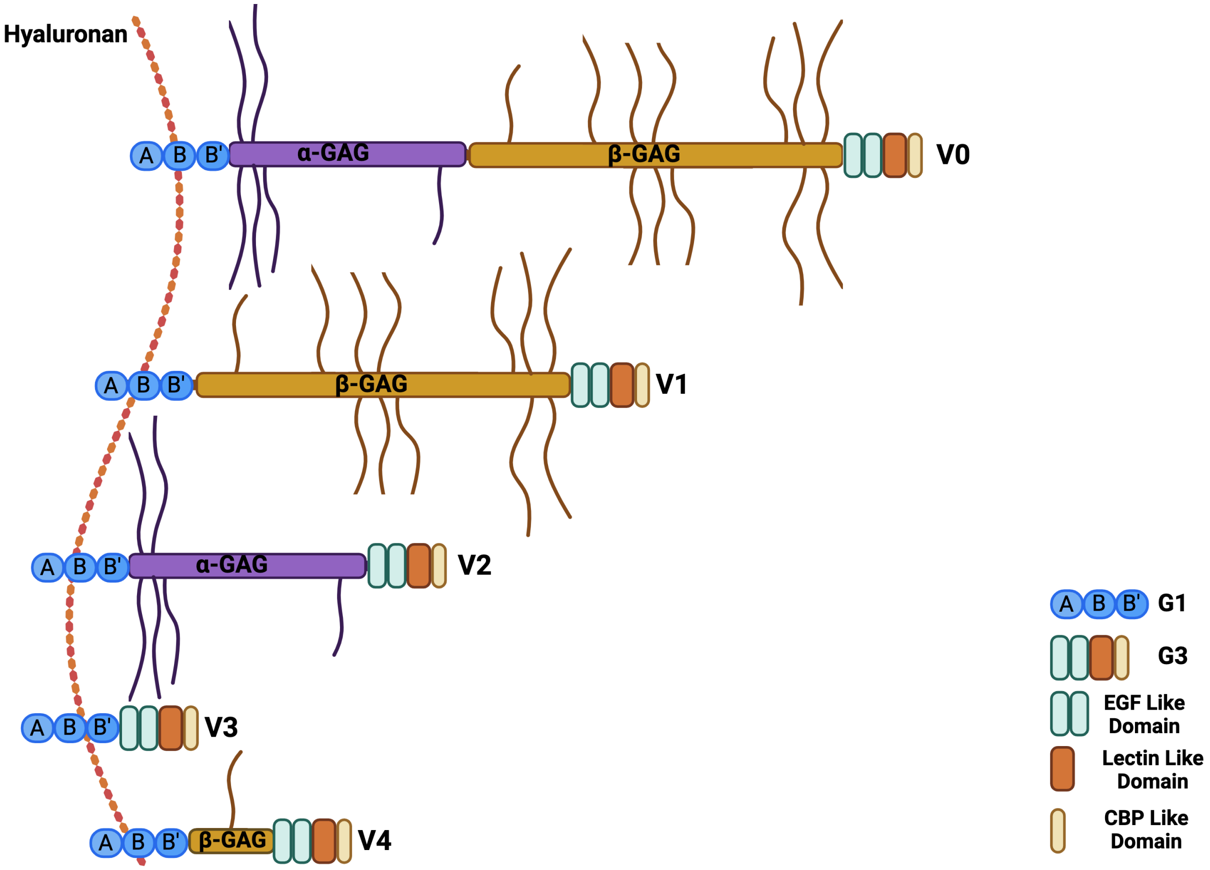

Figure 1.1 Isoforms of versican

Adapted from Tang et al.[1] The five isoforms of versican binding to hyaluronan through link modules in the G1 domain. V0 possesses both the α-GAG and β-GAG binding domains, V1 only has the β-GAG domain, V2 only has the α-GAG domain, V3 lacks GAG-binding domains, and V4 contains only the first 1194 base-pairs of the N-terminal of the β-GAG domain.

There are two signaling pathways that are responsible for versican expression. The canonical Wnt/β-catenin/T-cell factor (TCF) pathway has been shown to control the versican promoter in smooth muscle cells and β-catenin signaling was identified as being required for transforming growth factor-β1 (TGFβ1) -induced versican expression.[60,61] In macrophages, Trif-dependent and type I-interferon (IFN) -dependent signaling regulates versican expression, identifying versican as a type I IFN-stimulated gene.[62] Additionally, versican is necessary for type I IFN production by macrophages following exposure to toll-like receptor (TLR) agonists.[62] Increases in versican expression are therefore regulated in both a type I IFN-dependent and a type I IFN-independent manner. These signaling pathways are not exclusive to the cell types that they were initially demonstrated in, as both type I IFN-dependent and type I IFN-independent pathways have been shown to control versican expression in platelet-derived growth factor receptor β (PDGFRβ) positive stromal cells during IAV infection.[63]

Similar to other ECM molecules, degradation of versican by proteolysis generates bioactive matrikines. The cleavage of versican by proteases is thought to be sequential and yields bioactive fragments with distinct functions.[64,65] The majority of enzymes known to cleave the protein core of versican belong to the matrix metalloproteinase (MMP) and the A disintegrin and metalloproteinase with thrombospondin motifs (ADAMTS) families of proteases.[66] Both of these types of proteases require a zinc ion for catalytic activity, are synthesized as latent enzymes requiring activation, are active at neutral pH, and are known to catalyze the turnover of the ECM during development, homeostasis, and various disease conditions.[39,67-70] Four endogenous tissue inhibitors of metalloproteinases (TIMPs) have been identified that inhibit the activity of MMPs and ADAMTS proteases.[39,71,72]

Versican has multiple cleavage sites in its core protein that are known to be cleaved by ADAMTS proteases, including ADAMTS-1, -4, -5, -9, -15, and -20.[73-78] ADAMTS-8 is also predicted to cleave versican as it has been shown to cleave aggrecan and shares homology with the ADAMTS proteoglycanases that have activity against versican.[64] In the V0 isoform, ADAMTS cleavage sites are located at Glu^{405}-Gln^{406} in the α–GAG domain and at Glu^{1428}-Ala^{1429} in the β-GAG domain (V0 human sequence enumeration).[73,78] These cleavage sites correspond to single sites in the V1 and V2 isoforms at locations Glu^{441}-Ala^{442} and Glu^{405}-Gln^{406}, respectively.[73,78] Both cleavage sites have been validated in vivo using antibodies against the neoepitopes generated by ADAMTS cleavage with anti-DPEAAE441 (V1 human enumeration) corresponding to a β–GAG domain cleavage site and anti-NIVSFE405 (V0/V2 human enumeration) corresponding to the α-GAG domain cleavage site.[73,78]

The versican fragments generated from cleavage at these locations have been studied in various contexts.[55,64,79-83] The cleavage product of V1 at Glu^{441}-Ala^{442} generates a versican fragment with the neoepitope DPEAAE, which has been named versikine, and is conserved between humans and mice.[64,73] The cleavage product of V0/V2 at Glu^{405}-Gln^{406} that generates a versican fragment with the neoepitope NIVSFE has been named glial hyaluronate-binding protein (GHAP). This neoepitope has only been identified in humans and is found predominately in brain tissue.[78,84] In mice, the neoepitope NIVNSE, which corresponds to the Glu^{405}-Gln^{406} ADAMTS cleavage site within the mouse sequence was recently validated and will enable the researcher to better understand the bioactivity of GHAP in future studies.[81] Several other ADAMTS versican cleavage sites have been predicted from *in vitro* studies and computational modeling but still await *in vivo* validation.[85,86]

Versican's core protein is known to be cleaved by MMPs, including MMP-1, -2, -3, -7, -8, -9, and-12, but unfortunately, specific versican fragments and neoepitopes have not always been identified in these studies.[84,87-89] Versican derived from rabbit lungs with hydrostatic edema was shown to be sensitive to both MMP-2 and MMP-9 degradation, with the activity of MMP-2 being greater than that of MMP-9.[89] In atherosclerotic lesions, MMP-7 expression and positive immunostaining for versican were colocalized. Additionally, MMP-7 degraded versican *in vitro* more efficiently than MMP-1, -2, -3, and -9.[88] A versican cleavage site is known for MMP-1, -2, -3, and -9. These MMPs have been shown to cleave versican extracted from the bovine brain at Glu^{405}-Gln^{406} and generate GHAP as this is a cleavage site shared with ADAMTS proteases. In addition, MMP-8 and MMP-12 have been demonstrated to generate a bioactive versican degradation product named VCANM. VCANM is cleaved at position Tyr^{3305} in the G3 domain and has the neoepitope KTRFGKMKPRY.[87] VCANM is a potential biomarker for atherosclerotic disease, with high plasma levels correlating to patients with acute coronary syndrome; however, low levels of VCANM were associated with acute exacerbation of chronic obstructive pulmonary disease and idiopathic interstitial pneumonia.[87,90,91] Very little is known about the bioactivity of VCANM in different disease contexts. Therefore, more research is needed to better understand the role of VCANM in lung health and disease.

In addition to being cleaved by MMPs and ADAMTS, versican GAG side chains can bind directly with MMPs, ADAMTSs, and TIMPs, allowing their activity to be directly regulated by versican.[82,92-94] This regulatory effect is in part through the colocalization of protease with activators or inhibitors, some of which are members of the versican interactome, such as fibronectin or fibulin-1.[1,41,95,96] GAG side chains also indirectly regulate the function of proteases toward their chemokine and cytokine substrates which can be bound and sequestered by versican's GAG side chains, concealing them from proteolysis.[70,97] Cleavage of the versican protein core generating matrikines possessing GAG side chains may contribute to chemotactic gradients for these secreted factors and play an important role in inflammatory contexts.

The binding of secreted factors, such as chemokines, to versican is multifaceted due to the alternative splicing of GAG domains across versican isoforms. The work of Hirose et al. demonstrated that versican binds select chemokines and regulate their chemokine function. This work showed that versican binds to CCL2/MCP-1, CCL8/MCP-2, CXCL10/IP-10, CXCL4/PF4, CXCL12/SDF-1β, CCL5/RANTES, CCL20/LARC, and CCL21/SLC but not to CXCL5/ENA-78, CXCL1/GROα, CXCL8/IL-8, CCL7/MCP-3, CCL3/MIP-1α, CCL4/MIP1β, CCL18/PARC, CCL17/TARC, or CCL19/ELC.[97] Work by Tanino et al. showed that dermatan sulfate (also known as chondroitin sulfate-B, CS-B) inhibited the binding of mouse CXCL1/KC to immobilized heparin, suggesting that in mice, this key neutrophil chemotactic factor could bind to the versican side chain under certain conditions. In addition, they investigated how the kinetics of chemokine-GAG interactions contribute to chemokine functions and found that in the lungs, rapid association and disassociation of CXCL1/KC from heparin contributed to higher plasma CXCL1/KC levels and more effective neutrophil recruitment.[50] GAG chain sulfation pattern has also been shown to impact chemokine binding to versican with over-sulfated chains demonstrating inhibited binding of CCL21/SLC, CXCL-10/IP-10, CXCL4/PF-4, and CXCL12/SCF-1β compared with control versican.[98] The inhibition of KC binding to heparin by CS-B and the inhibition of chemokine binding due to altered sulfation are possible mechanisms by which versican may impact the kinetics of chemokine-GAG interactions and therefore chemokine activity in the lungs.

Beyond proteases and chemokines, versican interacts with many other important matrisome molecules. These include core matrisome proteins such as thrombospondin-1, tenascins, fibulin-1, fibulin-2, fibrillins, type I collagens and fibronectin; hyaluronan-associated factors such as tumor necrosis factor stimulated gene-6 (TSG-6), heavy chains (HC), and HAPLN1; adhesion molecules such as CD44, L-selectin, P-selectin glycoprotein ligand-1, and beta-1 integrins; and cell surface receptors such as TLR2, TLR4, and epidermal growth factor receptor (EGFR).[1] The diversity of versican's binding partners aligns with the diversity of biological activities that versican can influence. Previous studies have demonstrated that versican is able to modulate host immune responses by impacting leukocyte adhesion and chemotaxis, the biological activity of chemokines, and by altering macrophage phenotype.[83,97,99-101] These studies also demonstrate that the influence of versican over the host immune response is not only versatile but also contextual in nature. Biological outcomes related to versican may differ due to different cellular sources of versican, the signaling pathways involved in versican expression, the available versican binding partners within the ECM, and the inflammatory agonist under investigation. Studies of pulmonary inflammation utilizing conditionally versican-deficient mice show great promise in progressing our understanding of the contextual nature of versican-enriched ECM.

1.4 Contextual Role of Pulmonary Versican in Health and Disease

During embryonic development, versican is present throughout the lungs but is largely absent from mature, healthy lungs.[102] During pulmonary inflammation, versican reaccumulates in the lungs in both human patients and mouse models of lung injury.[27,66,89,100,102-111] Versican is expressed by a variety of cells involved in the pulmonary immune response including stromal cells, immune cells, and epithelial cells.[101,103-105] To understand better versican's role in lung inflammation and injury, preclinical studies must be conducted using conditionally versican-deficient mice because versican is required for embryonic development. The $\mathrm{Vcan}^{\mathrm{tm1.1Cwf}}$ mouse strain ($\mathrm{Vcan}^{\mathrm{fl/fl}}$) has loxP sites in introns 3 and 4. When these mice are exposed to Cre-recombinase, Vcan exon 4 is deleted and a resulting frameshift mutation creates a premature stop codon in exon 5. When $\mathrm{Vcan}^{\mathrm{fl/fl}}$ mice are crossed with various Cre-recombinase expressing mice, versican can be deleted in a time and cell-specific manner.

Studies using conditionally versican-deficient mice exposed to polyinosinic:polycytidylic acid (poly(I:C)), a synthetic analog of double-stranded RNA, and well established TLR-3 agonist, demonstrated the connection between the cellular source of versican and its immunomodulatory role in pulmonary inflammation.[100,103] These studies showed that mice with a global deficiency in versican (Rosa26/Vcan$^{-/-}$) treated with poly(I:C) have a decreased recovery of inflammatory leukocytes in the bronchoalveolar lavage (BAL) fluid (**Figure 1.2A**).[100] This suggests that versican plays a critical role in initiating leukocyte migration within the lungs, likely as part of a provisional pro-inflammatory matrix. In contrast, mice lacking versican in myeloid cells and type II epithelial cells (LysM/Vcan$^{-/-}$) had an increased recovery of inflammatory leukocytes in BAL fluid after instillation with poly(I:C) (**Figure 1.2B**).[100] This suggests an important role for macrophage and/or epithelial-derived versican during the period of resolution of lung injury and inflammation as part of a provisional pro-resolving matrix. Additionally, both Rosa26/Vcan$^{-/-}$ and LysM/Vcan$^{-/-}$ versican-deficient mice had significantly decreased levels of Type I IFN and IL-10 in lung tissue and BAL fluid following poly(I:C) exposure when compared to controls.[100] This highlights a critical role for versican in the pro-resolving matrix and links the production of these anti-inflammatory cytokines to versican expression in macrophages. Another study by Kellar et al. utilized airway epithelial cell versican-deficient mice (SPC/Vcan$^{-/-}$) infected with respiratory syncytial virus. Those data revealed increased migration of neutrophils and monocytes into the BAL fluid and lungs in SPC/Vcan$^{-/-}$ mice with elevated expression levels of chemokines CCL2, CCL3, and CCL4, suggesting that epithelial-derived versican attenuated leukocytes through chemokine mediated mechanisms (**Figure 1.2C**). [105]

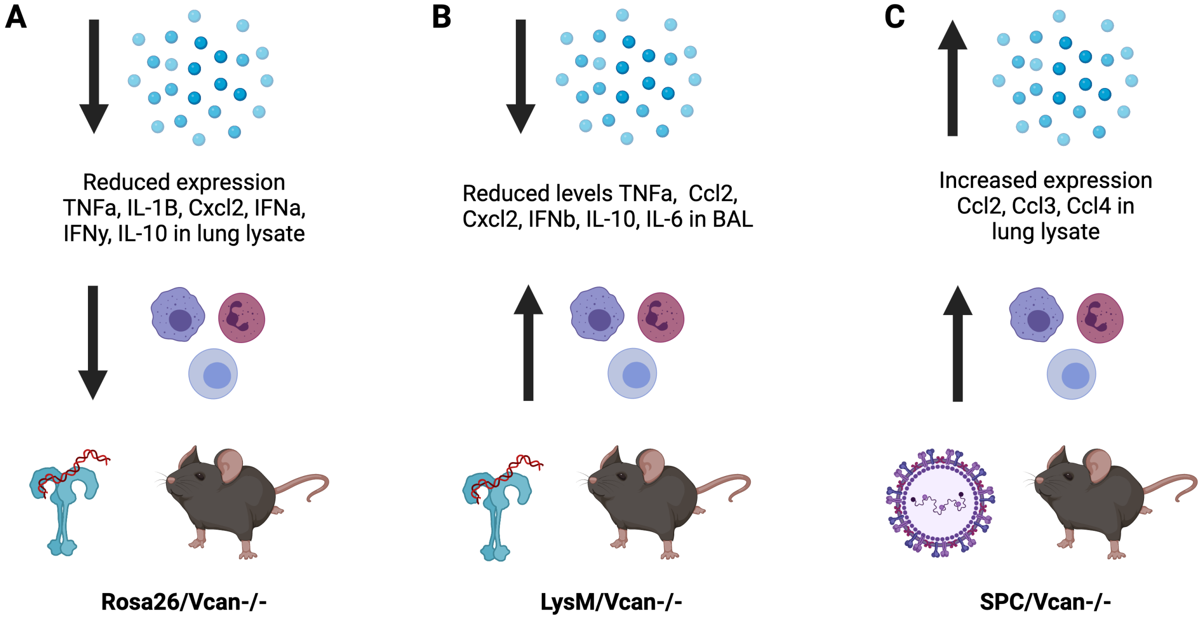

Figure 1.2 The role of versican in lung injury and inflammation

A summary of studies investigating the role of versican in lung injury and inflammation using mice that are deficient in versican in a time and cell specific manner. (A) RosaVcan$^{-/-}$ mice are globally deficient in versican and when exposed to poly(I:C) demonstrated a pro-inflammatory role for versican in lung injury while (B) LysM/Vcan$^{-/-}$ mice exposed to poly(I:C) demonstrated an anti-inflammatory role for myeloid-derived versican. (C) SPC/Vcan$^{-/-}$ mice infected with respiratory syncytial virus suggested an anti-inflammatory role for epithelial cell-derived versican.

Taken together these studies demonstrated both pro-inflammatory and anti-inflammatory roles for versican in lung injury and inflammation. The differential roles of versican from different cellular sources in the recruitment of immune cells and alteration of chemokines and cytokines highlight versican's potential as a modulator of host immunity in both the pro-inflammatory and pro-resolving provisional ECM during influenza infection. Additionally, this emphasizes that the cellular source implicated in versican expression is an important factor influencing versican's contextual control over immune cell migration into the lungs. One cellular source of versican that has not been specifically investigated in previous studies is fibroblast-derived versican. The phenotype of poly(I:C) instilled Rosa26/Vcan$^{-/-}$ mice likely captured some of the contributions of fibroblast-derived versican to the modulation of innate immunity but even when compared to poly(I:C) instilled LysM/Vcan$^{-/-}$ mice it is difficult to completely understand the role of fibroblast-derived versican in this model. Finally, additional factors such as the signaling pathway responsible for versican expression during lung injury and the agonist of lung inflammation under investigation should also be considered when evaluating the contextual nature of versican's role in pulmonary injury and inflammation.

In addition to studies leveraging mice that are conditionally deficient in versican, studies that utilize mice deficient in ECM proteases known to cleave versican give additional insight into versican's role during pulmonary injury and inflammation. Two important studies have investigated the role of ADAMTS proteases in the remodeling and degrading of the versican-enriched ECM in pulmonary organs during influenza infection. Boyd et al. investigated the role of ADAMTS-4 in the lungs. They found that mice lacking ADAMTS-4 had higher levels of versican accumulation combined with fewer CD8 lymphocytes, less alveolar inflammation, and less protein accumulation in the airways compared with wild-type controls at 9 days post infection (dpi) with influenza.[112] In ADAMTS-4-null mice, there was no change in the amount of gene expression of other known ADAMTS versicanases, thus identifying ADAMTS-4 as the primary ADAMTS protease in the lungs during influenza infection.[112] In addition, it was shown that ADAMTS-4-competent fibroblasts promoted T-cell migration across a versican barrier compared with ADAMTS-4-deficient fibroblasts in vitro.[112]

In contrast, McMahon et al. found that ADAMTS-5 was the primary ADAMTS protease responsible for the degradation of the versican-enriched ECM in the mediastinal lymph nodes during influenza infection.[113] Similar to the effect of ADAMTS-4 deficiency in the lungs, T-cell migration from the lymph nodes was impaired in influenza-infected ADAMTS-5-deficient mice.[113] In addition, versikine was decreased in the mediastinal lymph nodes of ADAMTS-5-deficient mice, suggesting that versican proteolysis by ADAMTS and/or the bioactivity of versikine may be necessary for T-cell migration in the context of influenza infection in pulmonary organs.[113] Although Boyd and colleagues did not assess versikine accumulation in the lungs, versikine accumulation has been shown to peak from baseline at 6 dpi with influenza in wild-type mice.[63]

Finally, a study by Bradley et al. identified neutrophils as the predominant pulmonary cellular source of MMP-9 during influenza infection. It was shown that the MMP-9-deficient mice had impaired neutrophil migration into airways, resulting in improved weight loss from severe influenza infection.[114] Although the activity of MMP-9 toward versican was not considered in this study, MMP-9 secretion by neutrophils was shown to be induced by TNF.[114] To investigate a possible mechanism between MMP-9, neutrophil migration, and versican during influenza infection, the predominant MMP-9 cleavage site on the versican core would need to be elucidated and any resulting versican fragments would need to be defined.

The findings of studies utilizing mice deficient in ECM proteases known to cleave versican underscore the complexity of the ECM during lung inflammation. Additionally, they highlight the potential for differences in available versican binding partners to influence the immunomodulatory properties of a versican-enriched ECM. Little is known about how temporal alterations in versican and its binding partners alter the host pulmonary immune response. As a versatile immunomodulatory integrator of the ECM, versican is an important potential target of host directed therapy for pulmonary inflammation.

1.5 Summary

Seasonal and pandemic influenza A virus strains remain a threat to human health globally.[2,3] As part of a classic host-pathogen arms race, influenza demonstrates the ability to undermine current prophylactics and therapeutics, especially those directly targeting viral replication and virion survival.[12,15] Additionally, the host immune response to IAV infection contributes to patient morbidity and mortality independently of viral burden, emphasizing that therapies which modulate the host immune response to IAV infection have potential for reducing the burden of severe influenza disease.[19,28,29] The host immune response is closely integrated with the pulmonary microenvironment of which the extracellular matrix is a critical component.[30,33,35] Our understanding of how the ECM regulates host innate immunity represents a critical knowledge gap and underscores the untapped potential of ECM targets for host-directed therapy in pulmonary injury and inflammation.

Versican is an immunomodulatory chondroitin sulfate proteoglycan that is a critical component of the host response to pulmonary inflammation and injury. As an integrator of the ECM, versican demonstrates potential as a host-directed target for immune modulation during pulmonary infection. Prior to the work of this thesis, the spatial-temporal changes in versican expression and accumulation during IAV infection in versican-competent mice were unknown. Additionally, studies utilizing conditionally versican-deficient mice infected with IAV had not been previously performed. Studies of poly(I:C) instilled globally versican-deficient mice and mice deficient in myeloid-derived versican are supportive of versican's potential to be a therapeutic target for IAV infection.[100,103] However, the role of fibroblast-derived versican in pulmonary innate immunity is a critical knowledge gap in our understanding of versican-enriched ECM.

This thesis aims to investigate the role of fibroblast-derived versican during the pulmonary immune response to IAV infection. Single-cell RNA sequencing data generously provided by David Boyd (University of California Santa Cruz, Santa Cruz, CA, **Figure 1.3**) revealed that versican is primarily expressed by cells that also have high expression of Col1a2 in the lungs of C57BL/6J mice prior to IAV infection. This data strongly supports that the utilization of mice that are versican-deficient in Col1a2 expressing cells will be important for testing the central hypothesis that fibroblast-derived versican is pro-inflammatory and enhances the innate immune response to IAV infection. To establish this mouse strain, $\text{Vcan}^{fl/fl}$ mice were crossed with mice carrying a transgene for a tamoxifen-inducible Cre-recombinase under the control of the Col1a2 promoter (B6.Cg-Tg(Col1a2-cre/ERT,-ALPP)7Cpd/J, Jackson Laboratory, Stock No: 029567) to generate B6. $\text{Col1a2-Cre}^{ERT+/-}/\text{Vcan}^{tm1.1Cwf}$ mice ($\text{Col1a2/Vcan}^{-/-}$). In addition to characterizing the spatiotemporal changes in versican expression and accumulation during IAV infection in versican-competent mice and investigating the role of fibroblast-derived versican during IAV infection, this thesis describes methodology for enhancing immune cell localization and characterization by combining dual *in vivo* CD45 labeling of leukocytes with spectral flow cytometry. Together the following chapters provide important insight into the role of versican during the innate immune response to IAV infection and present methodology that enhances the rigor and reproducibility of those findings.

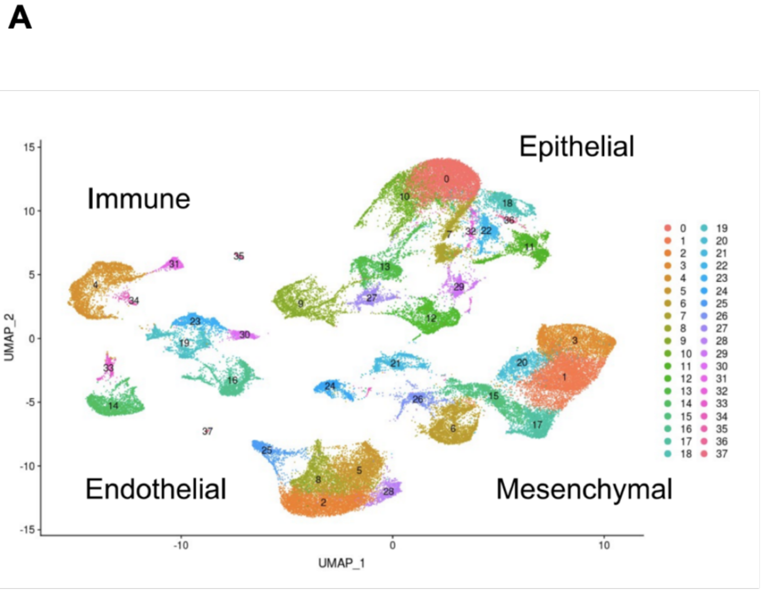

0 – AT2 (Epcam, Sftpc)
1 – Mfap5+ Fibroblasts (Pdgfra, Mfap5)
2 – Microvascular Endothelial Cells (Pecam1, Gpihbp1)
3 – Damage-responsive Fibroblasts (Pdgfra, Wt1)
4 – T cells (Ptprc, Cd3e)
5 – Activated Microvascular Endothelial Cells (Pecam1, Gpihdp1, S1pr1)
6 – Airway Smooth Muscle (Hhip, Acta2)
7 – IAV-infected Epithelial Cells (Epcam, Flu)
8 – Microvascular Endothelial Cells (Pecam1, Gpihdp1)
9 – High mitochondrial content Cells
10 – Krt8+ Epithelial Cells (Epcam, Krt8)
11 – AT2 (Epcam, Sftpc)
12 – Ciliated Epithelial Cells (Epcam, Foxj)
13 – Club Cells (Epcam, Scgb3a2)
14 – B cells (Ptprc, Cd19)
15 – Myofibroblasts (Pdgfra, Acta2)
16 – Neutrophils (Ptprc, Mmp9)
17 – Alveolar Fibroblasts (Pdgfra, Wnt2)
18 – Epcam+Pecam1+
19 – Monocytes (Ptprc, Ly6c2)
20 – Interferon-responsive fibroblasts (Pdgfra, Bst2)
21 – Mesothelial (Msln, Wt1)
22 – Epcam+Col1a2+
23 – Interstitial Macrophages (Ptprc, Cd68, C1qb)
24 – Lymphatic Endothelial Cells (Pecam1, Prox1)
25 – Car4 Endothelial Cells (Pecam1, Car4)
26 – Vascular Smooth Muscle Cells (Acta2, Pdgfrb, Notch3)
27 – AT1 (Epcam, Akap5, Ager)
28 – Macrovascular Endothelial Cells (Pecam1, Vwf)
29 – Ciliated Epithelial Cells (Epcam, Foxj)
30 – Alveolar Macrophages (Ptprc, Cd68, Chil3)
31 – NK Cells (Ptprc, Klrb1c)
32 – Epcam+Col1a2+
33 – Immune Doublets (Ptprc, Cd3e, Cd19)
34 – Regulatory T cells (Cd4, Il2ra)
35 – Basophils/Mast Cells (Ptprc, Fcer1a, Gata2)
36 – Multiplets
37 – Platelets

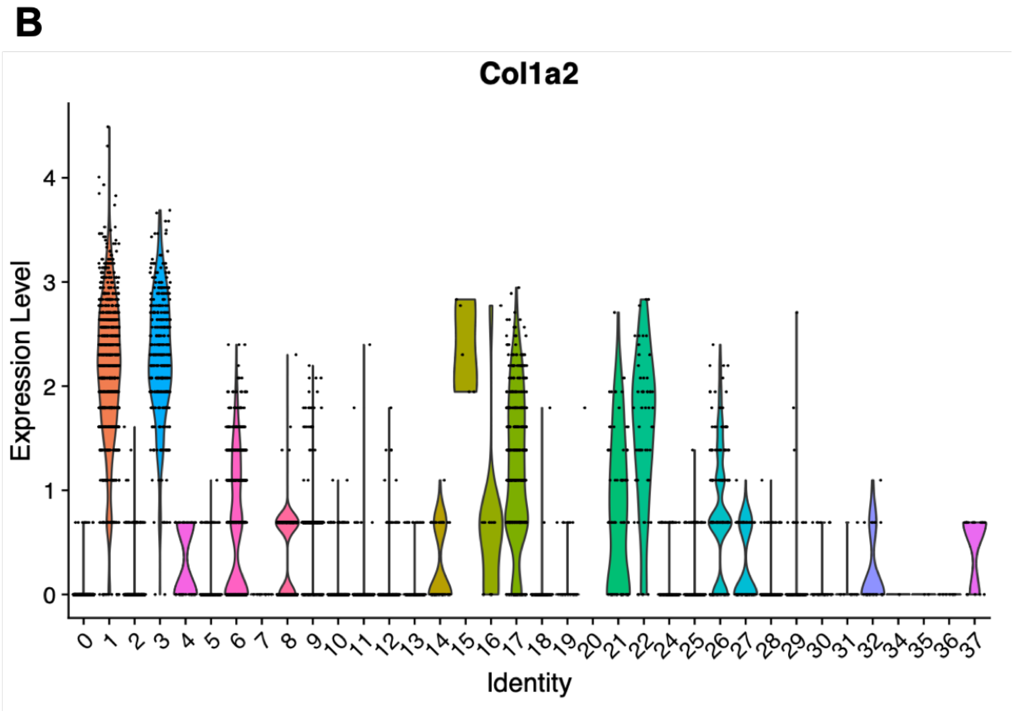

C

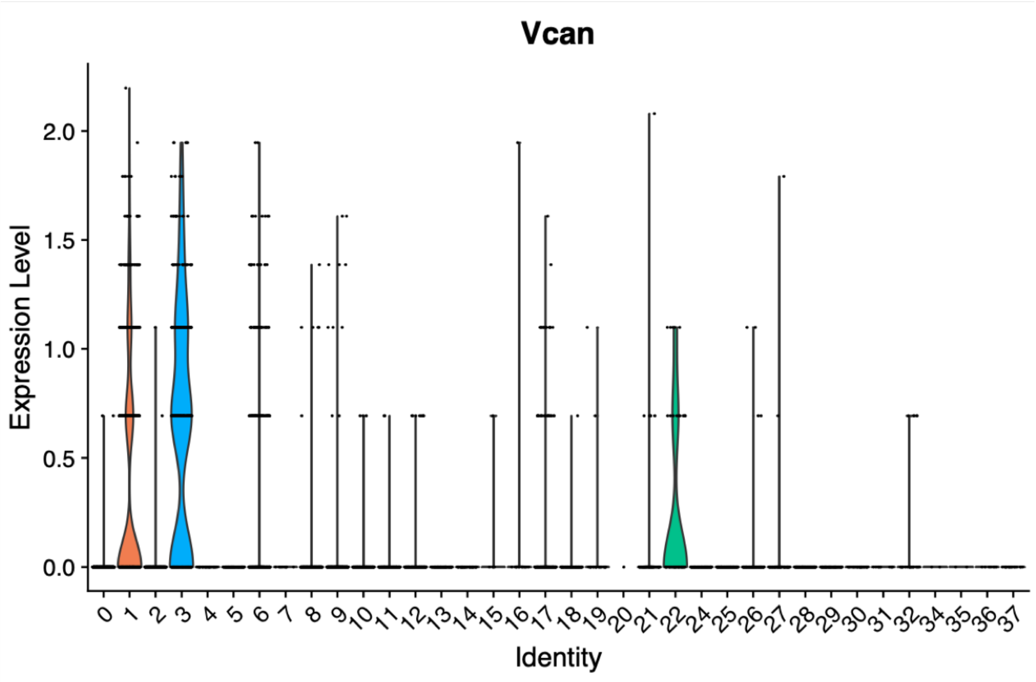

Figure 1.3 Expression of *Col1a2* and *Vcan* in Lung Cells

10x genomics single-cell RNA sequencing datasets of C57BL/6J mice infected with influenza A virus (A/Puerto Rico/8/1934), graciously provided by David Boyd. (A) Aggregate of datasets from day 0, 1, 3, 6, and 21 post-infection and key to numbered cell populations (B) In vehicle instilled mice (day 0), Col1a2 expression is predominant in Mfap5+ fibroblasts (Pdgfra, Mfap5), damage-responsive fibroblasts (Pdgfra, Wt1), airway smooth muscle (Hhip, Acta2), microvascular endothelial cells (Pecam1, Gpihbp1), myofibroblasts (Pdgfra, Acta2), neutrophils (Ptprc, Mmp9), alveolar fibroblasts (Pdgfra, Wnt2), mesothelial (Msln, Wt1), Epcam+Col1a2+ cells, vascular smooth muscle cells (Acta1, Pdgfrb, Notch3), and AT1 (Epcam, Akap5, Ager). (C) In vehicle instilled mice (day 0), Vcan expression is predominant in Mfap5+ fibroblasts (Pdgfra, Mfap5), damage-responsive fibroblasts (Pdgfra, Wt1), and Epcam+Col1a2+ cells.

Chapter 2. Type I Interferon Signaling Increases Versican Expression and Synthesis in Lung Stromal Cells During Influenza Infection

2.1 Introduction

Versican, a chondroitin sulfate proteoglycan, is an ECM molecule that is abundantly expressed in the lungs during embryonic development and is minimally expressed in the healthy lungs of adult mice and humans.[57,58,102] There are five isoforms of versican with different glycosaminoglycan (GAG)-binding domains: V0 containing α-GAG and β-GAG domains, V1 containing only the β-GAG domain, V2 containing only the α-GAG domain, V3 containing no GAG-binding domains, and V4 which contains a portion of the β-GAG domain.[54,57,58,102] Re-expression and accumulation of versican in the mature lung is a consistent finding in the study of various inflammatory lung diseases in human patients and studies using mouse models of pulmonary disease.[27,40,94,101,102,104,106-108,115,116] Versican is increasingly recognized as a critical component of the immune response, particularly regarding the interactions of the versican-enriched ECM with immune cells as they move from circulation to sites of pulmonary inflammation.[31,52,99,100,103,105,112,113] Versican interacts with immune cell surface receptors and impacts immune cell phenotype, adhesion, migration, activation, and retention within the inflamed lung.[42,66,99-101,117,118] Versican also retains, releases, and interacts with cytokines, chemokines, and growth factors, which further inform immune cell activity and direct the host inflammatory response.[48,97,119] Two signaling pathways, previously identified in vitro in specific cellular lineages, are responsible for versican expression. In smooth muscle cells, the canonical Wnt/β-catenin/T-cell factor (TCF) pathway controls versican promoter activity, and β-catenin signaling is required for transforming growth factor-β1–induced versican expression.[60,61,120,121] Our previous work demonstrated that Trif-dependent and type I interferon (IFN)–dependent signaling regulates versican expression, identifying versican as a type I IFN–stimulated gene in macrophages.[103] In addition, our studies showed versican is necessary for type I IFN production by macrophages following exposure to toll-like receptor agonists.[103] Type I IFNs play a critical role in regulating the immune response to viral infection and establishing the host antiviral state.[122,123] Taken together, these data indicated that type I IFN–stimulated versican likely plays an essential role in coordinating the immune response in viral pneumonia.

However, little is known about the expression and accumulation of versican in the context of viral pneumonia. In addition, the cellular specificity of the production of type I IFN–stimulated versican during lung infection is unknown. Studies using versican-deficient mice exposed by oropharyngeal instillation to polyinosinic:polycytidylic acid [poly(I:C)], a synthetic analog of double-stranded RNA, and toll-like receptor-3 (TLR3) agonist showed that versican is an immunomodulatory molecule.[100,103] These studies demonstrated that mice lacking versican in macrophages (LysM/Vcan$^{-/-}$) have an increased recovery of inflammatory leukocytes in bronchoalveolar lavage (BAL) fluid after instillation with poly(I:C), suggesting an anti-inflammatory role for type I IFN signaling–stimulated versican expression by macrophages. In contrast, mice with a global deficiency in versican (Rosa26/Vcan$^{-/-}$) treated with poly(I:C) had a decreased recovery of inflammatory leukocytes in the BAL fluid, suggesting that versican produced by stromal cells plays a critical role in initiating leukocyte migration within the lungs. The versatile activities of versican produced by different cell types in coordinating the host immune response to pulmonary infection and inflammation warrant further investigation into its roles in the host response to viral pneumonia pathogenesis.

Therefore, this study established the time course of changes in versican expression, versican accumulation, and leukocyte migration into the lungs during severe influenza A virus (IAV) infection. In addition, the study characterized the role of type I IFN signaling and identified the cellular source of type I IFN–stimulated versican during influenza infection in the lungs. The study encompassed a 12-day time frame after infection to focus on the entire disease phase (0–9 days post-infection) and a limited portion of the recovery phase (10–12 days post-infection). We observed the accumulation of versican and inflammatory cells from myeloid and lymphoid lineages in all lung compartments throughout influenza infection using immunohistochemical techniques and quantitative digital pathology.[124] We investigated the role of type I IFN during influenza infection and identified another cellular source, in addition to macrophages, in which type I IFN stimulates versican expression. Day 9 is a critical time point as this is when the transition from the disease to the recovery phase occurred and there was an increased accumulation of myeloid immune cell infiltration into the lungs. We used novel image analysis techniques to accomplish this work, and employed artificial intelligence and machine learning to perform high-quality quantitative digital pathology (QDP). These studies demonstrated that (1) versican mRNA expression and protein accumulation peak in influenza-infected lungs on 6 days post-infection (dpi) and 9 dpi, respectively, in concert with various immune cell populations; (2) versican expression correlates closely with type I IFN expression, particularly on 3 and 6 dpi; and (3) stromal cells contribute significantly to type I IFN–stimulated versican in the transition from the disease phase to recovery phase on 9 dpi. Our findings provide the basis for the development of future mechanistic studies.

2.2 Materials and Methods

2.2.1 Animal Model

Eight- to 10-week-old male C57BL/6J wild-type (WT) and B6(Cg)-Ifnar1$^{tm1.2Ees}$/J (Ifnar1^{-}) mice (The Jackson Laboratory; Bar Harbor, ME) housed under standard conditions and on a 10:14 hr dark:light cycle were infected with mouse-adapted IAV. The lungs were collected for immunohistochemistry, mRNA isolation, and in situ hybridization. In all experiments, the sample size (*n*) is the number of mice per group. All procedures were performed as part of an approved scientific protocol in accordance with the University of Washington Institutional Animal Care and Use Committee (IACUC).

2.2.2 Induction of IAV Pneumonia

Mouse-adapted influenza A/Puerto Rico/8/34 (A/PR/8/34; H1N1) was grown in the allantoic fluid of research-grade-specific pathogen-free (SPF) embryonic chicken eggs (Charles River Avian Vaccine Services; Norwich, CT), and a hemagglutination assay was performed to determine the viral titer.[125] Male mice were infected with 20 plaque-forming units (PFU) in 50 µL PBS by oropharyngeal aspiration under isoflurane anesthesia.[126] Our lab had previously found that a dose of 20 PFU caused severe influenza pneumonia in which mice approach humane euthanasia endpoint criteria but ultimately recover from infection. In addition, 20 PFU was an intermediate dose compromising 40% of the euthanasia dose 50, which was 50 PFU for C57BL/6J male mice infected with mouse-adapted influenza A/PR/8/34 H1N1.[127] Control mice received PBS alone. Mice were sacrificed at 3, 6, 9, and 12 dpi by exsanguination under isoflurane anesthesia.

2.2.3 Versican, Versikine, and Leukocyte Marker Quantitative Immunohistochemistry

Lungs for immunohistochemistry experiments were inflated with 10% neutral buffered formalin at 21 cm H_2O pressure and, along with the heart and mediastinal lymph nodes, immersed in 10% neutral buffered formalin for 24 hr, transferred to 70% ethanol, and embedded in paraffin.[62,128] A cutting instrument with trimming blades was used to section the mouse lungs into 2 mm sagittal sections to ensure uniform random sampling of all lung lobes.[124] Five to six sagittal lung sections were embedded per paraffin block and placed on corresponding slides.

All immunohistochemistry staining procedures including deparaffinization for 30 min at 72C were performed on the Leica Bond Automated Immunostainer (Leica Biosystems; Buffalo Grove, IL). For all protocols, except versican immunohistochemistry, deparaffinization was followed by antigen retrieval at 100C and peroxide block for 5 min at room temperature before combining with the primary antibody. The versican immunohistochemistry staining protocol includes an additional digestion step before peroxide block. Primary and secondary antibodies were applied as described for the specific protocol, followed by DAB detection, hematoxylin counterstain, and mounting as directed by the manufacturer for the BOND Polymer Refine (DAB) Detection system (Leica Biosystems).

Versican immunohistochemistry was performed using an anti-β-GAG antibody with reactivity to V0 and V1 versican isoforms based on the presence of β-GAG found in each isoform (V0 α-GAG and β-GAG, V1 β-GAG only). V0 and V1 isoforms predominate in inflamed lungs.[100] All lungs were pretreated with heat-induced epitope retrieval solution-1 (HIER1), a citrate-based buffer and surfactant (Leica Biosystems), for 10 min and then with 0.2 U/ml chondroitinase ABC (cat. no. C3667; MilliporeSigma, Burlington, MA) in 18 mM Tris, 1 mM sodium acetate, and 1 mg/ml BSA pH 8.0 for 1 hr at 37C as previously described.[104] Peroxide block was performed before combining with a polyclonal rabbit anti-mouse β-GAG antibody (cat. no. AB1033, lot no. 3050782; MilliporeSigma, Burlington, MA) at 1:250 in Leica primary antibody diluent for 30 min at room temperature to detect versican accumulation.

Versikine immunohistochemistry was performed using an anti-DPEAAE antibody with reactivity to the versican V0/V1 neoepitope degradation product. All lungs were pretreated with heat-induced epitope retrieval solution-2 (HIER2), an EDTA-based buffer and surfactant (Leica Biosystems), for 10 min before incubating with a polyclonal rabbit anti-mouse DPEAAE antibody (cat. no. PA1-1748A, lot no. MB153302; Invitrogen, Carlsbad, CA) at 1:800 in Leica primary antibody diluent for 60 min at room temperature.

For Ly6b, F4/80, CD3, and CD8 immunohistochemistry of lung tissue, antigen retrieval was performed with HIER2 for 10 min with Ly6b and 20 min with F4/80, CD3, and CD8. For CD68 and CD4 protocols, antigen retrieval was performed with HIER1 at 10 and 20 min, respectively, before incubating with a primary monoclonal antibody. The following primary monoclonal antibodies were used: rat anti-mouse Ly-6b.2 alloantigen antibody, clone 7/4 (cat. no. MCA771G, lot no. 1801; Bio-Rad, Hercules, CA) at 1:10,000; rat anti-mouse CD68 antibody, clone FA-11 (cat. no. MCA1957, lot no. 1807; Bio-Rad) at 1:1500; rabbit anti-mouse F4/80 antibody, clone D2S9R (cat. no. 70076S, lot no. 5; Cell Signaling, Beverly, MA) at 1:500; rat anti-mouse CD3 antibody, clone CD3-12 (cat. no. MCA1477, lot no. 1708Bio-Rad) at 1:100; rat anti-mouse CD8 antibody, clone 4SM15 (cat. no. 14-0808-80, lot no. 2144532; eBioscience, San Diego, CA) at 1:1000; and rat anti-mouse CD4 antibody, clone 4SM95 (cat. no. 14-9766-80, lot no. 4342629; eBioscience) at 1:800. All primary antibodies were diluted in Leica Primary antibody diluent for 30 min at room temperature except for the primary F4/80 antibody, which was diluted in Signal Stain(R) Ab Diluent (cat. no .8112L, lot no. 30; Cell Signaling) for 30 min at room temperature. For Ly6B, CD68, CD3, CD4, and CD8 protocols, the primary antibody was followed by a rabbit anti-rat IgG(H+L), Mouse Adsorbed, Unconjugated secondary antibody (cat. no. AI-4001, lot no. ZF-0513; Vector, Burlingame, CA) at 1:300 in 5% normal goat serum and tris-buffered saline (TBS) for 8 min at room temperature. For F4/80, the primary antibody was followed by a goat anti-rabbit polymer-HRP-IgG in 10% animal serum and TBS for 8 min at room temperature. Negative controls were performed using purified Rabbit IgG (cat. no. AB-105-C, lot no. ER1314071; R&D Systems, Minneapolis, MN) at 1:1000 or purified Rat IgG2b Isotype (cat. no. 553986; BD Pharmingen, San Jose, CA) at 1:1000 in Leica primary antibody diluent for 30 min at room temperature.

Image analysis was performed following immunohistochemistry using whole-slide digital images and automated image analysis. Bright-field whole-slide digital images were created using a 20× objective and the Nanozoomer Digital Pathology slide scanner (Hamamatsu; Bridgewater, NJ). Analysis of the whole-slide digital images was performed using Visiopharm software (Visiopharm; Hoersholm, Denmark). Regions of interest (ROIs) were manually defined by drawing around the visible area of the lung, excluding any cardiac or mediastinal lymph node tissue present on the slide. Digital features RGB-G, RGB-B, HDAB-DAB, H&E Eosin, and Chromaticity Red were trained to label positive staining for versican or leukocyte markers and the background tissue counterstain (hematoxylin) using project-specific configurations based on a threshold of pixel values. Images were processed to generate desired outputs (area of positive staining for leukocyte markers or versican as a ratio of positive staining to total tissue area). All ROIs were sampled at 100%. Based on the output for each slide analyzed, the mean value for percentage positive staining for each day post-infection was calculated by averaging the results for mice collected on particular days post-infection.

2.2.4 Acute Lung Injury Scoring

Histological assessment of lung inflammation and injury was completed using formalin-fixed paraffin-embedded lung tissue stained with hematoxylin and eosin (H&E).[129] The lung injury score was performed using a modified version of previously described semiquantitative scoring systems.[130-133] The analysis was performed by a comparative pathologist (C.W.F.) who was blinded to the treatment group. Assessment of lung inflammation and injury included the extent and severity of the following parameters: (1) lung involvement (%), (2) bronchiolitis/peribronchiolitis, (3) vasculitis/perivasculitis, (4) alveolitis and interstitial pneumonia, and (4) chronic active fibrosis, including dysplastic alveolar regeneration.[129,134-136] The score for each parameter was given a value from 0 to 3, with 0 being normal and 3 being the most severe. Due to the significance of lung involvement and chronic-active fibrosis to long-term health, the scores for these two parameters were weighted. The score was doubled for lung involvement and tripled for chronic-active fibrosis, resulting in the maximum lung injury score of 24. The complete scoring system used to evaluate lesions observed in H&E-stained lung tissue is described in **Table 2.1**.

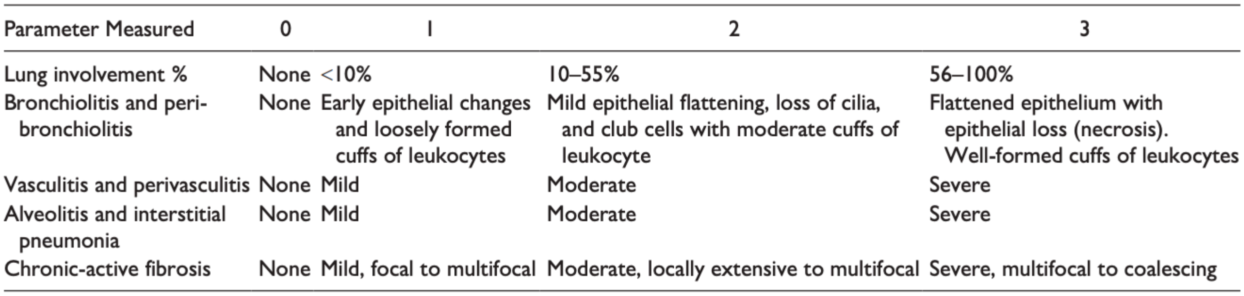

Parameter Measured	0	1	2	3
Lung involvement %	None	<10%	10–55%	56–100%
Bronchiolitis and peri-bronchiolitis	None	Early epithelial changes and loosely formed cuffs of leukocytes	Mild epithelial flattening, loss of cilia, and club cells with moderate cuffs of leukocyte	Flattened epithelium with epithelial loss (necrosis). Well-formed cuffs of leukocytes
Vasculitis and perivasculitis	None	Mild	Moderate	Severe
Alveolitis and interstitial pneumonia	None	Mild	Moderate	Severe
Chronic-active fibrosis	None	Mild, focal to multifocal	Moderate, locally extensive to multifocal	Severe, multifocal to coalescing

Table 2.1 Lung Injury Score

2.2.5 Quantitative Real-time Reverse-transcription PCR

The left lung lobe was used for mRNA isolation and was cut into small pieces with no dimension greater than 0.5 cm before being placed in 5 ml of RNAlater (Invitrogen). RNAlater solution containing lung pieces was gently rotated at 4C overnight. RNA was extracted using RNAeasy Mini Kit with on-column DNase digestion (Qiagen; Valencia, CA). RNA quality was measured, and an RNA integrity number (RIN) was determined for each sample (Bioanalyzer RNA 6000 Nano Kit; Agilent, Wilmington, DE). All samples had a RIN between 8.2 and 9.7. cDNA was reverse-transcribed using random primers with the High Capacity cDNA Reverse Transcription Kit (Applied Biosystems, Foster City, CA). Quantitative real-time reverse-transcription polymerase chain reaction (PCR) was performed on an ABI Prism 7900HT Fast Real-Time PCR System (Applied Biosystems) using PrimeTime Gene Expression Master Mix (Integrated DNA Technologies, Coralville, IA). Gene-specific TaqMan primer-probe mixes were used for quantitative real-time PCR of versican (Mm01283063_m1), interferon beta (IFN-β) (Mm00439552_s1), and TATA-box protein (Mm01277042_m1) mRNA (ThermoFisher Scientific; Grand Island, NY). The primer-probe mix spanning the junction of versican exon 3–4 was used to detect the expression of all five versican isoforms.

2.2.6 Versican, PDGFRβ, and CD68 Quantitative In Situ Hybridization

Lungs for in situ hybridization experiments were inflated with 10% neutral buffered formalin at 21 cm H_2O pressure, immersed in 10% neutral buffered formalin for 16–24 hr, washed in molecular-grade PBS, transferred to 70% ethanol for up to 48 hr, and embedded in paraffin. A cutting instrument with trimming blades was used to section the mouse lungs into 2 mm sagittal sections to ensure uniform random sampling of all lung lobes.[124] Five to six sagittal lung sections were embedded per paraffin block and on corresponding slides. Blocks were stored at 4C with desiccant. Instruments, work surfaces, gloves, and blades associated with microtomy were treated with RNAse Away, and RNAse free water was used for the floatation bath.

All in situ hybridization staining procedures were performed on the Leica Bond Automated Immunostainer (Leica Biosystems) with ready-to-use (RTU) 2.5 LS duplex target probes for mouse platelet–derived growth factor receptor beta (PDGFRβ) (cat. no. 411388, lot no. 19142A), CD68 (cat. no. 316618, lot no. 19142A), and versican (cat. no. 486238-C2, lot no. 19142A) at 1:50 in PDGFRβ RTU LS Probe or CD68 RTU LS Probe, control probes PPIB(C2) (cat. no.

313918-C2, lot no. 1914A) at 1:50 in POLR2A(C1) (cat. no. 320768, lot no. 19036A) RTU, negative control bacterial gene DapB-C2 (cat. no. 312038-C2, lot no. 19142A) at 1:50 in Duplex Negative Control Probe C1 (cat. no. 320758, lot no. 18344A) RTU, and the 2.5 LS duplex reagent kit (cat. no. 322440) as directed by the manufacturer (ACDBio; Newark, CA). Briefly, slides were baked and deparaffinized on the Leica Bond Automated Immunostainer, pretreated with HIER2 for 15 min at 95C, and underwent protease III digestion for 15 min at room temperature before combining with positive, negative, or test probes for 120 min at room temperature. In situ hybridization amplification steps specific to the protocol were followed by peroxide block, Leica bond mixed red detection (cat. no. DS9390, lot no. 64002), staining with ACD C1 green stain, counterstaining with hematoxylin, and baking at 60C for 30 min according to the manufacturer's instructions.

Image analysis was performed following immunohistochemistry using whole-slide digital images and automated image analysis. All slides were scanned in bright field with a 20× objective using a Nanozoomer Digital Pathology slide scanner (Hamamatsu). Whole-slide digital images were imported for analysis into Visiopharm software (Visiopharm). ROIs were manually defined by drawing around the visible area of the lung. The digital feature contrast red-green was used to label positive staining for versican (red) or cell markers CD68 and PDGFRβ (green), and the digital feature RGB-R with a mean filter was used to label background tissue counterstain (hematoxylin) using project-specific configurations based on a threshold of pixel values. Images were processed to generate desired outputs (total pixels of positive staining for PDGFRβ, CD68, and versican as a ratio of positive staining to total tissue area). All ROIs were sampled at 100%. Next, a digital feature to identify nuclei was created using the Deep Learning module in the Visiopharm APP Author software. This module was given examples of manually segmented nuclei and trained for 24,373 iterations to develop the algorithms used to identify nuclei. The machine learning algorithms were then used to identify and label nuclei in image ROIs randomly sampled at 20%. The labeled nuclei were then processed using a range of digital features and postprocessing steps to generate desired outputs, which included the number of nuclei that were single-positive for versican mRNA and double-positive for PDGFRβ/versican and CD68/versican mRNA, and the percentage of PDGFRβ nuclei that were double-positive for PDGFRβ/versican mRNA. Based on the output for each slide analyzed, the mean values were calculated and reported by mouse strain or cell marker of interest.

2.2.7 Stromal Cell Culture

Mouse lung fibroblasts were isolated from whole lung explants by digestion as previously described.[137] Lungs were aseptically removed from the thorax, minced, and transferred into a 15-ml conical tube with 2.5 ml digestion solution consisting of Dulbecco's Modified Eagle Medium/Nutrient Mixture F-12 (DMEM/F-12) high-glucose medium, 1000 U/ml Liberase TL, and 1000 U/ml DNase I. Lung digests were incubated in a shaking water bath for 60 min at 37C. Then digest was filtered through a 100-µm cell strainer with DMEM/F-12 containing 10% fetal bovine serum (FBS), and the red blood cells were lysed by suspending the cells in sterile water for 30 sec. The fibroblasts were then washed and plated in DMEM/F-12 with 20% FBS, 2 mM L-glutamine, 100 IU/ml penicillin, and 100 µg/ml streptomycin and incubated at 37C with 5% CO_2. The cell culture medium was changed every 3–4 days and fibroblasts were passaged once confluent. At each subsequent passage, FBS content was reduced by 5% through passage 2. Fibroblasts were maintained in DMEM/F-12, 10% FBS, 2 mM L-glutamine, 100 IU/ml penicillin, and 100 µg/ml streptomycin. For experiments, fibroblasts were used between passages 4 and 6. Fibroblasts were serum-starved with DMEM/F-12 medium containing 1% FBS for 24 hr before stimulation with IFN-β and lipopolysaccharide (LPS). Confluent cells were stimulated with LPS from *Escherichia coli* serotype 0111: B4 (lot no. 2014641; List Biological Laboratories, Campbell, CA) at 100 ng/ml and IFN-β (PBL Interferon Source; Piscataway, NJ) at 100 units/ml. After 4 hr of stimulation, the medium was removed, cells were washed with PBS, and RNA was extracted using RNAeasy Plus Mini Kit (Qiagen).

2.2.8 Statistics

Statistics and images were generated using GraphPad Prism (La Jolla, CA). For PCR analyses of gene expression, normalized mRNA levels were expressed as -fold of levels in untreated or vehicle-treated controls using the comparative cycle threshold (Ct) method compared with the housekeeping gene TATA-binding protein (TBP).[104,138] Quantitative PCR (qPCR) analyses were performed with two technical replicates. Comparisons of qPCR and quantitative immunohistochemistry and in situ hybridization data were analyzed by one-way ANOVA followed by Bonferroni's posttest for multiple comparisons, with the mean of every influenza-treated group compared with the mean of vehicle-treated groups. Comparisons for acute lung injury scoring were analyzed by Kruskal–Wallis followed by Dunn's posttest for multiple comparisons, with the mean of every influenza-treated group compared with the mean of vehicle-treated groups.[139] In vitro qPCR data were analyzed by one-way ANOVA followed by Bonferroni's posttest with all possible comparisons performed. Statistical results with a value of $p<0.05$ were considered statistically significant.

2.3 Results

2.3.1 Versican β-GAG Accumulation and Acute Lung Injury Scoring Correlated During IAV Infection

Versican accumulation was measured and correlated with weight loss and acute lung injury from IAV infection. Disease progression was monitored daily in mice infected with IAV by measuring changes to body weight. Mice infected with IAV had significant weight loss as measured by percentage of initial weight beginning on 3 dpi (98.3% ± 0.3%) and reached their maximum weight loss (73.0% ± 0.9%) at 10 dpi (**Figure 2.1A**). After 10 dpi, mice regained weight but maintained a significant percentage of weight loss compared with PBS-treated controls (**Figure 2.1A**).

The maximum percentage of versican protein accumulation coincided closely with the maximum weight loss time point and was observed on 9 dpi (34.3% ± 1.0%). In addition, versican accumulation was significantly increased on 6 dpi (31.5% ± 2.0%) and 12 dpi (31.0% ± 2.5%) in IAV-infected mice compared with PBS controls (**Figure 2.1B**).

The accumulation of versikine, a degradation product of versican after cleavage by A-Disintegrin-like and Metalloproteinase with Thrombospondin-1 motifs (ADAMTS) proteases, as measured by the detection of the anti-DPEAAE neoepitope was significantly increased on 6 dpi (0.64% ± 0.08%) in IAV-infected mice compared with PBS controls (**Figure 2.1C**).

Acute lung injury scores were increased similarly to trends observed in versican accumulation. Maximum lung injury scores were observed on 12 dpi (17.3 ± 1.1) and were significantly increased on 6 dpi (11.2 ± 0.3) and 9 dpi (12.8 ± 0.6) in IAV-infected mice compared with PBS controls (**Figure 2.1D**). Using a simple linear regression model, the correlation between versican accumulation and acute lung injury scoring was significant through 12 dpi ($r^2 = 0.4643$, $p<0.0001$; **Figure 2.1E**).

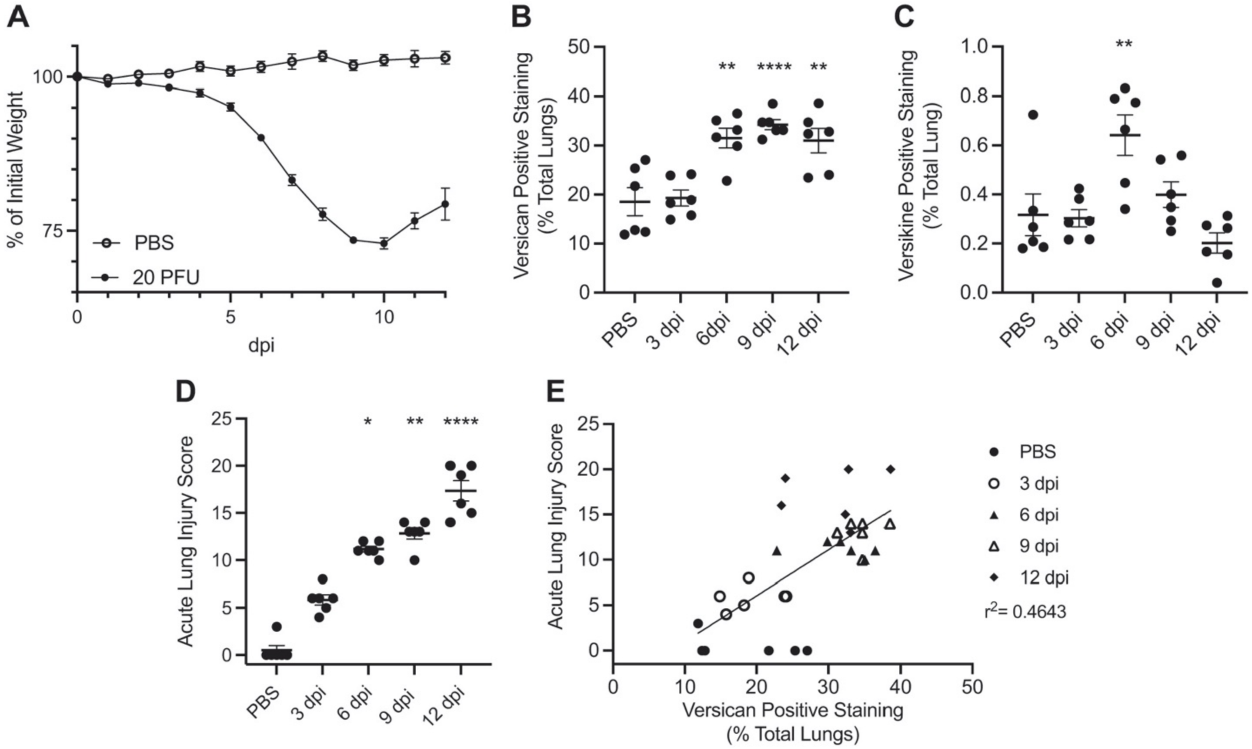

Figure 2.1 Weight loss, versican and versikine accumulation, and acute lung injury scores during influenza A virus infection

(A) Mouse percentage of initial body weight following infection with IAV over 12 days post-infection (dpi). Infected mice reached their maximum weight loss by 10 dpi. Values are mean ± SEM with *n*=24–6 per time. (B) Percentage of versican protein accumulation and (C) percentage of versikine accumulation in the lungs during IAV infection shown on days 3, 6, 9, and 12 after infection and in vehicle (PBS)-treated controls. Accumulation of versican and versikine was determined using immunohistochemistry and quantitative digital pathology. Values are mean ± SEM with *n*=6 per time. Asterisks show groups that are statistically significantly different (**$p \leq 0.005$; ****$p \leq 0.0001$) from PBS-treated controls using a one-way ANOVA with Bonferroni's multiple comparison test. (D) Acute lung injury scores during IAV infection shown on days 3, 6, 9, and 12 after infection and in vehicle (PBS)-treated controls. Values are mean ± SEM with *n*=6 per time. Asterisks show groups that are statistically significantly different (*$p \leq 0.05$; **$p \leq 0.005$; ****$p \leq 0.0001$) from PBS-treated controls using a Kruskal–Wallis followed by Dunn's posttest for multiple comparisons. (E) Percentage of versican protein accumulation correlation with acute lung injury score. Mice collected on 12 dpi demonstrated variable lung injury and versican accumulation as demonstrated by poor clustering of ◆ data points. Abbreviations: IAV, influenza A virus.

2.3.2 Versican b-GAG Accumulation Corresponded With Inflammatory Cell Infiltration in the Lungs of Mice During IAV Infection

To measure changes in versican accumulation in lungs infected with IAV, we performed immunohistochemistry using a polyclonal antibody developed to the β-GAG domain of versican. The accumulation of versican was measured using image analysis of whole-slide digital images.[124] Versican staining was observed in bronchiolar epithelial cells in the PBS-treated control mice. Alveolar septa in PBS-treated mice showed minimal immunoreactivity (**Figure 2.2A and 2.2B)** Throughout IAV infection, versican immunopositivity transitioned from being primarily associated with bronchiolar epithelial cells in controls to accumulations in peribronchiolar, perivascular, and alveolar septal regions in mice infected with IAV. Significant increases in total accumulation were observed beginning on 6 dpi when compared with PBS-treated mice (**Figures 2.1B, 2.2F, 2.2H, and 2.2J**).

At 3 dpi, there was intense positive staining for versican in the peribronchiolar spaces with a mild decrease in intensity of the positive staining of bronchiole epithelial cells compared with PBS controls. Staining of the perivascular areas was also strongly positive at 3 dpi. Multifocal areas of increased positive staining for versican in alveolar septa were seen at 3 dpi (**Figure 2.2D)** compared with the minimal immunoreactivity of alveolar septa observed in PBS controls. Increased versican accumulation in peribronchiolar, perivascular, and alveolar septal regions was associated with mild increases in inflammatory cell infiltrates on 3 dpi. Compared with PBS-instilled controls, there was no change in total versican accumulation measured in the lungs of mice 3 dpi (**Figure 2.1B**). A review of the tissues showed the location of intense versican staining shifted from being primarily in airway epithelial cells and smooth muscle cells of major vessels in PBS-treated mice to increased immunostaining staining for versican in the alveolar septa of influenza-infected mice 3 dpi.

On 6 dpi, increased intensity and expansion of the areas of positive staining for versican around bronchioles and pulmonary vessels contributed to statistically significant increases in versican accumulation as a percentage of total lung measured by QDP (**Figures 2.1B and 2.2F**). Densely packed and markedly increased numbers of inflammatory cells expanded peribronchiolar and perivascular spaces. Versican accumulation in the alveolar septal was multifocal and coincided with areas of inflammation. Compared with that observed on day 3 after infection, there was an increased intensity and moderate thickening of the alveolar septa in regions positively stained for versican.

On 9 dpi, the overall intensity of the staining of the endothelial basement membrane of the pulmonary vessels was reduced compared with 3 and 6 dpi (**Figure 2.2G and 2.2H**). Perivascular, peribronchiolar, and interstitial areas remain markedly expanded with inflammatory cells, with cells less densely packed into these spaces compared with 3 and 6 dpi. Positive staining of alveolar septa for versican on 9 dpi remained multifocal with thickened septa, closely associated with increased inflammatory cell infiltrates.

The alveolar spaces surrounded by positive versican staining appeared markedly expanded on 12 dpi (**Figure 2.2J**). The positive staining for versican surrounding expanded alveoli was closely associated with loosely packed inflammatory cell infiltrates. In addition, in comparison with earlier times, the versican staining adjacent to pulmonary blood vessels and bronchioles was of lower intensity. Versican accumulation in alveolar septa remained multifocal and associated with inflammatory cell infiltrates on 12 dpi. The changes in the accumulation of versican from being predominantly epithelial in PBS controls to developing strong immunopositivity in perivascular, peribronchiolar, and alveolar septal regions throughout influenza infection culminating in expanded alveoli surrounded by versican reflect the dynamic and fluid nature of the versican-enriched ECM.

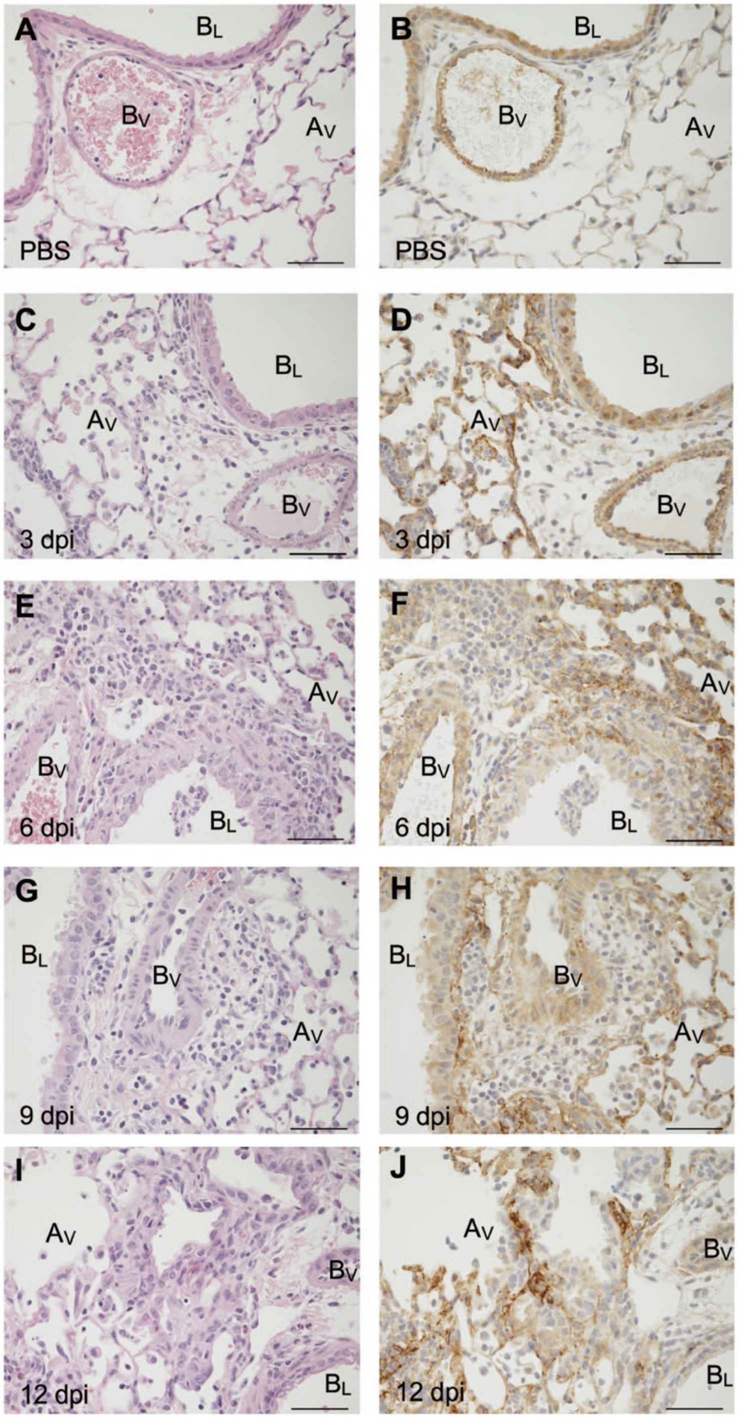

Figure 2.2 Versican β-GAG accumulation in the lungs of mice during IAV infection

Hematoxylin and eosin staining (A, C, E, G, I) and versican β-GAG accumulation (B, D, F, H, J) in PBS-treated mice at 3, 6, 9, and 12 dpi with IAV-infected lungs. For immunohistochemistry images, brown indicates positive staining for versican β-GAG domain; blue, hematoxylin counterstain. Scale (A–J) = 25 μm. Abbreviation: A_v = alveolus, B_L = bronchiole lumen, B_V = blood vessel; GAG = glycosaminoglycan; IAV, influenza A virus; dpi = days post-infection.

2.3.3 Accumulation of Myeloid and Lymphoid Lineage Leukocytes During IAV Infection

Versican immunohistochemistry showed a close association of versican with inflammatory cell infiltrates in IAV-infected lungs. Therefore, further characterization of changes to select populations of inflammatory cells throughout IAV infection were pursued using immunohistochemistry and QDP.[124] Neutrophils, mononuclear phagocytes, lymphocytes, and T-cells subsets were investigated using antibodies to cell-specific markers described below.

Ly6b is a differentiation antigen associated with mature and immature neutrophils and immature monocytes expressed in C57BL/6 mouse strains. The antigen is lost as monocytes differentiate into mature tissue-resident macrophages.[140] Positive staining for Ly6b demonstrated the relatively early influx of neutrophils into the lungs, compared with other leukocytes, during IAV infection. Mice infected with IAV had significant increases in Ly6b-positive staining beginning on 3 dpi (2.9% ± 0.5%). When compared with mice treated with PBS, the maximum percentage of positive staining for Ly6b occurred on 6 dpi (10.8% ± 0.9%) with significant increases on 9 dpi (2.5% ± 0.4%) but not on day 12 after infection (**Figure 2.3A**).

CD68 antigen is a glycoprotein associated with lysosomes in the cytoplasm of most cells from the mononuclear phagocyte lineage. Positive staining for CD68 captured the presence of macrophages and dendritic cells in the lung during IAV infection. Mice infected with IAV had significant increases in CD68-positive staining on 9 dpi (9.5% ± 1.7%) with no significant increases appreciated on any other days (**Figure 2.3B**).

F4/80 antigen is a glycoprotein with surface membrane and cytoplasmic expression by resident tissue macrophages, including alveolar and interstitial macrophages, and it is also present on a subset of recruited monocytes. Significant increases in F4/80-positive staining were seen on 6 dpi (6.0% ± 0.5%), 9 dpi (11.1% ± 0.7%), and 12 dpi (13.4% ± 0.4%) in IAV-infected mice compared with PBS-treated mice (**Figure 2.3C**). Recruited monocytes likely account for the continued increase in F4/80-positive staining even as CD68-positive staining declines on 12 dpi.

The CD3 antigen is a pan-T-cell marker present on the surface of mature T-lymphocytes and in the cytoplasm of immature T-lymphocytes. CD3-positive staining that was significantly increased compared with PBS-treated animals was seen on 6 dpi (2.5% ± 0.2%), 9 dpi (7.3% ± 0.3%), and 12 dpi (7.3% ± 0.3%) in IAV-infected mice (**Figure 2.3D**). The increases in CD3-positive staining were consistent with the combined percentage of positive staining of CD4 and

CD8 antigens, which were measured to characterize the type of T-lymphocytes recruited into the lungs. CD4 and CD8 antigens are surface membrane glycoproteins primarily of mutually exclusive, functionally different T-cell populations. CD4 is highly expressed on helper T-cells, whereas CD8 antigen is highly expressed on cytotoxic T-cells and subsets of natural killer cells. CD4-positive staining did not demonstrate significant increases in IAV-infected mice on any day post-infection. Significant elevations in CD8-positive staining mirrored the pattern of significant CD3-positive staining with significant increases seen on 6 dpi (2.2% ± 0.3%), 9 dpi (5.7% ± 0.8%), and 12 dpi (5.9% ± 0.4%) in IAV-infected mice compared with PBS-treated mice (**Figure 2.3E**). These results document the temporal changes in subpopulations of inflammatory cell infiltration into the lungs in response to influenza infection. These findings suggest increased versican accumulation in concert with inflammatory cell infiltration into the lungs is a feature of acute inflammatory response to IAV, spanning both the disease and recovery phases of our model of IAV infection.

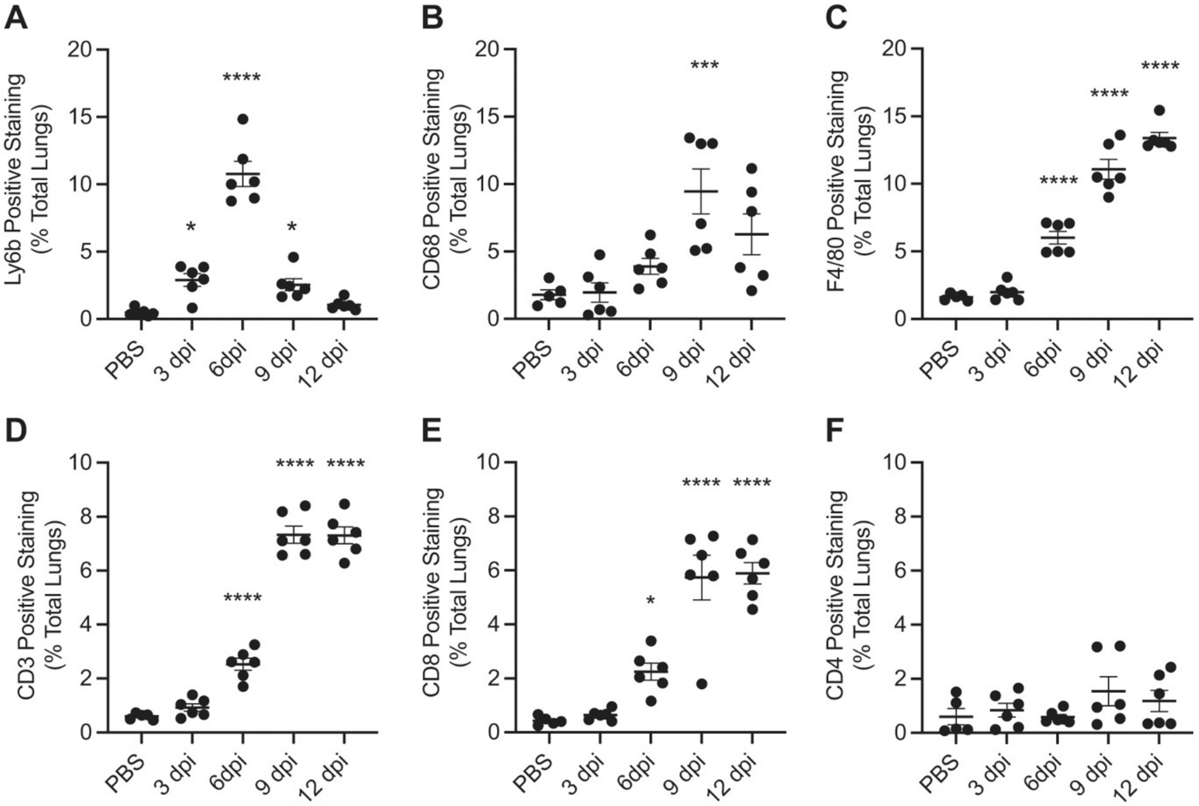

Figure 2.3 Accumulation of leukocytes during IAV infection

(A) Ly6b, (B) CD68, (C) F4/80, (D) CD3, (E) CD8, and (F) CD4 accumulation in the lungs during IAV infection shown on days 3, 6, 9, and 12 after infection and in vehicle (PBS)-treated controls. Accumulation was determined using immunohistochemistry and quantitative digital pathology. Values are mean ± SEM with n=5–6 per time. Asterisks show groups that are statistically significantly different (*$p \leq 0.05$; ***$p \leq 0.0005$; ****$p \leq 0.0001$) from PBS-treated lungs using a one-way ANOVA with Bonferroni's multiple comparison test. Abbreviations: IAV, influenza A virus.

2.3.4 Versican Expression Correlates With IFN-β Expression During IAV Infection

Type I IFNs are key contributors to effective antiviral responses, particularly in the acute response to viral infection. Versican is an IFN-stimulated gene in macrophages, and versican is necessary for type I IFN production by macrophages.[103] Therefore, we compared changes to versican and IFN-β mRNA expression in the lungs of mice infected with IAV by qPCR. Maximum versican expression was observed on 6 dpi (8.5 ± 0.6). Versican expression was also significantly increased on 3 dpi (5.2 ± 0.8), 9 dpi (4.2 ± 0.4), and 12 dpi (3.7 ± 0.3) in IAV-infected mice compared with PBS-treated controls (**Figure 2.4A**).

In mice infected with IAV, the maximum expression of IFN-β mRNA was observed on day 6 after infection (1593.3 ± 139.6). In addition, IFN-β expression was significantly increased on 3 dpi (511.0 ± 91.1) in IAV-infected mice but not on any other days measured compared with PBS-treated control mice (**Figure 2.4B**). A simple linear regression model shows that the expression of IFN-β and versican mRNA was positively correlated up through 6 dpi ($r^2 = 0.8621$, regression line not shown) compared with the correlation through 12 dpi ($r^2 = 0.7424$; **Figure 2.4C**).

Previous studies show that the activation of type I IFN receptor signaling increases versican expression in macrophages treated with poly(I:C).[103] Therefore, we investigated whether the increased pulmonary expression of versican mRNA in response to influenza depended on type I IFN receptor signaling. This was achieved by using B6(Cg)-Ifnar1$^{tm1.2Ees}$/J (Ifnar1$^-$) mice which produce type I IFNs such as IFN-β but have a non-functional type I IFN receptor. Versican expressed in response to IAV infection in the lungs of Ifnar1$^-$ mice would indicate an alternative pathway regulating versican expression. Versican mRNA was detected by in situ hybridization in wild-type and Ifnar1$^-$ mice that were 9 dpi with IAV and in PBS-treated controls. Image analysis was performed to quantify versican mRNA as a percentage of the total lung (**Figure 2.4D**). Wild-type IAV-infected mice had significantly more versican (0.66% ± 0.11%) compared with wild-type PBS-instilled (0.16% ± 0.02%) mice. Ifnar1$^-$ IAV-infected mice had significantly less versican mRNA detected (0.24% ± 0.07%) compared with wild-type IAV-infected mice as a percentage of total lung on 9 dpi. These findings show that the temporal pattern of versican expression was closely mirrored by the pattern of IFN-β expression throughout IAV infection and that increased versican expression in response to influenza in the lungs is partially mediated by type I IFN receptor signaling.

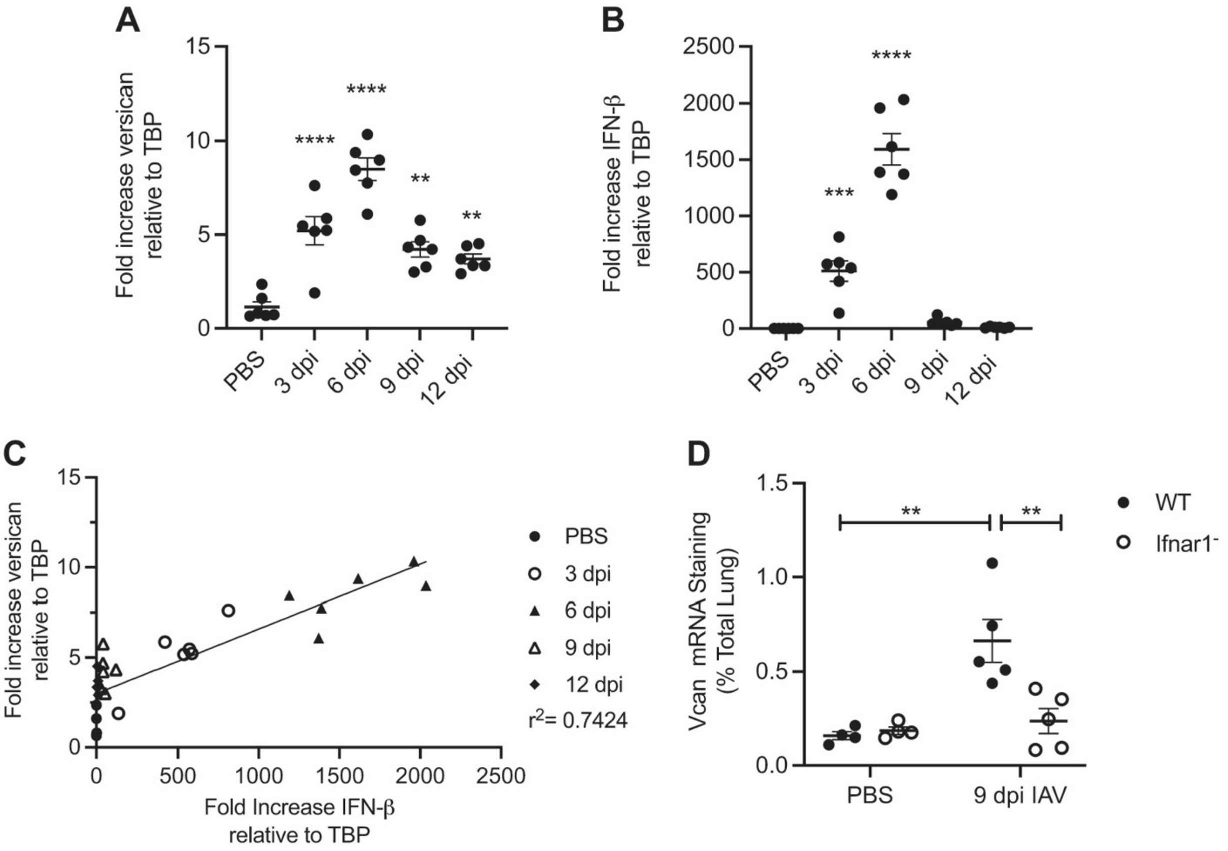

Figure 2.4 Versican expression correlation with IFN-β expression during influenza A virus (IAV) infection

(A) Total *Vcan* expression in the lungs by days post-infection (dpi) with influenza A virus shown on days 3, 6, 9, and 12 after infection and in vehicle (PBS)-treated controls. (B) Total IFN-β expression in the lungs by dpi with IAV shown on days 3, 6, 9, and 12 after infection and in PBS-treated controls. Change in the amount of mRNA was determined using mRNA collected from lung homogenates and quantitative real-time PCR. Values are mean ± SEM with *n*=6 per time. Asterisks show groups that are statistically significantly different (**$p \leq 0.005$; ***$p \leq 0.0005$; ****$p \leq 0.0001$) from PBS-treated lungs using a one-way ANOVA with Bonferroni's multiple comparison test. (C) *Vcan* expression correlation with IFN-β expression. (D) *Vcan* expression in wild-type and Ifnar1$^-$ mice on 9 dpi with IAV and in PBS-treated controls. *Vcan* mRNA was detected by in situ hybridization. Values are mean ± SEM with *n*=4–5 per group. Asterisks show groups that are statistically significantly different (**$p \leq 0.003$) using a one-way ANOVA with Bonferroni's multiple comparison test. Abbreviations: IAV, influenza A virus; PCR, polymerase chain reaction; IFN-β, interferon-beta.

2.3.5 Nuclear Colocalization of Versican mRNA and PDGFRβ mRNA by Duplex In Situ Hybridization

Previous studies have suggested that the cellular source of versican is an important factor in determining the role of versican in the context of pulmonary infection and inflammation.[100,103] To address this knowledge gap, we used duplex in situ hybridization to determine important cellular sources of versican mRNA using PDGFRβ to identify a subset of versican-expressing stromal cells, including pericytes and subset of activated fibroblasts, and CD68 to identify versican-expressing macrophages and dendritic cells.[141,142] PDGFRβ was selected to capture the versican expression of lung pericytes, which make up a vast network of stromal cells that are in close proximity to the lung microvascular and contribute to the vascular smooth muscle of the lung arterioles.[141] Versican expressed by PDGFRβ$^+$ cells may play an important role in the migration of leukocytes from the vasculature and into the airspaces. CD68 was selected based on our previous work demonstrating that versican is a type I IFN–stimulated gene in macrophages.[103] However, the cellular specificity of type I IFN–stimulated versican in the context of influenza infection is unknown. Therefore, we measured whether versican and PDGFRβ mRNA colocalized in nuclei in the lungs of wild-type (**Figure 2.5A**) vs Ifnar1$^-$ (**Figure 2.5C**) mice 9 dpi with IAV. Nuclei were defined using a deep learning module (Visiopharm) along with single-positive versican nuclei (red), single-positive PDGFRβ nuclei (green), and double-positive versican + PDGFRβ nuclei (yellow) in both wild-type (**Figure 2.5B**) and Ifnar1$^-$ (**Figure 2.5D**) lungs. A similar analysis was performed in which CD68 mRNA, to identify myeloid lineage cells, and versican mRNA were detected in wild-type and Ifnar1$^-$ mice 9 dpi with IAV (image not shown). These analyses allowed for the quantification of single-positive versican, CD68, and PDGFRβ nuclei, and double-positive versican + CD68, and versican + PDGFRβ nuclei (**Figure 2.6A-D**) in wild-type and Ifnar1$^-$ lungs.

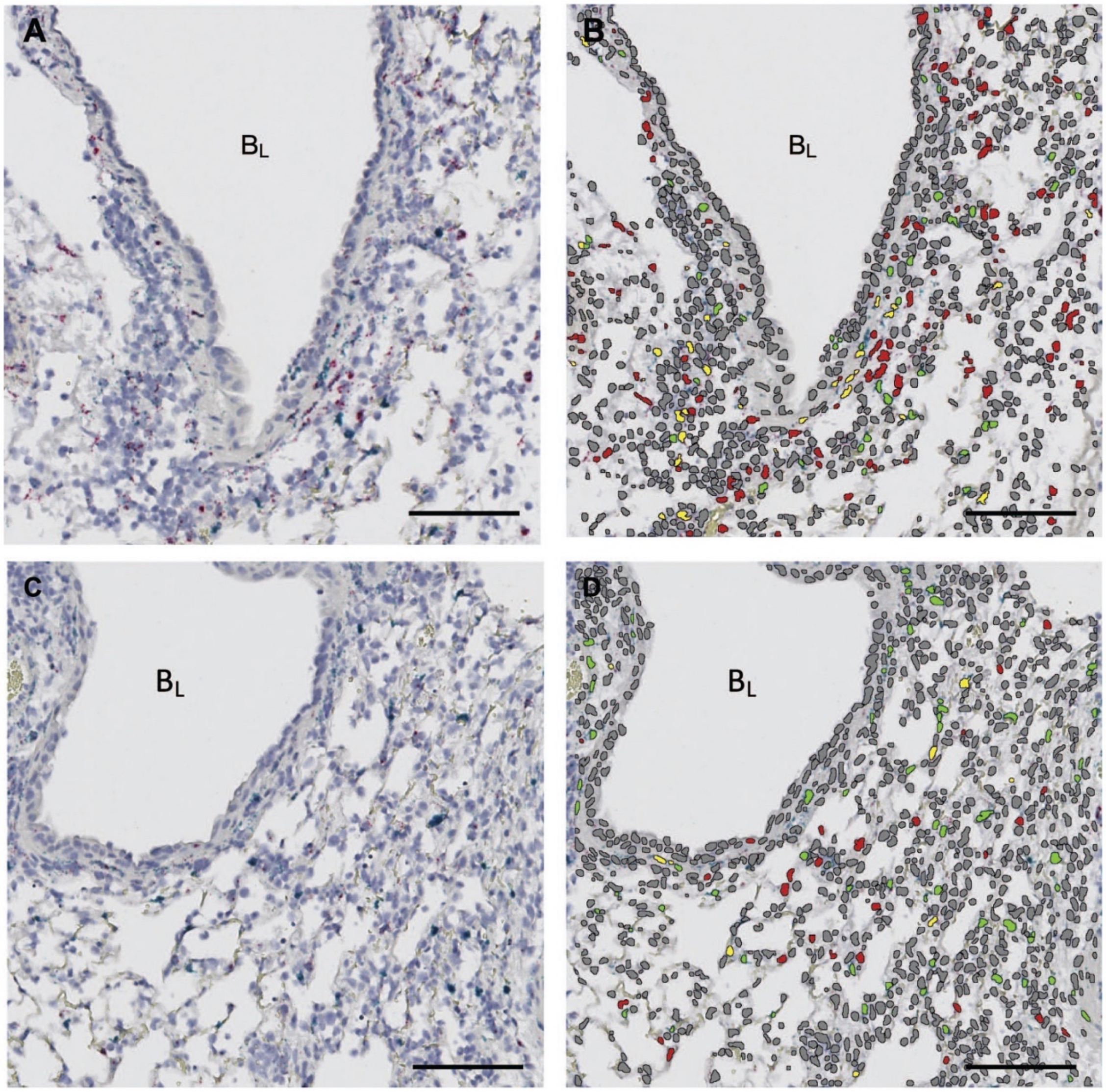

Figure 2.5 Nuclear colocalization of versican and PDGFRβ mRNA in IAV-infected mice

Digital images of wild-type (A) and Ifnar1⁻ (C) mouse lung tissue sections stained for versican (red) and PDGFRβ (green) mRNA by in situ hybridization. Digital images of wild-type (B) and Ifnar1⁻ (D) mouse lung tissue labeled with Visiopharm deep learning module overlay used to identify nuclei (gray) for nuclear segmentation and identify nuclei that were single-positive for versican mRNA (red), single-positive for PDGFRβ mRNA (green), and double-positive for versican and PDGFRβ mRNA (yellow). Scale (A–D) = 100 μm. Abbreviations: IAV, influenza A virus; PDGFRβ, platelet-derived growth factor receptor beta.

2.3.6 Type I IFN-stimulated Versican Expression in Fibroblasts During IAV Infection

Quantification of single-positive versican, CD68, and PDGFRβ nuclei, and double-positive versican + CD68, and versican + PDGFRβ nuclei in wild-type and Ifnar1⁻ lungs allowed for the identification of important cellular sources of versican and applied additional rigor to the quantification of total versican mRNA (**Figure 2.4D**). Consistent with the quantification of total versican mRNA (**Figure 2.4D**), we found that the total number of versican mRNA-positive nuclei was also significantly elevated in wild-type IAV-infected mice (5672 ± 967) compared with wild-type PBS-instilled mice (563 ± 69) and that there were significantly less versican mRNA-positive nuclei in the lungs of Ifnar1⁻ mice (1627 ± 546) compared with wild-type mice 9 dpi with IAV (**Figure 2.6A**). No statistically significant difference was observed between PBS-instilled and IAV-infected Ifnar1⁻ lungs (**Figures 2.4D and 2.6A**). These findings provide further evidence that increased versican expression in response to influenza in the lungs is partially mediated by type I IFN receptor signaling and that constitutive versican expression is mediated by signaling that is not type I IFN receptor–dependent.

Previously, we described the role of type I IFNs and the type I IFN receptor in regulating versican expression in macrophages.[103] Therefore, we were interested in this relationship during IAV infection and whether a similar relationship existed in stromal cells. To investigate this further, we performed duplex in situ hybridization on lung tissue from both wild-type and Ifnar1⁻ mice at 9 dpi with IAV for colocalization of versican/CD68 and versican/PDGFRβ. In Ifnar1⁻ mice 9 dpi with IAV, there were significantly fewer versican/CD68 (262 ± 94) and versican/ PDGFRβ (365 ± 140) mRNA colocalized nuclei compared with versican/CD68 (790 ± 174) and versican/PDGFRβ (850 ± 134) mRNA colocalized nuclei in wild-type mice (**Figure 2.6B**). It is important to point out that our quantification of versican mRNA-positive nuclei does not define the amount of versican expressed by each positive cell. The ability to measure the amount of versican mRNA in the nucleus of a cell using image analysis is an area for future refinement and study. However, these data indicate that both CD68- and PDGFRβ-positive cells are sources of versican and express versican partly by type I IFN receptor signaling during IAV infection. We expect CD68-positive macrophages to express versican in a type I IFN receptor signaling–dependent manner. Interestingly, versican/CD68 mRNA colocalized nuclei in IAV-infected Ifnar1⁻ mice (262 ± 94) compared with PBS-instilled Ifnar1⁻ mice (86 ± 18; **Figure 2.6B**) showed no statistically significant difference. This is suggestive that some CD68-positive cells constitutively express versican in a manner that is not dependent on type I IFN receptor signaling.

In addition to quantifying the number of versican/CD68 mRNA colocalized nuclei, we assessed the percentage of total CD68-positive nuclei that had versican/CD68 mRNA colocalized nuclei (**Figure 2.6C**). We found that in both PBS-instilled wild-type (13.8% ± 2.0%) and Ifnar1$^-$ mice (12.8% ± 2.3%), there was a greater percentage of CD68-positive nuclei that were constitutively expressing versican compared with IAV-infected wild-type (8.5% ± 0.4%, p=0.07) and Ifnar1$^-$ mice (6.6% ± 1.2%, p=0.03; **Figure 2.6C**). Untreated mouse alveolar macrophages express very little versican.[103] Therefore, it is likely that this increased proportion of constitutive expression is coming from a population of interstitial macrophages or dendritic cells that express versican in the lungs during homeostasis. When considering that there was a relative increase in the number of CD68-positive cells (9259 ± 1822) that move into the lungs of wild-type mice 9 dpi with IAV compared with PBS-instilled controls (475 ± 96; **Figure 2.6D**), we concluded that many of the CD68-positive cells that migrate into the lungs during IAV are not expressing versican. While not statistically significant, this trend was also observed in Ifnar1$^-$ mice which had increased CD68-positive cells in IAV-infected (4697 ± 1882) vs PBS-instilled mice (673 ± 107; **Figure 2.6D** A limitation of our study is that we are unable to define the subsets of CD68-positive cells in the lung and cannot positively identify the subsets of macrophages and myeloid cells that are contributing to versican expression during IAV. This represents an area of future study to further define the role of myeloid-derived versican during IAV infection.

Next, we assessed the percentage of total PDGFRβ-positive nuclei that had versican/PDGFRβ mRNA colocalized nuclei in both wild-type and Ifnar1$^-$ mice (**Figure 2.6E**). We found that in both IAV-infected wild-type (16.1% ± 1.9%) and Ifnar1$^-$ mice (8.9% ± 1.8%), there was a greater percentage of PDGFRβ-positive nuclei that were expressing versican compared with PBS-instilled wild-type (3.1% ± 0.4%, p<0.0001) and Ifnar1$^-$ mice (3.3% ± 0.6%, p=0.06; **Figure 2.6E**). There was also a statistically significant less colocalization of versican/PDGFRβ mRNA in wild-type vs Ifnar1$^-$ IAV-infected mice. Significant increases in the number of PDGFRβ–positive cells were observed with IAV infection (5315 ± 527), compared with PBS-instilled wild-type controls (2967 ± 287), but this increase was not observed in Ifnar1$^-$ mice (**Figure 2.6F**). Taken together, these results show that PDGFRβ$^+$ stromal cells express a significant amount of versican through type I IFN signaling on 9 dpi with IAV. However, in the Ifnar1^{-} PDGFRβ^{+} cells, versican expression was not completely abrogated, suggesting that the previously described β-catenin/TCF signaling may partially contribute to versican expression in stromal cells after influenza infection.

To confirm the role of type I IFN signaling in regulating versican expression in fibroblasts, in vitro studies were conducted in cultures of primary murine lung fibroblasts. For these studies, cells were treated with IFN-β or LPS, a TLR agonist known to activate type I IFN signaling and versican expression in macrophages.[103] These data show wild-type fibroblasts have significant increases in the expression of versican mRNA 4hr after stimulation with IFN-β (3.8 ± 0.3) and LPS (3.0 ± 0.3) compared with wild-type PBS-treated (1.3 ± 0.3) fibroblasts. When wild-type fibroblasts are compared with Ifnar1^{-} fibroblasts, we observed significant decreases in versican mRNA 4hr after stimulation with IFN-β (0.9 ± 0.1) and with LPS (1.8± 0.1; **Figure 2.6G**). These correlative data strengthen our finding that type I IFN signaling increases versican expression in lung fibroblasts of mice exposed to IAV in vivo.

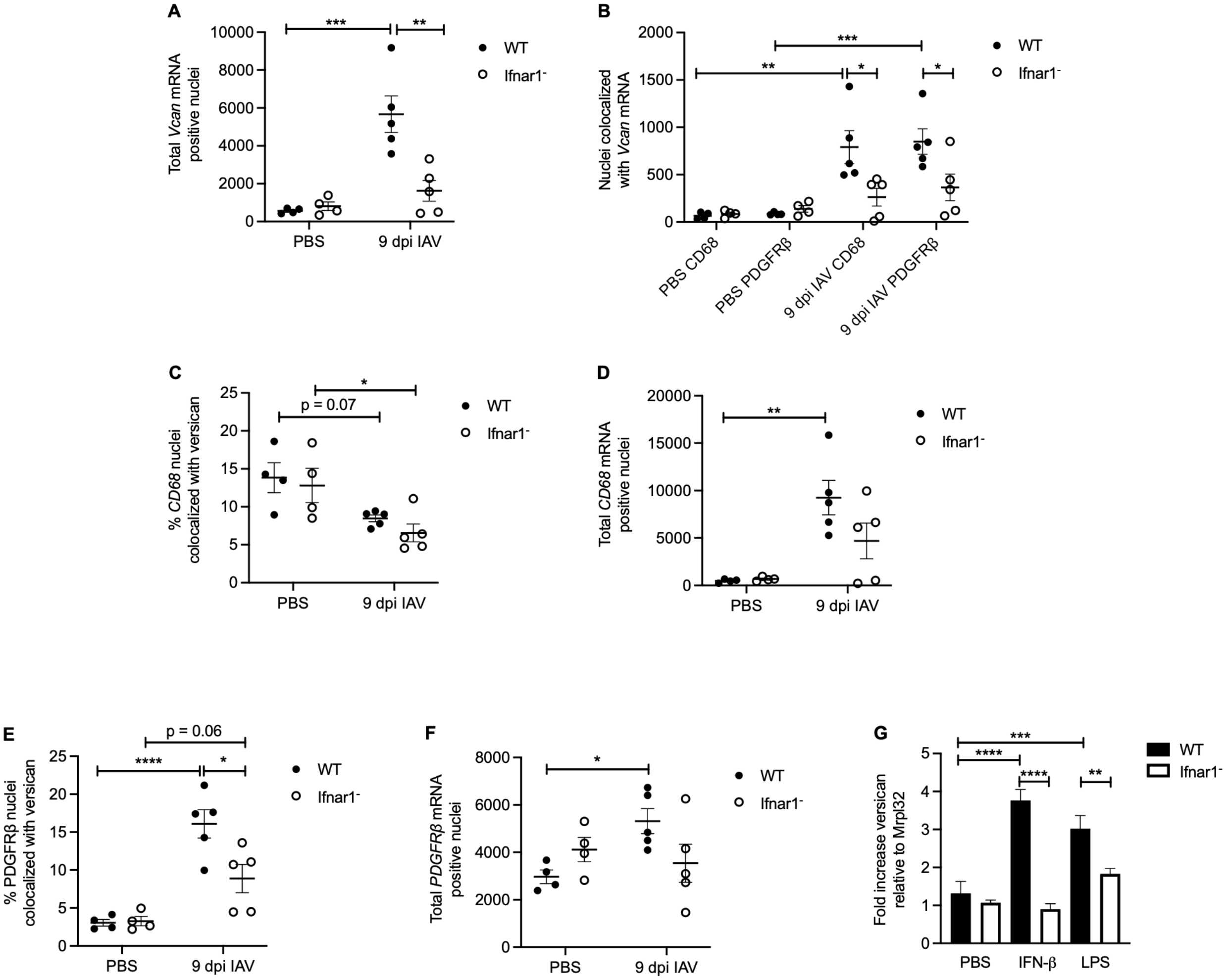

Figure 2.6 Type I IFN–stimulated versican expression in fibroblasts during IAV infection

(A) Total *Vcan* mRNA-positive nuclei in wild-type and Ifnar1^{-} mice treated with PBS and 9 dpi with IAV. (B) Total nuclei with colocalization of *Vcan* mRNA and either *CD68* or *PDGFRβ* mRNA in wild-type and Ifnar1^{-} mice treated with PBS and 9 dpi with IAV. (C) Percentage of *CD68* nuclei that colocalized with versican in wild-type and Ifnar1^{-} mice treated with PBS and 9 dpi with IAV. (D) Total CD68 mRNA positive nuclei in wild-type and Ifnar1^{-}mice treated with PBS and 9 dpi with IAV. (E) Percentage of *PDGFRβ* nuclei that colocalized with versican in wild-type and Ifnar1^{-} mice treated with PBS and 9 dpi with IAV. (F) Total PDGFRβ mRNA positive nuclei in wild-type and Ifnar1^{-} mice treated with PBS and 9 dpi with IAV. (G) Total versican expression in wild-type and Ifnar1^{-} primary lung fibroblasts 4 hr after exposure to PBS, IFN-β, or LPS. Values are mean ± SEM with n=3–6 per time. Asterisks show groups that are statistically significantly different (*$p \leq 0.05$; **$p \leq 0.005$; ***$p \leq 0.000$; ****$p \leq 0.0001$) from PBS-treated cells or mice using a one-way ANOVA with Bonferroni's multiple comparison test. Abbreviations: IAV, influenza A virus; IFN, interferon; LPS, lipopolysaccharide; PDGFRβ, platelet-derived growth factor receptor beta.

2.4 Discussion

Consistent with the study objectives, we determined the time course and magnitude of versican accumulation and expression in the mouse lungs during severe influenza infection, which has not been previously reported. In addition, we documented the following significant findings: (1) The temporal increase in versican accumulation in the lungs, in response to IAV, correlated with mouse acute lung injury scores and with pulmonary inflammatory cell infiltration; (2) the expression of versican was increased in both mononuclear phagocytic cells and stromal cells in the lungs in response to IAV; (3) the expression of versican in stromal cells was partially mediated by type I IFN receptor signaling; and (4) versican was increased in murine lung fibroblasts exposed *in vitro* to agonists that stimulate type I IFN signaling. These findings indicate that increased versican expression is a component of the acute inflammatory response to IAV in the lungs. In addition, versican is a type I IFN–stimulated gene in pulmonary stromal cells, both *in vivo* and *in vitro*. These data raise intriguing questions about the role(s) of versican in the early host response to IAV. This study did not directly address the function of versican. However, it provides a guide for future studies trying to determine the role of versican in the immune response to lung infection caused by IAV. Several potential aspects of versican's function are discussed.

In the context of IAV infection, versican likely has a vital role in coordinating the host immune response and is an IFN-stimulated gene in macrophages.[100,103] Unexpectedly, we found that PDGFRβ$^+$ stromal cells contribute to versican expression in response to IAV in a partially type I IFN–dependent manner. Type I IFNs directly contribute to the resolution of viral infection by creating the antiviral state in multiple cell types through the expression of IFN-stimulated genes. Type I IFNs are also known for limiting and resolving inflammation through stimulation of IL-10 production.[143] It is unknown whether stromal cell type I IFN–stimulated versican potentiates the expression of IFN-β and interleukin (IL)-10, as shown in macrophages, or how it contributes to the antiviral state through interactions with leukocytes, chemokines, cytokines, and growth factors.[115] The Wnt/β-catenin/TCF pathway, previously identified as controlling the versican promoter in stromal cells, could be the source of versican expression that was type I IFN–independent in stromal cells in our 9 dpi studies using Ifnar1$^-$ mice. This pathway has been implicated in regulating proteinases for which versican is a substrate, including secreted matrix metalloproteinases (MMPs) and members of the ADAMTS protein family.[55,66,73,82,101,144,145] In both stimulating versican expression and proteases, which cleave versican, the Wnt/β-catenin/TCF pathway may be important for regulating the versican-enriched matrix's turnover and enabling leukocyte migration through the lungs. Exploring the functional consequences of both type I IFN–dependent and type I IFN–independent pathways controlling stromal cell–derived versican is a crucial opportunity to understand the immunomodulatory effects of versican and identify host-directed therapies targeting the ECM and host response in the context of IAV pneumonia.

The importance of versican degradation in the immune response to influenza pneumonia was highlighted in two studies of the ADAMTS protein family of proteases. The work of McMahon et al. showed that the degradation of the versican-enriched ECM in the mediastinal lymph nodes by ADAMTS5 is required for the migration of influenza-specific lymphocytes from the lymph node to the lungs of IAV-infected mice.[113] ADAMTS5 is not increased in the lungs of mice exposed to IAV, but rather ADAMTS4 appears to be the protease responsible for versican degradation.[112,113] In a recent manuscript, Boyd and colleagues showed that the deficiency of ADAMTS4 activity in the lungs of mice infected with IAV preserves intact ECM-localized versican and decreases CD3 lymphocyte migration into areas of infection.[112] Our study found the greatest CD3 and CD8 migration into the lungs on days 9 and 12 after infection. Studies of lymphocyte migration into the lungs from studies of ADAMTS4- and ADAMTS5-deficient mice were performed between days 7 and 10 after infection, suggesting that versican degradation may explain this increase in T-cell migration into the lungs.[112,113] In both human lung fibroblasts *in vitro* and mice exposed to IAV, fibroblasts were identified as an important source of ADAMTS4, demonstrating that fibroblasts both contribute to the versican-enriched matrix and the degradation of the versican.[101,112] Measurement of versikine, the degradation product of versican after cleavage by ADAMTS proteases, at our established time points provided additional insight into the degradation of the versican-enriched matrix. Interestingly, we appreciated significant increases in versikine accumulation only on 6 dpi, coinciding with initial increases in lung injury scores and the initial wave of migration of various leukocyte populations into the lungs. The accumulation of versikine in our studies did not fully account for the expected amount of versican degradation, especially late in infection. Our data highlight the importance of versican degradation for future studies in versican-deficient mouse lines and the potential for other proteolytic enzymes and degradation products to be involved during IAV infection.

Much of the data presented have utility in informing future studies by providing a guide to the critical time points to measure leukocyte migration in the lungs within the context of the versican-enriched extracellular matrix stimulated by viral pneumonia. In particular, our data highlight the prominence of stromal cell–derived versican as both the number and proportion of versican/PDGFRβ mRNA colocalized nuclei increased during IAV infection. In contrast, many of the myeloid cells entering the lung are not expressing versican as the proportion of versican/CD68 mRNA colocalized nuclei of all CD68-positive nuclei decreased with IAV infection as total CD68-positive cells increased. A signature of decreased versican expression by human blood monocytes in response to LPS has been previously reported.[146] A limitation of our study is we do not know what subpopulations of monocytes and macrophages are entering the lungs and expressing versican in our tissues, but reduced expression of versican by newly recruited monocytes and macrophages is a possible mechanism explaining the reduction in the percentage of versican/CD68 mRNA colocalized nuclei during IAV infection.

The correlation of versican accumulation with the pulmonary recruitment of inflammatory cells suggests that versican influences leukocyte activity and orchestrates the host immune response in the lungs through direct and indirect mechanisms. Versican directly interacts with L-selectin and P-selectin, important mediators of cell adhesion and leukocyte rolling on the vascular endothelium.[117] Versican is also known to bind to P-selectin glycoprotein ligand-1 on neutrophils at the G3 domain and coordinate leukocyte aggregation.[147] Global knockdown of versican in mice exposed to poly(I:C) reduced leukocytes in the BAL fluid, suggesting a critical role for versican in promoting leukocyte migration into the lungs.[100] Versican can also provide indirect, fine control over leukocyte migration into the lungs through interactions of the negatively charged chondroitin sulfate chains on versican with chemokines.[48-50,97,119] Previous studies demonstrate that versican interacts with chemokine CCL2, creating a gradient that promotes monocyte migration and that globally versican-deficient animals exposed to poly(I: C) had reduced expression of chemokine CXCL2, a potent neutrophil chemoattractant.[100,148] Mice with epithelial-specific versican deficiency demonstrated increased recruitment of monocytes and neutrophils in BAL fluid and elevated expression levels of chemokines CCL2, CCL3, and CCL4 after infection with the respiratory syncytial virus, suggesting that epithelial versican attenuates leukocyte migration through chemokine-mediated mechanisms.[105] Future studies using cell-specific versican-deficient mouse strains could elucidate the potential mechanisms whereby versican directly or indirectly coordinates the migration and activation of leukocytes into lungs in response to bacterial and viral lung infection.

Viral pneumonia pathogenesis is heavily influenced by the host's reaction to the virus, making modulation of the host immune response a critical target for drug intervention.[27-29] The need to target the host response is especially true for IAV, which is equipped to undermine conventional therapies and prophylaxis through its ability to mutate rapidly and undergo genetic drift. These virulence traits enable IAV to develop resistance to antiviral medications and require the seasonal redesign of influenza vaccines.[12] In addition, IAV infection places a significant burden on global health, with estimates of 145,000 to 645,000 deaths attributed to influenza lower respiratory tract infections globally each year.[2,3] In the United States, influenza is one of the top causes of hospitalization among patients with community-acquired pneumonia.[4,5] Versican's potential as an immunomodulatory molecule makes it an inviting therapeutic target for providing fine tune control over the immune response to viral pneumonia and IAV infection.

In conclusion, we presented data showing coordination between versican gene expression patterns, versican accumulation, and leukocyte accumulation in the lungs during influenza infection. We further demonstrated that type I IFN signaling contributes significantly to versican expression in lung stromal cells during influenza infection. Of critical importance is the need to investigate the role of both type I IFN–dependent and type I IFN–independent pathways in modulating stromal cell–derived versican expression to target stromal cell versican expression and accumulation as a host-directed therapy for viral pneumonia. The data presented provide salient guidance for future studies to be performed *in vivo* in versican-deficient mouse models and expand upon previously published data that demonstrate the potential immunomodulatory activity of versican through direct and indirect interactions with leukocytes.

Chapter 3. Multi-Compartmental Analysis of the Murine Pulmonary Immune Response by Spectral Flow Cytometry

3.1 Introduction

Leukocyte trafficking in response to infection and injury is central to the pulmonary immune response. When successful, leukocyte recruitment leads to the containment of the threat, followed by clearance of immune cells and resolution of inflammation. However, many lung diseases are characterized by an immune response and leukocyte recruitment that results in severe lung injury or impaired resolution of inflammation. Understanding the fundamental processes underlying the pulmonary immune response has unique challenges due to the complex structure and composition of the lungs, with multiple compartments and leukocyte populations involved in the immune response, depending on the agonist or the kinetics of the host response. This complexity requires special attention to acquire high-quality data that accurately reflects lung pathophysiology. Here we describe the methodology necessary for accurately measuring the lung's immune response to the influenza virus by incorporating spectral flow cytometry and *in vivo* pulmonary compartmental analysis. The protocols described in this manuscript to measure leukocyte migration into the lungs of mice infected with the influenza virus can be easily adapted to other animal models.

Two aspects of spectral flow are well-suited for this approach. First, spectral cytometers collect data from detector arrays covering the entire emission wavelength spectrum. Full-spectrum analysis enables the ability of spectral cytometers to deconvolute or unmix spectra from fluorophores with similar emission peaks, thereby increasing the library of usable fluorophores compared to conventional cytometers with single bandpass filters. These advances maximize the information that can be obtained regarding the diverse leukocyte subpopulations involved in the pulmonary inflammatory response. Second, a unique capability of spectral flow cytometry is that it can utilize cellular autofluorescence (AF) to aid in identifying cell populations.[149] This is particularly useful to pulmonary biologists as the lungs have cell populations with intrinsically high AF properties. Multiple cellular factors (including cell size, granularity, metabolism, and activation), the heterogeneity of immune cell subtypes, and sample processing conditions contribute to AF.[150] While all cells contribute to AF, eosinophils and cells that produce and metabolize surfactants - alveolar type II cells and alveolar macrophages - have the highest AF intensity in the lungs; and inflammatory conditions can increase cellular AF.[151] Thus, a heterogeneous leukocyte response elicits AF complexity that can pose challenges for analyzing the pulmonary immune response by flow cytometry. In conventional flow, AF is generally viewed as an undesirable source of background that must be extracted, decreasing the sensitivity of fluorophore detection and potentially contributing to the misidentification of cell populations. In contrast, spectral flow cytometry can utilize cellular AF to define multiple heterogeneous AF signatures, which can be incorporated into a flow panel as discrete signatures, aiding in the resolution and identification of target-specific fluorescent signals.

Using *in vivo* compartmental analysis facilitates the precise determination of the location and phenotype of leukocytes within the multiple anatomical and functional compartments of the lungs.[152] Standard methods of bronchoalveolar lavage followed by lung perfusion and tissue digestion for defining leukocytes in the airways versus the lung interstitium are now recognized to provide limited and often incorrect information regarding pulmonary leukocyte localization. Both bronchoalveolar lavage and lung perfusion provide incomplete recovery and removal of leukocytes within the airways and vasculature, respectively.[130,153-159] It has been demonstrated that perfusion is inadequate to flush the vasculature of the lungs and that many immune cells remain adhered to the endothelium of blood vessels, or marginated to the vascular wall. Furthermore, certain lymphocyte sub-populations are preferentially marginated, depending on the agonist and the kinetics of the inflammatory response.[130] As the lungs are highly vascularized, these marginated lymphocytes could potentially include large numbers of cells. Similarly, it has been found that bronchoalveolar lavage is inadequate for recovering immune cells from the airways. In particular, it has been shown that increased macrophage activation and adherence in the airways occur in response to lung injury.[159,160] Understanding the biological roles that marginated and adherent leukocytes have in the inflammatory response requires more detailed and precise compartmental analyses of leukocyte trafficking in the lungs.

Thus, we developed a comprehensive protocol and fluorophore panel combining spectral flow cytometry with *in vivo* compartmental analysis to investigate leukocyte recruitment into the lungs and mediastinal lymph nodes of control and influenza A virus (IAV)-infected C57BL/6J wild-type mice. Within the lungs, three pulmonary compartments were analyzed: the marginated vasculature (i.e., non-perfusable leukocytes), the lung interstitium, and the airspaces of the lungs (i.e., the lavageable and non-lavageable airways). We incorporated a broad panel of antibodies for immunophenotyping multiple myeloid and lymphocyte populations participating in the inflammatory response. Whereas previous studies applied *in vivo* compartmental analysis to investigate select subsets of leukocytes, here we established a panel of twenty antibody-fluorophore conjugates that clearly define multiple myeloid and lymphoid cell phenotypes.[130,159,161,162] These included B cells, T cells (cytotoxic T, T helper, and γδ T cells), natural killer (NK) cells, macrophages (alveolar and recruited), monocyte-macrophages, monocytes (Ly6C^{lo} and Ly6C^{hi}), dendritic cells (CD103^{+} and CD11b^{+}), neutrophils, and eosinophils. Employing dual *in vivo* CD45-labeling of perfused and lavaged lungs offered more insight regarding the precise localization of adherent leukocytes not only in the vasculature but also those in the lung interstitium and the airspaces. Additionally, our panel design strategy accounted for AF heterogeneity, by incorporating AF as discrete signatures in our panel, thereby enhancing the panel resolution, and increasing the rigor and reproducibility of our results. To our knowledge, the analytical approach for incorporating AF heterogeneity as applied to studies in lungs has not been covered elsewhere. This is a novel contribution that markedly enhances the quality of experimental data collected from pulmonary tissues.

With this unique combination of methodologies, it was possible to establish an unbiased exploratory approach to investigating the pulmonary immune response to IAV in which no pre-existing hypothesis of cellular involvement was needed. Rather, it became possible to investigate multiple cell types, compartments, and time points to identify subclasses of myeloid and lymphoid cells that might have more prominent previously unidentified roles in individual compartments of the lungs depending on the kinetics of the immune response. Furthermore, the overarching goal was to define and detail experimental design and analysis elements supporting rigor and reproducibility in these studies.[163,164] We propose that this protocol will be of considerable benefit for the detailed understanding of leukocyte trafficking in the lungs in response to other inflammatory agonists and other mouse models.

3.2 Materials and Methods

3.2.1 Animals

All experiments were approved by the University of Washington Institutional Animal Care and Use Committee (IACUC). Mice were obtained from Jackson Laboratories (Bar Harbor, ME, USA) and bred at the University of Washington. Wild-type 9- to 12-week-old male C57BL/6J mice were used for all experiments.

3.2.2 Induction of IAV Pneumonia

Mice were infected with 20 plaque-forming units (PFU) of mouse-adapted Influenza A/Puerto Rico/8/34 (IAV PR8) in 50µL of PBS (Thermo Fisher Scientific Waltham, MA, USA) by oropharyngeal aspiration under isoflurane (Patterson Veterinary Supply, Houston, TX, USA) anesthesia.[63] A dose of 20 PFU causes severe influenza pneumonia in which mice approach humane euthanasia endpoint criteria but ultimately recover from infection.[127] Control mice were instilled with PBS.

3.2.3 Lipopolysaccharide, Bleomycin, House Dust Mite Administration

Lipopolysaccharide (LPS, *Escherichia coli* O111: B4, List Biological Laboratories, Campbell, CA, USA) was administered by oropharyngeal aspiration under isoflurane anesthesia at a dose of 2.0 mg/kg of mouse body weight in 50µL of PBS.

Bleomycin (Fresenius Kabi, Bad Homburym, Germany) was administered by oropharyngeal aspiration under isoflurane anesthesia at a dose of 2.0 U/kg of mouse body weight in 50µL of PBS.

House dust mite (HDM) extract (Greer Laboratories Inc, Lenoir, NC, USA) was administered by oropharyngeal aspiration under isoflurane anesthesia at a dose of 5.0 mg/kg of mouse body weight in 50µL of PBS. Additional instillations were performed on days 14, 26, 27, and 28 post-initial instillation.

3.2.4 Panel Design for Spectral Flow Cytometry

Our strategy was based on recommended workflows for high-dimensional immunophenotyping assays using spectral flow cytometry.[165-167] These workflows were developed for use on the Cytek® Aurora (Cytek Biosciences, CA) spectral flow cytometer, which we utilized for our experiments. This panel design strategy included assessment of each tissue for heterogeneous autofluorescent (AF) signatures, which were determined by evaluation of spectra from unstained bronchoalveolar lavage, lung, and lymph node cells from control (PBS instilled) and IAV PR8-infected mice collected at 3, 6, and 9-days post instillation (dpi). Unique AF spectral signatures were identified and designated as fluorescent tags in the SpectroFlo library. These signatures were given high consideration during the assignation of fluorophores to the panel as it is important to avoid selecting fluorophores that share the same peak emission channels or have similar spectral signatures to unique autofluorescence signatures. This panel design also incorporated multiple CD45 antibody-fluorophore conjugates for dual *in vivo* labeling of the pulmonary intravascular and airspace compartments. We utilized a fluorophore and antigen optical layout table (**Table 3.1**) and the Cytek Full Spectrum Viewer Similarity™ and Complexity™ matrix (**Figure 3.1**) as planning tools to prevent fluorophore spillover-spreading error, to reduce panel complexity, and to increase the rigor of the panel that was developed. Additionally, we titrated all antibody-fluorophore conjugates using cells from 9 dpi IAV PR8-infected lung homogenate tissue, to improve the resolution of cell populations in our supervised gating strategy. (**Figure 3.2**) A step-by-step guide to our panel design strategy follows below and is adaptable for other studies investigating pulmonary inflammation and injury.

The first step is to select the cell populations, lineage markers, and antibody clones for the panel (**Table 3.2**). These will vary from study to study based on the scientific questions under investigation and the cell populations to be studied. For our studies, we undertook an unbiased approach with the goal to measure changes in the immune cells we knew could be present in the controls or recruited into the lungs of mice during the first 9 days of influenza infection (**Figure 3.3**). When we identified the lineage markers of interest for our panel, we took note of the anticipated level of antigen expression for each marker and whether there was co-expression of that marker on multiple cell populations. These are important considerations during fluorophore selection (steps 3 and 4) Finally, antibody clones were selected based on their appropriateness for our mouse strain (step 4) and on published literature.

Emission Wavelength (nm)	Primary Laser Excitation				
	UV	**Violet**	**Blue**	**Yellow Green**	**Red**
380					
400	BUV 395-MHCII				
420		BV421-CD11c			
440					
450	Live/Dead Blue	Pacific Blue-Ly6G			
480	***AF channel***				
500					
510		***AF channel***			
520			AlexaFluor488-CD45 (IV)		
550					
570					
580				PE--CD8	
600		BV605-NKp46		PE-Dazzle 594-CD3	
610	BUV615-CD45 (IT)				
650					
665		BV650-Ly6C			
680			PerCP-CD45	PE-Cy5.5-CD19	AlexaFluor647-F4/80
700					APC-R700-CD11b
710		BV711-CD64	PerCP-eF710-γδTCR		
730	BUV737-CD103				
750		BV750-Siglec F			
780		BV785-CD4		PE-Cy7-CD24	APC-eF780-CD49b
800					

Table 3.1 Fluorophore and Antigen Reagent Optical Layout

Fluorophores are presented by primary laser excitation (columns) and approximate emission wavelengths of the peak detector (rows). Fluorophores which peak in the same detector share the same emission block. This table layout provided helpful information regarding potential sources of spread and helped to inform the assignment of markers to fluorophores to minimize any loss of population resolution during panel design.

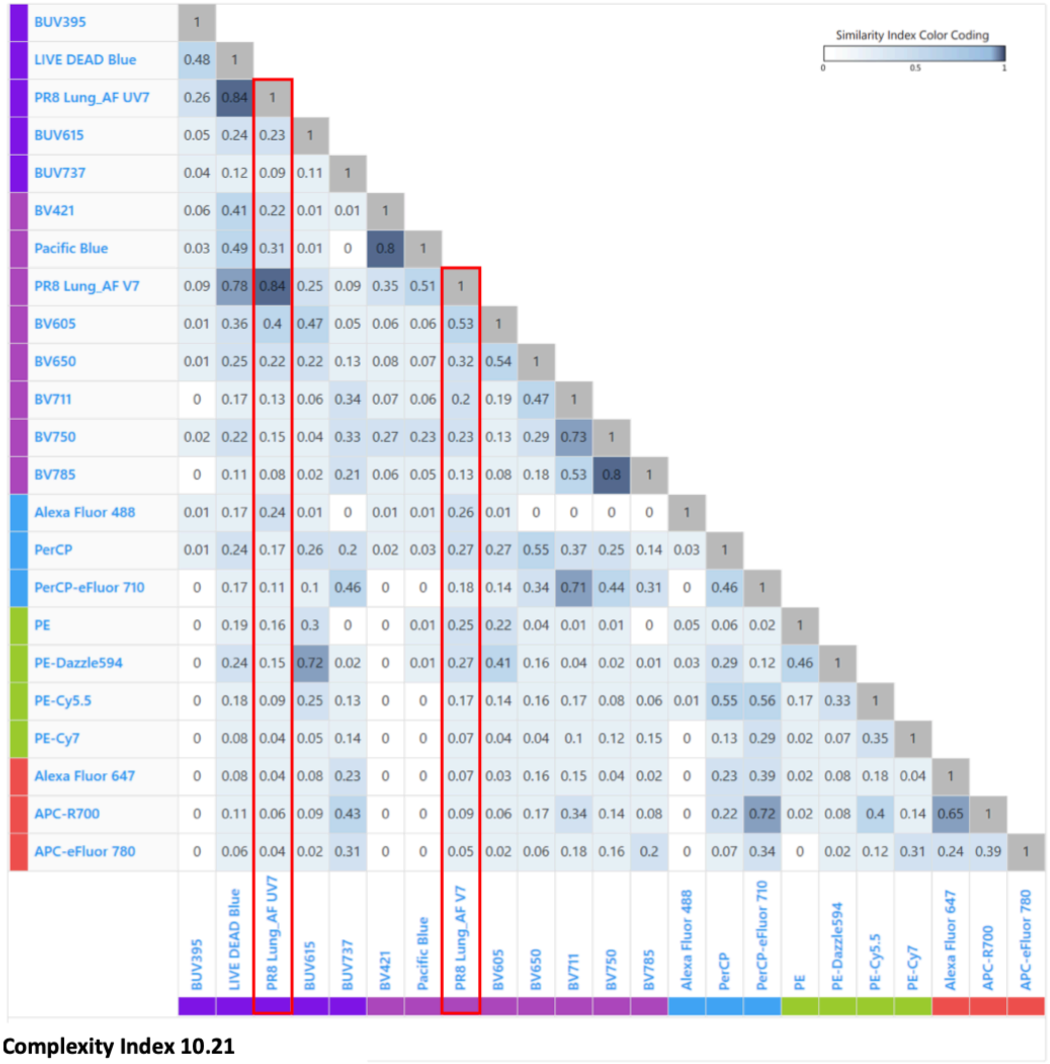

	BUV395	LIVE DEAD Blue	PR8 Lung_AF UV7	BUV615	BUV737	BV421	Pacific Blue	PR8 Lung_AF V7	BV605	BV650	BV711	BV750	BV785	Alexa Fluor 488	PerCP	PerCP-eFluor 710	PE	PE-Dazzle594	PE-Cy5.5	PE-Cy7	Alexa Fluor 647	APC-R700	APC-eFluor 780
BUV395	1																						
LIVE DEAD Blue	0.48	1																					
PR8 Lung_AF UV7	0.26	0.84	1																				
BUV615	0.05	0.24	0.23	1																			
BUV737	0.04	0.12	0.09	0.11	1																		
BV421	0.06	0.41	0.22	0.01	0.01	1																	
Pacific Blue	0.03	0.49	0.31	0.01	0	0.8	1																
PR8 Lung_AF V7	0.09	0.78	0.84	0.25	0.09	0.35	0.51	1															
BV605	0.01	0.36	0.4	0.47	0.05	0.06	0.06	0.53	1														
BV650	0.01	0.25	0.22	0.22	0.13	0.08	0.07	0.32	0.54	1													
BV711	0	0.17	0.13	0.06	0.34	0.07	0.06	0.2	0.19	0.47	1												
BV750	0.02	0.22	0.15	0.04	0.33	0.27	0.23	0.23	0.13	0.29	0.73	1											
BV785	0	0.11	0.08	0.02	0.21	0.06	0.05	0.13	0.08	0.18	0.53	0.8	1										
Alexa Fluor 488	0.01	0.17	0.24	0.01	0	0.01	0.01	0.26	0.01	0	0	0	0	1									
PerCP	0.01	0.24	0.17	0.26	0.2	0.02	0.03	0.27	0.27	0.55	0.37	0.25	0.14	0.03	1								
PerCP-eFluor 710	0	0.17	0.11	0.1	0.46	0	0	0.18	0.14	0.34	0.71	0.44	0.31	0	0.46	1							
PE	0	0.19	0.16	0.3	0	0	0.01	0.25	0.22	0.04	0.01	0.01	0	0.05	0.06	0.02	1						
PE-Dazzle594	0	0.24	0.15	0.72	0.02	0	0.01	0.27	0.41	0.16	0.04	0.02	0.01	0.03	0.29	0.12	0.46	1					
PE-Cy5.5	0	0.18	0.09	0.25	0.13	0	0	0.17	0.14	0.16	0.17	0.08	0.06	0.01	0.55	0.56	0.17	0.33	1				
PE-Cy7	0	0.08	0.04	0.05	0.14	0	0	0.07	0.04	0.04	0.1	0.12	0.15	0	0.13	0.29	0.02	0.07	0.35	1			
Alexa Fluor 647	0	0.08	0.04	0.08	0.23	0	0	0.07	0.03	0.16	0.15	0.04	0.02	0	0.23	0.39	0.02	0.08	0.18	0.04	1		
APC-R700	0	0.11	0.06	0.09	0.43	0	0	0.09	0.06	0.17	0.34	0.14	0.08	0	0.22	0.72	0.02	0.08	0.4	0.14	0.65	1	
APC-eFluor 780	0	0.06	0.04	0.02	0.31	0	0	0.05	0.02	0.06	0.18	0.16	0.2	0	0.07	0.34	0	0.02	0.12	0.31	0.24	0.39	1

Complexity Index 10.21

Figure 3.1 Similarity™ and Complexity™ Matrix

The Similarity™ Index is a measure of fluorophore dye pair uniqueness on a scale from 0 to 1. Values close to 0 indicate that the full spectrum signatures of the 2 dyes are very different from each other, and values close to 1 indicate that the signatures are very similar to each other. The Complexity™ Index is an overall measure of uniqueness of all dyes in a full spectrum cytometry panel. The lower the value, the easier it will be to work with the dyes in the panel as the overall spread in the panel will be low; the higher the value, the more challenging it will be to work with the dyes in the panel as the overall spread is higher. Well-designed small panels (e.g. 10 dyes or fewer) will have complexity indices around 2 to 3. Well-designed large panels (e.g. 35 to 40 colors) will have complexity indices around 40 to 50. This panel including 20 fluorophore-antibody conjugates, Live/Dead Blue viability dye and two AF signatures, has low similarity and complexity. Compatibility of the two lung AF signatures from lungs of PR9-infected mice with all other fluorophores in this panel are shown in the red boxes.

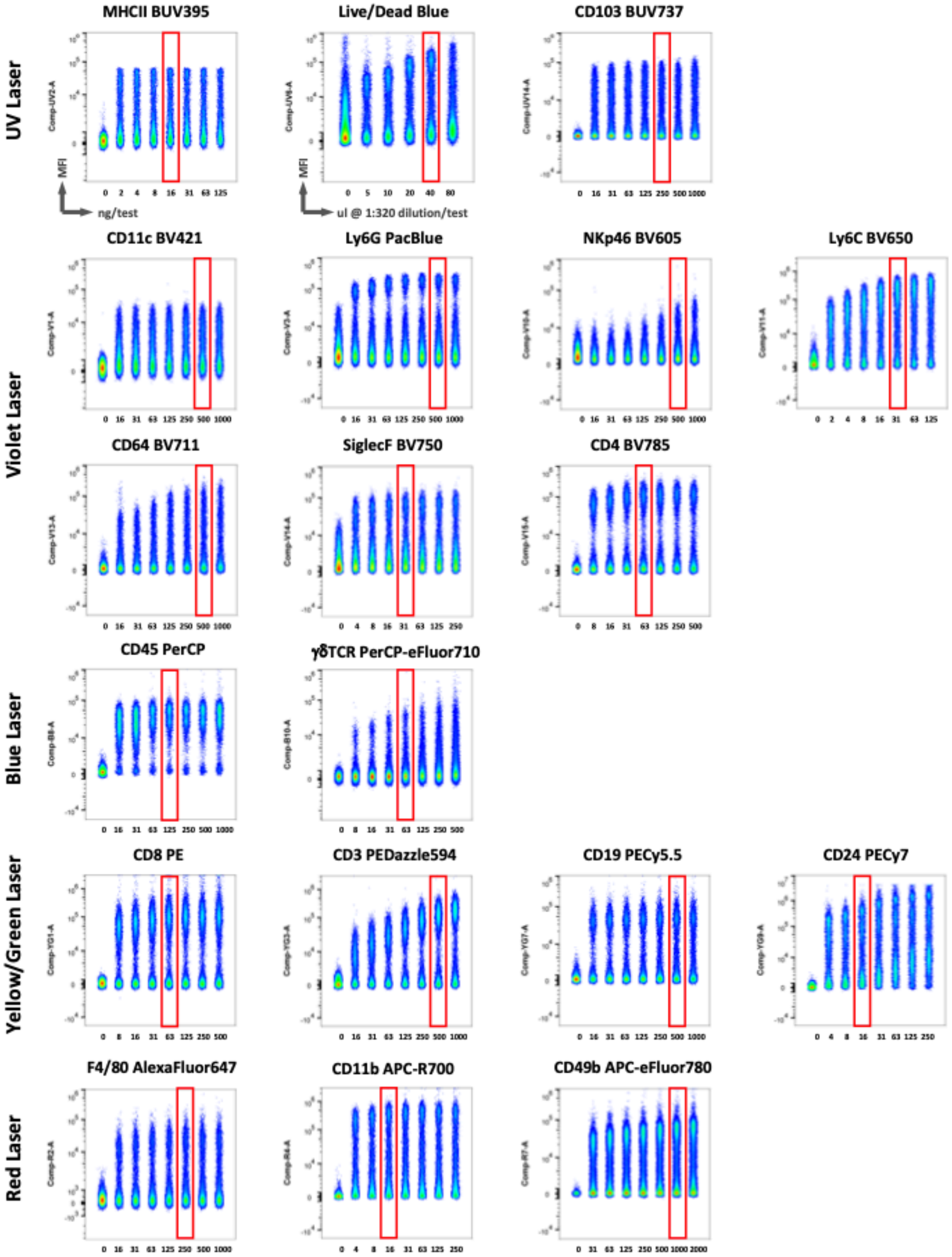

Figure 3.2 Antibody Titrations

Two-fold dilutions were tested for all fluorophores. The y-axis reflects mean fluorescence intensity (MFI); the x-axis reflects ng/test for conjugates or ul/test for Live/Dead Blue. Files were concatenated and staining indices determined with FlowJo 10.8.1. For each conjugate, the optimal amount selected for inclusion in the full-stained master mix is indicated by the red box.

Specificity	Fluorochrome	Clone	Vendor	Catalog #	Titer (ng/test)
MHCII-IA/IE	BUV395	2G9	BD Biosciences	743876	8
Viability	Live Dead Blue	-	ThermoFisher	L34962	20 μl of 1:320 stock
CD45	BUV615	I3/2.3	BD Biosciences	752418	1.25 μg/mouse IT
CD103	BUV737	M290	BD Biosciences	741739	125
CD11c	BV421	N418	BioLegend	117330	500
Ly6G	Pacific Blue	1A8	BioLegend	127612	500
NKp46	BV605	29A1.4	BD Biosciences	564069	500
Ly6C	BV650	HK1.4	BioLegend	128049	31
CD64	BV711	X54-5/7.1	BioLegend	139311	500
Siglec F	BV750	E50-2440	BD Biosciences	747316	31
CD4	BV785	GK1.5	BioLegend	100453	63
CD45.2	Alexa Fluor 488	104	BioLegend	109816	2.5 μg/mouse IV
CD45	PerCP	30-F11	BioLegend	103130	125
γδTCR	PerCP-eFluor710	GL-3	ThermoFisher	46-5711-82	63
CD8	PE	53-6.7	BioLegend	100708	63
CD3e	PE-Dazzle 594	145-2C11	BioLegend	100347	500
CD19	PE-Cy5.5	1D3	ThermoFisher	35-0193-80	500
CD24	PE-Cy7	M1/69	BioLegend	101822	16
F4/80	Alexa Fluor 647	BM8	BioLegend	123122	250
CD11b	APC-R700	M1/70	BD Biosciences	564985	16
CD49b	APC-eFluor780	DX5	ThermoFisher	47-5971-82	1000

Table 3.2 Fluorescent Reagents for Cell Staining

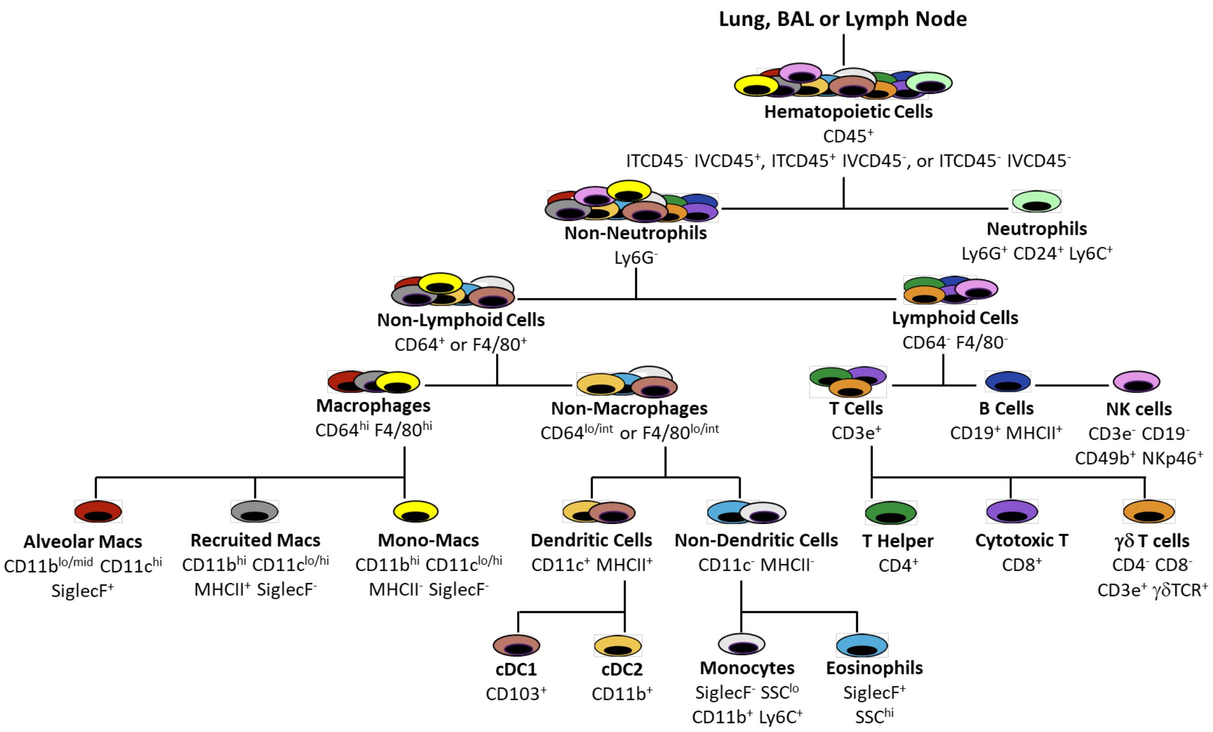

Figure 3.3 Gating Strategy

Our spectral flow cytometry panel allows for the characterization of the majority of immune cells involved in the pulmonary immune response to influenza virus including neutrophils, B cells, NK cells, T helper cells, cytotoxic T cells, γδ T cells, alveolar macrophages, recruited macrophages, monocyte-macrophages, monocytes, CD103+ dendritic cells, CD11b+ dendritic cells, and eosinophils.

The second step of our panel design was to determine the autofluorescence (AF) signatures of each tissue. These were determined by evaluation of spectral signatures from unstained BAL, lung, and lymph node cells from control (PBS instilled) and influenza infected mice collected at 3, 6, and 9-days post instillation (dpi) (**Figures 3.4-3.7**). Heterogeneous AF spectra were analyzed and multiple populations of cells with high-intensity AF signatures in each tissue were identified as previously described.[168] Briefly, we applied the N x N approach to raw spectral data from unstained samples. N is equal to 64, the number of fluorescence detectors on the Cytek® Aurora 5 Laser 16UV-16V-14B-10YG-8R. 4,096 detector combinations were observed for unstained cells from each tissue and treatment condition to find the combination that separated the greatest number of cell populations from one another with good resolution. Unique AF signatures were designated as fluorescent tags in the SpectroFlo library and given priority consideration during assignation of fluorophores for other markers to the panel (step 3). It is critically important to avoid selecting fluorophores that share the same peak emission channels or that have similar spectral signatures to unique autofluorescence signatures. Therefore, assessing the complexity of heterogeneous AF is an essential spectral flow panel design step.

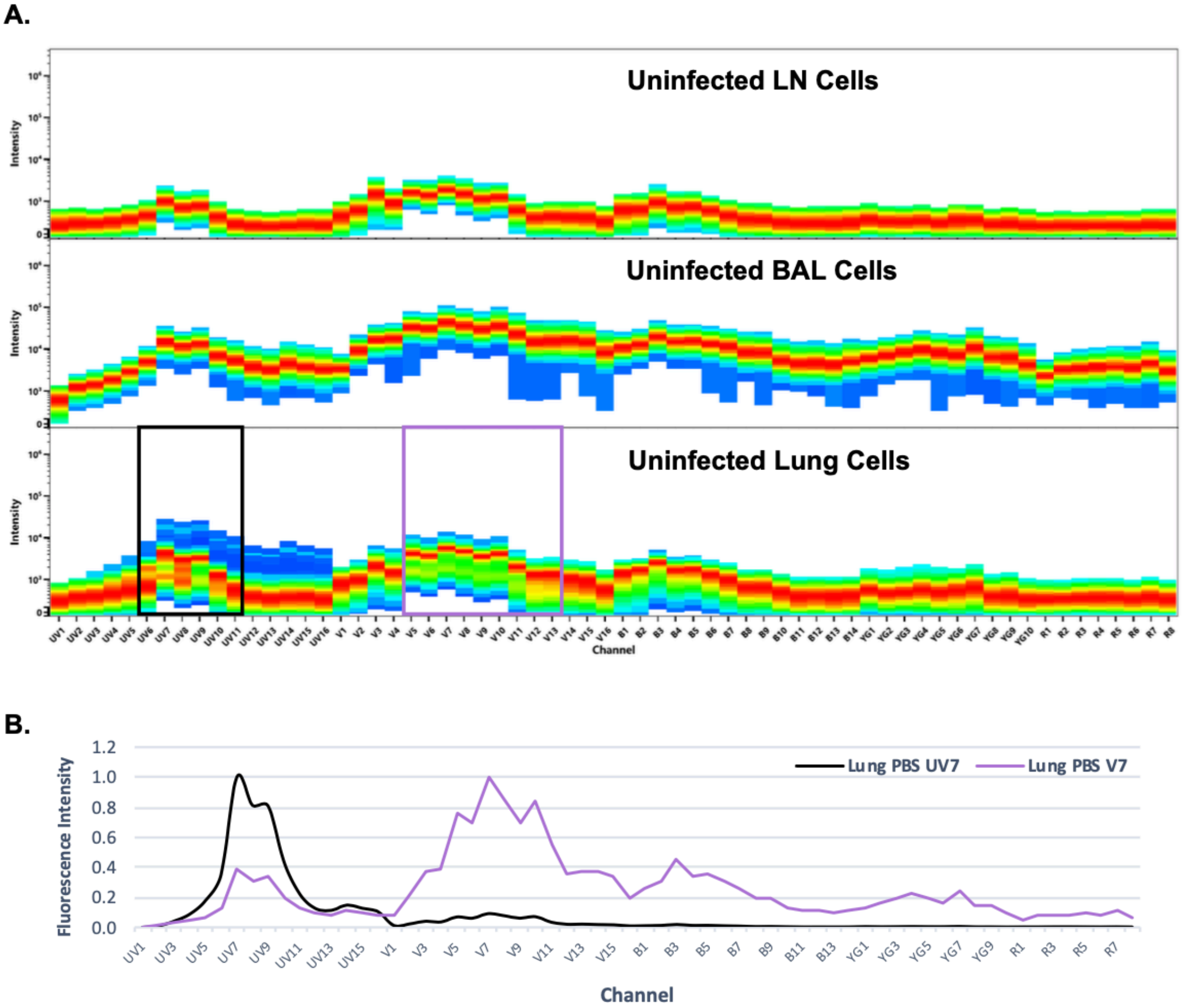

Figure 3.4 Spectral Signatures of Uninfected Lymph Node, Alveolar Airway and Lung Cells

(A) Representative spectra are shown for unstained BAL, lungs, and lymph node from an uninfected male mouse. Spectra reflect samples that were processed for removal of debris and aggregates with SpectroFlo software. Heterogeneous AF is observable in select ultraviolet (black box) and violet channels (purple box) in control lung tissue while lymph node and BAL cells from control mice have homogeneous AF signatures. (B) A spectral overlay of the UV7 AF signature and V7 AF signature identifies the distinct AF signatures present in control lungs.

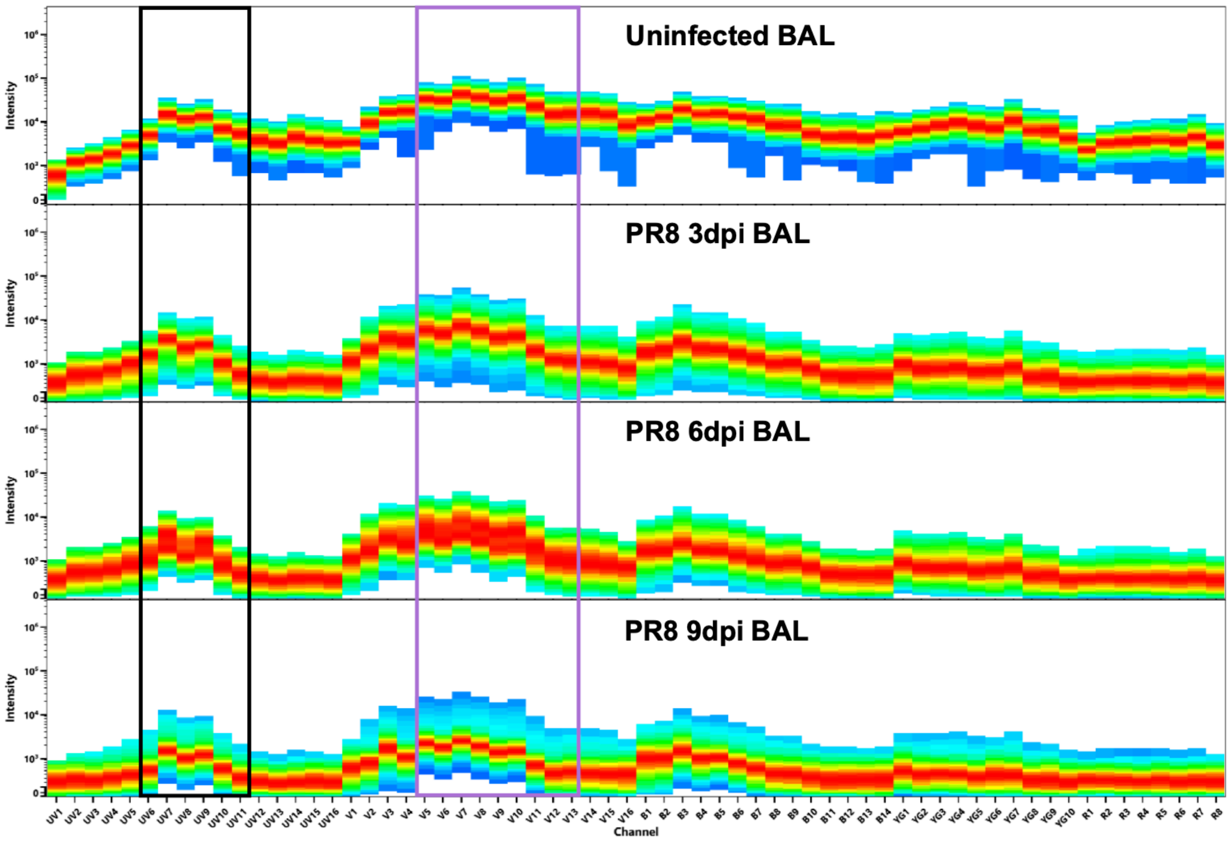

Figure 3.5 BAL Spectral Signatures

Representative spectra are shown for unstained alveolar airway cells from an uninfected mouse or mice infected with 20 PFU IAV PR8 and sacrificed at 3, 6, or 9 dpi. Spectra reflect samples that were processed for removal of debris and aggregates with SpectroFlo software. While the range of fluorescence intensity changes over the course of infection, multiple heterogeneous AF signatures were not detected at any time point.

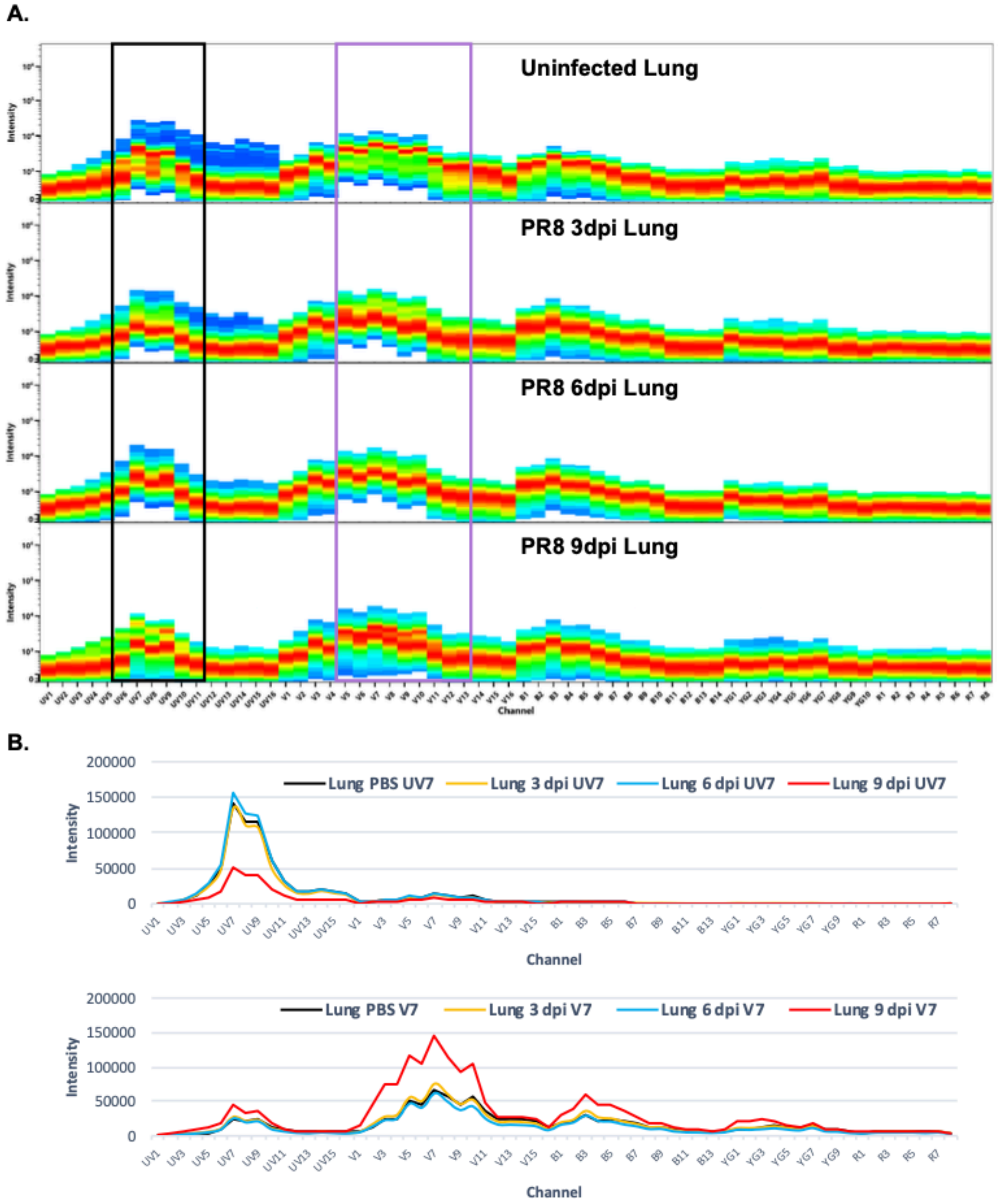

Figure 3.6 Lung Spectral Signatures

(A) Representative spectra are shown for unstained lung cells from an uninfected mouse or mice infected with 20 PFU IAV PR8 and sacrificed at 3, 6, or 9 dpi. Spectra reflect samples that were processed for removal of debris and aggregates with SpectroFlo software. Divergence of spectral characteristics over time is particularly notable in select ultraviolet (black box) and violet (purple box) channels. (B) Overlays show that these heterogeneous AF signatures peak in UV7 and V7 and change in intensity over the course of infection.

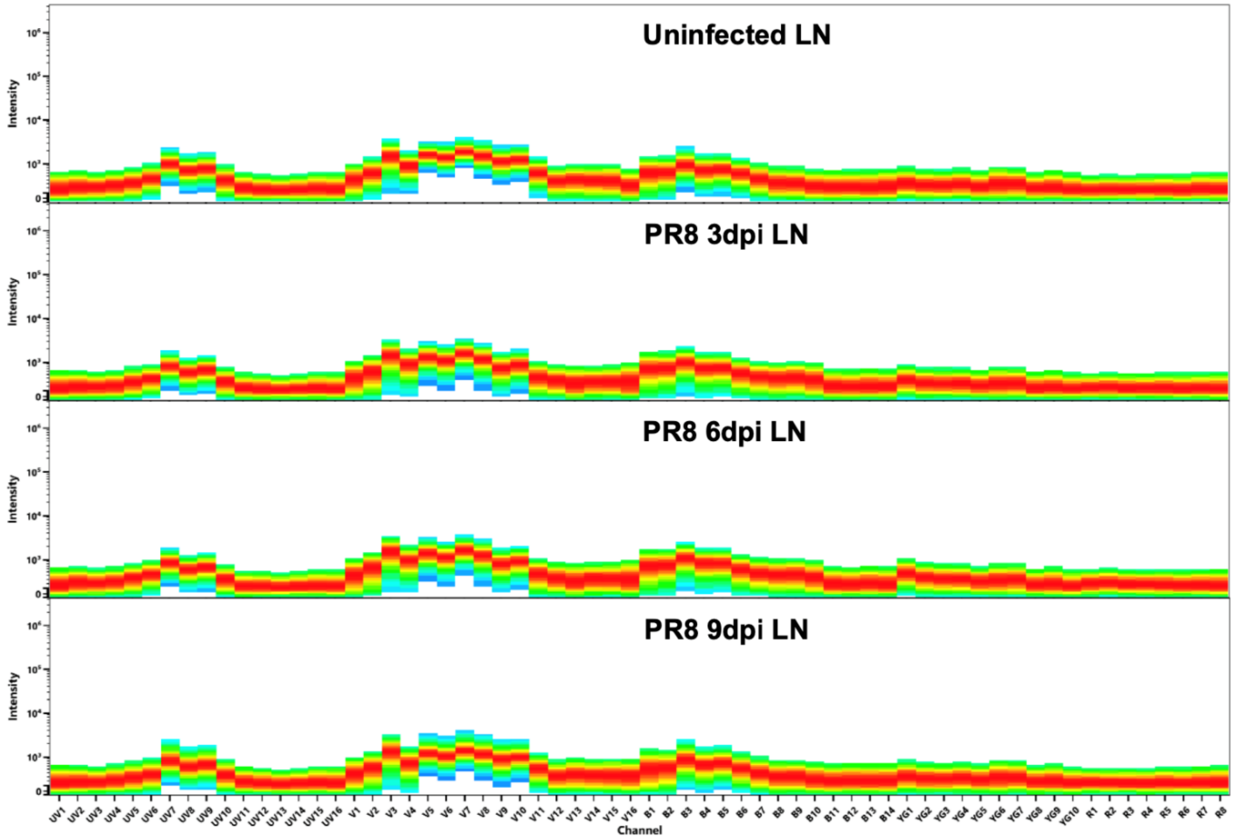

Figure 3.7 Lymph Node Spectral Signatures

Representative spectra are shown for unstained lymph node cells from an uninfected mouse or mice infected with 20 PFU IAV PR8 and sacrificed at 3, 6, or 9 dpi. Spectra reflect samples that were processed for removal of debris and aggregates with SpectroFlo software. Spectra reflect homogeneous, low intensity autofluorescence at every time point.

In step 3, the selection of specific fluorophore-antibody conjugates, fluorophores were assigned to channels with unique peaks and appropriate emission wavelengths (**Table 3.1**). The following criteria were followed: (i) reagents that shared a peak channel with the Live/Dead Fixable Blue viability dye (UV6) were avoided; (ii) reagents that shared peak channels with AF signatures were avoided; (iii) reagents that had unique peak channels but shared highly similar spectra with AF signatures (e.g., AlexaFluor532 or BV570) were avoided as they yield poor resolution of cell populations due to spread into AF signatures. Further considerations were given to balancing fluorophore stain index vs antigen expression level, minimizing similarity and spread of fluorophores, and assignment of distinct fluorophores to co-expressed antigens. All fluorophore-antibody conjugates used for these studies were commercially available, and only surface antigens were chosen for detection.

Step 4 was incorporating dual *in vivo* CD45 labeling in our panel. The two antibodies chosen for dual *in vivo* labeling were of different clonality, recognizing different epitopes from the CD45 antibody chosen for *in vitro* labeling. Additionally, the CD45.2 epitope was chosen for one of the *in vivo* epitopes due to its compatibility with the C57BL/6J mice used in our study. This reduced the likelihood of saturating CD45 sites with the intravascular and intratracheal antibodies which could diminish the intensity of *in vitro* staining. We assigned fluorophores with low to medium staining intensity to CD45 to reduce the likelihood of spillover and spread. This was important because CD45 is expressed at high levels on all leukocytes and co-expressed with all other markers in the panel. The fluorophores also had low similarity in their spectral profiles to ensure good resolution of leukocytes from different compartments. Preliminary experiments were conducted with the selected antibodies, AlexaFluor488-CD45.2 (IVCD45) and BUV615-CD45 (ITCD45), to establish titers yielding good resolution of IVCD45+ ITCD45- vs IVCD45- ITCD45+ vs IVCD45- ITCD45- populations in our gating strategy.

In step 5, assessing potential spillover-spreading in our panel that could contribute to unmixing errors, we evaluated our AF spectral signatures with all other selected fluorophores computationally using the Cytek® Full Spectrum Viewer Similarity^{TM} & Complexity^{TM} matrix (**Figure 3.1**). Well-designed panels have similarity indices < 0.98. Panels with a similarity index > 0.98 between two signatures will result in spillover- spreading and unmixing errors. Well-designed small panels (e.g. 10 dyes or fewer) will have complexity indices around 2 to 3. Well-designed large panels (e.g. 35 to 40 colors) will have complexity indices around 40 to 50. Our panel's complexity fell well below this benchmark due to our panel design strategy which ensured we that had fluorophore and autofluorescence spectral signatures that were very different from each other (Similarity Indices < 0.8). Evaluation of similarity and complexity indices is an important consideration when optimizing a spectral flow panel.

Step 6 was optimizing our panel to minimize nonspecific antibody-fluorophore binding and to obtain accurate resolution of fluorophores and autofluorescence signatures. To achieve this, all antibody-fluorophore conjugates were titrated using cells from 9 dpi IAV PR8-infected lung homogenate tissue with approximately 100,000 cells per test (**Figure 3.2**). Conjugates were tested in 2-fold serial dilutions within the range of 2 to 2000 ng per test, as indicated; preliminary tests were performed to determine the range to be evaluated for each conjugate. FlowJo was used to determine the Separation Index (SI), a metric for defining the separation between positive vs negative populations, for each dilution and to concatenate populations for visualization.[169] Selected titers are reported in **Table 3.2**. In some cases, the selected titer was not necessarily the one with the highest SI value; consideration was also given to the appropriate alignment of negative populations with zero median fluorescence intensity (MFI), adequate separation of positive and negative populations, and maintenance of positive populations below 10^6 MFI.

Finally, in step 7 we determined whether beads or cells would be the appropriate reference control material for each fluorophore-antibody conjugate in our panel. The normalized full spectrum spectra for all of our reagents on both single stain beads and single stain cells from IAV PR8-infected lung homogenates was determined as previously described.[167] Discrepancies in spectra were found with the following fluorophores: BV421, BV711, BV750, and PerCP-eFluor 710. Therefore, these 4 fluorophores were run as single-stain controls using cells for our experiments while all remaining fluorophore single-stain controls were run using beads. The live/dead viability reference control was based on a mixture of live and heat-killed cells. The resolution of every fluorophore in the panel was checked by comparing the single stain control tube with the same fluorophore in the full-stained sample. We found that the resolutions were identical and no changes to the selected titrations were made.

3.2.5 *In vivo* Antibody Labeling and Tissue Harvest

Mice were sacrificed at 3, 6, or 9 days post-instillation (dpi) with IAV PR8, 3 days post-instillation with LPS, 10 days post-instillation with bleomycin, and 31 days post initial instillation with HDM extract. Prior to euthanasia, mice were anesthetized with isoflurane in an induction chamber. Alexa Fluor 488-conjugated anti-CD45.2 antibody, clone 104 (BioLegend, San Diego, CA, USA), diluted 1:40 (v:v) with PBS, in a total volume of 200µL (2.5µg/per mouse), was injected retro-orbitally to label the intravascular (IV) leukocytes (IVCD45$^+$). After 3 minutes, while keeping the mouse anesthetized with isoflurane delivered by nose cone, the left renal artery was transected, and the mouse was euthanized by exsanguination to reduce the chance that the IVCD45 conjugate would bind non-specifically to airway or interstitial lung leukocytes. Undesired cross-labeling of lung parenchyma leukocytes with the blood-borne antibody could result from loss of vascular integrity allowing leakage of the intravascular CD45 antibody into the parenchyma. Vascular integrity can be evaluated with Evan's blue dye.[153,162] In our preliminary studies we did not find increased leakage of Evan's blue dye into the lungs of IAV PR8 mice compared to uninfected mice. Next, the trachea was cannulated with an 18-guage angiocath via tracheostomy and BUV615-conjugated anti-CD45 antibody, clone I3/2.3 (BD Biosciences, San Jose, CA, USA) diluted to 1.25 µg/mL with PBS, in a total volume of 1mL per mouse, was instilled by intratracheal (IT) administration into the lungs (ITCD45). The antibody was allowed to remain in the lungs for 3 minutes. To reduce the chance that the ITCD45 conjugate will bind to lung interstitial leukocytes, the airways were immediately lavaged with 1 mL PBS/0.5M EDTA two additional times. The thoracic cavity was opened via midline sternotomy and the lungs were perfused by injection of 5mL of PBS into the right ventricle. Using a dissecting microscope, the largest mediastinal lymph node was removed from the right dorsal aspect of the trachea. The lymph node was placed directly into 0.5 ml of RPMI containing 10% fetal bovine serum (FBS, Thermo Fisher Scientific Waltham, MA, USA) on ice. Lung tissue was removed by blunt dissection from the primary bronchi and placed on ice. Mice that were utilized for the harvest of unstained tissue did not receive IVCD45 or ITCD45. With these tissue handling practices, we achieved good compartmentalization of ITCD45$^-$ IVCD45$^+$, ITCD45$^+$ IVCD45$^-$, and ITCD45$^-$ IVCD45$^-$ leukocytes, with minimal (<0.6%) double-positive cells in our experimental model. A higher percentage of co-positive cells might indicate transvascular leakage into airways due to injury caused by the disease process under study or excessive force during the bronchoalveolar lavage or lung perfusion procedures.

3.2.6 Preparation of Single-Cell Suspension

Cells in the bronchoalveolar lavage (BAL) fluid were pelleted and RBC lysis buffer (Thermo Fisher Scientific Waltham, MA, USA) was applied according to manufacturer instructions. After

RBC lysis, BAL cells were pelleted and suspended in Flow Cytometry Straining (FCS) buffer (Thermo Fisher Scientific Waltham, MA, USA).

A stock solution of Liberase TM (Sigma-Aldrich, St. Louis, MO, USA) was prepared at 10 mg/ml (26 U/ml) in RPMI 1640 w/o phenol red or fetal bovine serum (FBS) (Thermo Fisher Scientific Waltham, MA, USA), stored in single-use aliquots at -30C, and used by the expiration date per the manufacturer's recommendation. A stock solution of recombinant DNase I (Sigma-Aldrich, St. Louis, MO, USA) was prepared at 10,000 U/ml in H2O and stored in single-use aliquots at -30C for up to 1 month. Just prior to harvest, a working solution of enzyme digestion mixture, containing Liberase TM (0.26 U/ml) and recombinant DNase I (10 U/ml), was prepared in RPMI 1640 without phenol red or FBS in a volume of 2 ml per mouse and stored on ice until needed for enzymatic digestion of lungs.

The lungs were minced using a razor blade and then incubated for 45 minutes at 37C in 2mL RPMI 1640 without phenol red or FBS (Thermo Fisher Scientific Waltham, MA, USA) containing 0.26U/mL Liberase TM (Sigma-Aldrich, St. Louis, MO, USA) and 10U/mL recombinant DNase I (Sigma-Aldrich, St. Louis, MO, USA). After digestion, samples were pipetted up and down and then filtered through 70µm cell strainers (VWR, Brisbane, CA, USA) with RPMI/10% FBS. Lung cells were pelleted and RBC lysis buffer was applied according to manufacturer instructions. After RBC lysis, lung cells were pelleted and suspended in FCS buffer.

Lymph nodes were transferred onto 70µm cell strainers and gently mashed with the rubber end of the plunger from a 3 ml syringe. The filters were rinsed with RPMI/10% FBS and then the lymph node cells were pelleted and suspended in FCS buffer. Total live cells from each BAL, lung, and lymph node sample were counted using ViaStain AO/PI staining solution (PerkinElmer Inc, Waltham, MA, USA) and SD100 counting chambers (PerkinElmer Inc, Waltham, MA, USA) on a Cellometer Auto 2000 Cell Counter (Nexcelom, Lawrence, MA, USA).

3.2.7 *In vitro* Antibody Staining

Antibody manufacturer, clone numbers, and titers are available in **Table 3.2**. All antibodies are commercially available and unstained, single-stain, and fluorescence-minus-one controls were used to define gating for positive and negative populations. Antibody specificity was not independently validated for antibodies in our panel; however, emphasis was made to select antibody clones recommended from published studies.[170-176]

The following reagents were prepared for *in vitro* antibody staining:

(i) Fc Block TruStain FcX PLUS (anti-mouse CD16/32) (BioLegend, San Diego, CA, USA) was diluted 1:100 (v:v) with Flow Cytometry Staining (FCS) buffer (Thermo Fisher Scientific Waltham, MA, USA) in a total volume of 50µL per test and stored on ice until use

(ii) Just before use, one vial of LIVE/DEAD Fixable Blue Dead Cell Stain Kit (Thermo Fisher Scientific Waltham, MA, USA) was resuspended with 50 µL DMSO and then diluted 1:320 (v:v) in PBS in a total volume of 20µL per test. LIVE/DEAD Blue Cell Stain must be prepared in a protein-free solution, without FCS, as protein can impact the efficiency of LIVE/DEAD Blue staining

(iii) To prepare the full-stain antibody master mix, all antibodies were first gently vortexed and centrifuged at 10,000x*g* for 3 minutes at 4C. Antibodies were diluted in Brilliant Stain Buffer (BD Biosciences San Jose, CA, USA) to achieve the final titers indicated in **Table 3.2**, allowing for a total volume of 100µL per test. The antibody master mix excluded the antibody conjugates used for *in vivo* staining, Alexa Fluor 488 anti-CD45.2 (IVCD45) and BUV615 anti-CD45 (ITCD45) and was stored on ice until use.

The following cells and beads were prepared for *in vitro* staining:

(i) For full-stained samples, up to 1 x 10^6 cells from BAL fluid, lungs, and lymph nodes of mice that received both IVCD45 and ITCD45 were used.

(ii) Tissue from a mouse that did not receive IVCD45 or ITCD45 was used for preparation of unstained controls, the single-stain viability control, and single-stain cell controls (CD11c-BV421, CD64-BV711, SiglecF-BV750, and γδTCR-PerCP-eFluor 710). For unstained controls, up to 1 x 10^6 cells from BAL fluid, lungs, and lymph nodes were used. For the viability control, 2.5 x 10^5 lungs cells were heat-killed for 10 minutes at 75C, and after chilling for 10 minutes on ice were combined with 2.5 x 10^5 additional lung cells. For each single-stain cell control, 2.5 x 10^5 cells from the lungs were used. Single-stained controls for the remaining fluorophore-antibody conjugates were prepared using UltraComp eBeads™ (Thermo Fisher Scientific Waltham, MA, USA), following the manufacturer's instructions.

The following steps were followed for in vitro staining:

(i) In vitro antibody staining was performed in a 96-well V-bottom plate (Thermo Fisher Scientific Waltham, MA, USA).

(ii) The appropriate number of cells and beads were aliquoted and pelleted via centrifugation at 400xg for 3 minutes at 4^{o}C.

(iii) The supernatant was carefully removed, and all samples were washed with 200µL of PBS.

(iv) Samples were pelleted, supernatant removed, and samples were resuspended with 100µL of PBS.

(v) 20 µl of viability dye dilution was added to viability control and full-stained samples, mixed well, and incubated for 15 minutes at room temperature in the dark. Unstained and single-stained controls received 20µL of PBS instead of viability dye dilution.

(vi) After incubation 100µL of FCS buffer was added to all samples.

(vii) Samples were pelleted, supernatant removed, and samples were resuspended with 200µL of FCS buffer.

(viii) Samples were pelleted, supernatant removed, and 10µL of Brilliant Stain Buffer was added to all full-stained samples and mixed well.

(ix) 50µL of Fc Block was added to all samples and incubated for 5 minutes at room temperature in the dark.

(x) 100µL of the full-stain antibody master mix was added to samples for full staining. 100µL FCS buffer was added to unstained controls and viability control. Single-stained cell controls (CD11c-BV421, CD64-BV711, SiglecF-BV750, and γδTCR-PerCP-eFluor 710) received the appropriate titer of their designated fluorophore-antibody conjugate as indicated in **Table 3.2**. Single-stain bead controls received 0.5µL of their fluorophore-antibody conjugate diluted in 100µL of FCS.

(xi) All samples were incubated for 30 minutes at room temperature in the dark, after which 100µL of FCS buffer was added to all samples.

(xii) Samples were centrifuged, supernatant removed, and samples were resuspended with 200µL of FCS buffer.

(xiii) Samples were pelleted, supernatant removed, and samples were resuspended with 100µL of Cytofix (BD Biosciences, San Jose, CA, USA).

(xiv) All samples were incubated for 15 minutes at room temperature in the dark, after which 100µL of FCS buffer was added to all samples.

(xv) The samples were centrifuged, supernatant removed, and samples were resuspended with 200µL of FCS buffer.

(xvi) The samples were centrifuged again, supernatant removed, and samples were resuspended with 200µl of FCS buffer.

(xvii) Finally, samples were transferred to 5 ml tubes (VWR, Brisbane, CA, USA) and stored overnight at 4°C in the dark until acquisition on the flow cytometer the following day.

3.2.8 Flow Cytometry

The optical design, detection modules, number of detectors per laser module, detector module configurations, and methodology for establishing the optimal instrument gain settings, known as CytekAssaySetting, for commercially available fluorophores has been previously reported. [167] For our studies, we utilized CytekAssaySetting, which automatically update gain settings during daily QC on calibrated bead MFI targets to ensure consistent instrument setup over time. Before all data collection, QC on calibrated beads was performed and data was only collected when the instrument passed QC.

It was imperative to ensure our samples were on scale as our panel was designed to detect relatively small cells such as lymphocytes and very large cells such as alveolar macrophages. To address this, the FSC, SSC, and SSC-B gain settings were adjusted using tissue-specific unstained samples immediately before acquisition. SSC-B-A was set to a log scale to improve visualization of especially large cells, such as alveolar macrophages, on SSC-B-A plots. FSC Area Scaling Factor was reduced to 0.9 in CytekAssaySetting. For each tissue type, FSC, SSC, and SSC-B gain settings were adjusted immediately before data acquisition to ensure >95% of all cells were on scale. The FSC threshold was set at 250,000. Acquisition stopping gates were set to 200,000 events or 125µL, and were recorded at low-medium flow.

Spectral cytometry was performed using the Aurora cytometer (Cytek Biosciences, Fremont, CA, USA). Our gating strategy is detailed in **Figures 3.3, 3.8, 3.9, and 3.10**. It supports the identification of neutrophils, macrophages, dendritic cells, monocytes, eosinophils, lymphocytes, and natural killer cells. The cell surface markers used were chosen after carefully reviewing the literature, particularly the works of Misharin, McCubbrey, Gibbings, and Tighe and OMIPs -032, -061, and -069.[170-177] All cytometry data was analyzed using SpectroFlo® (Cytek Biosciences, CA) or FlowJo® (Becton, Dickinson & Company, OR) flow cytometry software.

Raw data were converted to unmixed data with SpectroFlow software v3.0 using an ordinary least squares algorithm to deconvolute individual fluorophore signatures within a fully stained sample. As part of our assessment of our panel's performance, we compared spectral unmixing of our panel with and without AF spectral signatures that initially presented as heterogeneous AF in our unstained samples. Identification of AF signatures was necessary for lung cells and was dependent on the day post instillation. AF signatures were saved as discrete fluorochrome tags in the SpectroFlo library as previously described. These were then incorporated into our panel as single-stain reference controls for unmixing and data analysis. It was not necessary to define AF signatures for lymph nodes as cells from these compartments had low, homogeneous AF over the course of these studies.

In both unmixing strategies, we utilized the "AF as a tag" (AF) function in the SpectroFlo® (Cytek Biosciences, CA) software. As with fluorescent dyes, AF is susceptible to spillover interactions with other fluorophores that have emission spectra in similar wavelength ranges. This was evaluated computationally using the Cytek® Full Spectrum Viewer Similarity^{TM} & Complexity^{TM} Index functionality (**Figure 3.1**). The 21 fluorophore panel presented here has a low predicted complexity index of 7.46 (not shown). Inclusion of two unique AF signatures for lungs of 9dpi PR8 mice increases the complexity index only to 10.21 (**Figure 3.1**). Additionally, we visualized unmixing errors in both unmixing strategies by evaluating Nx1 permutations of all fluorophores in the panel against AF on unstained lungs from a mouse 9 dpi with IAV PR8. Finally, we applied our supervised gating strategy (**Figures 3.3, 3.8, 3.9, and 3.10**) to both unmixing strategies and compared cell counts for individual cell populations from both unmixing strategies.

t-SNE analysis was initiated downstream of single live CD45^{+} gating on BAL and lung digest cells. Cells were down-sampled to 40,000 events and concatenated for t-SNE analysis in FlowJo. Cell subsets defined by our supervised gating strategy were projected onto the t-SNE space to define leukocyte populations in each compartment.

3.2.9 Statistical Analysis

Statistical analyses and graphs were generated using GraphPad Prism (GraphPad Software, Inc., San Diego, CA, USA). Statistical analyses were performed using ordinary two-way ANOVA with correction for multiple comparisons. Statistical results with a value of $p<0.05$ were considered statistically significant. All graphs show medians with standard errors.

A. PBS 9dpi Marginated Vasculature

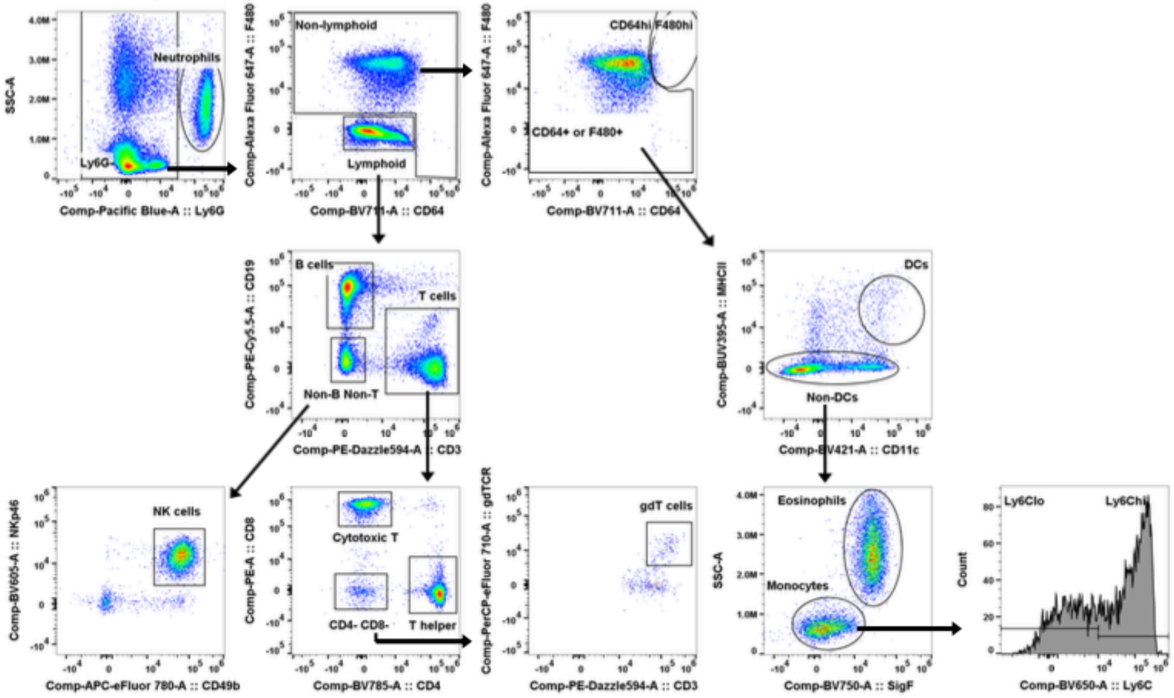

B. PBS 9dpi Lung Interstitium

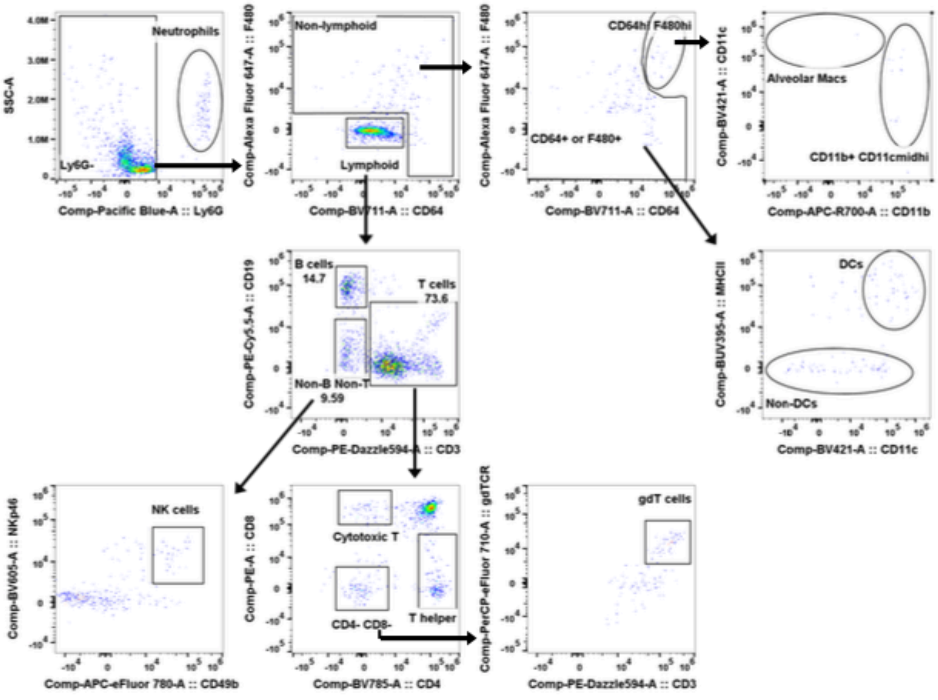

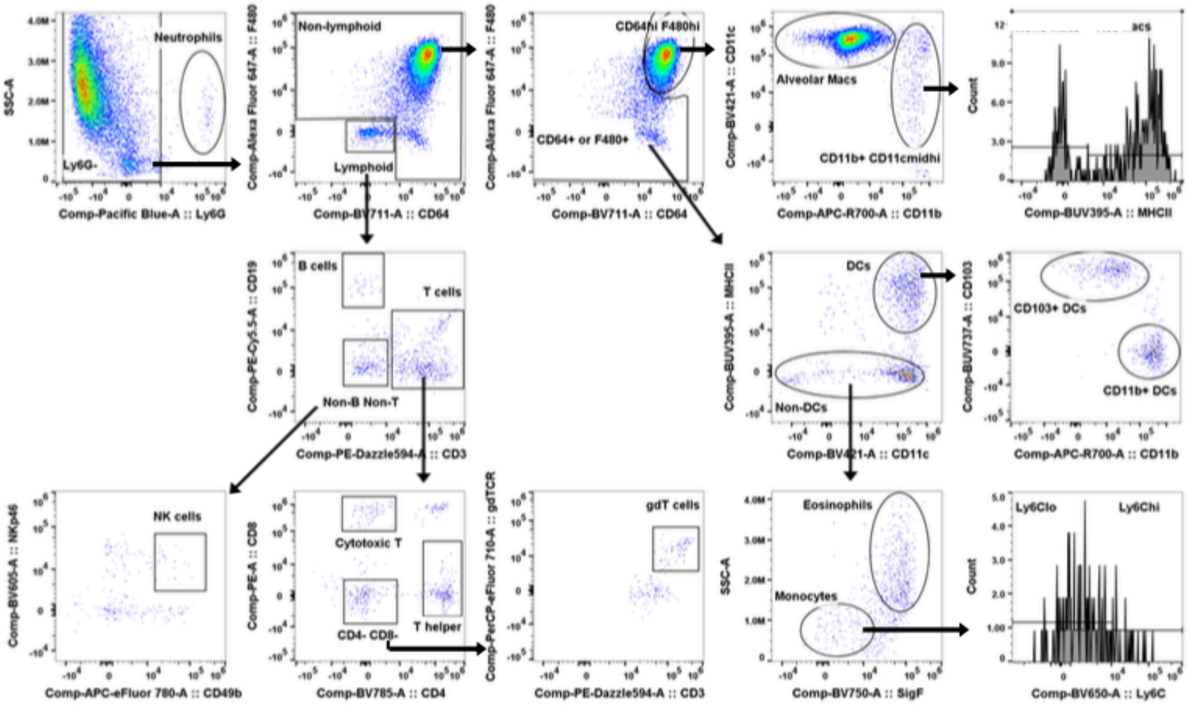

C. PBS 9dpi Non-Lavageable Airway

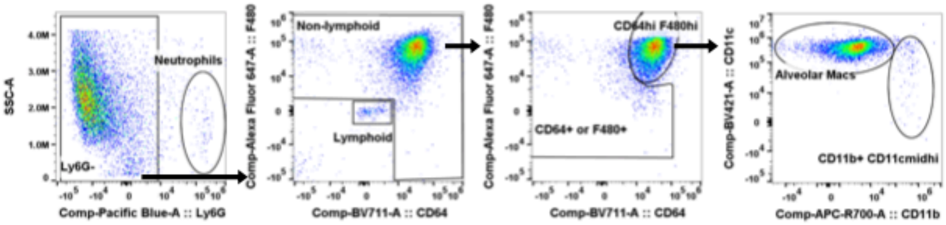

D. PBS 9dpi Lavageable Airway

Figure 3.8 Gating Tree on PBS 9 dpi Lung and BAL Leukocytes

The supervised gating strategy was applied to single live CD45+ cells from a male control mouse. Representative gating trees are shown for leukocytes in the (A) marginated vasculature; (B) lung interstitium; (C) non-lavageable airway; and (D) lavageable airway. Populations representing <2% of the parent gate were not further characterized. See text for full description of gating strategy.

A. PR8 9dpi Marginated Vasculature

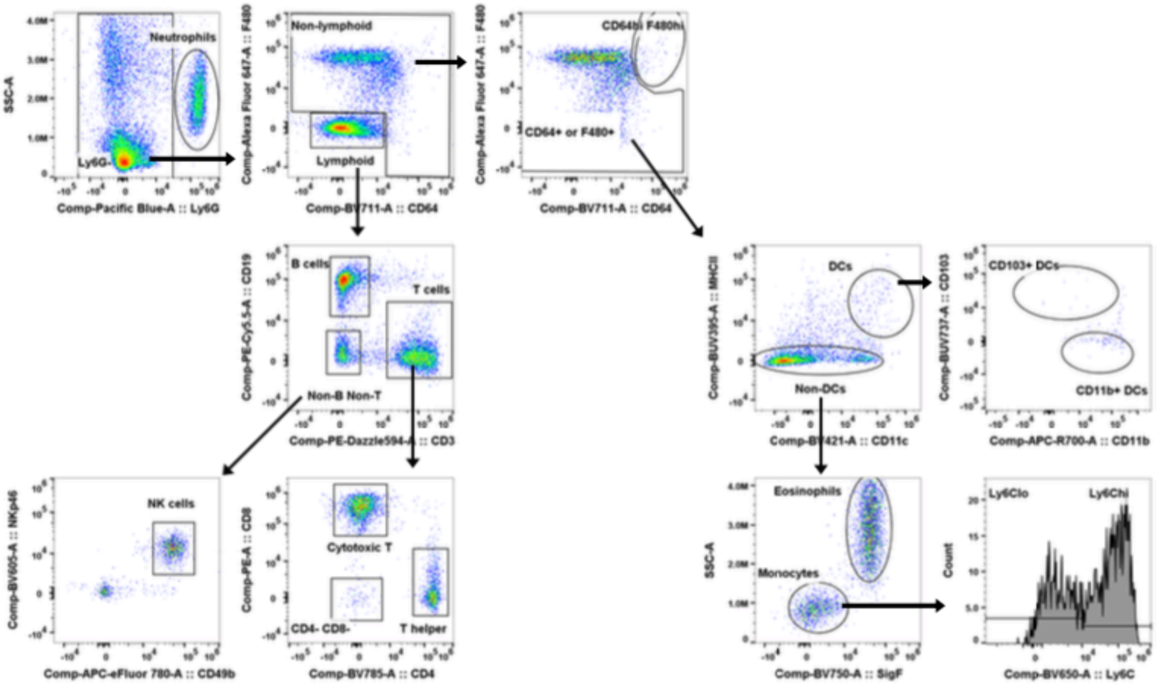

B. PR8 9dpi Lung Interstitium

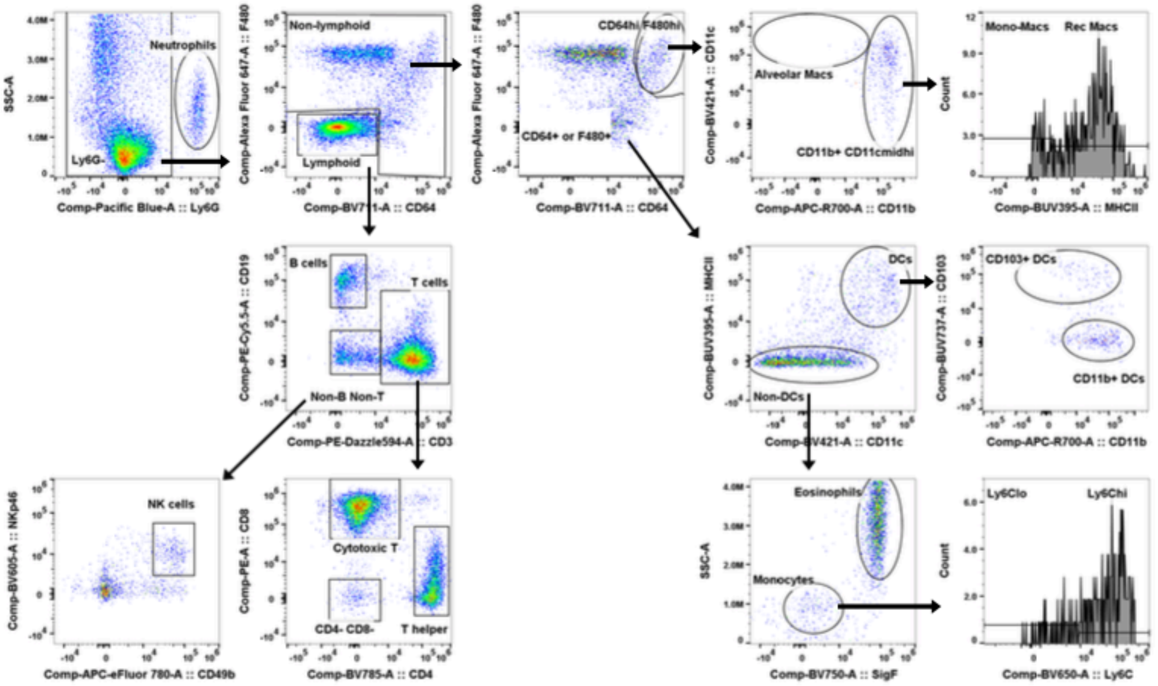

C. PR8 9dpi Non-Lavageable Airway

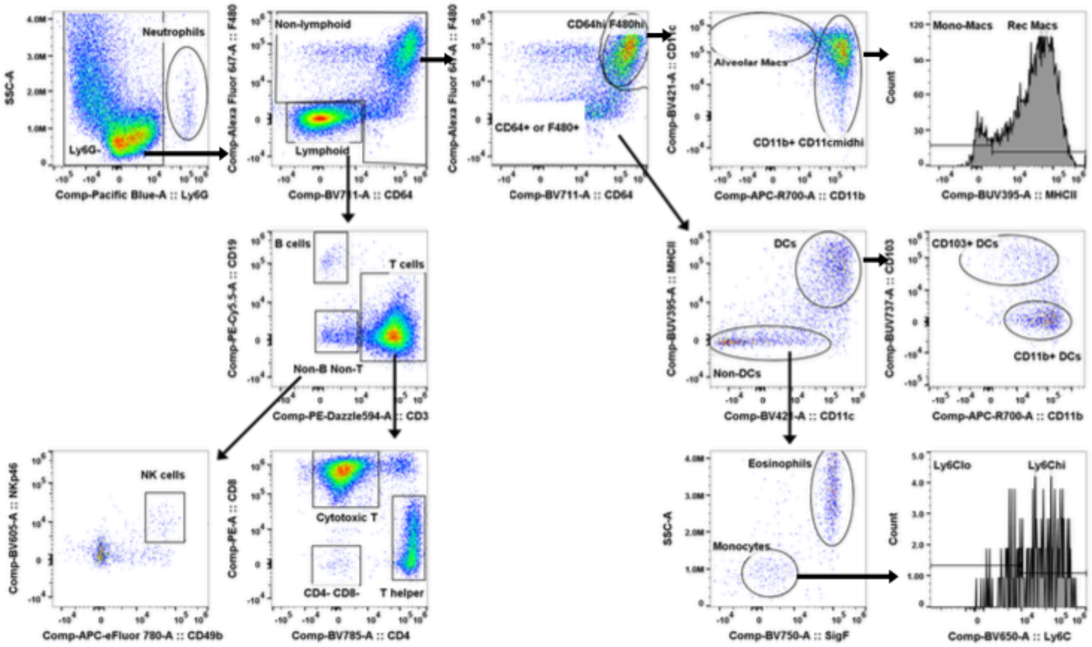

D. PR8 9dpi Lavageable Airway

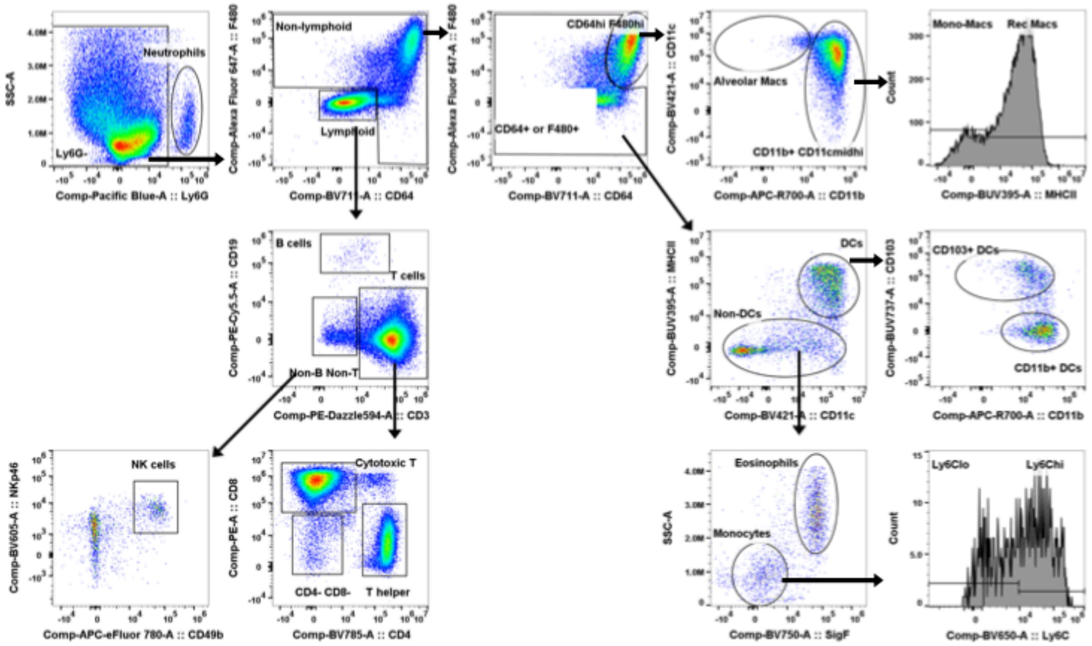

Figure 3.9 Gating Tree on PR8 9dpi Lung and BAL Leukocytes

The supervised gating strategy was applied to single live CD45+ cells from a PR8-infected male mouse. Representative gating trees are shown for leukocytes in the (A) marginated vasculature; (B) lung interstitium; (C) non-lavageable airway; and (D) lavageable airway. Populations representing <2% of the parent gate were not further characterized. See text for full description of gating strategy.

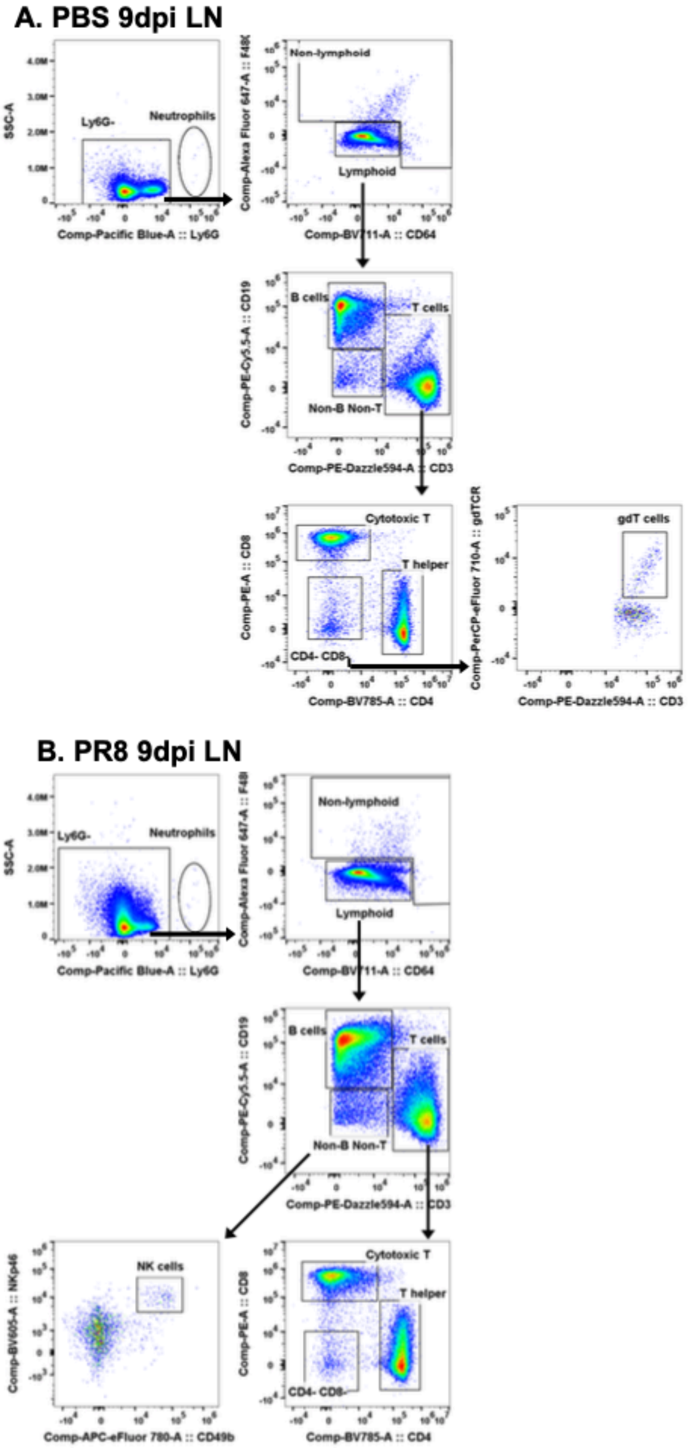

Figure 3.10 Gating Tree on PBS and PR8 9 dpi Lymph Node Leukocytes

The supervised gating strategy was applied to single live CD45+ cells from the lymph nodes of (A) a control male mouse, and (B) a 9 dpi PR8-infected male mouse. Populations representing <2% of the parent gate were not further characterized. See text for full description of gating strategy.

3.3 Results

3.3.1 Spectral Flow Cytometry Panel for Compartmental Analysis of the Pulmonary Immune Response

We developed a gating strategy (**Figure 3.3, Table 3.3**) and fluorophore panel (**Table 3.2**) for spectral flow cytometry that is compatible with heterogeneous AF and characterizes B cells, T cells (cytotoxic T, T helper, and γδ T cells), NK cells, macrophages (alveolar and recruited), monocyte-macrophages, monocytes (Ly6C^{lo} and Ly6C^{hi}), dendritic cells (CD103^{+} and CD11b+), neutrophils, and eosinophils in the pulmonary tissues during influenza infection. Our panel includes dual *in vivo* CD45 labeling for compartmental analysis of immune cells in the marginated vasculature, lung interstitium, lavageable airway, and non-lavageable airway. Additionally, our tissue collection procedures include the collection of the mediastinal lymph nodes for an enhanced understanding of immune trafficking in response to influenza A infection. This approach and protocol leverage spectral flow cytometry to locate with high precision and resolution a wide variety of leukocytes during the pulmonary immune response; this combination of approaches is not currently available in published protocols.

In our gating strategy, after defining single live cells, CD45^{+} leukocytes are segregated based on the expression of ITCD45 and IVCD45. Next, neutrophils are identified as Ly6G^{+} and verified as CD24^{+} with variable expression of Ly6C. From the non-neutrophil gate, lymphoid cells are distinguished from other non-lymphoid cells based on CD64 and F4/80 expression. Lymphoid cells are CD64^{-} F4/80^{-}; within the lymphoid gate are CD19^{+} B cells, CD3e^{+} T cells, and CD19^{-} CD3e^{-} non-B non-T cells. B cells are verified as CD19^{+} and MHCII^{+}. The T cell population is further characterized as CD4^{+} T helper cells, CD8^{+} cytotoxic T cells, or CD4^{-} CD8^{-} γδ-TCR^{+} γδ T cells. The non-B non-T lymphoid cell population includes NK cells, as identified with NKp46 and CD49b. Non-lymphoid cells are identified from those that express CD64 or F4/80; within the non-lymphoid gate are monocytes, macrophages, dendritic cells, and eosinophils. CD64^{hi} F4/80^{hi} cells include resident alveolar macrophages (AMs) that are CD11b^{-} CD11c^{+} in control animals or CD11b$^{mid/hi}$ CD11c^{+} in PR8-infected animals; AMs are verified as SiglecF^{+} Ly6C^{mid} MHCII^{-}. CD64^{hi} F4/80^{hi} cells also include a CD11b^{+} CD11c$^{lo/hi}$ subset, which includes MHCII^{-} monocyte-macrophages and MHCII^{+} recruited macrophages (RMs); monocyte-macrophages are verified as SiglecF^{-} Ly6C^{hi}. Cells that are positive for either, but not both, CD64 or F4/80 include CD11c^{+} MHCII^{+} dendritic cells which are further identified as CD11b^{+} or CD103^{+} dendritic cell sub-populations. Non-dendritic cells include SiglecF^{-} SSC-A^{lo} monocytes which are verified as CD11b^{+} with both Ly6C^{lo} and Ly6C^{hi} subsets, and SiglecF^{+} SSC-A^{hi} eosinophils which are verified to be Ly6G^{-} CD11c^{-} MHCII^{-}.

Tissue type	Antigen markers
Marginated vasculature	IVCD45^{+}ITCD45^{-}CD45^{+} collected from lung homogenate
Lung interstitium	IVCD45^{-}ITCD45^{-}CD45^{+} collected from lung homogenate
Non-lavageable airways	IVCD45^{-}ITCD45^{+}CD45^{+} collected from lung homogenate
Lavageable airways	IVCD45^{-}ITCD45^{+}CD45^{+} collected from bronchoalveolar lavage fluid
Mediastinal lymph nodes	IVCD45^{-}CD45^{+} collected from lymph node
Cell type	**Antigen markers**
Neutrophils	Ly6G^{+} CD24^{+} Ly6C$^{lo/hi}$
Lymphoid cells	CD64^{-} F4/80^{-}
B cells	CD64^{-} F4/80^{-} CD19^{+} MHCII^{+}
T cells	CD64^{-} F4/80^{-} CD3e^{+}
Cytotoxic T cells	CD64^{-} F4/80^{-} CD3e^{+} CD8^{+}
T helper cells	CD64^{-} F4/80^{-} CD3e^{+} CD4^{+}
γδ T cells	CD64^{-} F4/80^{-} CD3e^{+} CD4^{-} CD8^{-} γδTCR^{+}
NK cells	CD64^{-} F4/80^{-} CD3e^{-} CD19^{-} NKp46^{+} CD49b^{+}
Non-B Non-T Non-NK cells	CD64^{-} F4/80^{-} CD3e^{-} CD19^{-} NKp46^{-} CD49b^{-}
Non-lymphoid cells	CD64^{+} or F4/80^{+}
Macrophages	CD64^{hi} F4/80^{hi}
Resident alveolar macrophages (Vehicle instilled mice)	CD64^{hi} F4/80^{hi} CD11b^{-} CD11c^{+} SigF^{hi} Ly6C^{mid} MHCII^{-}
Resident alveolar macrophages (Influenza infected mice)	CD64^{hi} F4/80^{hi} CD11b$^{mid/hi}$ CD11c^{+} SigF^{hi} Ly6C^{mid} MHCII^{-}
Recruited macrophages	CD64^{hi} F4/80^{hi} CD11b^{+} CD11c$^{lo/hi}$ SigF^{lo} Ly6C^{hi} MHCII^{+}
Mono-macrophages	CD64^{hi} F4/80^{hi} CD11b^{+} CD11c$^{lo/hi}$ SigF^{lo} Ly6C^{hi} MHCII^{-}
Dendritic cells	CD64$^{lo/int}$ or F4/80$^{lo/int}$ CD11c^{+} MHCII^{+}
CD11b^{+} dendritic cells	CD64$^{lo/int}$ or F4/80$^{lo/int}$ CD11c^{+} MHCII^{+} CD11b^{+}
CD103^{+} dendritic cells	CD64$^{lo/int}$ or F4/80$^{lo/int}$ CD11c^{+} MHCII^{+} CD103^{+}
Monocytes	CD64$^{lo/int}$ or F4/80$^{lo/int}$ CD11b^{+} CD11c^{-} MHCII^{-} SigF^{-} Ly6C$^{lo/hi}$ SSC^{lo}
Eosinophils	CD64$^{lo/int}$ or F4/80$^{lo/int}$ CD11c^{-} MHCII^{-} SigF^{+} SSC^{hi}

Table 3.3 Gating Strategy

3.3.2 Identification of Autofluorescence Signatures

We leveraged the capability of spectral flow cytometry to manage autofluorescence (AF) signatures effectively by first identifying AF from raw spectral data of unstained lymph node, BAL, and lung cells from control (PBS) and IAV-infected mice at 3, 6, and 9 dpi. In the lymph nodes of a control mouse the spectral signature shows low fluorescence intensity with little variation across the emission spectrum, indicating high spectral homogeneity of cell populations within this tissue and low AF complexity (**Figure 3.4**). In the BAL of a control mouse the spectral signature shows high fluorescence intensity of a fairly homogenous cell population across the emission spectrum (**Figure 3.4**). In lung cells from a control mouse the spectral signature reveals a broader range of intensity across the spectrum, with the primary (red) band exhibiting lower fluorescence intensity than for BAL cells. In addition, the primary band is notably broad in the ultraviolet and violet channels and discontinuous, with multiple prominent bands (red-orange or yellow) in the mid-UV channels and in the mid-V channels, indicating AF complexity due to the presence of multiple spectrally distinct cell populations (**Figure 3.4**).

On evaluating unstained BAL and lung digests samples we find that AF signature varies with the kinetics of the immune response **(Figure 3.5-3.6)**. BAL cells have homogenous AF signatures that shift to lower fluorescence intensity over the course of infection **(Figure 3.5)**. BAL cells have a broad range of intensity of AF at 6 dpi, reflecting heterogeneous AF, that narrows by 9 dpi **(Figure 3.5)**. Lung cells display distinct spectral characteristics at each of the time points examined **(Figure 3.6)**. These shifts reflect the dynamic nature of recruitment and maturation of different leukocyte populations with heterogeneous AF over the time course of the inflammatory response. In contrast, the spectral signatures of lymph node cells remained similar over the course of infection with low indication of spectrally distinct cell populations or AF heterogeneity **(Figure 3.7)**.

Using the approach for managing heterogeneous AF, described in detail by Ferrer-Font et al., two distinct high-intensity AF signatures, with peaks in the UV7 and V7 channels, were identified in control uninfected lungs **(Figure 3.4)**, but not in a control lymph node or BAL cells.[168] These signatures change subtly over the course of infection **(Figure 3.6)**. Overlays of the UV7 signatures from control, 3, 6, and 9 dpi lungs reveal differences in intensity over the course of infection, particularly for the 9 dpi signature which is reduced in intensity in the ultraviolet region of the spectrum compared to other UV7 signatures (**Figure 3.6**); whereas the 9 dpi V7 signature has increased intensity in the violet channels compared to other V7 AF signatures (**Figure 3.6**). Correct identification of AF spectra that are of high intensity is particularly important for unmixing as these signatures act as single stain controls once entered into the SpectroFlo library. Erroneously using the low intensity 9 dpi UV7 AF spectra for unmixing data from control, 3, or 6 dpi results in significant unmixing errors. This is similarly true if low-intensity V7 AF spectra from control, 3, or 6 dpi is used to unmix data from 9 dpi. These findings emphasize the importance of identifying AF spectra at each time point investigated in addition to investigating AF spectra for control and infected mice.

Notably, the spectral characteristics of lung tissues change not only with time but also with the inflammation model. We have performed studies to evaluate AF in other murine pulmonary inflammation models, including the response to lipopolysaccharide from *E. coli*, bleomycin, and house dust mite extract from *D. pteronyssinus* **(Figure 3.11)**. The spectral characteristics of unstained lungs from these models are distinct from each other and those observed in the IAV PR8 model **(Figure 3.11)**. The house dust mite model is particularly complicated, with three unique AF signatures identified **(Figure 3.11).** The increased AF is likely due to high eosinophil recruitment and the inherent highly autofluorescent properties of the chitin structural component within house dust mite extracts.[178]

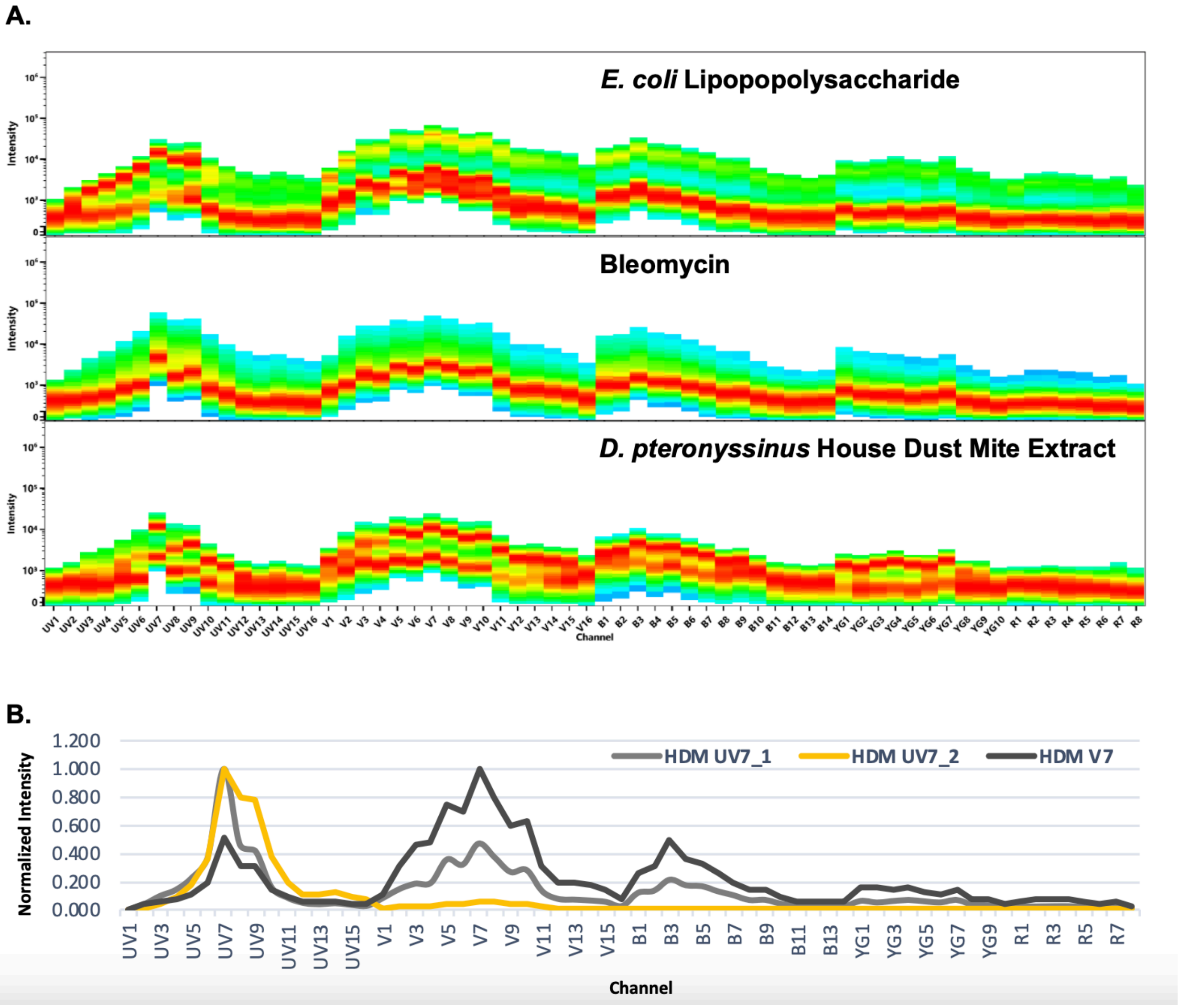

Figure 3.11 Lung Spectral Signatures for Mouse Models of Pulmonary Inflammation

(A) Representative spectral profiles are shown for unstained lungs from mice infected with lipopolysaccharide from *E. coli*, bleomycin, or house dust mite extract from *D. pteronyssinus*. Spectra reflect samples that were processed for removal of debris and aggregates with SpectroFlo software. Divergence of spectral characteristics is notable in ultraviolet, violet, blue and yellow-green laser channels for both lipopolysaccharide and house dust mite extract. (B) A spectral overlay of the UV7 AF and V7 AF signature identifies the distinct AF signatures present in lungs of mice infected with house dust mite antigen.

3.3.3 Comparison of Autofluorescence Management Strategies

We further examined the ability of the deconvolution algorithm to clearly resolve fluorophore signatures in our complex panel by evaluating processed data for unstained lung leukocytes that were unmixed by two strategies – with standard AF extraction or with the inclusion of multiple AF signatures. For this, we visualized Nx1 plots of AF versus every other fluorophore and looked for unmixing errors. In both strategies, the “AF as a tag” feature in the SpectroFlo software was utilized. Without the inclusion of distinct AF signatures, errors were observed with many of the fluorophores in our panel, as evidenced by both positive and negative skewing of populations as opposed to being symmetrically centered around zero (**Figure 3.12A**). Here we show fluorophores conjugated to antibodies primarily for phenotyping non-lymphoid cells (macrophages, dendritic cells and monocytes), but errors were observed with several fluorophores conjugated to antibodies for lymphoid cells as well (not shown). These unmixing errors indicate improper resolution of positive and negative populations and can cause fluorescence from endogenous AF to be improperly assigned to other fluorophores. Including our two unique AF signatures achieves well-shaped clean and round populations centered around zero, which should markedly improve the assignation of fluorescence signatures to their correct fluorophores (**Figure 3.12B**).

A. Unmixing with AF Extraction

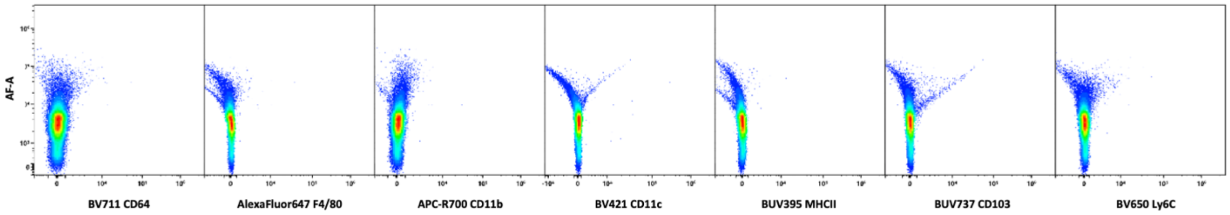

B. Unmixing with Multiple AF Signatures

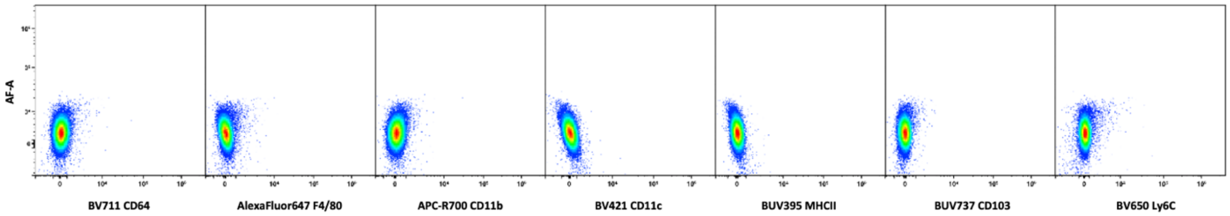

Figure 3.12 Comparison of AF management strategies

The two strategies of unmixing with AF extraction vs multiple AF signatures were assessed for unmixing errors using unstained lungs of a 9dpi PR8 mouse. Select N X 1 plots are shown here for fluorophores conjugated to antibodies for phenotyping macrophages, dendritic cells, and monocytes. (A) Errors were observed when unmixed with AF extraction, as indicated by both positive and negative skewing of populations, while (B) well-shaped round populations were achieved when unmixed with multiple AF signatures. Certain fluorophores were more negatively impacted by AF (e.g., AlexaFluor 647, BV421, BUV395, BUV737, and BV650) than others.

3.3.4 Compartmentalization of the Pulmonary Inflammatory Response Using Dual *In Vivo* CD45 Labeling

The compartmental localization of leukocytes in the pulmonary inflammatory response was defined by labeling leukocytes *in vivo*, first with intravenous AlexaFluor488-conjugated anti-CD45 (IVCD45) and second with intratracheal BUV615-conjugated anti-CD45 (ITCD45). After tissue collection and preparation of single-cell suspensions, leukocytes were labeled *in vitro* with a full-stain fluorophore-antibody master mix including PerCP anti-CD45 (CD45) and analyzed by flow cytometry. After gating on single live $CD45^+$ leukocytes, we used quadrant gating to evaluate events for IVCD45 or ITCD45 staining (**Figure 3.13, Table 3.4)**. The four quadrants reflect $ITCD45^-$ $IVCD45^+$ (top left), $ITCD45^+$ $IVCD45^+$ (top right), $ITCD45^+$ $IVCD45^-$ (bottom right), and $ITCD45^-$ $IVCD45^-$ (bottom left) events. In BAL of both control and PR8-infected mice, >98% of $CD45^+$ cells are $ITCD45^+$ $IVCD45^-$ and represent lavageable leukocytes; we call these lavageable leukocytes; <2% of BAL cells fall into the other quadrants. In the lungs of control mice 73.73 ± 1.49% of $CD45^+$ cells are $ITCD45^-$ $IVCD45^+$ and represent vascular cells that remain in the lung after IV perfusion; these are marginated vascular leukocytes. 19.43 ± 1.66% of $CD45^+$ cells are $ITCD45^+$ $IVCD45^-$ and represent alveolar cells that remain in the lungs after three lavages with PBS/0.5M EDTA; these are non-lavageable leukocytes. Only 6.61 ± 1.02% of $CD45^+$ cells in control mice are double-negative for the IT and IV labels; these are true lung interstitial leukocytes. In the lungs of PR8-infected mice, the distribution of leukocytes in the lung compartments changes, with 23.21 ± 2.27% in the marginated vascular, 48.39 ± 1.23% in the non-lavageable airway, and 27.60 ± 2.75% in the interstitial compartment. In the lungs of both PBS and PR8 mice, <0.6% of cells are double-positive for the IT and IV labels, indicating negligible vascular leakage into airway compartments. In the lymph nodes of both control and PR8-infected mice, ~99% of $CD45^+$ cells are double-negative for both ITCD45 and IVCD45 and represent lymph node leukocytes. Thus, this analysis reflects good segregation of leukocytes in the four pulmonary compartments. It also reveals that the majority of airway leukocytes are resistant to three lavages at 9 dpi with IAV PR8.

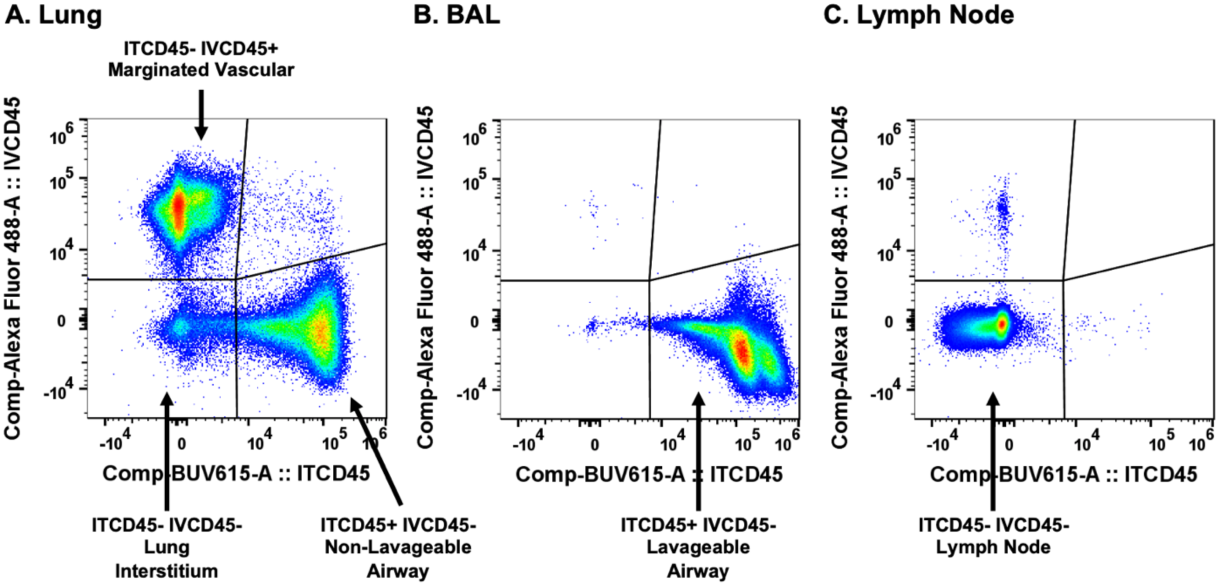

Figure 3.13 Compartmentalization of the pulmonary inflammatory response

Leukocytes were labeled *in vivo* with intravascular AlexaFluor 488 anti-CD45 (IVCD45), intratracheal BUV615 anti-CD45 (ITCD45) and *ex vivo* with PerCP anti-CD45(CD45). Single live CD45+ cells were evaluated for IVCD45 and ITCD45 staining in (A) lungs, (B) BAL, and (C) lymph nodes of a representative 9 dpi male PR8-infected mouse.

	% Single Live CD45$^+$ Cells			
	ITCD45$^-$ IVCD45$^+$	**ITCD45$^+$ IVCD45$^+$**	**ITCD45$^+$ IVCD45$^-$**	**ITCD45$^-$ IVCD45$^-$**
PBS BALs$^\wedge$	0.54 ± 0.17	0.08 ± 0.02	98.44 ± 0.36	0.94 ± 0.25
PR8 BALs$^\wedge$	0.04 ± 0.03	0.01 ± 0.00	99.44 ± 0.11	0.51 ± 0.12
PBS Lungs$^\#$	73.73 ± 1.49	0.24 ± 0.10	19.43 ± 1.66	6.61 ± 1.02
PR8 Lungs$^\#$	23.21 ± 2.27	0.56 ± 0.04	48.39 ± 1.23	27.60 ± 2.75
PBS LNs$^\wedge$	0.45 ± 0.19	0.00 ± 0.00	0.25 ± 0.14	98.78 ± 0.18
PR8 LNs$^\wedge$	0.10 ± 0.08	0.00 ± 0.00	0.06 ± 0.03	99.72 ± 0.08

Table 3.4 Compartmentalization of Leukocytes

Quadrant gating was used to evaluate single live CD45$^+$ cells for ITCD45 or IVCD45 staining in BALs, lungs and lymph nodes of PBS or 9 dpi PR8-infected mice. ITCD45$^-$ IVCD45$^+$ reflect marginated vascular cells in the lungs; ITCD45$^+$ IVCD45$^-$ reflect lavageable and non-lavageable airway cells in the BAL and lungs, respectively; ITCD45$^-$ IVCD45$^-$ reflect cells in the lung interstitium or lymph nodes. ITCD45$^+$ IVCD45$^+$ reflects leakage from the vasculature into the airways and was negligible. (Data reflect n = 5 male PBS mice and n= 6 male PR8 mice; means ± sem are shown.)

$^\wedge$ BAL and LN samples did not have heterogeneous AF and were unmixed with AF extraction.

$^\#$ Lung samples had heterogeneous AF and were unmixed with multiple AF signatures.

3.3.5 Supervised Gating on Pulmonary Leukocytes of PR8-Infected Mice

Representative supervised gating trees on leukocytes in the marginated vasculature, lung interstitium, non-lavageable airways, lavageable airways, and mediastinal lymph nodes are shown in **Figures 3.8, 3.9, and 3.10.** By applying our gating strategy to each compartment in PR8-infected mice, we immunophenotype 94.27 ± 0.26% of all leukocytes in the marginated vasculature, 90.51 ± 0.38% in the lung interstitium, 99.63 ± 0.25% in the airways, and 96.6 ± 0.25% in the lymph nodes. The largest population of undefinable cells (3.75 ± 0.26%) are CD45$^+$ ITCD45$^-$ IVCD45$^-$ Ly6G$^-$ CD64$^-$ F480$^-$ CD19$^-$ CD3$^-$ NKp46$^-$ CD49b$^-$, which are lymphoid cells that are non-B non-T non-NK cells within the lung interstitial compartment.

The distribution of leukocyte subpopulations across the multiple pulmonary compartments is shown in **Figure 3.14**. This analysis also further examines unmixing strategy options. Several findings are observed when incorporating multiple AF signatures. First, 60.5 ± 12.4% of all neutrophils remain marginated in the pulmonary vasculature rather than migrating into other compartments, and 4.9 ± 2.1% remain non-lavageable. Second, 18.7 ± 1.7% of lymphoid cells and 17.1 ± 2.6% of non-lymphoid (not including neutrophils) are marginated in the vasculature. Third, most leukocytes, 50.5 ± 1.3% of lymphoid and 67.5 ± 1.7% of non-lymphoid cells, are non-lavageable. Fourth, 44.5% more ($p < 0.01$) non-lymphoid cells are identified in the non-lavageable airway compartment when unmixed with the inclusion of two AF signatures than without (**Figure 3.14A**). Simultaneously, there are fewer numbers of unidentified cells that do not fall into any of our immune cell phenotypes when unmixing with inclusion of AF signatures than without (not shown). Finally, incorporating AF complexity significantly improves the quantification of alveolar macrophages in the non-lavageable airways, revealing 6.0-fold more ($p <0.0001$) cells compared to unmixing with standard AF extraction (**Figure 3.14B**). This reflects the improved resolution and assignation of fluorescence as shown in **Figure 3.12**. Together, these findings validate the importance of defining the compartmentalization of the pulmonary immune response. Without a dual *in vivo* CD45 labeling approach, immune cells within the marginated vasculature and non-lavageable airspaces would be incorrectly pooled with lung interstitial leukocytes. In addition, without mitigation of AF complications, highly autofluorescent alveolar macrophages would be under-quantified and their involvement in the pulmonary inflammatory response would be misinterpreted.

A. Distribution of leukocytes in pulmonary compartments

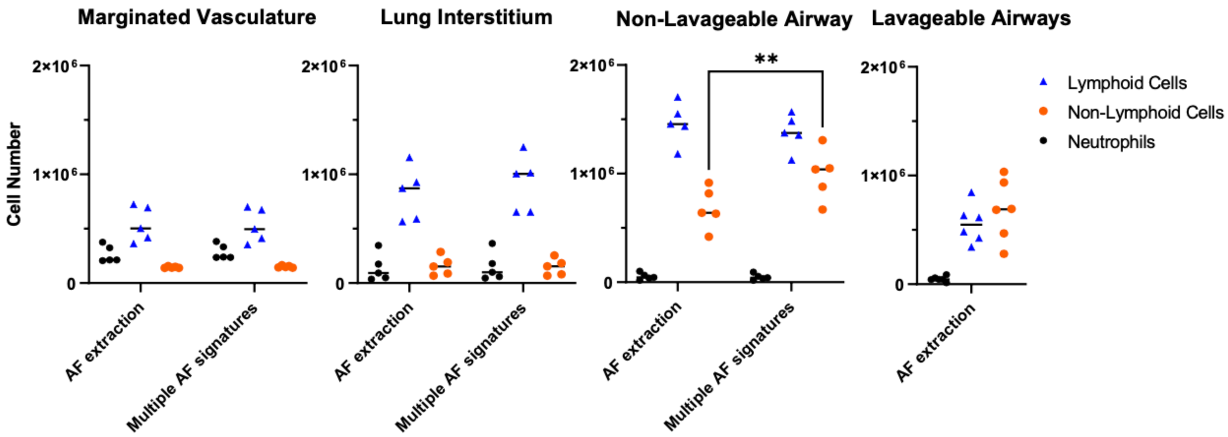

B. Distribution of lymphoid and non-lymphoid subsets in non-lavageable airways

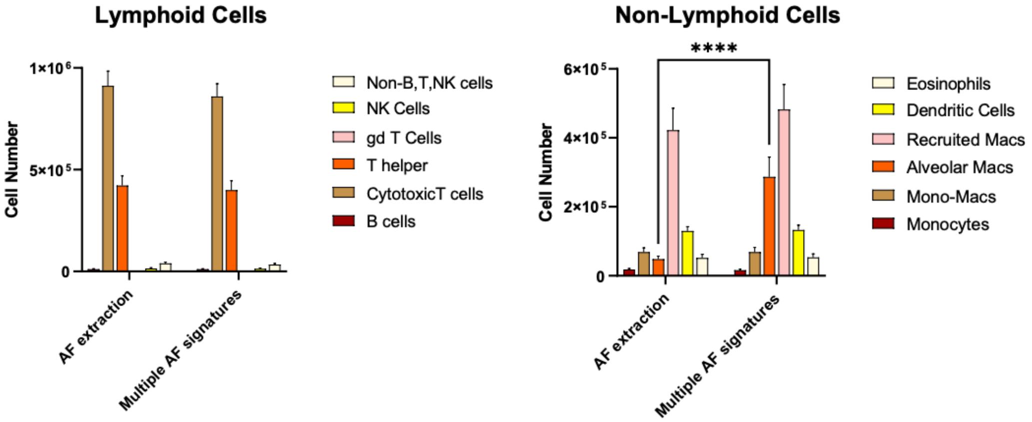

Figure 3.14 Compartmental Localization of Leukocytes

Unmixing strategies with AF extraction or with multiple AF signatures were compared for their ability to quantify (A) neutrophils, lymphoid cells and non-lymphoid cells in four pulmonary compartments, and (B) lymphoid and non-lymphoid sub-populations in the non-lavageable airway compartment of 9 dpi PR8-infected mice. (Data reflect n = 6 male mice; means ± sem are shown; ** $p < 0.01$ and **** $p < 0.0001$.)

3.3.6 Unsupervised Gating on Pulmonary Leukocytes of PR8-Infected Mice

We performed t-SNE analysis to aid in visualizing and localizing immune cells within distinct pulmonary compartments of PR8-infected mice (**Figure 3.15**). As previously reported, lymphoid cells can be difficult to perfuse and all subclasses are seen in the marginated vascular compartment in this PR8 model.[130] Here we demonstrate that neutrophils, monocytes and eosinophils also remain in the vasculature after perfusion. This analysis also reflects that individual non-lymphoid sub-populations are distinctly localized within the different pulmonary compartments. While monocytes are abundant in the marginated vasculature, they are a minor component of the lung interstitium and not found in the airways. Conversely, mono-macs, recruited macrophages and dendritic cells are identified in the airways but not in the marginated vasculature. This distribution reflects differentiation and maturation of monocytic cells as they are recruited from the circulation into the airways in response to oropharyngeal PR8. In contrast, most lymphoid cell subpopulations, except for B cells, are relatively uniformly distributed across the lung. This t-SNE analysis demonstrates a high correlation with most populations in our supervised gating strategy and confirms many observations from that strategy. It also provides visualization which reflects the dynamic nature of leukocyte migration, recruitment, and activation from the circulation across the lung parenchyma and into the airways in response to an inhaled inflammatory agonist.

A. Non-lymphoid cell subclasses

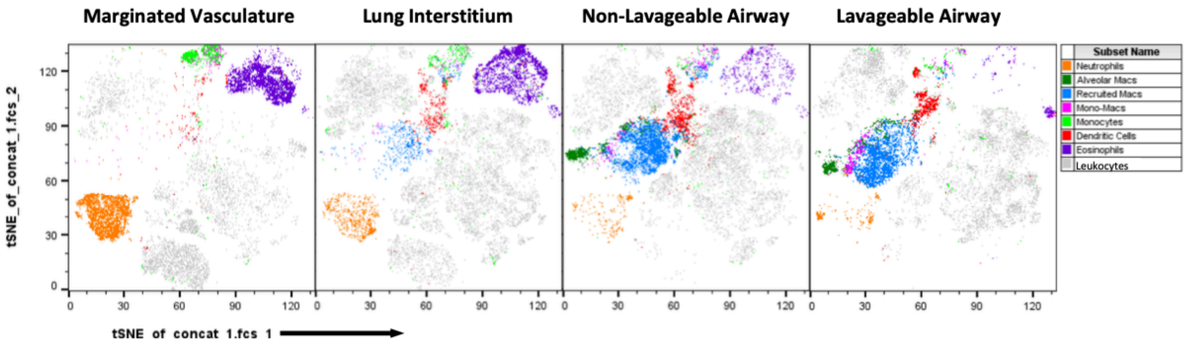

B. Lymphoid cell subclasses

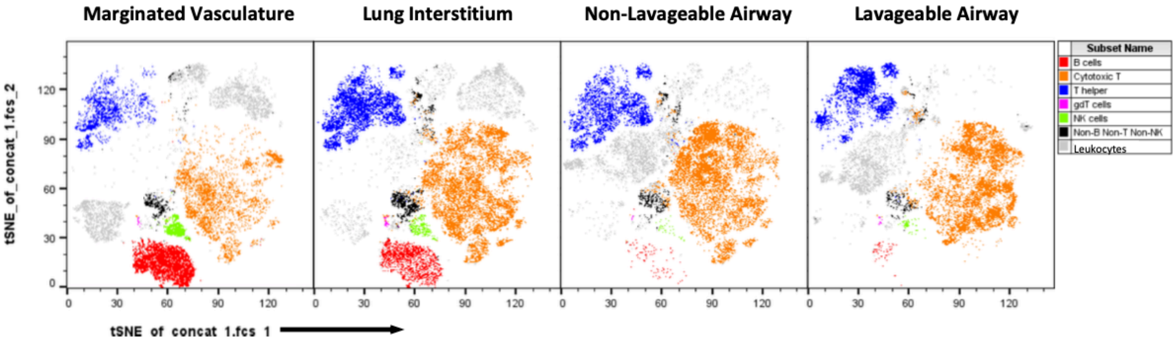

Figure 3.15 Unsupervised Gating

t-SNE analysis was initiated downstream of singlet and viability gating on 40,000 lung digest cells from a representative 9 dpi male PR8-infected mouse. Cell subsets defined by the supervised manual gating strategy were projected into the t-SNE space using specific colors to define (A) non-lymphoid and (B) lymphoid cell populations in the marginated vasculature, the lung interstitium, the non-lavaged airway, and the lavaged airway.

3.4 Discussion

In summary, we present a complete protocol, incorporating spectral flow cytometry with *in vivo* compartmental analysis, for the precise localization of multiple lymphoid and non-lymphoid cell populations participating in the pulmonary immune response. Here we apply this methodology to studies over the time course of the early immune response to IAV/PR8 in wild-type C57BL/6J mice, with an emphasis on 9 dpi. Key aspects of this protocol are that it: (i) describes changes in the AF characteristics of control and PR8-infected lungs over the time course of the transition from innate to adaptive immunity; (ii) incorporates a meticulously assembled broad panel of 20 antibody-fluorophore conjugates that are compatible with these AF characteristics and spectral flow cytometry; (iii) validates that incorporating multiple heterogeneous AF signatures from the lungs improves the resolution and identification of fluorescence signals, which is of particular importance when alveolar macrophages are a component of the immune response; (iv) establishes a robust gating strategy for identification of B cells, T cells (cytotoxic T, T helper, and γδ T cells), NK cells, macrophages (alveolar, recruited and monocyte-macrophages), monocytes (Ly6C^{lo} and Ly6C^{hi}), dendritic cells (CD103^{+} and CD11b^{+}), neutrophils, and eosinophils; (v) combines a dual *in vivo* CD45 labeling protocol with *in vitro* CD45 labeling to facilitate identification of these immune cell populations in four pulmonary compartments; (vi) implements both informed gating and dimensionality reduction algorithms to visualize the recruitment and migration of leukocytes from the vasculature, across the lung interstitium and into the alveolar airways; and (vii) finds that the majority of immune cells are localized within the non-lavageable airways in this model at 9 dpi with IAV PR8.

In developing this protocol, we heavily considered the best practices outlined in the American Thoracic Society Workshop Report, whose intent was to improve the rigor and reproducibility of flow cytometry experiments related to studies in the lungs, as well to broad mandates to improve the rigor and reproducibility of biomedical research.[163,164,177] The abilities of spectral flow cytometry are particularly well-suited for these goals as it mitigates AF interference and utilizes AF characteristics to significantly improve resolution and identification of leukocyte populations. Combined with *in vivo* compartmental analysis we can describe > 99% of the cellular immune response within the non-lavageable airways, a compartment that has not previously been quantitatively described with precision. We find these procedures to yield high-quality data with easily resolvable cell populations and highly consistent quantitative results between multiple users and over multiple experiments. The clarity of resolution gained by including AF considerations enhances the rigor of unsupervised analyses.

Previous studies also have used *in vivo* compartmental approaches to better define the localization of pulmonary immune cells. Anderson, et. al., used intravascular labeling to demonstrate that up to 97% of CD8+ T cells thought to be located within the lungs of perfused LCMV-infected mice were not in the tissue, but remained adherent in the vasculature.[162] Patel, et. al., used intravascular and intratracheal labeling to characterize myeloid cells in the non-lavaged lungs of naïve mice and those with acid inspiration-induced injury.[159] While they were able to segregate vascular and alveolar cells from those within the lung interstitium, they did not identify those alveolar cells that were non-lavageable within the alveolar epithelium. Leukocytes that are marginated and non-lavageable, whether in the vasculature or in the airway lumen, warrant more investigation. They could be transitory and poised to leave or they could be restricted from exiting these highly specialized compartments. The precise immunophenotyping and quantification of these populations could aid in understanding the biological roles that these cells have and could inform future therapeutic approaches for pulmonary inflammation.

The protocol presented here enables precise quantitative tracking of lymphoid and non-lymphoid leukocytes in four compartments within perfused and lavaged lungs: the marginated vasculature, the lung interstitium, the lavageable and the non-lavageable airspaces. In our model of IAV PR8 at 9 dpi we show that most pulmonary B cells and NK cells, as well as large populations of CD4$^+$ T helper cells and CD8$^+$ cytotoxic T cells, remain adherent in the vasculature after perfusion. While T helper cells were distributed across these four compartments, the majority were localized to the non-lavageable airspace compartment, making this location the site with the greatest number of lymphoid cells. We also show that the majority of Ly6C^{hi} monocytes as well as large populations of neutrophils and eosinophils remain adherent in the vasculature, while the majority of Ly6C^{mid} monocytes, recruited macrophages and dendritic cells (primarily CD11b$^+$) are adherent in the airways. A small population of alveolar macrophages also are localized in both the lavageable and non-lavageable airspaces. In short, the previously unquantified non-lavageable airspace is the site of the largest number of lymphoid and non-lymphoid cells within the lungs at 9 dpi with IAV/PR8. Thus, by including bronchoalveolar lavage in this protocol it becomes possible to identify immune cells within the non-lavageable airspace. This approach could potentially offer insight into functionally different subsets of immune cells and could be an area of future study. Inclusion of lavage offers two additional advantages. First, by rapidly diluting and removing the ITCD45 conjugate, lavage reduces the opportunity for cross-labeling of lung interstitial leukocytes. Second, additional valuable information can be obtained from the cell-free BAL fluid, including analytes such as total protein, immunoglobulins, and cytokines. While some of this information might be more accurately obtained by performing lavage in separate animals, the inclusion of lavage in this protocol allows for more information to be obtained from the same animals, thereby reducing the number of animals in a study. One caveat to our approach is that it used three lavages. If additional lavages were performed one would expect a decrease in the non-lavageable cells and an increase in the lavageable cells with each additional lavage.

It is notable that this analysis shows that monocytes in the marginated vasculature of both control and IAV PR8-infected mice include both Ly6C^{hi} and Ly6C^{lo} populations, while Ly6C^{hi} monocytes are the majority in the airways of PR8-infected mice (**Figures 3.8 and 3.9**). This is consistent with the characterization of “classical” and “non-classical” monocytes, with shifting Ly6C expression as they transit from the circulation and are recruited into the airways during pulmonary inflammation.[179,180] It is also notable that at 9 dpi the airspaces contain relatively few alveolar macrophages compared to recruited macrophages, and that the majority of alveolar macrophages are localized to the non-lavageable airway. This contributes to highly heterogeneous AF in the lungs, but not in the BAL. In contrast, though not shown here, at the earlier time points of 3 and 6 dpi with PR8, we found considerably more alveolar macrophages in the lavageable airways which contribute to heterogeneous AF. Thus, while at 9 dpi it was not necessary to define and incorporate discrete AF signatures in the BAL compartment, it was necessary to do so at the earlier time points (not shown). These findings are consistent with the understanding of macrophage turnover during the transition from innate to adaptive immunity.[181-183] Furthermore, these findings emphasize the changing nature of AF in different pulmonary compartments over the time course of the immune response.

We also observe from t-SNE analysis a high eosinophil content within the lungs of IAV PR8-infected mice at 9 dpi, with eosinophils constituting 33.0% and 58.3% of all non-lymphoid cells within the marginated vasculature and lung interstitium, respectively. This population is SiglecF^{+} SSC-A^{lo} and are back-gated to confirm that they do not express Ly6G, CD11c or MHCII in order to validate their identity as eosinophils rather than neutrophils, alveolar macrophages, recruited macrophages, dendritic cells or monocytes. While eosinophils are well-recognized to be modulators of adaptive immune responses and are released from the bone marrow following exposure to allergens or intestinal parasites, their role(s) in host defenses against respiratory viruses is (are) less well-known.[184-187] With respect to IAV, it has been described that eosinophils have very low presence in the airways during early time points of infection but increasing numbers that correlate with T cell recruitment into the lungs; and, more recently, that eosinophils modify the respiratory barrier during IAV infection, helping to neutralize the virus and protect the airways.[188,189] Our observations are consistent with these novel findings and suggest that the capabilities of the protocol described here would be of considerable utility in further studies investigating the dynamics of eosinophil recruitment and migration in response to IAV and other respiratory viruses. These unexpected findings also provide evidence for the utility of taking an unbiased approach to measure changes in leukocyte populations in pulmonary research.

Less than five percent of lung leukocytes cannot be immunophenotyped using the strategies defined here. These are non-B non-T non-NK lymphoid cells and are most prevalent within the lung interstitial compartment. Employing the t-SNE algorithm, these cells are seen to cluster within the two-dimensional space located between T cells and dendritic cells. These could reflect shortcomings in our gating strategy or perhaps lineage negative innate lymphoid cells (ILCs) that could be investigated with additional antibodies.[190] While the panel presented here includes 20 antibody-fluorophore conjugates, it has a low overall complexity index and is amenable to substitution or expansion for investigations of additional leukocyte populations.

As emphasized in our fluorophore panel design strategy, it is essential to assess AF complexity within each pulmonary tissue as part of the experimental design process; knowing the peak emission channels of AF signatures is necessary to ensure compatibility with fluorophores in the in vitro staining panel. We demonstrate that the intensity and signature of heterogeneous AF can change over the course of the immune response to each agonist. Therefore; it is important to assess AF complexity for each agonist and time point of interest. Additionally, day-to-day variations in tissue processing can affect AF, therefore it is necessary to include an additional mouse within each experiment for the collection of unstained controls for BAL, lung, and lymph node cells to determine AF signatures unique to each experiment. While these procedures require considerable effort for optimization and set-up, the clarity of resolution that is gained enables the acquisition of a large amount of high-quality data which could improve efficiency and reduce the numbers of mice required to assess meaningful differences between groups. It has been suggested that apparent inconsistencies in the literature regarding the response of alveolar macrophages to influenza infection might be understood by identifying mouse strain-dependent differences.[191] Our results demonstrate that another important consideration for the accurate quantification of alveolar macrophages is the identification of heterogeneous AF signatures which must be given due consideration in order to generate rigorous and reproducible flow cytometry data as shown in **Figure 3.14B**.

It is expected that different cell populations will be enumerated in different lung compartments during the innate versus adaptive versus resolution and repair phases of the immune response, depending on the disease model under study. Thus, this panel was carefully designed to enable flexibility for expansion to include additional fluorophore-antibody conjugates and to incorporate multiple AF signatures. This flexibility will accommodate deeper probing into leukocyte subpopulations of interest (e.g., M1 vs. M2 macrophages, or subsets of activated dendritic cells); extension to acquired immunity (e.g., T regulatory or T memory cells); or application to different inflammatory models in which additional leukocyte populations might be of interest (e.g., basophils and mast cells in allergic airway inflammation). Although not included as part of this protocol, it would be feasible to collect whole blood at sacrifice (e.g., by cardiac puncture) and apply the procedures described here for a more thorough characterization of circulating immune cells.

Precise characterization and localization of the cellular participants in the immune response is crucial to understanding the fundamental processes underlying pulmonary inflammation and for designing therapeutic approaches that target the aberrant leukocyte recruitment in pathological situations. We hope that this protocol will serve as a resource in these further studies of the innate and adaptive immune responses in the lungs.

Chapter 4. Fibroblast-derived versican is a pro-inflammatory mediator of innate immunity during influenza A virus infection

4.1 Introduction

Influenza A virus (IAV) is a major causative pathogen of hospitalization from community-acquired pneumonia and places a significant burden on global health. [4,5] Globally, an estimated 145,000 to 645,000 annual deaths are attributed to IAV infection.[2,3] Annually, vulnerable populations experience morbidity and mortality associated with seasonal IAV while intermittently, pandemic IAV strains pose a significant health threat to the general populous. The disease burden from both seasonal and pandemic influenza A viruses, and the growth of high-risk patient populations, underscore the need for continued influenza A research. Increasingly, the extracellular matrix (ECM) is recognized for its role in the host immune response to pulmonary diseases.[30,33,35] Accumulation of hyaluronan (HA) and versican, a chondroitin sulfate proteoglycan, in the provisional pulmonary ECM is a hallmark of many lung diseases.[1,27,40,94,101,102,104,106-108,115,116] The accumulation of versican in the lungs and its close association with leukocytes migrating into the pulmonary tissue has been recently described in C57BL/6J mice infected with a mouse-adapted IAV (A/PR/8/34; H1N1).[63] However, much is still unknown about the immunomodulatory potential of versican and the importance of the cellular source of versican regarding its contextual role in the host immune response to IAV.

Previous studies utilizing versican-deficient mice have focused on mice globally deficient in versican (Rosa26/Vcan$^{-/-}$), mice deficient in myeloid- and epithelial-derived versican (LysM/Vcan$^{-/-}$), and mice deficient in epithelial-derived versican (SPC/Vcan$^{-/-}$). These studies demonstrated that Rosa26/Vcan$^{-/-}$ mice treated with polyinosinic:polycytidylic acid (poly(I:C)), a TLR3-agonist, have decreased recovery of inflammatory leukocytes in the bronchoalveolar lavage (BAL) fluid.[100] This is in contrast to LysM/Vcan$^{-/-}$ mice which had increased recovery of inflammatory leukocytes in BAL fluid after instillation with poly(I:C).[103] Additionally, both Rosa26/Vcan$^{-/-}$ and LysM/Vcan$^{-/-}$ versican-deficient mice had significantly decreased levels of Type I IFN and IL-10 in lung tissue and BAL fluid following poly(I:C) exposure when compared to controls.[100] Another study utilizing SPC/Vcan$^{-/-}$ mice infected with respiratory syncytial virus revealed increased migration of neutrophils and monocytes into the BAL fluid and lungs, along with elevated expression levels of chemokines CCL2, CCL3, and CCL4 suggesting that epithelial-derived versican attenuates leukocyte recruitment through chemokine mediated mechanisms.[105] Taken together, these studies demonstrate the immunomodulatory potential of versican and the importance of the cellular source of versican with regards to its contextual role in the host immune response. However, studies investigating the role of fibroblast-derived versican are lacking. In naïve mice, fibroblasts are the predominant source of versican in the lungs and constitute a major cell population responsible for versican expression and accumulation in the lungs under inflammatory conditions.

Therefore, this study investigated the role of fibroblast-derived versican during the innate immune response to IAV infection by utilizing a tamoxifen-inducible versican-deficient mouse (B6. Col1a2-Cre$^{ERT+/-}$/Vcan$^{tm1.1Cwf}$, Col1a2/Vcan$^{-/-}$). This study established the time course of changes in fibroblast-derived versican expression and the impact of fibroblast-derived versican on leukocyte migration into pulmonary and vascular microenvironments during IAV infection. We report that fibroblast-derived versican facilitates neutrophil, monocyte, mono-macrophage, dendritic cell, and eosinophil migration into the lungs and airways early in IAV infection. Additionally, we found that Col1a2/Vcan$^{-/-}$ mediastinal lymph nodes demonstrate a transient increase in the number of lymphocytes on day 6 post infection with IAV.

4.2 Materials and Methods

4.2.1 Animal Model

Vcan$^{\text{tml.1Cwf}}$ (Vcan$^{\text{fl/fl}}$) mice were bred with mice carrying a transgene for a tamoxifen-inducible Cre recombinase under the control of the Col1a2 promoter (B6.Cg-Tg(Col1a2-cre/ERT, -ALPP)7Cpd/J (Strain: 029567; Jackson Laboratories) in order to generate B6.Col1a2-Cre$^{\text{ERT+/-}}$/Vcan$^{\text{tm1.1Cwf}}$ (Col1a2/Vcan$^{-/-}$) and B6.Col1a2-Cre$^{\text{ERT-/-}}$/Vcan$^{\text{tm1.1Cwf}}$ littermate controls (Col1a2/Vcan$^{+/+}$, WT).[100] In Col1a2/Vcan$^{-/-}$ mice, Cre recombinase-mediated deletion of Vcan exon 4 initiates a frameshift resulting in a STOP codon near the beginning of exon 5. The resulting mice are deficient in fibroblast-derived versican. All mice were housed under standard conditions in Allentown individually ventilated cages in a specific pathogen-free animal facility. Room lighting was on a 10:14 hr dark:light cycle, and mice had free access to food and water. Col1a2/Vcan$^{-/-}$ mice and their littermate controls (Col1a2/Vcan$^{+/+}$, WT) were weaned at three-weeks of age and fed tamoxifen citrate chow (Inotiv, 400mg/kg, TD.130859, West Lafayette, IN). After being provided tamoxifen citrate chow for four weeks, mice were fed standard mouse chow (LabDiet, PicoLab® Mouse Diet 20 – 5053, St. Louis, MO). At eight- to eleven-weeks of age, male Col1a2/Vcan$^{-/-}$ mice and their littermate controls were infected with a mouse-adapted influenza A virus. All procedures were performed as part of an approved scientific protocol in accordance with the University of Washington Institutional Animal Care and Use Committee (IACUC).

4.2.2 Induction of IAV Pneumonia

Mouse-adapted influenza A/Puerto Rico/8/34 (A/PR/8/34; H1N1) was grown in allantoic fluid of research-grade-specific pathogen-free embryonic chicken eggs (Charles River Avian Vaccine Services, Norwich, CT), and a hemagglutination assay was performed to determine the viral titer.[125] Male mice were infected with 20 plaque-forming units (PFU) in 50 µL PBS by oropharyngeal aspiration under isoflurane anesthesia.[126] This dose caused severe influenza pneumonia as previously described.[63] Control mice received instillation of PBS alone, and mice were sacrificed at 3, 6, and 9 days post-infection (dpi) by exsanguination under isoflurane anesthesia.

4.2.3 Quantitative Real-time Reverse-transcription PCR

Mice were sacrificed at 3, 6, or 9 days post-instillation (dpi) with influenza virus A/PR/8/34. Under aseptic conditions, the left lung lobe was removed from the thoracic cavity and used for mRNA isolation and prepared as previously described.[63] Briefly, lung tissue was placed in 5ml of RNAlater (Invitrogen) at 4C overnight. Lungs were homogenized, and RNA was extracted using RNAeasy Mini Kit with on-column DNase digestion (Qiagen, Valencia, CA) according to the manufacturer's instructions. cDNA was reverse-transcribed using random primers with the High Capacity cDNA Reverse Transcription Kit (Applied Biosystems, Foster City, CA). Quantitative real-time reverse-transcription polymerase chain reaction (PCR) was performed on an ABI Prism 7900HT Fast Real-Time PCR System (Applied Biosystems) using PrimeTime Gene Expression Master Mix (Integrated DNA Technologies, Coralville, IA). Gene-specific TaqMan primer-probe mixes were used for quantitative real-time PCR of versican (Mm01283063_m1) and TATA-box protein (Mm01277042_m1) mRNA (ThermoFisher Scientific, Grand Island, NY). Quantitative real-time PCR was performed to amplify the matrix protein (*M1*) gene of the PR8 flu virus. The following primers and probe were used: forward: CAGCACTACAGCTAAGGCTATG; reverse: CTCATCGCTTGCACCATTTG, probe /56-FAM/CCTCTGCTG/ZEN/CTTG CTCACTCGATC/3IABkFQ with 20ng of sample cDNA per reaction. DNA from purified plasmid was used to generate a standard curve for copy number determination using RNA isolated from mouse lung. Samples and log10 dilutions of standards were run in triplicate on an ABI 7900 real time PCR machine and viral copy number determined from the standard curve of Ct values.

4.2.4 Tissue Harvest and *In Vivo* Antibody Labeling for Spectral Flow Cytometry

Mice were sacrificed at 3, 6, or 9 days post-instillation (dpi) with influenza virus A/PR/8/34. Before euthanasia, mice were anesthetized with isoflurane in an induction chamber. Alexa Fluor 488-conjugated anti-CD45.2 antibody, clone 104 (BioLegend, San Diego, CA, USA), diluted 1:40 (v:v) with PBS, in a total volume of 200µL (2.5µg/per mouse), was injected retro-orbitally to label the intravascular (IV) leukocytes (IVCD45$^+$). After 3 minutes, while keeping the mouse anesthetized with isoflurane delivered by nose cone, the left renal artery was transected, and the mouse was euthanized by exsanguination to reduce the chance that the IVCD45 conjugate would bind non-specifically to airway or interstitial lung leukocytes. In separate experiments investigating circulating leukocytes, mice were euthanized by exsanguination via intracardiac blood draw into an EDTA-coated syringe and did not receive IVCD45 antibody-conjugate injections.

After euthanasia, the trachea was cannulated with an 18-gauge angiocath via tracheostomy and the airways were immediately lavaged with 1 mL PBS three times. The first 1 mL lavage was separated from the second and third lavages for chemokine and cytokine analysis with multiplex ELISA. The thoracic cavity was opened via midline sternotomy and the lungs were perfused by injecting 5mL of PBS into the right ventricle. Using a dissecting microscope, the largest mediastinal lymph node was removed from the right dorsal aspect of the trachea. The lymph node was placed directly into 0.5 mL of RPMI containing 10% fetal bovine serum (FBS, Thermo Fisher Scientific Waltham, MA, USA) on ice. Lung tissue was removed by blunt dissection from the primary bronchi and placed on ice.

4.2.5 Preparation of Single-Cell Suspensions for Spectral Flow Cytometry

Cells in the bronchoalveolar lavage (BAL) fluid were pelleted by centrifugation. The first 1 mL of lavage was collected and combined with protease inhibitor according to the manufacturer's instructions (Pierce™ Protease Inhibitor Moni Tablets, EDTA-Free, A32955, Thermo Fisher Scientific Waltham, MA, USA). These samples were stored at -80°C until chemokine and cytokine analysis. Cells from all three BAL fractions were then combined and RBC lysis buffer (Thermo Fisher Scientific Waltham, MA, USA) was applied according to manufacturer instructions. After RBC lysis, BAL cells were pelleted and suspended in Flow Cytometry Straining (FCS) buffer (Thermo Fisher Scientific Waltham, MA, USA).

A stock solution of Liberase TM (Sigma-Aldrich, St. Louis, MO, USA) was prepared at 10 mg/ml (26 U/ml) in RPMI 1640 w/o phenol red or fetal bovine serum (FBS) (Thermo Fisher Scientific Waltham, MA, USA), stored in single-use aliquots at -30°C, and used by the expiration date per the manufacturer's recommendation. A stock solution of recombinant DNase I (Sigma-Aldrich, St. Louis, MO, USA) was prepared at 10,000 U/ml in H_2O and stored in single-use aliquots at -30°C for up to 1 month. Just before harvest, a working solution of enzyme digestion mixture, containing Liberase TM (0.26 U/ml) and recombinant DNase I (10 U/ml), was prepared in RPMI 1640 without phenol red or FBS in a volume of 2 ml per mouse and stored on ice until needed for enzymatic digestion of lungs. The lungs were minced using a razor blade and then incubated for 45 minutes at 37°C in 2 mL RPMI 1640 without phenol red or FBS (Thermo

Fisher Scientific Waltham, MA, USA) containing 0.26U/mL Liberase TM (Sigma-Aldrich, St. Louis, MO, USA) and 10U/mL recombinant DNase I (Sigma-Aldrich, St. Louis, MO, USA). After digestion, samples were pipetted up and down and then filtered through 70μm cell strainers (VWR, Brisbane, CA, USA) with RPMI/10% FBS. Lung cells were pelleted and RBC lysis buffer was applied according to manufacturer instructions. After RBC lysis, lung cells were pelleted and suspended in an FCS buffer.

Lymph nodes were transferred onto 70μm cell strainers and gently mashed with the rubber end of the plunger from a 3 mL syringe. The filters were rinsed with RPMI/10% FBS and then the lymph node cells were pelleted and suspended in FCS buffer. Total live cells from each BAL, lung, and lymph node sample were counted using ViaStain AO/PI staining solution (PerkinElmer Inc, Waltham, MA, USA) and SD100 counting chambers (PerkinElmer Inc, Waltham, MA, USA) on a Cellometer Auto 2000 Cell Counter (Nexcelom, Lawrence, MA, USA).

Whole blood samples were centrifuged at 2,000xg for 15 minutes at 4C. After centrifugation, plasma was combined with protease inhibitor according to the manufacturer’s instructions (Pierce™ Protease Inhibitor Moni Tablets, EDTA-Free, A32955, Thermo Fisher Scientific Waltham, MA, USA) and stored at -80°C until chemokine and cytokine analysis. Blood cells were then combined with 10 mL of Gibco™ ACK Lysing Buffer at room temperature for 4 minutes. Cells were pelleted by centrifugation and combined with 12 mL of cold PBS. Finally, cells were pelleted by centrifugation and suspended in FCS buffer.

4.2.6 *In Vitro* Antibody Staining for Spectral Flow Cytometry

The following reagents were prepared for *in vitro* antibody staining:

(i) Fc Block TruStain FcX PLUS (anti-mouse CD16/32) (BioLegend, San Diego, CA, USA) was diluted 1:100 (v:v) with Flow Cytometry Staining (FCS) buffer (Thermo Fisher Scientific Waltham, MA, USA) in a total volume of 50μL per test and stored on ice until use

(ii) Just before use, one vial of LIVE/DEAD Fixable Blue Dead Cell Stain Kit (Thermo Fisher Scientific Waltham, MA, USA) was resuspended with 50 μL DMSO and then diluted 1:320 (v:v) in PBS in a total volume of 20μL per test. LIVE/DEAD Blue Cell Stain must be prepared in a protein-free solution, without FCS, as protein can impact the efficiency of LIVE/DEAD Blue staining

(iii) To prepare the full-stain antibody master mix, all antibodies were gently vortexed and then centrifuged at 10,000x*g* for 3 minutes at 4C. Antibody manufacturer, clone numbers, and titers are available in **Table 4.1**. Antibodies were diluted in Brilliant Stain Buffer (BD Biosciences San Jose, CA, USA) to achieve the final titers indicated in **Table 4.1**, allowing for a total volume of 100µL per test. The antibody master mix excluded the antibody conjugate used for *in vivo* staining, Alexa Fluor 488 anti-CD45.2 (IVCD45), and was stored on ice until use. The following cells and bead controls were prepared for *in vitro* staining:

(i) For full-stained samples, up to 1 x 10^6 cells from BAL fluid, lungs, and lymph nodes from mice that received IVCD45$^+$ were used. For full-stained blood samples, up to 1 x 10^6 cells from mice that did not receive IVCD45$^+$ were used.

(ii) BAL fluid, lungs, and lymph nodes from a mouse that did not receive IVCD45$^+$ were used for the preparation of unstained controls, the single-stain viability control, and single-stain cell controls (CD11c-BV421, CD64-BV711, SiglecF-BV750, and γδTCR-PerCP-eFluor 710) for each flow cytometry experiment. Up to 1 x 10^6 cells from BAL fluid, lungs, and lymph nodes were used for unstained controls. For the viability control, 2.5 x 10^5 lungs cells were heat-killed for 10 minutes at 75C, and after chilling for 10 minutes on ice were combined with 2.5 x 10^5 additional unstained lung cells. 2.5 x 10^5 cells from the lungs were used for each single-stain cell control. Single-stained controls for the remaining fluorophore-antibody conjugates were prepared using UltraComp eBeads$^{\text{TM}}$ (Thermo Fisher Scientific Waltham, MA, USA), following the manufacturer's instructions.

All antibodies are commercially available and unstained, single-stain, and fluorescence-minus-one controls were used to define gating for positive and negative populations. Antibody specificity was not independently validated for antibodies in our panel; however, emphasis was made to select antibody clones recommended from published studies.[170-176] For full-stained samples, *in vitro* antibody staining was performed on single-cell suspensions from the BAL, lungs, and lymph nodes of mice that received *in vivo* antibody labeling of IVCD45$^+$. *In vitro* antibody staining was performed on single-cell suspensions from whole blood from mice that did not receive *in vivo* antibody labeling of IVCD45$^+$. Cells were washed in PBS before incubating in LIVE/DEAD Fixable Blue Dead Cell Stain (Thermo Fisher Scientific Waltham, MA, USA) for 15 minutes. This incubation must be performed in a protein-free solution, without FCS, as protein can impact the efficiency of LIVE/DEAD Blue staining. Next, cells were washed with FCS, and Brilliant Stain Buffer was added to each sample. Cells were incubated with Fc Block for 5 minutes and then incubated with fluorophore-conjugated antibodies for 30 minutes. Cells were washed with FCS and then incubated with Cytofix (BD Biosciences San Jose, CA, USA) for 15 minutes. Cells were washed with FCS before being transferred to 5 ml tubes and stored at 4°C in the dark overnight. Flow cytometry was performed the following day.

Specificity	Fluorochrome	Clone	Vendor	Catalog #	Titer (ng/test)
MHCII-IA/IE	BUV395	2G9	BD Biosciences	743876	8
Viability	Live Dead Blue	-	ThermoFisher	L34962	20 μl of 1:320 stock
CD103	BUV737	M290	BD Biosciences	741739	125
CD11c	BV421	N418	BioLegend	117330	500
Ly6G	Pacific Blue	1A8	BioLegend	127612	500
NKp46	BV605	29A1.4	BD Biosciences	564069	500
Ly6C	BV650	HK1.4	BioLegend	128049	31
CD64	BV711	X54-5/7.1	BioLegend	139311	500
Siglec F	BV750	E50-2440	BD Biosciences	747316	31
CD4	BV785	GK1.5	BioLegend	100453	63
CD45.2	Alexa Fluor 488	104	BioLegend	109816	2.5 μg/mouse IV
CD45	PerCP	30-F11	BioLegend	103130	125
γδTCR	PerCP-eFluor710	GL-3	ThermoFisher	46-5711-82	63
CD8	PE	53-6.7	BioLegend	100708	63
CD3e	PE-Dazzle 594	145-2C11	BioLegend	100347	500
CD19	PE-Cy5.5	1D3	ThermoFisher	35-0193-80	500
CD24	PE-Cy7	M1/69	BioLegend	101822	16
F4/80	Alexa Fluor 647	BM8	BioLegend	123122	250
CD11b	APC-R700	M1/70	BD Biosciences	564985	16
CD49b	APC-eFluor780	DX5	ThermoFisher	47-5971-82	1000

Table 4.1 Fluorescent Reagents for Cell Staining

4.2.7 Spectral Flow Cytometry

Spectral cytometry was performed using the Aurora 5 laser cytometer (Cytek Biosciences, Fremont, CA, USA). The optical design, detection modules, number of detectors per laser module, detector module configurations, and methodology for establishing the optimal instrument gain settings, known as CytekAssaySetting, for commercially available fluorophores has been previously reported. [167] Our studies utilized CytekAssaySetting, which automatically updates gain settings during daily QC on calibrated bead MFI targets to ensure consistent instrument setup over time. Before all data collection, QC on calibrated beads was performed and data was only collected when the instrument passed QC. Additionally, the FSC, SSC, and SSC-B gain settings were adjusted immediately before the acquisition using tissue-specific unstained samples. SSC-B-A was set to a log scale to improve visualization of especially large cells, such as alveolar macrophages, on SSC-B-A plots. FSC Area Scaling Factor was reduced to 0.9 in CytekAssaySetting. FSC, SSC, and SSC-B gain settings were adjusted immediately before data acquisition to ensure >95% of all cells were on scale for each tissue type. The FSC threshold was set at 250,000. Acquisitions were recorded at low-medium flow.

Raw data were converted to unmixed data with SpectroFlow software v3.0 using an ordinary least squares algorithm to deconvolute individual fluorophore signatures within a fully stained sample. Identification of multiple autofluorescence (AF) signatures was necessary to unmix specific tissues accurately.[166] AF signatures from unstained BAL, lung, and whole blood tissues were identified and saved as discrete fluorochrome tags in the SpectroFlo library. These were then incorporated into our panel as single-stain reference controls for unmixing and data analysis. It was not necessary to define AF signatures for lymph nodes as cells from this tissue had low, homogeneous AF over the course of these studies. For all unmixing, the “AF as a tag” feature in the SpectroFlo software was utilized, in addition to the incorporation of distinct AF spectral signatures into the panel when appropriate. Without the inclusion of distinct AF signatures, unmixing errors were observed with many of the fluorophores in our panel when Nx1 permutations of all fluorophores in the panel against AF on unstained tissues were visualized. These unmixing errors indicate improper resolution of positive and negative populations and can cause fluorescence from endogenous AF to be improperly assigned to other fluorophores.[166]

Our gating strategy is detailed in **Figure 4.1** and **Table 4.2.** It supports the identification of neutrophils, macrophages, dendritic cells, monocytes, eosinophils, lymphocytes, and natural killer cells. The cell surface markers used were chosen after carefully reviewing the literature, particularly the works of Misharin, McCubbrey, Gibbings, and Tighe and OMIPs -032, -061, and -069.[170-177] All cytometry data was analyzed using SpectroFlo® (Cytek Biosciences, CA) or FlowJo® (Becton, Dickinson & Company, OR) flow cytometry software.

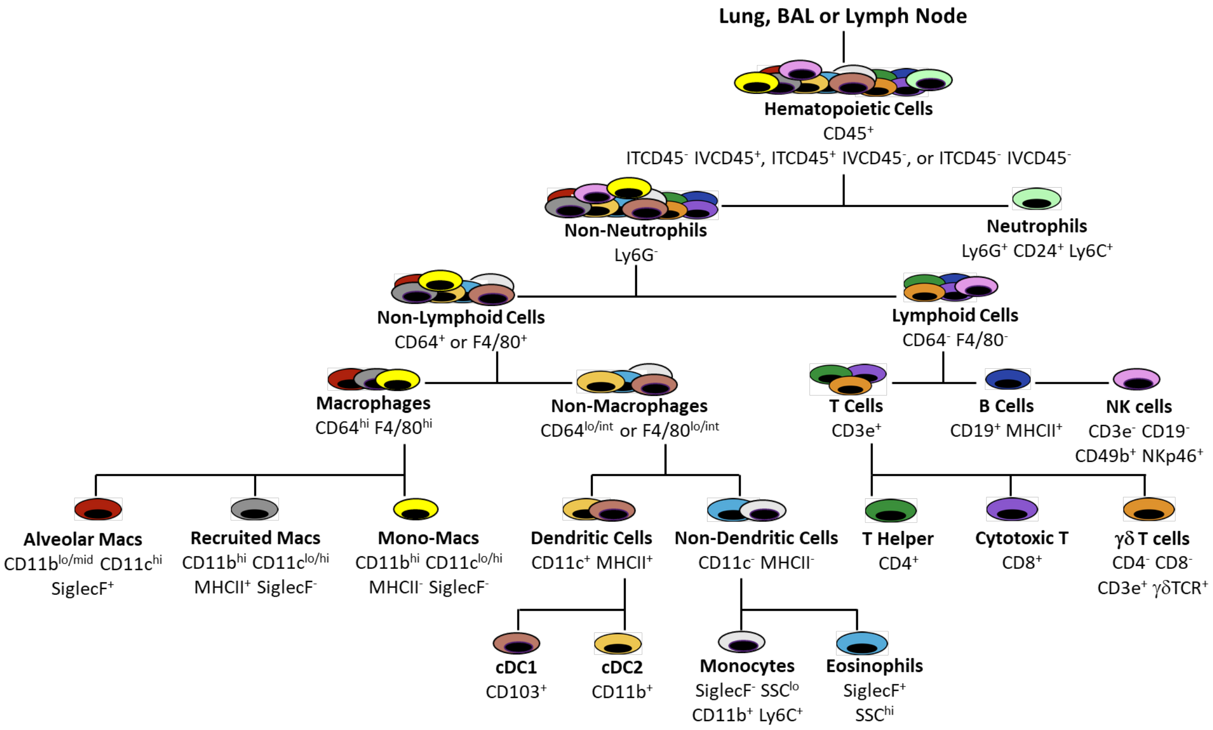

Figure 4.1 Gating Strategy

Our spectral flow cytometry panel allows for the characterization of the majority of immune cells involved in the pulmonary immune response to influenza virus including neutrophils, B cells, NK cells, T helper cells, cytotoxic T cells, γδ T cells, alveolar macrophages, recruited macrophages, monocyte-macrophages, monocytes, CD103+ dendritic cells, CD11b+ dendritic cells, and eosinophils.

Tissue type	**Antigen markers**
Airways	IVCD45^{-}CD45^{+} collected from bronchoalveolar lavage fluid
Lung	IVCD45^{-}CD45^{+} collected from lung homogenate
Marginated vasculature	IVCD45^{+}CD45^{+} collected from lung homogenate
Circulating vasculature	CD45^{+} collected from whole blood via cardiac puncture
Mediastinal lymph nodes	IVCD45^{-}CD45^{+} collected from lymph node
Cell type	**Antigen markers**
Neutrophils	Ly6G^{+} CD24^{+} Ly6C$^{lo/hi}$
Lymphoid cells	CD64^{-} F4/80^{-}
B cells	CD64^{-} F4/80^{-} CD19^{+} MHCII^{+}
T cells	CD64^{-} F4/80^{-} CD3e^{+}
Cytotoxic T cells	CD64^{-} F4/80^{-} CD3e^{+} CD8^{+}
T helper cells	CD64^{-} F4/80^{-} CD3e^{+} CD4^{+}
$\gamma\delta$ T cells	CD64^{-} F4/80^{-} CD3e^{+} CD4^{-} CD8^{-} $\gamma\delta$TCR^{+}
NK cells	CD64^{-} F4/80^{-} CD3e^{-} CD19^{-} NKp46^{+} CD49b^{+}
Non-B Non-T Non-NK cells	CD64^{-} F4/80^{-} CD3e^{-} CD19^{-} NKp46^{-} CD49b^{-}
Non-lymphoid cells	CD64^{+} or F4/80^{+}
Macrophages	CD64^{hi} F4/80^{hi}
Resident alveolar macrophages (Vehicle instilled mice)	CD64^{hi} F4/80^{hi} CD11b^{-} CD11c^{+} SigF^{hi} Ly6C^{mid} MHCII^{-}
Resident alveolar macrophages (Influenza infected mice)	CD64^{hi} F4/80^{hi} CD11b$^{mid/hi}$ CD11c^{+} SigF^{hi} Ly6C^{mid} MHCII^{-}
Recruited macrophages	CD64^{hi} F4/80^{hi} CD11b^{+} CD11c$^{lo/hi}$ SigF^{lo} Ly6C^{hi} MHCII^{+}
Mono-macrophages	CD64^{hi} F4/80^{hi} CD11b^{+} CD11c$^{lo/hi}$ SigF^{lo} Ly6C^{hi} MHCII^{-}
Dendritic cells	CD64$^{lo/int}$ or F4/80$^{lo/int}$ CD11c^{+} MHCII^{+}
CD11b^{+} dendritic cells	CD64$^{lo/int}$ or F4/80$^{lo/int}$ CD11c^{+} MHCII^{+} CD11b^{+}
CD103^{+} dendritic cells	CD64$^{lo/int}$ or F4/80$^{lo/int}$ CD11c^{+} MHCII^{+} CD103^{+}
Monocytes	CD64$^{lo/int}$ or F4/80$^{lo/int}$ CD11b^{+} CD11c^{-} MHCII^{-} SigF^{-} Ly6C$^{lo/hi}$ SSC^{lo}
Eosinophils	CD64$^{lo/int}$ or F4/80$^{lo/int}$ CD11c^{-} MHCII^{-} SigF^{+} SSC^{hi}

Table 4.2 Gating strategy

4.2.8 Measurement of Total Protein and Inflammatory Mediators in BAL Fluid

Total protein and select cytokines and chemokines were measured in BAL fluid collected from mice instilled with PBS (0 dpi), and IAV at days 3 and 6 post instillation. Total protein concentration of BAL fluid was measured using the Pierce® BCA Protein Assay Kit (Cat. 23225, Thermo Fisher Scientific, Waltham, MA) following the manufacturer's instructions. Cytokines and chemokine analysis were performed using a Milliplex ZMAP Mouse Cytokine/Chemokine magnetic bead panel (EMD Millipore Corporation, Billeric, MA) with specificity for IL-4, IL-6, IL-10, IL-13, CCL2, CXCL1, CXCL2, TNFα, and VEGF.

4.2.9 CXCL1 and CXCL2 ELISA

Paired BAL, plasma, and whole lung homogenate samples were collected from mice 3 dpi with IAV for evaluation of CXCL1 and CXCL2 chemokine gradients. BAL and plasma samples were collected as described previously in the methods for tissue harvest for spectral flow cytometry and stored at -80C until analysis. After intravascular perfusion, the left lung was collected by blunt dissection to generate whole lung homogenate. The left lung was placed in 1 mL PBS containing protease inhibitor according to the manufacturer's instructions (Pierce™ Protease Inhibitor Moni Tablets, EDTA-Free, A32955, Thermo Fisher Scientific Waltham, MA, USA). Lung tissue was homogenized using an Omni Bead Rupter 24 (Omni International, Kennesaw, GA) and 2.8mm Ceramic Beads (Omni International, Kennesaw, GA). After homogenization, samples were aliquoted and stored at -80C. The DuoSet Elisa Mouse CXCL1/KC and Mouse CXCL2/MIP-2 kits (R&D Systems, Inc. Minneapolis, MN) were used according to the manufacturer's instructions to evaluate CXCL1 and CXCL2 levels in these paired samples.

4.2.10 Acute Lung Injury Score

Histological assessment of lung inflammation and injury was completed using formalin-fixed paraffin-embedded tissue consisting of the right lung lobes stained with hematoxylin and eosin (H&E).[129] The lung injury score was performed using a modified semiquantitative scoring system as previously described.[63] The analysis was performed by a comparative pathologist (C.W.F) blinded to the mouse genotype and treatment group.

4.2.11 Stromal Cell Culture

As previously described, mouse lung fibroblasts were isolated from whole lung explants of naïve mice.[63,137] Lungs were aseptically removed from the thorax, minced and digested for 60 minutes at 37°C in 2.5 mL DMEM containing 1000 U/mL of Liberase TL and 1000U/mL of DNase I. Digests were filtered through 100μm cell strainer with DMEM containing 10% FBS, and the red blood cells were lysed by suspending the cells in sterile water for 30 seconds. Fibroblasts were then plated with DMEM containing 20% FBS, 2 mM L-glutamine, 100 IU/ml penicillin, and 100 μg/ml streptomycin and incubated at 37°C with 5% CO_2. The cell culture medium was changed every 3–4 days and fibroblasts were passaged once confluent. Fibroblasts were maintained in DMEM 10% FBS, 2 mM L-glutamine, 100 IU/ml penicillin, and 100 μg/ml streptomycin.

For experiments, fibroblasts were used between passages 2 and 4. For versican western blotting, mouse lung fibroblasts (mLFs) were grown to 80% confluency in 60mm cell culture in 10% FBS DMEM. Cells were serum starved for 24 hours in DMEM without FBS before being incubated with either DMEM 2% FBS with 10 μg/mL of poly(I:C) or fresh DMEM 2% FBS without poly(I:C) for 24 hours. For hyaluronan ELISA and neutrophil adhesion assays, mLFs were seeded in 96-well plates at 3.7 x 10^4/cm^2 (1.2 x 10^4 cells/well) in DMEM 10% FBS. After 24 hours, the medium was changed to DMEM without FBS, and the cells were incubated for 24 hours. Then cells were incubated with either fresh DMEM 2% FBS with 10 μg/mL of poly(I:C) or fresh DMEM 2% FBS without poly(I:C) for 24 hours.

4.2.12 Versican Western Blot

Versican quantification by western blotting was assessed using a modification of reported methods.[192] Briefly, mLF cell preparations were concentrated and purified by ion-exchange chromatography on diethylaminoethyl (DEAE) Sephacel (Sigma-Aldrich, St Louis, MO) in 8M Urea buffer (8M Urea, 2mM EDTA, 50mM Tris base, 0.25M NaCl, 0.5% TX-100, pH 7.5). The columns were washed with 8M Urea buffer and eluted with 8M urea buffer containing 2M NaCl. Samples were ethanol precipitated and digested with 2.0U/mL chondroitinase ABC lyase at 37C for 3 hours. Samples were loaded under reducing conditions and run on 4-12% gradient polyacrylamide-SDS gels with 3% polyacrylamide stacking gels overnight at 20V. Samples were then transferred to nitrocellulose and blocked with 10% Aqua Block (EastCoast Bio, North

Berwick, ME) in TBS-T containing 0.1% Tween-20) for 2 hours at room temperature. Versican was detected with rabbit polyclonal antibody against mouse versican β-GAG domain (cat. no. AB1033, Millipore, Burlington, MA). Results were visualized using a LI-COR Odyssey scanner and software (LI-COR Biotechnology). Densitometry was performed using Empiria Studio 2.3 (LI-COR Biotechnology, Lincoln, NE).

4.2.13 Hyaluronan ELISA

HA quantification was assessed using a modification of reported methods. [193] Cell culture media and cell layer samples were digested with pronase (0.5 mg/ml, Roche) in 0.5 M Tris buffer (pH 6.5) for 18h at 37°C. Frozen lung tissue was minced using a blade while still frozen and digested with proteinase K (0.25 mg/ml, ThermoFisher) at 60°C for 24h. Following digestion, the pronase and proteinase K were heat inactivated by incubation at 100°C for 20 min. HA quantity was assayed by a competitive ELISA developed in-house as previously described.[194]

4.2.14 Neutrophil Adhesion Assay

Leukocyte binding was assessed using a modification of reported methods. [195] Prior to the adhesion assay, human promyelocytic leukemia (HL-60) cells were differentiated into neutrophil-like cells (dHL-60s) by incubation of 10^6 cells with 190μL of dimethylsulfoxide (DMSO) in 15mL of Iscove's medium for 5 days at 37C with 5% CO_2.[196] For adhesion on mLFs, cells were seeded in a 96-well plate and stimulated as described above. On the day of the adhesion assay, media was removed from all wells and Hoescht stain (2µg/ml) in serum and phenol red-free RPMI medium was applied to each well and incubated for 10 minutes at 37C. mLF cell counts were quantified using live-cell fluorescent microscopy (ImageXpress Pico, Molecular Devices). After initial imaging, wells were washed once with phenol red-free RPMI.

On the day of the adhesion assay, dHL-60 cells were washed three times in Gey's medium and resuspended in the same medium at 2 x 10^6 cells/ml. Next dHL-60s were incubated with calcein-AM (1µg/mL, Invitrogen, Carlsbad, CA) for 15 minutes at room temperature. Afterwards, cells were washed twice in serum and phenol red-free RPMI and then applied to mLFs wells and allowed to adhere for 60 minutes at 4°C. Cultures were washed twice with cold phenol red-free RPMI to remove nonadherent cells to remove non-adherent leukocytes. The adherent dHL-60 cell area was quantified using live-cell fluorescent microscopy (ImageXpress Pico, Molecular Devices).

4.2.15 Statistical Analysis

Statistics and images were generated using GraphPad Prism (La Jolla, CA). For PCR analyses of gene expression, normalized mRNA levels were expressed as -fold of levels in untreated or vehicle-treated controls using the comparative cycle threshold method compared with the designated housekeeping gene.[104,138] Quantitative PCR (qPCR), BCA protein, Milliplex, and ELISA analyses were performed with two technical replicates. All data are expressed as the average ± S.E., unless otherwise specified. Differences were identified by two-way ANOVA followed by Bonferroni's posttest for multiple comparisons, with the mean of every wild-type group compared with the mean of every Col1a2/Vcan$^{-/-}$ group with the same treatment (PBS, 3 dpi IAV, 6 dpi IAV, or 9 dpi IAV), unless otherwise specified. Statistical results with a value of $p<0.05$ were considered statistically significant.

4.3 Results

4.3.1 IAV-induced Increase in Expression of Versican is Significantly Attenuated in Col1a2/Vcan$^{-/-}$ Mice

Changes in body weight, influenza virus RNA, and total protein in the bronchoalveolar lavage (BAL) fluid were measured in mice exposed to tamoxifen and infected with IAV. Body weight was monitored daily in mice infected with IAV. Col1a2/Vcan$^{-/-}$ mice and their littermate controls (WT) did not have significant differences in body weight loss, as measured by the percentage of initial weight throughout the course of infection observed (**Figure 4.2A**). In WT and Col1a2/Vcan$^{-/-}$ mice, viral copies in whole lung homogenates peaked at 6 dpi, with no differences in viral copy numbers between strains at any time point observed (**Figure 4.2B**). Additionally, Col1a2/Vcan$^{-/-}$ and WT mice had similar progressive increases in total protein in their BAL fluid throughout infection, with no difference between strains (**Figure 4.2C**).

Versican expression was measured from whole lung homogenates in PBS-instilled and IAV-instilled mice on 3, 6, and 9 days post-infection (dpi). In WT mice, maximum versican expression was observed on 6 dpi (8.02 ± 1.27) consistent with previously published findings in C57BL/6J mice (**Figure 4.2D**).[63] Col1a2/Vcan$^{-/-}$ mice had significantly less versican expression on 6 dpi (3.91 ± 0.56) compared to wild-type mice (**Figure 4.2C**). There were no significant differences in the amount of versican expression between Col1a2/Vcan$^{-/-}$ and WT controls in vehicle instilled mice (0 dpi), and IAV instilled mice at 3 dpi or 9 dpi.

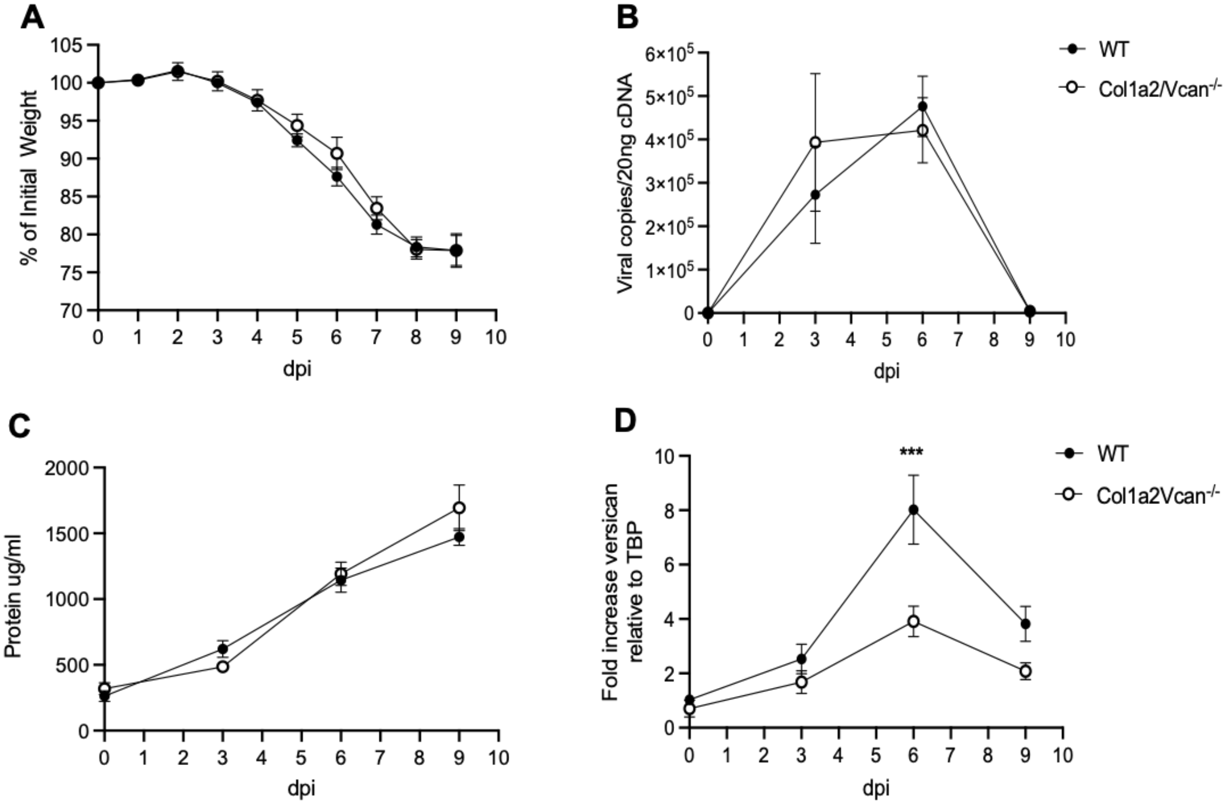

Figure 4.2 Weight loss, viral quantification, and versican reduction during in influenza A infection in Col1a2/Vcan$^{-/-}$ mice

(A) Mouse percentage of initial body weight following infection with IAV over 9 dpi. Values are mean ± SEM with *n*=6 per time point. (B) Viral copies per 20ng/cDNA in PBS (day 0) and IAV infected mice 3, 6, and 9 dpi with IAV. Values are mean ± SEM with *n*=6 per time point. (C) Total protein measured from bronchoalveolar lavage with IAV over 9 dpi. Values are mean ± SEM with *n*=4-14 per time point. (D) Total *Vcan* expression in the lungs in PBS (dpi 0) and IAV infected mice 3, 6, and 9 dpi with IAV. Change in the amount of mRNA was determined using mRNA collected from lung homogenates and quantitative real-time PCR. Values are mean ± SEM with *n*=6 per time point. Asterisks show groups that are statistically significantly different (***$p \leq 0.0002$) using two-way ANOVA with Bonferroni's for multiple comparison test. Abbreviations: IAV, influenza A virus; days post infection, dpi.

2.3.2 IAV-induced Accumulation of Neutrophils and Monocytes in the Lungs is Significantly Attenuated in Col1a2/Vcan$^{-/-}$ Mice

Leukocyte accumulation during IAV infection was assessed by spectral flow cytometry in five distinct microenvironments relevant to the host immune response. These microenvironments included the airways, lung, marginated vasculature, circulating vasculature, and mediastinal lymph nodes. Cells measured in the airspaces were those collected by bronchoalveolar lavage, while cells measured in the lungs were collected from single-cell suspensions of lung homogenates that were negative for the intravascular CD45 label (CD45IV^{-}). Marginated vasculature cells were differentiated from circulating vasculature cells by the method of collection. The circulating vasculature cells were collected by cardiac blood draw; the marginated vasculature cells were CD45IV^{+} cells collected from the single-cell suspensions of lung tissue. Marginated vasculature cells remained within the pulmonary vessels after perfusion of the vasculature and potentially could have been poised to enter the lung interstitium. Spectral flow cytometry analysis from PBS-instilled mice (0 dpi) and IAV-instilled mice (3, 6, and 9 dpi) was conducted on cells from these five microenvironments utilizing a broad immunophenotyping panel. The cellular phenotypes our panel (**Figure 4.1** and **Table 4.2)** defined included neutrophils, alveolar macrophages, recruited macrophages, mono-macrophages, monocytes, dendritic cells, eosinophils, B cells, helper T cells, cytotoxic T cells, γδ T cells, and natural killer (NK) cells. This panel allowed for the immunophenotyping of > 90% of all leukocytes within each microenvironment.

In Col1a2/Vcan$^{-/-}$ mice, there were significantly fewer leukocytes (i.e., CD45+ cells) in the airways on 3 dpi with IAV ($1.36 \times 10^5 \pm 2.63 \times 10^4$) compared with WT mice ($3.61 \times 10^5 \pm 8.61 \times 10^4$, **Figure 4.3C**) but no significant differences in the number of leukocytes in the lung (**Figure 4.3B**), marginated vasculature (**Figure 4.3A**), and circulating vasculature (**Figure 4.4A**) at any time point. The difference observed in total leukocyte numbers on 3 dpi between Col1a2/Vcan$^{-/-}$ and WT mice were accounted for by two cell populations, neutrophils and monocytes. Col1a2/Vcan$^{-/-}$ have fewer neutrophils in the marginated vasculature (**Figure 4.3D**, $3.01 \times 10^5 \pm 4.24 \times 10^4$), lungs (**Figure 4.3E**, $1.65 \times 10^5 \pm 2.63 \times 10^4$), and airways (**Figure 4.3F**, $4.16 \times 10^4 \pm 9.53 \times 10^3$) compared to WT mice (**Figure 4.3D** $4.97 \times 10^5 \pm 7.49 \times 10^4$, **Figure 4.3E** $4.20 \times 10^5 \pm 9.21 \times 10^4$, **Figure 4.3F** $1.44 \times 10^5 \pm 2.59 \times 10^4$) on 3 dpi with IAV. However, there was no difference in the number of circulating neutrophils (**Figure 4.4B**). Additionally, Col1a2/Vcan$^{-/-}$ had fewer monocytes in the lungs (**Figure 4.3H**, 1.10 x 10^5 ± 2.06 x 10^4) and airways (**Figure 4.3I**, 2.24 x 10^4 ± 5.80 x 10^3) compared to WT mice (**Figure 4.3H** 2.01 x 10^5 ± 4.45 x 10^4, **Figure 4.3I** 6.58 x 10^4 ± 1.62 x 10^4) on 3 dpi with IAV. There was no difference in the number of monocytes in the marginated vasculature (**Figure 4.3G**) or circulating vasculature (**Figure 4.4C**). A lack of fibroblast-derived versican significantly diminishes the migration of neutrophils and monocytes during the peak time (3 dpi) of their recruitment from the marginated vasculature into the lungs, suggesting that fibroblast-derived versican plays an essential role in neutrophil and monocyte recruitment.

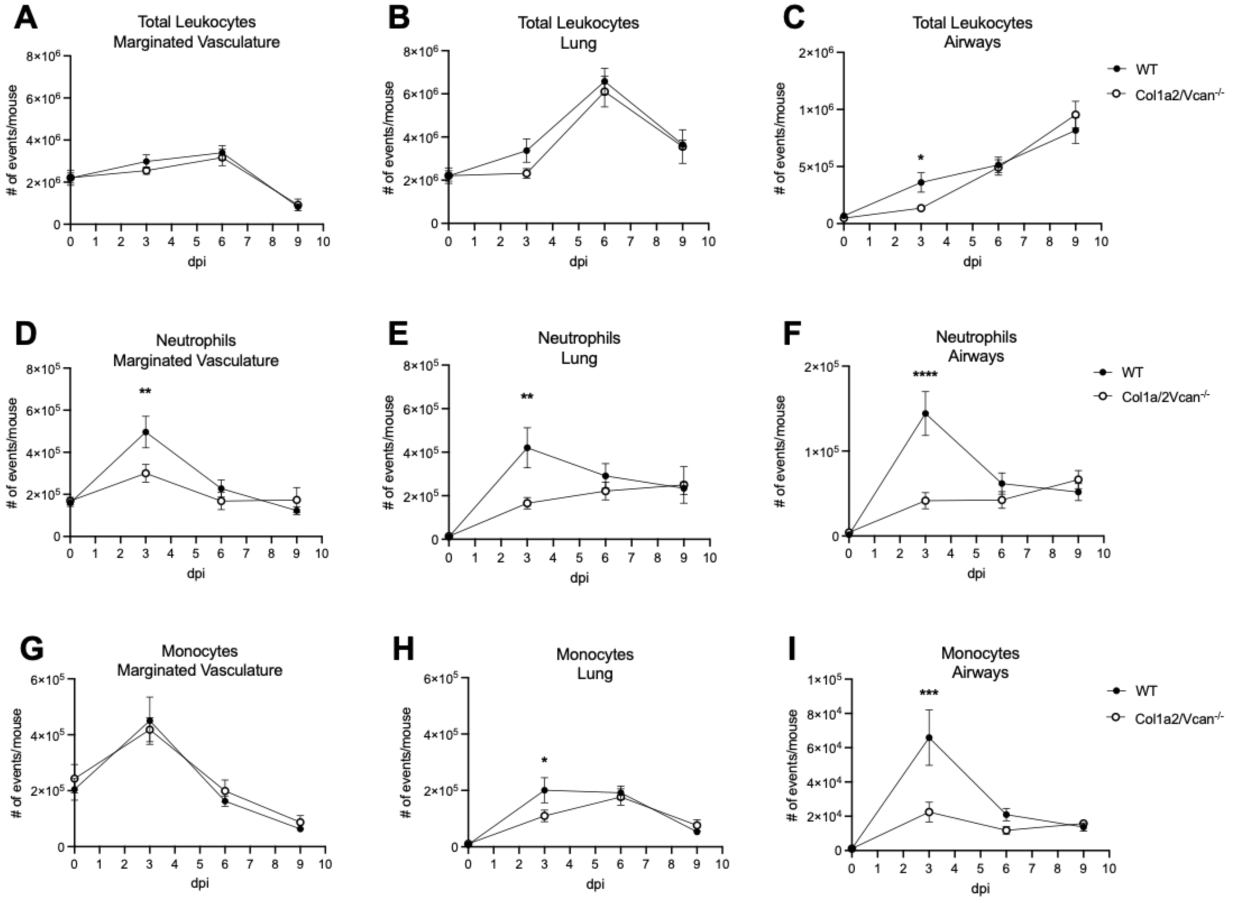

Figure 4.3 Total Leukocytes, Neutrophils, and Monocytes in the Marginated Vasculature, Lung, and Airways During IAV Infection

(A-I) Values are mean ± SEM with *n*=7-14 per time point. Asterisks show groups that are statistically significantly different (**p*≤0.03, ***p*≤0.003, ****p*≤0.0002, *****p*≤0.0001) using two-way ANOVA with Bonferroni's for multiple comparison test. Abbreviations: IAV, influenza A virus.

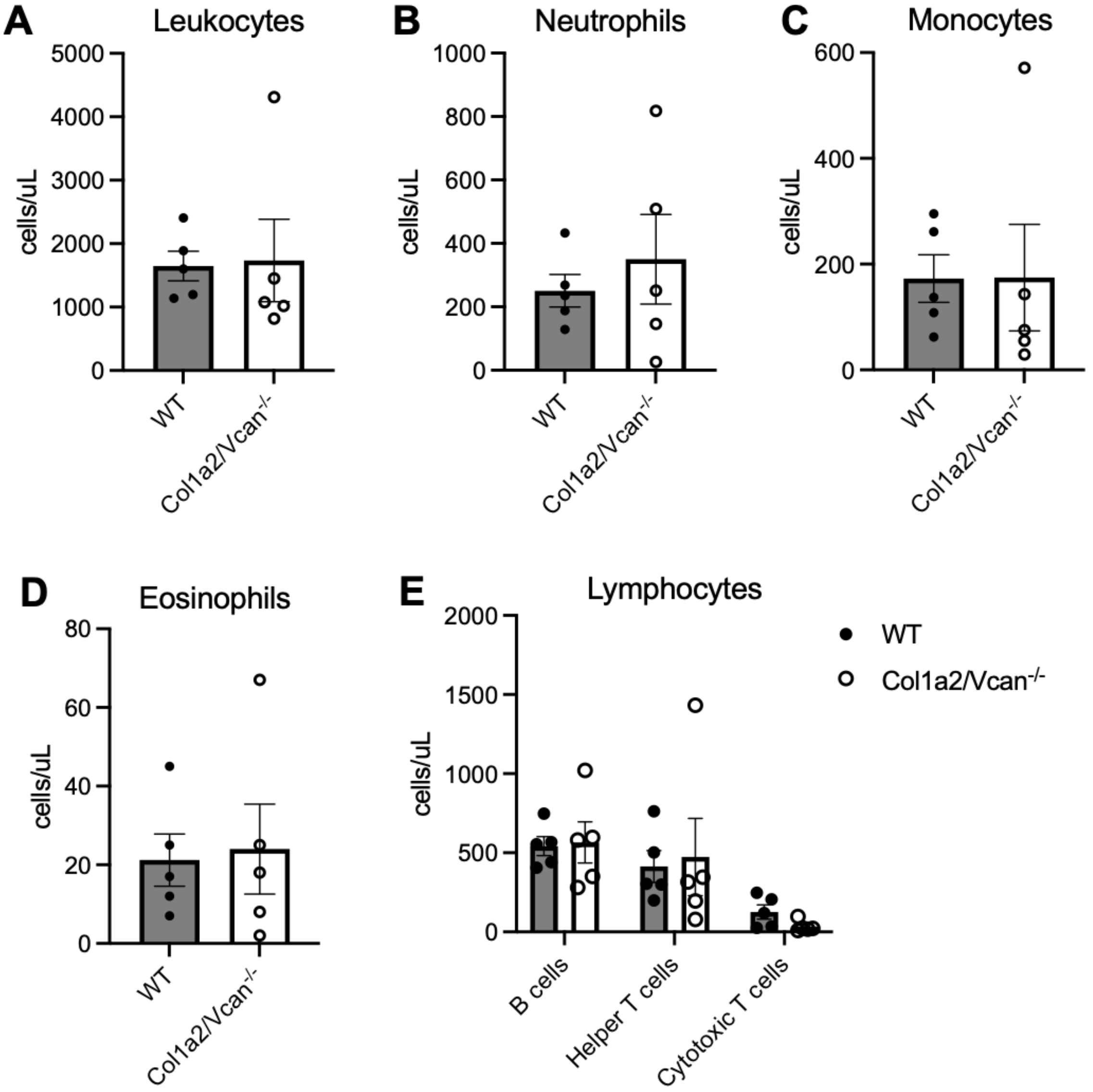

Figure 4.4 Total Leukocytes, Neutrophils, Monocytes, Eosinophils and Lymphocytes in the Circulating Vasculature During IAV Infection

(A-E) Circulating leukocyte subpopulations on 3 dpi. Values are mean ± SEM with *n*=5 per time point. No groups are statistically significantly different using unpaired t-test. Abbreviations: IAV, influenza A virus

4.3.3 IAV-induced Accumulation of Mono-Macrophages is Significantly Attenuated in the Marginated Vasculature and Lungs of Col1a2/Vcan$^{-/-}$ Mice

Macrophages are resident phagocytic cells of the tissues they are localized in. While our spectral flow cytometry panel was compatible with immunophenotyping for alveolar macrophages, recruited macrophages, and mono-macrophages in all five microenvironments investigated, macrophages were not expected to localize to vascular microenvironments. However, a low number of cells with phenotypes consistent with macrophages (CD64^{hi}F4/80^{hi}), along with a substantial population of mono-macrophages, were observed in the marginated vasculature (IVCD45^{+}) but not in the circulating vasculature (not shown). We have designated these macrophages as marginated vasculature mono-macrophages (**Figure 4.5A**), marginated vasculature CD64^{hi}F4/80^{hi}MHCII^{+} macrophages (**Figure 4.5D**), and marginated vasculature CD64^{hi}F4/80^{hi}MHCII^{-} macrophages (**Figure 4.5G**). The identification of these cells in the marginated vasculature is unexpected and there are several possible explanations for their localization in the vasculature, including that they may be monocyte-derived cells in the process of emigrating into the lungs. Col1a2/Vcan$^{-/-}$ mice had significantly fewer mono-macrophages in the marginated vasculature on 6 dpi with IAV ($1.99 \times 10^5 \pm 1.67 \times 10^4$) compared with WT mice ($3.16 \times 10^5 \pm 3.90 \times 10^4$, **Figure 4.5A**). There were no significant differences in the number of CD64^{hi}F4/80^{hi}MHCII^{+} or CD64^{hi}F4/80^{hi}MHCII^{-} macrophages in Col1a2/Vcan$^{-/-}$ mice compared to WT mice in the marginated vasculature (**Figure 4.5D and Figure 4.5G**).

A known limitation of bronchoalveolar lavage (BAL) is that it does not remove all cells from the pulmonary airspace and that there is considerable mouse-to-mouse variability in the recovery of CD45+ cells with this technique.[130,153-159] This limitation was evident in our evaluation of interstitial macrophages, which identified alveolar macrophages in the lung compartment. The comparisons of alveolar macrophages in Col1a2/Vcan$^{-/-}$ and WT mice is presented consistently with previous data, with separation of lung and airway macrophages, even though we expect that lung alveolar macrophages represent non-lavageable macrophages occupying the airways. Col1a2/Vcan$^{-/-}$ mice had significantly fewer mono-macrophages in the lungs on 6 dpi with IAV ($1.35 \times 10^5 \pm 2.02 \times 10^4$) compared with WT mice ($2.46 \times 10^5 \pm 4.16 \times 10^4$, **Figure 4.5B**). Additionally, there was no significant difference in the number of macrophages in the Col1a2/Vcan$^{-/-}$ mice compared to WT mice in the lungs and airways (**Figure 4.5E-F and Figure 4.5H-I**). Although there were no differences in total CD45+ leukocytes seen in any compartment at 6 dpi (**Figure 4.3A-C**), mono-macrophages are the one subpopulation of leukocytes that is significantly diminished in Col1a2/Vcan$^{-/-}$ in the lungs at 6 dpi. This may be due to the reduced number of monocytes observed in the lungs and airways on 3 dpi (**Figure 4.3H-I**).

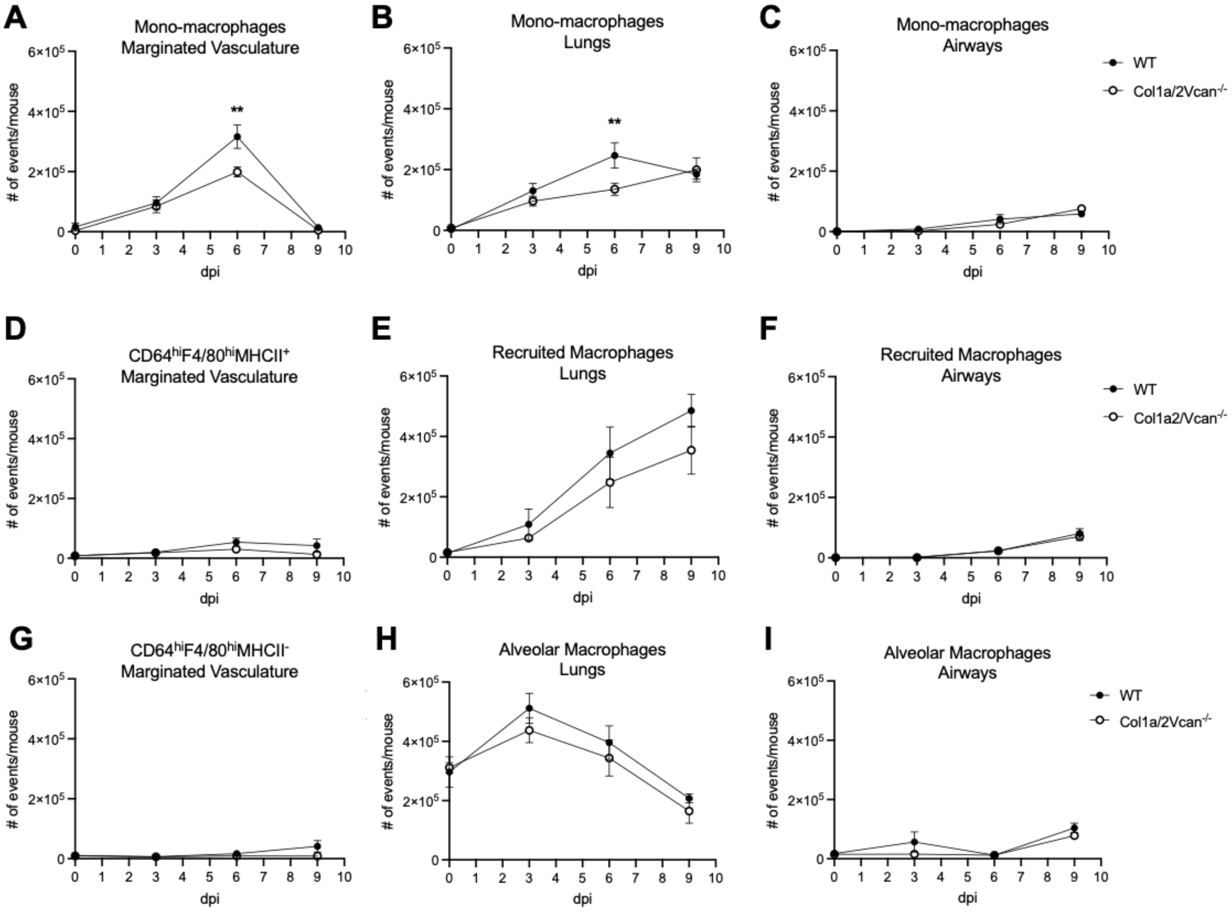

Figure 4.5 Macrophages Associated with the Marginated Vasculature, Lungs, and Airways During IAV Infection

(A-I) Values are mean ± SEM with *n*=7-14 per time point. Asterisks show groups that are statistically significantly different (**$p \leq 0.003$) using two-way ANOVA with Bonferroni's for multiple comparison test. Abbreviations: IAV, influenza A virus.

4.3.4 IAV-induced Accumulation of Dendritic Cells and Eosinophils is Attenuated in the Airways of Col1a2/Vcan$^{-/-}$ Mice

In Col1a2/Vcan$^{-/-}$ mice, there were no significant differences in the number of dendritic cells and eosinophils in the marginated vasculature and lungs at any time point compared to WT mice (**Figure 4.6A-B** and **Figure 4.6D-E**) However, in Col1a2/Vcan$^{-/-}$ mice there were significantly less dendritic cells in the airways on 3 dpi with IAV ($9.08 \times 10^3 \pm 2.05 \times 10^3$) compared with WT mice ($2.35 \times 10^4 \pm 2.05 \times 10^3$, **Figure 4.6C**). Inflammatory dendritic cells are monocyte-derived and are recruited to the lungs during IAV infection, therefore it is possible this difference is downstream effect of the reduced monocytes observed in the lungs and airways on 3 dpi (**Figure 4.3H-I**).[197] Additionally, there were significantly less eosinophils in the airways on 9 dpi with IAV ($3.13 \times 10^4 \pm 9.39 \times 10^3$) compared with WT mice ($5.88 \times 10^4 \pm 1.54 \times 10^4$, **Figure 4.6F**). Although there are no differences in total CD45$^+$ leukocytes seen in any compartment at 9 dpi (**Figure 4.3A-C**), eosinophils are the one subpopulation of leukocytes that is significantly diminished in Col1a2/Vcan$^{-/-}$ airways at 9 dpi. Eosinophils have been recognized as playing a role in antiviral immunity and these findings warrant further investigation.[198]

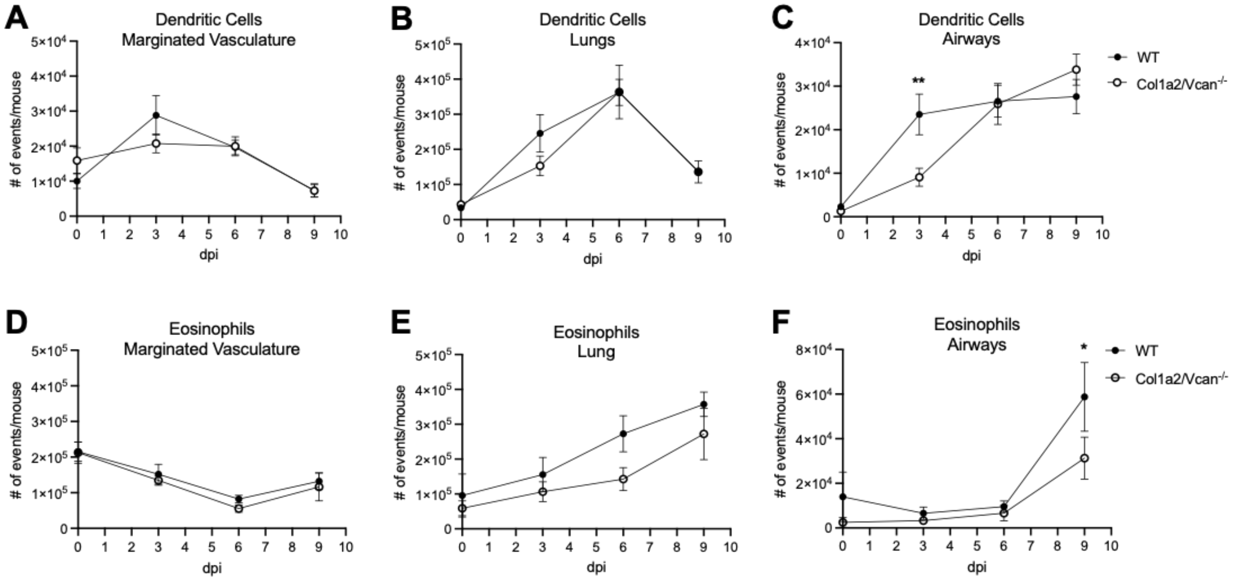

Figure 4.6 Dendritic Cells and Eosinophils in the Marginated Vasculature, Lung, and Airways During IAV Infection

(A-F) Values are mean ± SEM with *n*=7-14 per time point. Asterisks show groups that are statistically significantly different (*$p \leq 0.03$, **$p \leq 0.003$) using two-way ANOVA with Bonferroni's for multiple comparison test. Abbreviations: IAV, influenza A virus.

4.3.5 IAV-induced Accumulation of Lymphocytes in the Mediastinal Lymph Nodes is Enhanced in Col1a2/Vcan$^{-/-}$ Mice

In Col1a2/Vcan$^{-/-}$ mice, the accumulation of lymphocytes in the mediastinal lymph nodes during IAV infection was greater compared to WT mice on 6 dpi (**Figure 4.7A-E**). While the increase in the number of leukocytes was not statistically significant, the trend for Col1a2/Vcan$^{-/-}$ to have more lymphocytes was consistent across all subpopulations (B-cells, cytotoxic T-cells, helper T-cells, and γδ T-cells) and was statistically significant for helper T-cells ($*p \leq 0.03$, **Figure 4.7C**). The trend for increases in lymphocyte subpopulations in Col1a2Vcan$^{-/-}$ mice compared to WT mice was observed in other microenvironments, including B-cells in the lungs on 6 dpi (ns, **Figure 4.8E**), and airways on 6 and 9 dpi (ns, **Figure 4.8F**), helper T cells in the lungs on 6 dpi (ns, **Figure 4.8H)** and airways on 9 dpi ($**p \leq 0.003$ **Figure 4.8I**), and cytotoxic T cells in the airways on 9 dpi ($*p \leq 0.03$, **Figure 4.8L**). There were no significant differences in the number of lymphocyte subpopulations between Col1a2/Vcan$^{-/-}$ mice and WT mice in the circulating vasculature (**Figure 4.4**). The increased number of lymphocyte subpopulations in the mediastinal lymph nodes on 6 dpi with subsequent increases in airway helper T-cells and cytotoxic T-cells on 9 dpi is suggestive that Col1a2/Vcan$^{-/-}$ mice have altered immune response kinetics to IAV infection. Lymphocyte subpopulations in the lymph nodes and lung tissue of Col1a2/Vcan$^{-/-}$ mice are reduced compared to those of WT mice on 9 dpi, suggesting that the increase in lymphocyte subpopulations is in the lymph node and subsequently increased trafficking of lymphocytes to the airspaces is transient.

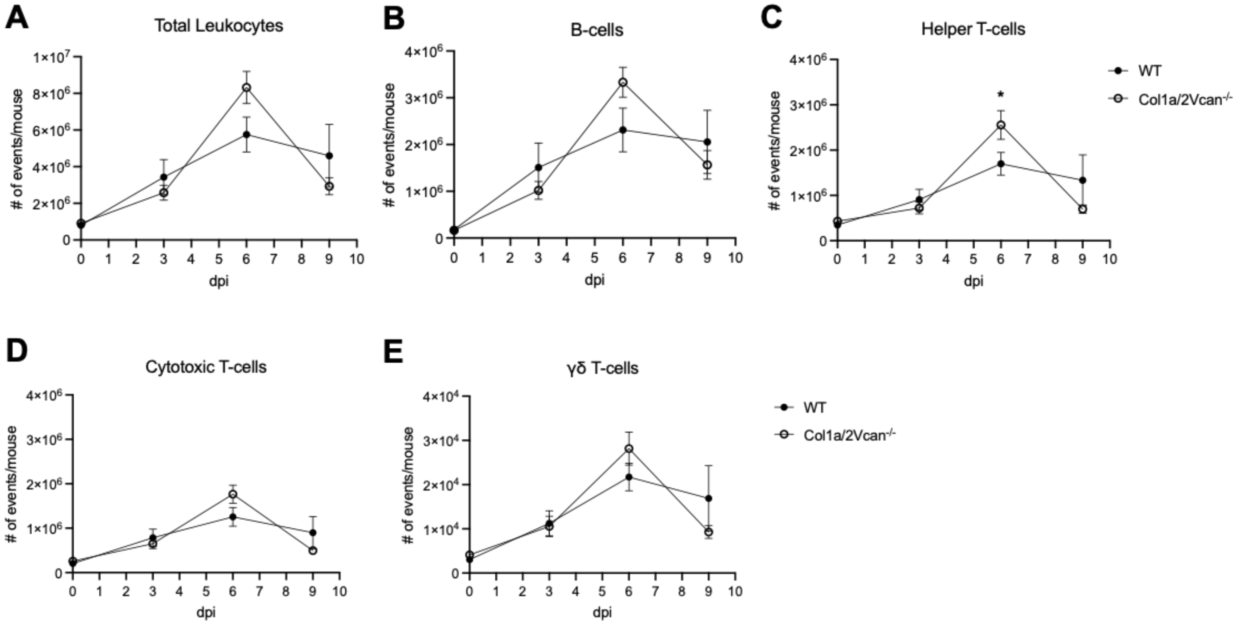

Figure 4.7 Total Leukocytes and Lymphoid Subpopulations in the Mediastinal Lymph Nodes During IAV Infection

(A-F) Values are mean ± SEM with *n*=7-14 per time point. Asterisks show groups that are statistically significantly different (**p*≤0.03) using two-way ANOVA with Bonferroni's for multiple comparison test. Abbreviations: IAV, influenza A virus.

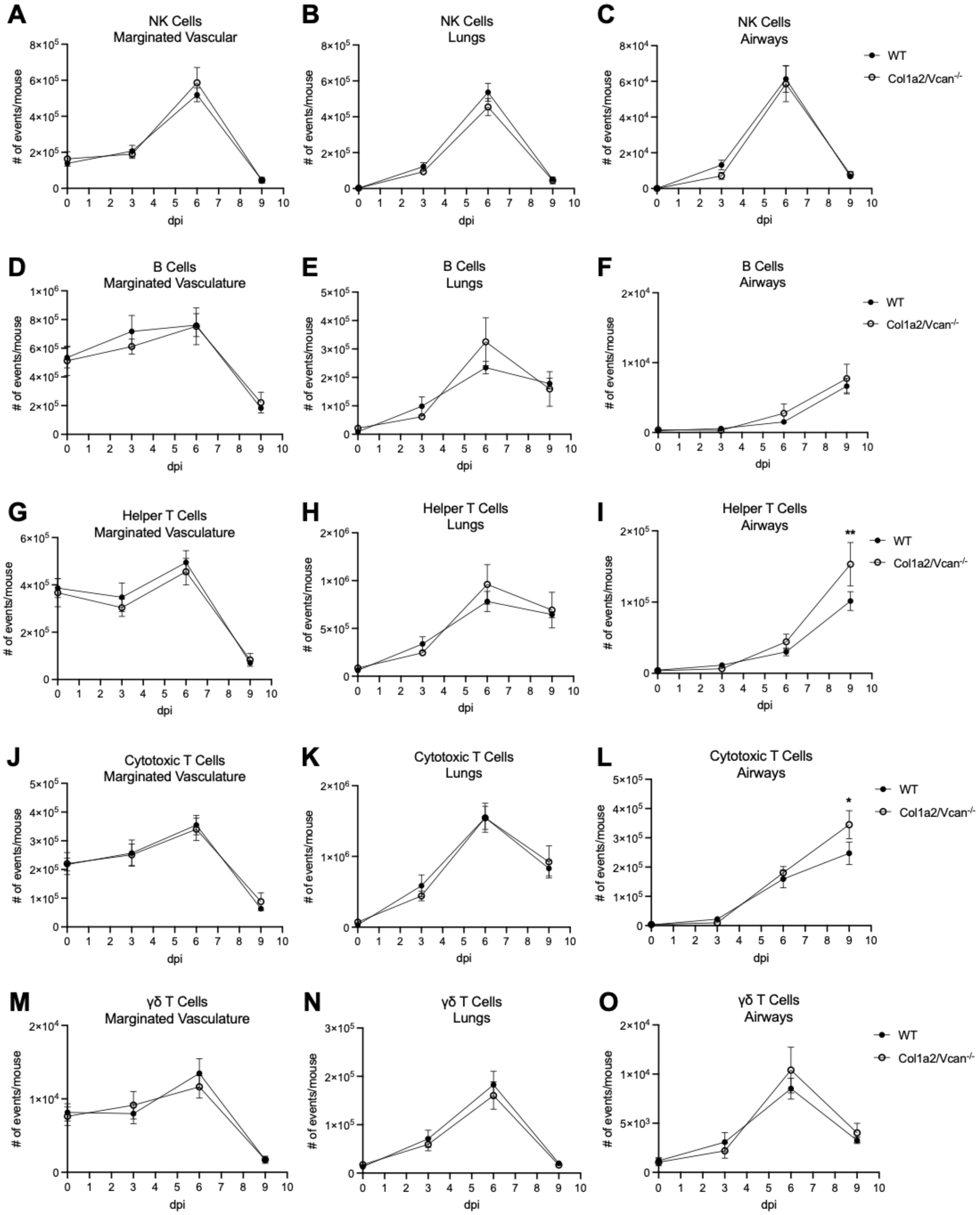

Figure 4.8 Lymphocyte Subpopulations in the Marginated Vasculature, Lung, and Airways During IAV Infection

(A-O) Values are mean ± SEM with *n*=7-14 per time point. Asterisks show groups that are statistically significantly different (**p*≤0.03, ***p*≤0.003) using two-way ANOVA with Bonferroni's for multiple comparison test. Abbreviations: IAV, influenza A virus; NK, natural killer.

4.3.6 Fibroblast-derived Versican Does Not Alter Expression of Inflammatory Cytokines and Chemokines during IAV infection

To investigate if fibroblast-derived versican impacted the inflammatory profile during IAV infection, protein concentrations of inflammatory mediators were evaluated in BAL fluid using a mouse immunology multiplex panel in PBS-instilled and IAV-instilled Col1a2/Vcan$^{-/-}$ and WT mice. No significant differences were detected at any time point between mouse strains (**Figure 4.9A-I**) To investigate neutrophil chemokine gradients for CXCL1 and CXCL2, paired plasma, lung homogenates, and BAL fluid samples were assessed by ELISA. No significant differences in CXCL1 and CXCL2 concentrations were observed across plasma, lung homogenate and BAL samples between Col1a2/Vcan$^{-/-}$ and WT mice (**Figure 4.10**).

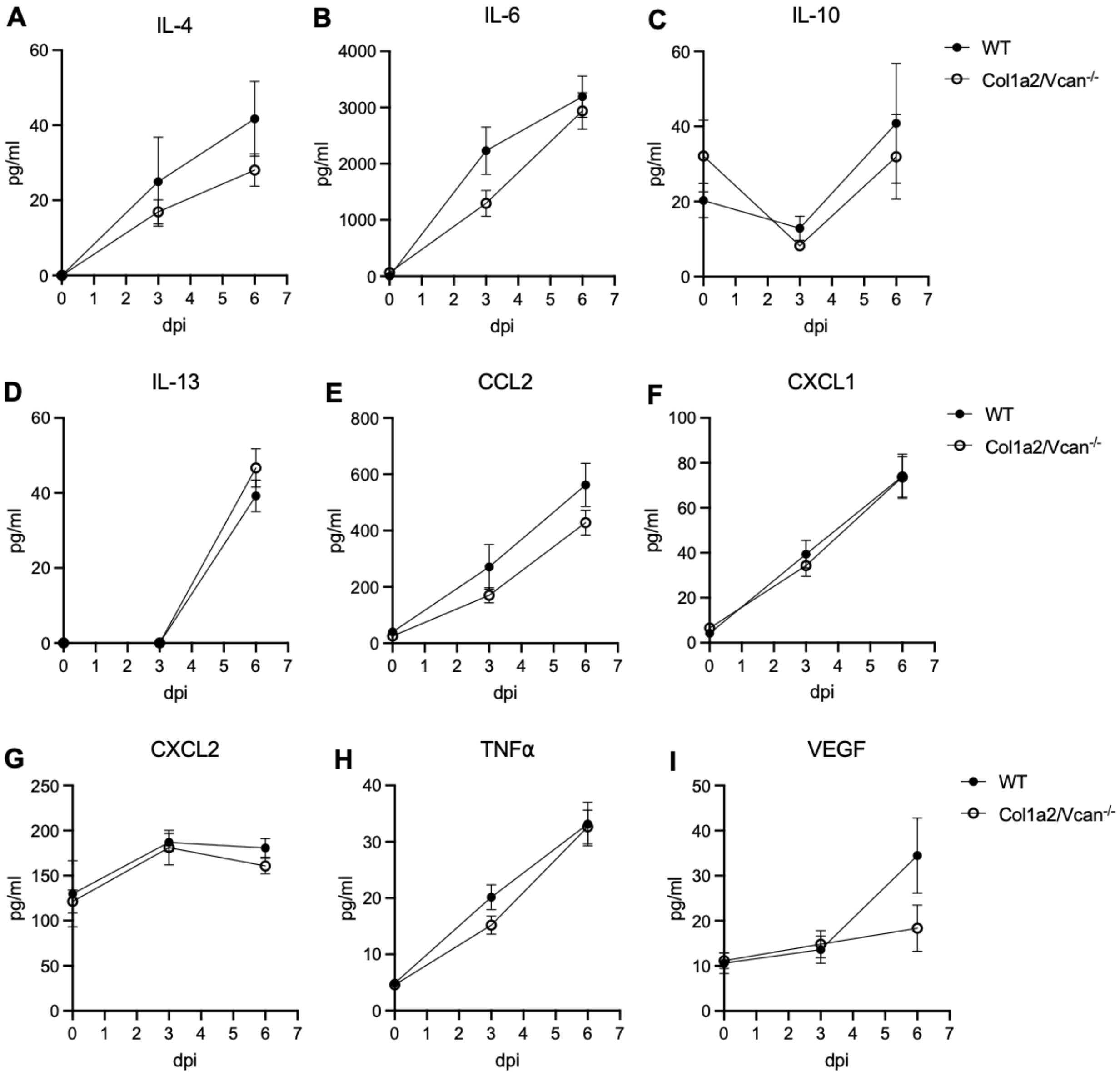

Figure 4.9 Concentrations of chemokines and cytokines from BAL fluid during IAV Infection

(A-I) Values are mean ± SEM with *n*=3-14 per time point. Groups were statistically tested using two-way ANOVA with Bonferroni's for multiple comparison test. Abbreviations: IAV, influenza A virus; BAL, bronchoalveolar lavage; dpi, days post infection.

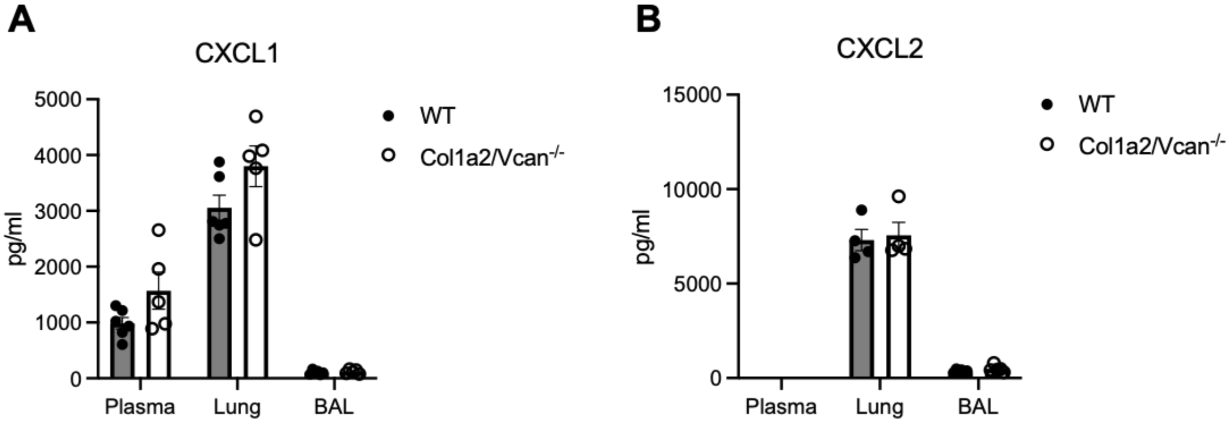

Figure 4.10 Concentrations of CXCL1 and CXCL2 from Paired Plasma, Lung Homogenate, and BAL fluid at 3 dpi with IAV

(A-B) Values are mean ± SEM with *n*=4-6 per time point. Groups were statistically tested using two-way ANOVA with Bonferroni's for multiple comparison test. Abbreviations: BAL, bronchoalveolar lavage; dpi, days post infection; IAV, influenza A virus.

4.3.7 Poly(I:C)-induced Versican-Enriched ECM Neutrophil Adhesion was Significantly Reduced in Cultures of Lung Fibroblasts from Col1a2/Vcan$^{-/-}$ Mice

Fibroblasts were stimulated with poly(I:C) to generate a versican enriched matrix. A representative western blot for versican isoform V1 is shown in **Figure 4.11A**. Col1a2/Vcan$^{-/-}$ mouse lung fibroblasts (mLFs) demonstrated 66% knockdown of V1 (~263 kDa) when treated with PBS and 77% knockdown of versican when treated with poly(I:C). Hyaluronan (HA) is an important binding partner of versican and has previously been shown to be important for monocyte adhesion to versican-enriched ECM generated by lung fibroblasts.[1,100] To quantify the HA present in lung fibroblast cultures, HA ELISA was performed on cell culture media and cell layers from mLF cultures generated from Col1a2/Vcan$^{-/-}$ and WT mice stimulated with poly(I:C). After poly(I:C) stimulation, mLFs from Col1a2/Vcan$^{-/-}$ mice had less cell associated HA compared to WT mice (**Figure 4.11B**). No differences were observed when the amount of HA recovered in the culture media of the mLFs from the two strains of mice were compared (not shown). To investigate whether versican was important for neutrophil adhesion to lung fibroblasts, differentiated HL60 (dHL60) cells were used in adhesion assays with mLFs collected from Col1a2/Vcan$^{-/-}$ mice and compared to fibroblasts collected from WT control mice. dHL-60s were significantly less adherent to Col1a2/Vcan$^{-/-}$ mLFs stimulated with poly(I:C) compared to WT mLFs (**Figure 4.11C**).

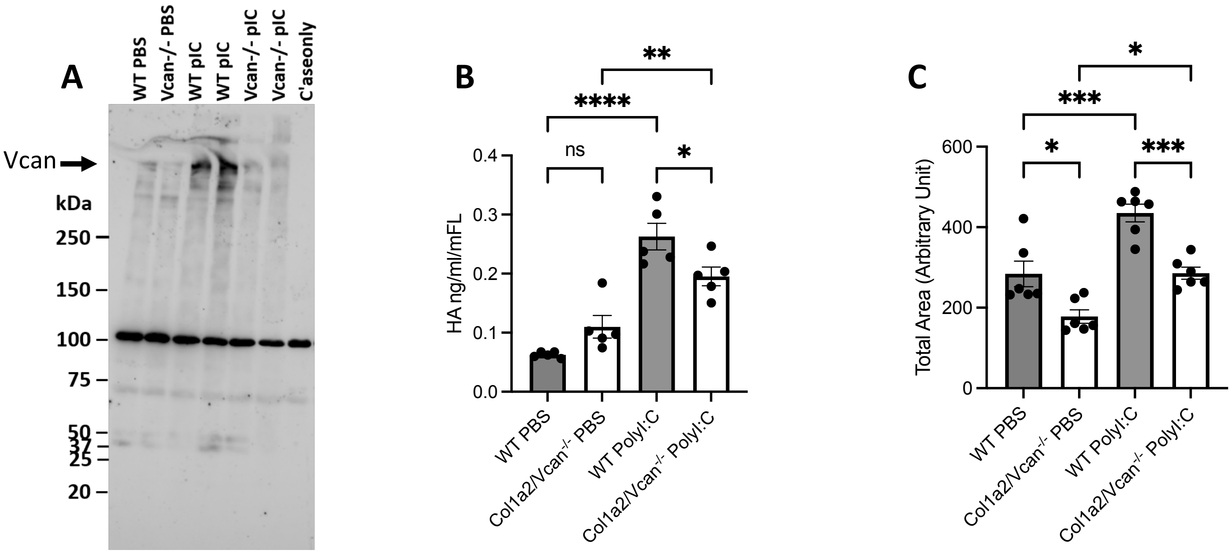

Figure 4.11 Versican Protein, Cell-Associated Hyaluronan, and Neutrophil Adhesion in mLFs Stimulated with Poly(I:C)

(A) Protein of versican isoform V1 (~263 kDa, black arrow) in mFLs from Col1a2/Vcan$^{-/-}$ and WT mice stimulated with poly(I:C) measured by Western blot. (B) Cell-associated hyaluronan in mFLs from Col1a2/Vcan$^{-/-}$ and WT mice stimulated with poly(I:C) measured by ELISA. (C) Adhesion of dHL-60s to mFLs from Col1a2/Vcan$^{-/-}$ and WT mice stimulated with poly(I:C) quantified using live-cell fluorescent microscopy. Values are mean ± SEM with *n*=5. Asterisks show groups that are statistically significantly different (*$p \leq 0.03$, **$p \leq 0.003$, ***$p \leq 0.0002$, ****$p \leq 0.0001$) using one-way ANOVA with Bonferroni's for multiple comparison test. Abbreviations: mLFs, mouse lung fibroblasts

4.4 Discussion

Consistent with the study objectives, we determined the time course of changes in fibroblast-derived versican expression and the impact of fibroblast-derived versican deficiency on leukocyte migration into pulmonary and vascular microenvironments during IAV infection, which has not been previously reported. In addition we document the following significant findings: (1) neutrophils in the airways, lungs, and marginated vasculature are significantly reduced in Col1a2/Vcan$^{-/-}$ mice compared to WT controls on 3 dpi with IAV; (2) monocytes in the airways and lungs are significantly reduced on 3 dpi with IAV and this is followed by significantly reduced numbers of mono-macrophages on 6 dpi in Col1a2/Vcan$^{-/-}$ mice compared to WT controls; (3) neutrophil-like cells are less adherent to versican-deficient fibroblasts *in vitro* and versican-deficient fibroblasts have significantly reduced cell-associated hyaluronan (HA) content; and (4) the mediastinal lymph nodes demonstrate a trend for increased numbers of lymphoid cells on 6 dpi with IAV in Col1a2/Vcan$^{-/-}$ mice compared to WT controls. These findings suggest that fibroblast-derived versican, and associated HA, are necessary for adhesion of neutrophils and monocytes to lung fibroblasts as they transit into the lung interstitium and airways from the pulmonary vasculature of mice infected with influenza virus. Additionally, we did not find evidence of attenuation of neutrophil or monocyte recruitment by fibroblast-derived versican through chemokine or cytokine mediated mechanisms. These findings confirm that fibroblast-derived versican is critical for generating specialized provisional matrices in distinct microenvironments as part of the host immune response to IAV infection.

During IAV infection, fibroblast-derived versican plays an important contextual role in regulating leukocyte migration in distinct pulmonary and vascular microenvironments. Interestingly, we find that neutrophil migration into the lungs and airways is reduced by 60.7% and 71.1%, respectively, in Col1a2/Vcan$^{-/-}$ mice during peak neutrophil emigration from the vasculature. Additionally, neutrophils are reduced in the marginated vasculature of Col1a2/Vcan$^{-/-}$ mice on 3 dpi by 39.6%, but there is no difference in circulating neutrophils between Col1a2/Vcan$^{-/-}$ mice and WT controls. Naive and inflamed lungs possess a reservoir of neutrophils with 40-65 times more neutrophils sequestered in the pulmonary capillaries compared to larger vessels.[199] This is largely due to mechanical trapping of neutrophils in pulmonary capillaries, which occurs independently of adhesion mechanisms initiated by selectins and β2-integrins.[199,200] Under inflammatory conditions, the role of selectins and β2-integrins in neutrophil adhesion to the pulmonary endothelium and recruitment into the lungs has been shown to vary with the type of inflammatory stimuli.[200] While it is unknown whether neutrophil adhesion and emigration during IAV infection occurs via β2-integrin or L-selectin dependent or independent processes, in our study, neutrophils in the pulmonary marginated vasculature are those that are resistant to vascular perfusion. Thus, we interpret that Col1a2/Vcan$^{-/-}$ mice have neutrophils that are less adherent to the pulmonary endothelium. This raises important questions about the role of fibroblast-derived versican on endothelial cell activation and function. Additionally, this finding suggests that neutrophils may be less adherent to versican-deficient fibroblasts, which they are near when emigrating through tricellular junctions in the distal airways.[201]

To investigate neutrophil adhesion to versican-deficient fibroblasts, we performed adhesion assays with mouse lung fibroblasts (mLFs) from Col1a2/Vcan$^{-/-}$ mice and WT controls. Neutrophil-like cells were derived by differentiating human promyelocytic leukemia (dHL-60) cells. We found that versican-deficient mLFs had reduced cell-associated hyaluronan (HA) and reduced adhesion of dHL-60s after stimulation with poly(I:C), a TLR-3 agonist which stimulates a versican-enriched ECM in WT cells.[202] These findings are novel for a neutrophil cell line. However, versican-deficient fibroblasts have previously been demonstrated to have reduced adhesion to monocytes.[100] Additionally, mice with a global versican deficiency (Rosa/Vcan$^{-/-}$) and instilled with poly(I:C) had reduced HA accumulation in the lungs. It is unknown whether versican or HA are required for neutrophil adhesion and additional experiments applying versican antibody or hyaluronidase to WT mLFs have the potential to clarify this point.[99] We did not observe a significant reduction of HA accumulation from whole lung homogenates of IAV infected mice (data not shown), but this could be due to other cellular sources of HA obscuring potential differences in the HA content associated with fibroblasts in the pulmonary interstitium.

Similar to neutrophils, we find that fibroblast-derived versican plays an important role in regulating monocyte migration in the lungs and airspaces during IAV infection. Monocyte migration into the lungs and airways is reduced by 45.2% and 66.0%, respectively, in Col1a2/Vcan$^{-/-}$ mice compared to WT controls. We did not observe differences in monocytes in the marginated vasculature as we did with neutrophils and therefore, interpret that monocytes are equally adherent to the pulmonary endothelium during IAV infection between mouse strains. This may suggest that monocytes emigrate into the tissues by utilizing an alternative adhesion pathway than neutrophils. However, adhesion to lung fibroblasts is likely important for both cell types for emigration into the airways. The monocyte cell line, U937, has previously been shown to have reduced adhesion to mLFs stimulated with poly(I:C).[100] The reduction of monocytes into the lungs and airways on 3 dpi with IAV may also contribute to the observed reductions in monocyte-derived cell populations such as the 61.4% reduction of airway dendritic cells on 3 dpi and 21.8% reduction of mono-macrophages observed shortly after on 6 dpi. Additionally, monocyte and neutrophil trafficking into the lung are interdependent with monocytes facilitating neutrophil transendothelial migration from the vasculature into the lungs.[200,203] Thus we conclude that reduced adhesion to versican-deficient fibroblasts explains, at least in part, the reduction in neutrophils observed on 3 dpi with IAV infection in Col1a2/Vcan$^{-/-}$ mice.

One of our results of interest is the unexpected identification of IVCD45^{+} labeled macrophages in the marginated vasculature. One explanation is that IVCD45+ labeled macrophages were monocytes that had become adherent to the pulmonary vasculature and increased their expression of F4/80 and CD64 while in the process of migrating from the systemic vasculature into the pulmonary interstitium. The decreased adhesion of monocytes to the pulmonary endothelium that transition to mono-macrophages as they migrate into the lungs (**Figure 4.5A**) could explain the decreased number of mono-macrophages recovered from the lung tissue and airways (**Figure 4.5B-C**). A second possibility is that these IVCD45^{+} labeled macrophages are monocytes that became adherent to pulmonary endothelial cells and are remaining in the pulmonary circulation as macrophages. Work from several groups show that rats exposed to 0111:84 lipopolysaccharide (LPS) intravenously or intraperitoneally have a significant but transient increase in activated phagocytic mononuclear cells in the pulmonary microvasculature.[204,205] This population of monocytes have been referred to as induced pulmonary intravascular macrophages since they take on some but not all the characteristics of the pulmonary intravascular macrophages found in sheep, goats, pigs and other species.[206,207] Finally, we cannot rule out the possibility that the IVCD45+ stained cells are interstitial cells labeled due to increased vascular permeability. Future studies will need to determine the origin of the IVCD45^{+} macrophages identified in this study.

In addition to alterations of cell migration to the lungs and airways, we also observed a trend for increased numbers of lymphocytes in the mediastinal lymph nodes of Col1a2/Vcan$^{-/-}$ mice compared to WT controls on 6 dpi with IAV. While this trend was not statistically significant for any of the subpopulations of lymphocytes, except helper T cells, this is an intriguing observation. Additionally, we found slight increases of cytotoxic T cells and helper T cells in the airways on 9 dpi which could reflect mobilization of the increased number lymphocytes observed in the lymph nodes. The work of McMahon et al. in ADAMTS5 knockout mice infected with IAV, found an increase in the accumulation of versican in the mediastinal lymph nodes, which resulted in decreased T cell migration from the lymph node to the lung, ultimately compromising immunity to influenza. It is interesting that in mice lacking fibroblast-derived versican we see increased lymphocytes in the mediastinal lymph nodes and in the lungs. Future studies will need to address how fibroblast-derived versican controls lymphocyte populations in the regional lymph nodes and lungs as well as host immunity to IAV.

In our studies, we looked for evidence of differences of disease and lung injury between Col1a2/Vcan$^{-/-}$ mice and WT controls by several different methodologies. Mice from both strains lost weight during IAV infection similarly. Additionally, there were no significant differences seen in total protein levels in the BAL fluid over the course of infection. Acute lung injury scores (data not shown) did not reveal differences between mouse strains. Additionally, vascular permeability was assessed using fluorescein-labeled dextran intravenously injected immediately prior to harvest at 3 dpi, but no differences were appreciated between Col1a2/Vcan$^{-/-}$ and WT mice. A limitation of our assessment of IAV disease and lung injury in our study is that we did not investigate beyond 9 dpi with IAV by any methodology. The nidus for weight loss at this dose of IAV is 9-10 dpi.[63] Lung injury and resolution occur simultaneously during IAV infection. Neutrophils, monocytes, and mono-macrophage recruitment have all been implicated as prominent actors in immune-mediated lung injury. It is possible that Col1a2/Vcan$^{-/-}$ have improved recovery of weight loss or improved acute lung injury scores at later time points secondary to reduced recruitment of these cell populations to the lungs.

In conclusion, our study demonstrates that loss of versican from fibroblasts has a direct impact on pulmonary inflammation by reducing recruitment and accumulation of neutrophils, monocytes, mono-macrophages, and dendritic cells early during the course IAV infection. Our findings demonstrate that fibroblast-derived versican is a key integrator of the early host immune response to IAV.

Chapter 5. Conclusions and Future Directions

Seasonal influenza A virus (IAV) infections and IAV pandemics will remain a significant threat to human health for the foreseeable future. Host-directed therapeutic strategies possess an untapped potential for reducing the burden of severe influenza disease outcomes. Increasingly, the extracellular matrix (ECM) is recognized for its vital role in the host immune response and for its potential to contain targets for host-directed pulmonary disease therapies.[30,33,35] Versican is an ECM proteoglycan that demonstrates immunomodulatory properties and is potentially a target for host-directed therapies. However, prior to the work included in this thesis, the role of versican during IAV infection was a significant knowledge gap limiting our understanding of the immunomodulatory potential of versican.

The advent of conditional versican knock-out mice provided a foundation for the work presented. When Vcan$^{tm1.1Cwf}$ mice (Vcan$^{fl/fl}$) are crossed with a Cre-recombinase expressing mouse, the versican gene can be deleted in a specific spatiotemporal manner. This thesis adds a mouse strain that lacks fibroblast-derived versican (Col1a2/Vcan$^{-/-}$), to existing versican-deficient mouse strains. Previously existing strains included mice globally deficient in versican (Rosa26/Vcan$^{-/-}$), mice deficient in myeloid-derived versican (LysM/Vcan$^{-/-}$), and mice deficient in epithelial-derived versican (SPC/Vcan$^{-/-}$). Col1a2/Vcan$^{-/-}$ mice were critical for testing the central hypothesis that fibroblast-derived versican is pro-inflammatory and enhances the innate immune response to IAV infection.

Before experiments with Col1a2/Vcan$^{-/-}$ mice could be initiated, it was essential to characterize the spatiotemporal changes in versican expression and accumulation during IAV infection in versican-competent mice. Important insights from this published work, comprising Chapter 2, include that versican increases in the lungs in response to IAV, versican accumulation correlates with mouse acute lung injury scores and with pulmonary inflammatory cell infiltration, and that versican is a type I interferon–stimulated gene in pulmonary stromal cells. These data raised intriguing questions about versican's role(s) in the early host response to IAV. Based on published studies in Rosa26/Vcan$^{-/-}$ and LysM/Vcan$^{-/-}$ mice instilled with a TLR-3 agonist, we hypothesized that Col1a2/Vcan-/- mice would have reductions in leukocyte recruitment to the lungs and airways during IAV infection.[100,103]

A rigorous and robust protocol combining spectral flow cytometry with *in vivo* compartmental analysis, for precise localization of multiple lymphoid and non-lymphoid cell populations participating in the pulmonary immune response is described in Chapter 3. After addressing reviewer comments, this protocol was resubmitted for publication as an innovative methodology and is currently under review. The strategies and analysis developed in Chapter 3 were applied to studies in Col1a2/Vcan$^{-/-}$ mice during IAV infection in Chapter 4 and a corresponding manuscript being prepared for submission. Novel alterations in the recruitment of leukocytes to pulmonary microenvironments were identified in Col1a2/Vcan$^{-/-}$ mice. These include reduced numbers of neutrophils, monocytes, and mono-macrophages Col1a2/Vcan$^{-/-}$ mice and echo previous findings in Rosa/Vcan$^{-/-}$ mice instilled with a TLR-3 agonist, which also demonstrated reduced leukocyte recruitment into the lungs.[100] Rosa/Vcan$^{-/-}$ mouse lung fibroblasts (mLFs) stimulated with a TLR-3 agonist had reduced adhesion to monocytes, and similarly, we find stimulated Col1a2/Vcan$^{-/-}$ fibroblasts demonstrate reduced adhesion to neutrophils.[100] These findings suggest that the contribution of fibroblast-derived versican to the host immune response to IAV infection is a pro-inflammatory mediator acting through direct adhesion with monocytes and neutrophils as they emigrate from the vasculature to the lungs.

Although we have identified fibroblast-derived versican as a pro-inflammatory mediator during IAV infection, our work has raised several questions to be addressed in future studies. A top priority is investigating whether versican, hyaluronan (HA), or both are necessary for neutrophil and monocyte adhesion to mLFs. In addition to reduced adhesion to neutrophils. Stimulated Col1a2/Vcan$^{-/-}$ mLFs demonstrate reduced cell-associated HA, echoing similar findings in Rosa/Vcan$^{-/-}$ mLFs.[100] Application of hyaluronidase and versican blocking antibodies to mLFs could help elucidate the role of versican and HA in neutrophil adhesion.[99]

Our studies identified a diminished inflammatory response in Col1a2/Vcan$^{-/-}$ mice infected with IAV. However, the phenotype of Col1a2/Vcan$^{-/-}$ mice with regards to alterations in other domains of lung injury such as histologic evidence of tissue injury, alteration of the alveolar-capillary barrier, and physiologic dysfunction, remains largely unknown.[208] Despite pilot investigations of lung injury differences early in the course of IAV infection, no differences were found between Col1a2/Vcan$^{-/-}$ and WT mice. Future studies could investigate features of acute lung injury in Col1a2/Vcan$^{-/-}$ mice at time points beyond 9 dpi with IAV. Neutrophils, monocytes, and mono-macrophages have all been implicated as prominent actors in immune-mediated acute lung injury.[209-211] Reduction in the recruitment of these cell populations to the lung could be accompanied by reduced lung injury and/or the improved resolution of injury in

Col1a2/Vcan$^{-/-}$ mice compared to controls after IAV clearance. If demonstrated, this phenotype of Col1a2/Vcan$^{-/-}$ mice would expedite the relevance of our findings to human health.

The need to research host-directed therapeutic targets for IAV infections is great, and Col1a2/Vcan,$^{-/-}$ mice, demonstrate a marked reduction of neutrophils into the lungs and airways during IAV. Neutrophils are well known for mediating acute lung injury during bacterial lung infections.[212] Given this consideration, fibroblast-derived versican and Col1a2/Vcan$^{-/-}$ mice may prove to be especially important and useful in studies investigating acute lung injury from lipopolysaccharide, *Pseudomonas aeruginosa*, or staphylococcal pneumonia.

In conclusion, the work presented in this thesis expands on the existing literature and addresses important gaps in knowledge regarding the immunomodulatory potential of versican during IAV infection. Our findings provide multiple opportunities for further investigation of the mechanisms of immunomodulation by fibroblast-derived versican and to relate the relevance of our findings to human health.

Bibliography

1. Tang F, Brune JE, Chang MY, Reeves SR, Altemeier WA, Frevert CW. Defining the versican interactome in lung health and disease. *Am J Physiol Cell Physiol*. Aug 1 2022;323(2):C249-C276. doi:10.1152/ajpcell.00162.2022 PMC9291419
2. Collaborators GBDI. Mortality, morbidity, and hospitalisations due to influenza lower respiratory tract infections, 2017: an analysis for the Global Burden of Disease Study 2017. *Lancet Respir Med*. Jan 2019;7(1):69-89. doi:10.1016/S2213-2600(18)30496-X PMC6302221
3. Iuliano AD, Roguski KM, Chang HH, et al. Estimates of global seasonal influenza-associated respiratory mortality: a modelling study. *Lancet*. Mar 31 2018;391(10127):1285-1300. doi:10.1016/S0140-6736(17)33293-2 PMC5935243
4. Mizgerd JP. Lung infection--a public health priority. *PLoS Med*. Feb 2006;3(2):e76. doi:10.1371/journal.pmed.0030076 PMC1326257
5. Quinton LJ, Walkey AJ, Mizgerd JP. Integrative Physiology of Pneumonia. *Physiol Rev*. Jul 1 2018;98(3):1417-1464. doi:10.1152/physrev.00032.2017 PMC6088146
6. Flerlage T, Boyd DF, Meliopoulos V, Thomas PG, Schultz-Cherry S. Influenza virus and SARS-CoV-2: pathogenesis and host responses in the respiratory tract. *Nat Rev Microbiol*. Jul 2021;19(7):425-441. doi:10.1038/s41579-021-00542-7 PMC8023351
7. Boyd DF, Wilson TL, Thomas PG. One hundred years of (influenza) immunopathology. *Adv Virus Res*. 2020;107:247-284. doi:10.1016/bs.aivir.2020.06.005
8. Simonsen L, Spreeuwenberg P, Lustig R, et al. Global mortality estimates for the 2009 Influenza Pandemic from the GLaMOR project: a modeling study. *PLoS Med*. Nov 2013;10(11):e1001558. doi:10.1371/journal.pmed.1001558 PMC3841239
9. Long JS, Mistry B, Haslam SM, Barclay WS. Host and viral determinants of influenza A virus species specificity. *Nat Rev Microbiol*. Jan 2019;17(2):67-81. doi:10.1038/s41579-018-0115-z
10. Francis ME, King ML, Kelvin AA. Back to the Future for Influenza Preimmunity-Looking Back at Influenza Virus History to Infer the Outcome of Future Infections. *Viruses*. Jan 30 2019;11(2)doi:10.3390/v11020122 PMC6410066
11. Poovorawan Y. Epidemic of avian influenza A (H7N9) virus in China. *Pathog Glob Health*. Jun 2014;108(4):169-70. doi:10.1179/2047772414Z.000000000206 PMC4069331
12. Govorkova EA, McCullers JA. Therapeutics against influenza. *Curr Top Microbiol Immunol*. 2013;370:273-300. doi:10.1007/82_2011_198 PMC7121838
13. Lytras T, Mouratidou E, Andreopoulou A, Bonovas S, Tsiodras S. Effect of Early Oseltamivir Treatment on Mortality in Critically Ill Patients With Different Types of Influenza: A Multiseason Cohort Study. *Clin Infect Dis*. Nov 13 2019;69(11):1896-1902. doi:10.1093/cid/ciz101
14. Muthuri SG, Venkatesan S, Myles PR, et al. Effectiveness of neuraminidase inhibitors in reducing mortality in patients admitted to hospital with influenza A H1N1pdm09 virus infection: a meta-analysis of individual participant data. *The Lancet Respiratory Medicine*. 2014;2(5):395-404. doi:10.1016/S2213-2600(14)70041-4
15. Lee N, Hurt AC. Neuraminidase inhibitor resistance in influenza: a clinical perspective. *Curr Opin Infect Dis*. Dec 2018;31(6):520-526. doi:10.1097/QCO.0000000000000498
16. Ali SO, Takas T, Nyborg A, et al. Evaluation of MEDI8852, an Anti-Influenza A Monoclonal Antibody, in Treating Acute Uncomplicated Influenza. *Antimicrob Agents Chemother*. Nov 2018;62(11)doi:10.1128/aac.00694-18 PMC6201130

17. Hayden FG, Sugaya N, Hirotsu N, et al. Baloxavir Marboxil for Uncomplicated Influenza in Adults and Adolescents. *N Engl J Med*. Sep 6 2018;379(10):913-923. doi:10.1056/NEJMoa1716197
18. Uehara T, Hayden FG, Kawaguchi K, et al. Treatment-Emergent Influenza Variant Viruses With Reduced Baloxavir Susceptibility: Impact on Clinical and Virologic Outcomes in Uncomplicated Influenza. *J Infect Dis*. Jan 14 2020;221(3):346-355. doi:10.1093/infdis/jiz244
19. Newton AH, Cardani A, Braciale TJ. The host immune response in respiratory virus infection: balancing virus clearance and immunopathology. *Semin Immunopathol*. Jul 2016;38(4):471-82. doi:10.1007/s00281-016-0558-0 PMC4896975
20. Lee CK, Lee HK, Loh TP, et al. Comparison of pandemic (H1N1) 2009 and seasonal influenza viral loads, Singapore. *Emerg Infect Dis*. Feb 2011;17(2):287-91. doi:10.3201/eid1702.100282 PMC3204747
21. Granados A, Peci A, McGeer A, Gubbay JB. Influenza and rhinovirus viral load and disease severity in upper respiratory tract infections. *J Clin Virol*. Jan 2017;86:14-19. doi:10.1016/j.jcv.2016.11.008
22. Meschi S, Selleri M, Lalle E, et al. Duration of viral shedding in hospitalized patients infected with pandemic H1N1. *BMC Infect Dis*. May 23 2011;11:140. doi:10.1186/1471-2334-11-140 PMC3123568
23. Oshansky CM, Gartland AJ, Wong SS, et al. Mucosal immune responses predict clinical outcomes during influenza infection independently of age and viral load. *Am J Respir Crit Care Med*. Feb 15 2014;189(4):449-62. doi:10.1164/rccm.201309-1616OC PMC3977720
24. Sanders CJ, Vogel P, McClaren JL, Bajracharya R, Doherty PC, Thomas PG. Compromised respiratory function in lethal influenza infection is characterized by the depletion of type I alveolar epithelial cells beyond threshold levels. *American Journal of Physiology-Lung Cellular and Molecular Physiology*. 2013;304(7):L481-L488. doi:10.1152/ajplung.00343.2012
25. Lee N, Chan PK, Hui DS, et al. Viral loads and duration of viral shedding in adult patients hospitalized with influenza. *J Infect Dis*. Aug 15 2009;200(4):492-500. doi:10.1086/600383 PMC7110250
26. Hanula R, Bortolussi-Courval E, Mendel A, Ward BJ, Lee TC, McDonald EG. Evaluation of Oseltamivir Used to Prevent Hospitalization in Outpatients With Influenza: A Systematic Review and Meta-analysis. *JAMA Intern Med*. Jun 12 2023;doi:10.1001/jamainternmed.2023.0699 PMC10262060
27. Andersson-Sjoland A, Hallgren O, Rolandsson S, et al. Versican in inflammation and tissue remodeling: the impact on lung disorders. *Glycobiology*. Mar 2015;25(3):243-51. doi:10.1093/glycob/cwu120 PMC4310351
28. Troy NM, Bosco A. Respiratory viral infections and host responses; insights from genomics. *Respir Res*. Nov 21 2016;17(1):156. doi:10.1186/s12931-016-0474-9 PMC5117516
29. Zumla A, Rao M, Wallis RS, et al. Host-directed therapies for infectious diseases: current status, recent progress, and future prospects. *Lancet Infect Dis*. Apr 2016;16(4):e47-63. doi:10.1016/S1473-3099(16)00078-5 PMC7164794
30. Boyd DF, Thomas PG. Towards integrating extracellular matrix and immunological pathways. *Cytokine*. Oct 2017;98:79-86. doi:10.1016/j.cyto.2017.03.004 PMC5581707
31. Wight TN, Frevert CW, Debley JS, Reeves SR, Parks WC, Ziegler SF. Interplay of extracellular matrix and leukocytes in lung inflammation. *Cell Immunol*. Feb 2017;312:1-14. doi:10.1016/j.cellimm.2016.12.003 PMC5290208

32. Ito JT, Lourenco JD, Righetti RF, Tiberio I, Prado CM, Lopes F. Extracellular Matrix Component Remodeling in Respiratory Diseases: What Has Been Found in Clinical and Experimental Studies? *Cells*. Apr 11 2019;8(4)doi:10.3390/cells8040342 PMC6523091
33. O'Dwyer DN, Gurczynski SJ, Moore BB. Pulmonary immunity and extracellular matrix interactions. *Matrix Biol*. Nov 2018;73:122-134. doi:10.1016/j.matbio.2018.04.003 PMC6177325
34. Zhou Y, Horowitz JC, Naba A, et al. Extracellular matrix in lung development, homeostasis and disease. *Matrix Biol*. Nov 2018;73:77-104. doi:10.1016/j.matbio.2018.03.005 PMC6129220
35. Burgess JK, Mauad T, Tjin G, Karlsson JC, Westergren-Thorsson G. The extracellular matrix - the under-recognized element in lung disease? *J Pathol*. Dec 2016;240(4):397-409. doi:10.1002/path.4808 PMC5129494
36. Bruce Alberts AJ, Julian Lewis, Martin Raff, Keith Roberts, Peter Walter. The Extracellular Matrix of Animals. *Molecular Biology of the Cell*. 4th Edition ed. Garland Science; 2002. https://www.ncbi.nlm.nih.gov/books/NBK26810/
37. Hynes RO, Naba A. Overview of the matrisome--an inventory of extracellular matrix constituents and functions. *Cold Spring Harb Perspect Biol*. Jan 1 2012;4(1):a004903. doi:10.1101/cshperspect.a004903 PMC3249625
38. Sivaraman K, Shanthi C. Matrikines for therapeutic and biomedical applications. *Life Sci*. Dec 1 2018;214:22-33. doi:10.1016/j.lfs.2018.10.056
39. Malemud CJ. Matrix metalloproteinases (MMPs) in health and disease: an overview. *Front Biosci*. May 1 2006;11:1696-701. doi:10.2741/1915
40. Papadas A, Arauz G, Cicala A, Wiesner J, Asimakopoulos F. Versican and Versican-matrikines in Cancer Progression, Inflammation, and Immunity. *J Histochem Cytochem*. Dec 2020;68(12):871-885. doi:10.1369/0022155420937098 PMC7711242
41. Tocchi A, Parks WC. Functional interactions between matrix metalloproteinases and glycosaminoglycans. *Febs j*. May 2013;280(10):2332-41. doi:10.1111/febs.12198
42. Vallet SD, Clerc O, Ricard-Blum S. Glycosaminoglycan-Protein Interactions: The First Draft of the Glycosaminoglycan Interactome. *J Histochem Cytochem*. Aug 6 2020:22155420946403. doi:10.1369/0022155420946403
43. Iozzo RV, Schaefer L. Proteoglycan form and function: A comprehensive nomenclature of proteoglycans. *Matrix Biol*. Mar 2015;42:11-55. doi:10.1016/j.matbio.2015.02.003 PMC4859157
44. Wight TN. Provisional matrix: A role for versican and hyaluronan. *Matrix Biol*. Jul 2017;60-61:38-56. doi:10.1016/j.matbio.2016.12.001 PMC5438907
45. Alberts BJ, A.; Lewis, J.; Raff, M.; Roberts, K.; Walter, P. *Molecular Biology of the Cell*. 4th Edition ed. The Extracellular Matrix of Animals. Garland Science; 2002.
46. Little PJ, Ballinger ML, Burch ML, Osman N. Biosynthesis of natural and hyperelongated chondroitin sulfate glycosaminoglycans: new insights into an elusive process. *Open Biochem J*. 2008;2:135-42. doi:10.2174/1874091x00802010135 PMC2627520
47. Wu YJ, La Pierre DP, Wu J, Yee AJ, Yang BB. The interaction of versican with its binding partners. *Cell Res*. Jul 2005;15(7):483-94. doi:10.1038/sj.cr.7290318
48. Graham GJ, Handel TM, Proudfoot AEI. Leukocyte Adhesion: Reconceptualizing Chemokine Presentation by Glycosaminoglycans. *Trends Immunol*. Jun 2019;40(6):472-481. doi:10.1016/j.it.2019.03.009

49. Sawant KV, Sepuru KM, Lowry E, et al. Neutrophil recruitment by chemokines Cxcl1/KC and Cxcl2/MIP2: Role of Cxcr2 activation and glycosaminoglycan interactions. *J Leukoc Biol*. Sep 2 2020;doi:10.1002/JLB.3A0820-207R
50. Tanino Y, Coombe DR, Gill SE, et al. Kinetics of chemokine-glycosaminoglycan interactions control neutrophil migration into the airspaces of the lungs. *J Immunol*. Mar 1 2010;184(5):2677-85. doi:10.4049/jimmunol.0903274 PMC4113427
51. Bandtlow CE, Zimmermann DR. Proteoglycans in the developing brain: new conceptual insights for old proteins. *Physiol Rev*. Oct 2000;80(4):1267-90. doi:10.1152/physrev.2000.80.4.1267
52. Islam S, Watanabe H. Versican: A Dynamic Regulator of the Extracellular Matrix. *J Histochem Cytochem*. Nov 2020;68(11):763-775. doi:10.1369/0022155420953922 PMC7649968
53. Evanko SP, Gooden MD, Kang I, Chan CK, Vernon RB, Wight TN. A Role for HAPLN1 During Phenotypic Modulation of Human Lung Fibroblasts In Vitro. *J Histochem Cytochem*. Nov 2020;68(11):797-811. doi:10.1369/0022155420966663 PMC7649966
54. Dours-Zimmermann MT, Zimmermann DR. A novel glycosaminoglycan attachment domain identified in two alternative splice variants of human versican. *J Biol Chem*. Dec 30 1994;269(52):32992-8.
55. Islam S, Chuensirikulchai K, Khummuang S, et al. Accumulation of versican facilitates wound healing: Implication of its initial ADAMTS-cleavage site. *Matrix Biol*. May 2020;87:77-93. doi:10.1016/j.matbio.2019.10.006
56. Ito K, Shinomura T, Zako M, Ujita M, Kimata K. Multiple forms of mouse PG-M, a large chondroitin sulfate proteoglycan generated by alternative splicing. *J Biol Chem*. Jan 13 1995;270(2):958-65. doi:10.1074/jbc.270.2.958
57. Kischel P, Waltregny D, Dumont B, et al. Versican overexpression in human breast cancer lesions: known and new isoforms for stromal tumor targeting. *Int J Cancer*. Feb 1 2010;126(3):640-50. doi:10.1002/ijc.24812
58. Zako M, Shinomura T, Ujita M, Ito K, Kimata K. Expression of PG-M(V3), an alternatively spliced form of PG-M without a chondroitin sulfate attachment in region in mouse and human tissues. *J Biol Chem*. Feb 24 1995;270(8):3914-8. doi:10.1074/jbc.270.8.3914
59. Wight TN. Versican: a versatile extracellular matrix proteoglycan in cell biology. *Curr Opin Cell Biol*. Oct 2002;14(5):617-23. doi:10.1016/s0955-0674(02)00375-7
60. Rahmani M, Carthy JM, McManus BM. Mapping of the Wnt/beta-catenin/TCF response elements in the human versican promoter. *Methods Mol Biol*. 2012;836:35-52. doi:10.1007/978-1-61779-498-8_3
61. Rahmani M, Read JT, Carthy JM, et al. Regulation of the versican promoter by the beta-catenin-T-cell factor complex in vascular smooth muscle cells. *J Biol Chem*. Apr 1 2005;280(13):13019-28. doi:10.1074/jbc.M411766200
62. Hsia CC, Hyde DM, Ochs M, Weibel ER, Structure AEJTFoQAoL. An official research policy statement of the American Thoracic Society/European Respiratory Society: standards for quantitative assessment of lung structure. *Am J Respir Crit Care Med*. Feb 15 2010;181(4):394-418. doi:10.1164/rccm.200809-1522ST PMC5455840
63. Brune JE, Chang MY, Altemeier WA, Frevert CW. Type I Interferon Signaling Increases Versican Expression and Synthesis in Lung Stromal Cells During Influenza Infection. *J Histochem Cytochem*. Nov 2021;69(11):691-709. doi:10.1369/00221554211054447 PMC8554580

64. Timms KP, Maurice SB. Context-dependent bioactivity of versican fragments. *Glycobiology*. May 19 2020;30(6):365-373. doi:10.1093/glycob/cwz090
65. Kenagy RD, Plaas AH, Wight TN. Versican degradation and vascular disease. *Trends Cardiovasc Med*. Aug 2006;16(6):209-15. doi:10.1016/j.tcm.2006.03.011 PMC3169384
66. Wight TN, Kang I, Evanko SP, et al. Versican-A Critical Extracellular Matrix Regulator of Immunity and Inflammation. *Front Immunol*. 2020;11:512. doi:10.3389/fimmu.2020.00512 PMC7105702
67. Apte SS. ADAMTS Proteins: Concepts, Challenges, and Prospects. *Methods Mol Biol*. 2020;2043:1-12. doi:10.1007/978-1-4939-9698-8_1
68. Apte SS, Parks WC. Metalloproteinases: A parade of functions in matrix biology and an outlook for the future. *Matrix Biol*. May-Jul 2015;44-46:1-6. doi:10.1016/j.matbio.2015.04.005
69. Parks WC. Matrix metalloproteinases in lung repair. *Eur Respir J Suppl*. Sep 2003;44:36s-38s. doi:10.1183/09031936.03.00001203
70. Parks WC, Shapiro SD. Matrix metalloproteinases in lung biology. *Respir Res*. 2001;2(1):10-9. doi:10.1186/rr33 PMC59564
71. Apte SS. A disintegrin-like and metalloprotease (reprolysin type) with thrombospondin type 1 motifs: the ADAMTS family. *Int J Biochem Cell Biol*. Jun 2004;36(6):981-5. doi:10.1016/j.biocel.2004.01.014
72. Kenagy RD, Fischer JW, Davies MG, et al. Increased plasmin and serine proteinase activity during flow-induced intimal atrophy in baboon PTFE grafts. *Arterioscler Thromb Vasc Biol*. Mar 1 2002;22(3):400-4. doi:10.1161/hq0302.105376
73. Sandy JD, Westling J, Kenagy RD, et al. Versican V1 proteolysis in human aorta in vivo occurs at the Glu441-Ala442 bond, a site that is cleaved by recombinant ADAMTS-1 and ADAMTS-4. *J Biol Chem*. Apr 20 2001;276(16):13372-8. doi:10.1074/jbc.M009737200
74. Dancevic CM, Fraser FW, Smith AD, Stupka N, Ward AC, McCulloch DR. Biosynthesis and expression of a disintegrin-like and metalloproteinase domain with thrombospondin-1 repeats-15: a novel versican-cleaving proteoglycanase. *J Biol Chem*. Dec 27 2013;288(52):37267-76. doi:10.1074/jbc.M112.418624 PMC3873579
75. Longpré JM, McCulloch DR, Koo BH, Alexander JP, Apte SS, Leduc R. Characterization of proADAMTS5 processing by proprotein convertases. *Int J Biochem Cell Biol*. May 2009;41(5):1116-26. doi:10.1016/j.biocel.2008.10.008
76. Silver DL, Hou L, Somerville R, Young ME, Apte SS, Pavan WJ. The secreted metalloprotease ADAMTS20 is required for melanoblast survival. *PLoS Genet*. Feb 29 2008;4(2):e1000003. doi:10.1371/journal.pgen.1000003 PMC2265537
77. Somerville RP, Longpre JM, Jungers KA, et al. Characterization of ADAMTS-9 and ADAMTS-20 as a distinct ADAMTS subfamily related to Caenorhabditis elegans GON-1. *J Biol Chem*. Mar 14 2003;278(11):9503-13. doi:10.1074/jbc.M211009200
78. Westling J, Gottschall PE, Thompson VP, et al. ADAMTS4 (aggrecanase-1) cleaves human brain versican V2 at Glu405-Gln406 to generate glial hyaluronate binding protein. *Biochem J*. Feb 1 2004;377(Pt 3):787-95. doi:10.1042/bj20030896 PMC1223897
79. Hope C, Emmerich PB, Papadas A, et al. Versican-Derived Matrikines Regulate Batf3-Dendritic Cell Differentiation and Promote T Cell Infiltration in Colorectal Cancer. *J Immunol*. Sep 1 2017;199(5):1933-1941. doi:10.4049/jimmunol.1700529 PMC5568487
80. McCulloch DR, Nelson CM, Dixon LJ, et al. ADAMTS metalloproteases generate active versican fragments that regulate interdigital web regression. *Dev Cell*. Nov 2009;17(5):687-98. doi:10.1016/j.devcel.2009.09.008 PMC2780442

81. Nandadasa S, Burin des Roziers C, Koch C, et al. A new mouse mutant with cleavage-resistant versican and isoform-specific versican mutants demonstrate that proteolysis at the Glu(441)-Ala(442) peptide bond in the V1 isoform is essential for interdigital web regression. *Matrix Biol Plus*. Jun 2021;10:100064. doi:10.1016/j.mbplus.2021.100064 PMC8233476
82. Foulcer SJ, Nelson CM, Quintero MV, et al. Determinants of versican-V1 proteoglycan processing by the metalloproteinase ADAMTS5. *J Biol Chem*. Oct 3 2014;289(40):27859-73. doi:10.1074/jbc.M114.573287 PMC4183820
83. Hope C, Foulcer S, Jagodinsky J, et al. Immunoregulatory roles of versican proteolysis in the myeloma microenvironment. *Blood*. Aug 4 2016;128(5):680-5. doi:10.1182/blood-2016-03-705780 PMC4974200
84. Perides G, Asher RA, Lark MW, Lane WS, Robinson RA, Bignami A. Glial hyaluronate-binding protein: a product of metalloproteinase digestion of versican? *Biochem J*. Dec 1 1995;312 (Pt 2)(Pt 2):377-84. doi:10.1042/bj3120377 PMC1136273
85. Jönsson-Rylander AC, Nilsson T, Fritsche-Danielson R, et al. Role of ADAMTS-1 in atherosclerosis: remodeling of carotid artery, immunohistochemistry, and proteolysis of versican. *Arterioscler Thromb Vasc Biol*. Jan 2005;25(1):180-5. doi:10.1161/01.Atv.0000150045.27127.37
86. Martin DR, Santamaria S, Koch CD, Ahnström J, Apte SS. Identification of novel ADAMTS1, ADAMTS4 and ADAMTS5 cleavage sites in versican using a label-free quantitative proteomics approach. *J Proteomics*. Oct 30 2021;249:104358. doi:10.1016/j.jprot.2021.104358 PMC8713443
87. Barascuk N, Genovese F, Larsen L, et al. A MMP derived versican neo-epitope is elevated in plasma from patients with atherosclerotic heart disease. *Int J Clin Exp Med*. 2013;6(3):174-84. PMC3609693
88. Halpert I, Sires UI, Roby JD, et al. Matrilysin is expressed by lipid-laden macrophages at sites of potential rupture in atherosclerotic lesions and localizes to areas of versican deposition, a proteoglycan substrate for the enzyme. *Proc Natl Acad Sci U S A*. Sep 3 1996;93(18):9748-53. doi:10.1073/pnas.93.18.9748 PMC38500
89. Passi A, Negrini D, Albertini R, Miserocchi G, De Luca G. The sensitivity of versican from rabbit lung to gelatinase A (MMP-2) and B (MMP-9) and its involvement in the development of hydraulic lung edema. *FEBS Lett*. Jul 30 1999;456(1):93-6. doi:10.1016/s0014-5793(99)00929-1
90. Sand JM, Knox AJ, Lange P, et al. Accelerated extracellular matrix turnover during exacerbations of COPD. *Respir Res*. Jun 11 2015;16(1):69. doi:10.1186/s12931-015-0225-3 PMC4491243
91. Sand JMB, Tanino Y, Karsdal MA, et al. A Serological Biomarker of Versican Degradation is Associated with Mortality Following Acute Exacerbations of Idiopathic Interstitial Pneumonia. *Respir Res*. May 4 2018;19(1):82. doi:10.1186/s12931-018-0779-y PMC5935977
92. Malla N, Berg E, Theocharis AD, Svineng G, Uhlin-Hansen L, Winberg JO. In vitro reconstitution of complexes between pro-matrix metalloproteinase-9 and the proteoglycans serglycin and versican. *Febs j*. Jun 2013;280(12):2870-87. doi:10.1111/febs.12291
93. Ra HJ, Harju-Baker S, Zhang F, Linhardt RJ, Wilson CL, Parks WC. Control of promatrilysin (MMP7) activation and substrate-specific activity by sulfated glycosaminoglycans. *J Biol Chem*. Oct 9 2009;284(41):27924-27932. doi:10.1074/jbc.M109.035147 PMC2788844
94. Gill S, Wight TN, Frevert CW. Proteoglycans: key regulators of pulmonary inflammation and the innate immune response to lung infection. *Anat Rec (Hoboken)*. Jun 2010;293(6):968-81. doi:10.1002/ar.21094 PMC4121077

95. Nandadasa S, Foulcer S, Apte SS. The multiple, complex roles of versican and its proteolytic turnover by ADAMTS proteases during embryogenesis. *Matrix Biol*. Apr 2014;35:34-41. doi:10.1016/j.matbio.2014.01.005 PMC5525047
96. Apte SS. A disintegrin-like and metalloprotease (reprolysin-type) with thrombospondin type 1 motif (ADAMTS) superfamily: functions and mechanisms. *J Biol Chem*. Nov 13 2009;284(46):31493-7. doi:10.1074/jbc.R109.052340 PMC2797218
97. Hirose J, Kawashima H, Yoshie O, Tashiro K, Miyasaka M. Versican interacts with chemokines and modulates cellular responses. *J Biol Chem*. Feb 16 2001;276(7):5228-34. doi:10.1074/jbc.M007542200
98. Kawashima H, Atarashi K, Hirose M, et al. Oversulfated chondroitin/dermatan sulfates containing GlcAbeta1/IdoAalpha1-3GalNAc(4,6-O-disulfate) interact with L- and P-selectin and chemokines. *J Biol Chem*. Apr 12 2002;277(15):12921-30. doi:10.1074/jbc.M200396200
99. Evanko SP, Potter-Perigo S, Bollyky PL, Nepom GT, Wight TN. Hyaluronan and versican in the control of human T-lymphocyte adhesion and migration. *Matrix Biol*. Mar 2012;31(2):90-100. doi:10.1016/j.matbio.2011.10.004 PMC3288568
100. Kang I, Harten IA, Chang MY, et al. Versican Deficiency Significantly Reduces Lung Inflammatory Response Induced by Polyinosine-Polycytidylic Acid Stimulation. *J Biol Chem*. Jan 6 2017;292(1):51-63. doi:10.1074/jbc.M116.753186 PMC5217699
101. Potter-Perigo S, Johnson PY, Evanko SP, et al. Polyinosine-polycytidylic acid stimulates versican accumulation in the extracellular matrix promoting monocyte adhesion. *Am J Respir Cell Mol Biol*. Jul 2010;43(1):109-20. doi:10.1165/rcmb.2009-0081OC PMC2911565
102. Snyder JM, Washington IM, Birkland T, Chang MY, Frevert CW. Correlation of Versican Expression, Accumulation, and Degradation during Embryonic Development by Quantitative Immunohistochemistry. *J Histochem Cytochem*. Dec 2015;63(12):952-67. doi:10.1369/0022155415610383 PMC4823801
103. Chang MY, Kang I, Gale M, Jr., et al. Versican is produced by Trif- and type I interferon-dependent signaling in macrophages and contributes to fine control of innate immunity in lungs. *Am J Physiol Lung Cell Mol Physiol*. Dec 1 2017;313(6):L1069-L1086. doi:10.1152/ajplung.00353.2017 PMC5814701
104. Chang MY, Tanino Y, Vidova V, et al. A rapid increase in macrophage-derived versican and hyaluronan in infectious lung disease. *Matrix Biol*. Feb 2014;34:1-12. doi:10.1016/j.matbio.2014.01.011 PMC4019684
105. Kellar GG, Barrow KA, Rich LM, et al. Loss of versican and production of hyaluronan in lung epithelial cells are associated with airway inflammation during RSV infection. *J Biol Chem*. Nov 13 2020;doi:10.1074/jbc.RA120.016196 PMC7949086
106. Merrilees MJ, Ching PS, Beaumont B, Hinek A, Wight TN, Black PN. Changes in elastin, elastin binding protein and versican in alveoli in chronic obstructive pulmonary disease. *Respir Res*. May 18 2008;9:41. doi:10.1186/1465-9921-9-41 PMC2397404
107. Bensadoun ES, Burke AK, Hogg JC, Roberts CR. Proteoglycan deposition in pulmonary fibrosis. *Am J Respir Crit Care Med*. Dec 1996;154(6 Pt 1):1819-28. doi:10.1164/ajrccm.154.6.8970376
108. Bensadoun ES, Burke AK, Hogg JC, Roberts CR. Proteoglycans in granulomatous lung diseases. *Eur Respir J*. Dec 1997;10(12):2731-7. doi:10.1183/09031936.97.10122731
109. Reeves SR, Kaber G, Sheih A, et al. Subepithelial Accumulation of Versican in a Cockroach Antigen-Induced Murine Model of Allergic Asthma. *J Histochem Cytochem*. Jun 2016;64(6):364-80. doi:10.1369/0022155416642989 PMC4888411

110. Said N, Sanchez-Carbayo M, Smith SC, Theodorescu D. RhoGDI2 suppresses lung metastasis in mice by reducing tumor versican expression and macrophage infiltration. *J Clin Invest*. Apr 2012;122(4):1503-18. doi:10.1172/JCI61392 PMC3314474
111. Kim S, Takahashi H, Lin WW, et al. Carcinoma-produced factors activate myeloid cells through TLR2 to stimulate metastasis. *Nature*. Jan 1 2009;457(7225):102-6. doi:10.1038/nature07623 PMC2746432
112. Boyd DF, Allen EK, Randolph AG, et al. Exuberant fibroblast activity compromises lung function via ADAMTS4. *Nature*. Nov 2020;587(7834):466-471. doi:10.1038/s41586-020-2877-5
113. McMahon M, Ye S, Izzard L, et al. ADAMTS5 Is a Critical Regulator of Virus-Specific T Cell Immunity. *PLoS Biol*. Nov 2016;14(11):e1002580. doi:10.1371/journal.pbio.1002580 PMC5113859
114. Bradley LM, Douglass MF, Chatterjee D, Akira S, Baaten BJ. Matrix metalloprotease 9 mediates neutrophil migration into the airways in response to influenza virus-induced toll-like receptor signaling. *PLoS Pathog*. 2012;8(4):e1002641. doi:10.1371/journal.ppat.1002641 PMC3320598
115. Kang I, Chang MY, Wight TN, Frevert CW. Proteoglycans as Immunomodulators of the Innate Immune Response to Lung Infection. *J Histochem Cytochem*. Apr 2018;66(4):241-259. doi:10.1369/0022155417751880 PMC5958380
116. Wight TN, Kang I, Merrilees MJ. Versican and the control of inflammation. *Matrix Biol*. Apr 2014;35:152-61. doi:10.1016/j.matbio.2014.01.015 PMC4039577
117. Kawashima H, Hirose M, Hirose J, Nagakubo D, Plaas AH, Miyasaka M. Binding of a large chondroitin sulfate/dermatan sulfate proteoglycan, versican, to L-selectin, P-selectin, and CD44. *J Biol Chem*. Nov 10 2000;275(45):35448-56. doi:10.1074/jbc.M003387200
118. Wight TN, Kinsella MG, Evanko SP, Potter-Perigo S, Merrilees MJ. Versican and the regulation of cell phenotype in disease. *Biochim Biophys Acta*. Aug 2014;1840(8):2441-51. doi:10.1016/j.bbagen.2013.12.028 PMC4074575
119. Handel TM, Dyer DP. Perspectives on the Biological Role of Chemokine:Glycosaminoglycan Interactions. *J Histochem Cytochem*. Dec 7 2020:22155420977971. doi:10.1369/0022155420977971
120. Baarsma HA, Menzen MH, Halayko AJ, Meurs H, Kerstjens HA, Gosens R. beta-Catenin signaling is required for TGF-beta1-induced extracellular matrix production by airway smooth muscle cells. *Am J Physiol Lung Cell Mol Physiol*. Dec 2011;301(6):L956-65. doi:10.1152/ajplung.00123.2011
121. Venkatesan N, Tsuchiya K, Kolb M, et al. Glycosyltransferases and glycosaminoglycans in bleomycin and transforming growth factor-beta1-induced pulmonary fibrosis. *Am J Respir Cell Mol Biol*. Mar 2014;50(3):583-94. doi:10.1165/rcmb.2012-0226OC
122. Samuel CE. Antiviral actions of interferons. *Clin Microbiol Rev*. Oct 2001;14(4):778-809, table of contents. doi:10.1128/CMR.14.4.778-809.2001 PMC89003
123. Stetson DB, Medzhitov R. Type I interferons in host defense. *Immunity*. Sep 2006;25(3):373-81. doi:10.1016/j.immuni.2006.08.007
124. Davis AS, Chang MY, Brune JE, et al. The Use of Quantitative Digital Pathology to Measure Proteoglycan and Glycosaminoglycan Expression and Accumulation in Healthy and Diseased Tissues. *J Histochem Cytochem*. Sep 16 2020:22155420959146. doi:10.1369/0022155420959146

125. Cottey R, Rowe CA, Bender BS. Influenza virus. *Curr Protoc Immunol*. May 2001;Chapter 19:Unit 19 11. doi:10.1002/0471142735.im1911s42
126. Foster WM, Walters DM, Longphre M, Macri K, Miller LM. Methodology for the measurement of mucociliary function in the mouse by scintigraphy. *J Appl Physiol (1985)*. Mar 2001;90(3):1111-7. doi:10.1152/jappl.2001.90.3.1111
127. Felgenhauer JL, Brune JE, Long ME, et al. Evaluation of Nutritional Gel Supplementation in C57BL/6J Mice Infected with Mouse-Adapted Influenza A/PR/8/34 Virus. *Comp Med*. Dec 1 2020;70(6):471-486. doi:10.30802/AALAS-CM-20-990138 PMC7754200
128. Matute-Bello G, Downey G, Moore BB, et al. An official American Thoracic Society workshop report: features and measurements of experimental acute lung injury in animals. *Am J Respir Cell Mol Biol*. May 2011;44(5):725-38. doi:10.1165/rcmb.2009-0210ST PMC7328339
129. Dietert K, Gutbier B, Wienhold SM, et al. Spectrum of pathogen- and model-specific histopathologies in mouse models of acute pneumonia. *PLoS One*. 2017;12(11):e0188251. doi:10.1371/journal.pone.0188251 PMC5695780
130. Anderson KG, Mayer-Barber K, Sung H, et al. Intravascular staining for discrimination of vascular and tissue leukocytes. *Nat Protoc*. Jan 2014;9(1):209-22. doi:10.1038/nprot.2014.005 PMC4428344
131. Gauger PC, Vincent AL, Loving CL, et al. Kinetics of lung lesion development and pro-inflammatory cytokine response in pigs with vaccine-associated enhanced respiratory disease induced by challenge with pandemic (2009) A/H1N1 influenza virus. *Vet Pathol*. Nov 2012;49(6):900-12. doi:10.1177/0300985812439724
132. Henningson JN, Rajao DS, Kitikoon P, et al. Comparative virulence of wild-type H1N1pdm09 influenza A isolates in swine. *Vet Microbiol*. Mar 23 2015;176(1-2):40-9. doi:10.1016/j.vetmic.2014.12.021
133. Sunwoo SY, Schotsaert M, Morozov I, et al. A Universal Influenza Virus Vaccine Candidate Tested in a Pig Vaccination-Infection Model in the Presence of Maternal Antibodies. *Vaccines (Basel)*. Sep 14 2018;6(3)doi:10.3390/vaccines6030064 PMC6161263
134. Fernanda de Mello Costa M, Weiner AI, Vaughan AE. Basal-like Progenitor Cells: A Review of Dysplastic Alveolar Regeneration and Remodeling in Lung Repair. *Stem Cell Reports*. Nov 10 2020;15(5):1015-1025. doi:10.1016/j.stemcr.2020.09.006 PMC7560757
135. Kanegai CM, Xi Y, Donne ML, et al. Persistent Pathology in Influenza-Infected Mouse Lungs. *Am J Respir Cell Mol Biol*. Oct 2016;55(4):613-615. doi:10.1165/rcmb.2015-0387LE PMC5070109
136. Vaughan AE, Brumwell AN, Xi Y, et al. Lineage-negative progenitors mobilize to regenerate lung epithelium after major injury. *Nature*. Jan 29 2015;517(7536):621-5. doi:10.1038/nature14112 PMC4312207
137. Edelman BL, Redente EF. Isolation and Characterization of Mouse Fibroblasts. *Methods Mol Biol*. 2018;1809:59-67. doi:10.1007/978-1-4939-8570-8_5
138. Livak KJ, Schmittgen TD. Analysis of relative gene expression data using real-time quantitative PCR and the 2(-Delta Delta C(T)) Method. *Methods*. Dec 2001;25(4):402-8. doi:10.1006/meth.2001.1262
139. Meyerholz DK, Beck AP. Principles and approaches for reproducible scoring of tissue stains in research. *Lab Invest*. Jul 2018;98(7):844-855. doi:10.1038/s41374-018-0057-0
140. Rehg JE, Bush D, Ward JM. The utility of immunohistochemistry for the identification of hematopoietic and lymphoid cells in normal tissues and interpretation of proliferative and

inflammatory lesions of mice and rats. *Toxicol Pathol*. 2012;40(2):345-74. doi:10.1177/0192623311430695
141. Hung C, Linn G, Chow YH, et al. Role of lung pericytes and resident fibroblasts in the pathogenesis of pulmonary fibrosis. *Am J Respir Crit Care Med*. Oct 1 2013;188(7):820-30. doi:10.1164/rccm.201212-2297OC PMC3826269
142. Kishi M, Aono Y, Sato S, et al. Blockade of platelet-derived growth factor receptor-β, not receptor-α ameliorates bleomycin-induced pulmonary fibrosis in mice. *PLoS One*. 2018;13(12):e0209786. doi:10.1371/journal.pone.0209786 PMC6312310
143. Arimori Y, Nakamura R, Yamada H, et al. Type I interferon limits influenza virus-induced acute lung injury by regulation of excessive inflammation in mice. *Antiviral Res*. Sep 2013;99(3):230-7. doi:10.1016/j.antiviral.2013.05.007
144. Chen WP, Hu ZN, Jin LB, Wu LD. Licochalcone A Inhibits MMPs and ADAMTSs via the NF-kappaB and Wnt/beta-Catenin Signaling Pathways in Rat Chondrocytes. *Cell Physiol Biochem*. 2017;43(3):937-944. doi:10.1159/000481645
145. Wu B, Crampton SP, Hughes CC. Wnt signaling induces matrix metalloproteinase expression and regulates T cell transmigration. *Immunity*. Feb 2007;26(2):227-39. doi:10.1016/j.immuni.2006.12.007 PMC1855210
146. Wurfel MM, Park WY, Radella F, et al. Identification of high and low responders to lipopolysaccharide in normal subjects: an unbiased approach to identify modulators of innate immunity. *J Immunol*. Aug 15 2005;175(4):2570-8. doi:10.4049/jimmunol.175.4.2570
147. Zheng PS, Vais D, Lapierre D, et al. PG-M/versican binds to P-selectin glycoprotein ligand-1 and mediates leukocyte aggregation. *J Cell Sci*. Nov 15 2004;117(Pt 24):5887-95. doi:10.1242/jcs.01516
148. Reutershan J, Morris MA, Burcin TL, et al. Critical role of endothelial CXCR2 in LPS-induced neutrophil migration into the lung. *J Clin Invest*. Mar 2006;116(3):695-702. doi:10.1172/JCI27009 PMC1366502
149. Nolan JP. The evolution of spectral flow cytometry. *Cytometry A*. Oct 2022;101(10):812-817. doi:10.1002/cyto.a.24566
150. Surre J, Saint-Ruf C, Collin V, Orenga S, Ramjeet M, Matic I. Strong increase in the autofluorescence of cells signals struggle for survival. *Sci Rep*. Aug 14 2018;8(1):12088. doi:10.1038/s41598-018-30623-2 PMC6092379
151. Maus U, Rosseau S, Seeger W, Lohmeyer J. Separation of human alveolar macrophages by flow cytometry. *Am J Physiol*. Mar 1997;272(3 Pt 1):L566-71. doi:10.1152/ajplung.1997.272.3.L566
152. Tschernig T, Pabst R. What is the clinical relevance of different lung compartments? *BMC Pulmonary Medicine*. 2009/08/11 2009;9(1):39. doi:10.1186/1471-2466-9-39
153. Barletta KE, Cagnina RE, Wallace KL, Ramos SI, Mehrad B, Linden J. Leukocyte compartments in the mouse lung: distinguishing between marginated, interstitial, and alveolar cells in response to injury. *J Immunol Methods*. Jan 31 2012;375(1-2):100-10. doi:10.1016/j.jim.2011.09.013 PMC3328189
154. Doerschuk CM, Downey GP, Doherty DE, et al. Leukocyte and platelet margination within microvasculature of rabbit lungs. *J Appl Physiol (1985)*. May 1990;68(5):1956-61. doi:10.1152/jappl.1990.68.5.1956
155. Doyle NA, Bhagwan SD, Meek BB, et al. Neutrophil margination, sequestration, and emigration in the lungs of L-selectin-deficient mice. *J Clin Invest*. Feb 1 1997;99(3):526-33. doi:10.1172/JCI119189 PMC507828

156. Frevert CW, Warner AE, Weller E, Brain JD. The effect of endotoxin on in vivo rat alveolar macrophage phagocytosis. *Exp Lung Res*. Nov-Dec 1998;24(6):745-58. doi:10.3109/01902149809099593
157. Kubo H, Graham L, Doyle NA, Quinlan WM, Hogg JC, Doerschuk CM. Complement fragment-induced release of neutrophils from bone marrow and sequestration within pulmonary capillaries in rabbits. *Blood*. Jul 1 1998;92(1):283-90.
158. Mizgerd JP, Meek BB, Kutkoski GJ, Bullard DC, Beaudet AL, Doerschuk CM. Selectins and neutrophil traffic: margination and Streptococcus pneumoniae-induced emigration in murine lungs. *J Exp Med*. Aug 1 1996;184(2):639-45. doi:10.1084/jem.184.2.639 PMC2192708
159. Patel BV, Tatham KC, Wilson MR, O'Dea KP, Takata M. In vivo compartmental analysis of leukocytes in mouse lungs. *Am J Physiol Lung Cell Mol Physiol*. Oct 1 2015;309(7):L639-52. doi:10.1152/ajplung.00140.2015 PMC4593833
160. Frank JA, Wray CM, McAuley DF, Schwendener R, Matthay MA. Alveolar macrophages contribute to alveolar barrier dysfunction in ventilator-induced lung injury. *Am J Physiol Lung Cell Mol Physiol*. Dec 2006;291(6):L1191-8. doi:10.1152/ajplung.00055.2006
161. Abate O, Bollo E, Lotti D, Bo S. Cytological, immunocytochemical and biochemical cerebrospinal fluid investigations in selected central nervous system disorders of dogs. *Zentralbl Veterinarmed B*. Mar 1998;45(2):73-85. doi:10.1111/j.1439-0450.1998.tb00769.x
162. Anderson KG, Sung H, Skon CN, et al. Cutting edge: intravascular staining redefines lung CD8 T cell responses. *J Immunol*. Sep 15 2012;189(6):2702-6. doi:10.4049/jimmunol.1201682 PMC3436991
163. Collins FS, Tabak LA. Policy: NIH plans to enhance reproducibility. *Nature*. Jan 30 2014;505(7485):612-3. doi:10.1038/505612a PMC4058759
164. Freedman LP, Venugopalan G, Wisman R. Reproducibility2020: Progress and priorities. *F1000Res*. 2017;6:604. doi:10.12688/f1000research.11334.1 PMC5461896
165. Bonilla DL, Reinin G, Chua E. Full Spectrum Flow Cytometry as a Powerful Technology for Cancer Immunotherapy Research. *Front Mol Biosci*. 2020;7:612801. doi:10.3389/fmolb.2020.612801 PMC7878389
166. Ferrer-Font L, Pellefigues C, Mayer JU, Small SJ, Jaimes MC, Price KM. Panel Design and Optimization for High-Dimensional Immunophenotyping Assays Using Spectral Flow Cytometry. *Curr Protoc Cytom*. Mar 2020;92(1):e70. doi:10.1002/cpcy.70
167. Park LM, Lannigan J, Jaimes MC. OMIP-069: Forty-Color Full Spectrum Flow Cytometry Panel for Deep Immunophenotyping of Major Cell Subsets in Human Peripheral Blood. *Cytometry A*. Oct 2020;97(10):1044-1051. doi:10.1002/cyto.a.24213 PMC8132182
168. Ferrer-Font L, Small SJ, Lewer B, et al. Panel Optimization for High-Dimensional Immunophenotyping Assays Using Full-Spectrum Flow Cytometry. *Curr Protoc*. Sep 2021;1(9):e222. doi:10.1002/cpz1.222
169. Laboratory UFC. FlowJo for Antibody Titrations: Separation Index and Concatenation. . https://www.uwhealth.org/files/uwhealth/docs/cancer_for_researchers/Flow/FlowJo-Antibody-Titrations.pdf
170. DiPiazza AT, Hill JP, Graham BS, Ruckwardt TJ. OMIP-061: 20-Color Flow Cytometry Panel for High-Dimensional Characterization of Murine Antigen-Presenting Cells. *Cytometry A*. Dec 2019;95(12):1226-1230. doi:10.1002/cyto.a.23880
171. Gibbings SL, Jakubzick CV. Isolation and Characterization of Mononuclear Phagocytes in the Mouse Lung and Lymph Nodes. *Methods Mol Biol*. 2018;1809:33-44. doi:10.1007/978-1-4939-8570-8_3 PMC6262824

172. Lin KL, Suzuki Y, Nakano H, Ramsburg E, Gunn MD. CCR2+ monocyte-derived dendritic cells and exudate macrophages produce influenza-induced pulmonary immune pathology and mortality. *J Immunol*. Feb 15 2008;180(4):2562-72. doi:10.4049/jimmunol.180.4.2562
173. McCubbrey AL, Allison KC, Lee-Sherick AB, Jakubzick CV, Janssen WJ. Promoter Specificity and Efficacy in Conditional and Inducible Transgenic Targeting of Lung Macrophages. *Front Immunol*. 2017;8:1618. doi:10.3389/fimmu.2017.01618 PMC5705560
174. Misharin AV, Morales-Nebreda L, Mutlu GM, Budinger GR, Perlman H. Flow cytometric analysis of macrophages and dendritic cell subsets in the mouse lung. *Am J Respir Cell Mol Biol*. Oct 2013;49(4):503-10. doi:10.1165/rcmb.2013-0086MA PMC3824047
175. Unsworth A, Anderson R, Haynes N, Britt K. OMIP-032: Two multi-color immunophenotyping panels for assessing the innate and adaptive immune cells in the mouse mammary gland. *Cytometry A*. Jun 2016;89(6):527-30. doi:10.1002/cyto.a.22867
176. Yu YR, O'Koren EG, Hotten DF, et al. A Protocol for the Comprehensive Flow Cytometric Analysis of Immune Cells in Normal and Inflamed Murine Non-Lymphoid Tissues. *PLoS One*. 2016;11(3):e0150606. doi:10.1371/journal.pone.0150606 PMC4777539
177. Tighe RM, Redente EF, Yu YR, et al. Improving the Quality and Reproducibility of Flow Cytometry in the Lung. An Official American Thoracic Society Workshop Report. *Am J Respir Cell Mol Biol*. Aug 2019;61(2):150-161. doi:10.1165/rcmb.2019-0191ST PMC6670040
178. Savic AG, Preus S, Rebecchi L, Guidetti R. New multivariate image analysis method for detection of differences in chemical and structural composition of chitin structures in tardigrade feeding apparatuses. *Zoomorphology*. 2016/03/01 2016;135(1):43-50. doi:10.1007/s00435-015-0295-2
179. Jakubzick CV, Randolph GJ, Henson PM. Monocyte differentiation and antigen-presenting functions. *Nat Rev Immunol*. Jun 2017;17(6):349-362. doi:10.1038/nri.2017.28
180. Rose S, Misharin A, Perlman H. A novel Ly6C/Ly6G-based strategy to analyze the mouse splenic myeloid compartment. *Cytometry A*. Apr 2012;81(4):343-50. doi:10.1002/cyto.a.22012 PMC3987771
181. Ghoneim HE, Thomas PG, McCullers JA. Depletion of alveolar macrophages during influenza infection facilitates bacterial superinfections. *J Immunol*. Aug 1 2013;191(3):1250-9. doi:10.4049/jimmunol.1300014 PMC4907362
182. McCullers JA. The co-pathogenesis of influenza viruses with bacteria in the lung. *Nat Rev Microbiol*. Apr 2014;12(4):252-62. doi:10.1038/nrmicro3231
183. Rynda-Apple A, Robinson KM, Alcorn JF. Influenza and Bacterial Superinfection: Illuminating the Immunologic Mechanisms of Disease. *Infect Immun*. Oct 2015;83(10):3764-70. doi:10.1128/IAI.00298-15 PMC4567631
184. Carvalho AT, Elia CC, de Souza HS, et al. Immunohistochemical study of intestinal eosinophils in inflammatory bowel disease. *J Clin Gastroenterol*. Feb 2003;36(2):120-5. doi:10.1097/00004836-200302000-00006
185. Klion AD, Nutman TB. The role of eosinophils in host defense against helminth parasites. *J Allergy Clin Immunol*. Jan 2004;113(1):30-7. doi:10.1016/j.jaci.2003.10.050
186. LeMessurier KS, Samarasinghe AE. Eosinophils: Nemeses of Pulmonary Pathogens? *Curr Allergy Asthma Rep*. Jun 19 2019;19(8):36. doi:10.1007/s11882-019-0867-1 PMC6993982
187. Rosenberg HF, Dyer KD, Domachowske JB. Eosinophils and their interactions with respiratory virus pathogens. *Immunol Res*. 2009;43(1-3):128-37. doi:10.1007/s12026-008-8058-5 PMC2777531

188. LeMessurier KS, Rooney R, Ghoneim HE, et al. Influenza A virus directly modulates mouse eosinophil responses. *J Leukoc Biol*. Jul 2020;108(1):151-168. doi:10.1002/JLB.4MA0320-343R PMC7859173
189. Tiwary M, Rooney RJ, Liedmann S, LeMessurier KS, Samarasinghe AE. Eosinophil Responses at the Airway Epithelial Barrier during the Early Phase of Influenza a Virus Infection in C57BL/6 Mice. *Cells*. 2021;10(3):509.
190. Spits H, Artis D, Colonna M, et al. Innate lymphoid cells--a proposal for uniform nomenclature. *Nat Rev Immunol*. Feb 2013;13(2):145-9. doi:10.1038/nri3365
191. Califano D, Furuya Y, Metzger DW. Effects of Influenza on Alveolar Macrophage Viability Are Dependent on Mouse Genetic Strain. *J Immunol*. Jul 1 2018;201(1):134-144. doi:10.4049/jimmunol.1701406 PMC6008236
192. Evanko SP, Chan CK, Johnson PY, Frevert CW, Wight TN. The biochemistry and immunohistochemistry of versican. *Methods Cell Biol*. 2018;143:261-279. doi:10.1016/bs.mcb.2017.08.015 PMC6419768
193. Reed MJ, Damodarasamy M, Pathan JL, et al. Increased Hyaluronan and TSG-6 in Association with Neuropathologic Changes of Alzheimer's Disease. *Journal of Alzheimer's Disease*. 2019;67:91-102. doi:10.3233/JAD-180797
194. Wilkinson TS, Potter-Perigo S, Tsoi C, Altman LC, Wight TN. Pro- and Anti-Inflammatory Factors Cooperate to Control Hyaluronan Synthesis in Lung Fibroblasts. *American journal of respiratory cell and molecular biology*. 2004/07/01 2004;31(1):92-99. doi:10.1165/rcmb.2003-0380OC
195. Reeves SR, Barrow KA, Rich LM, et al. Respiratory Syncytial Virus Infection of Human Lung Fibroblasts Induces a Hyaluronan-Enriched Extracellular Matrix That Binds Mast Cells and Enhances Expression of Mast Cell Proteases. *Front Immunol*. 2019;10:3159. doi:10.3389/fimmu.2019.03159 PMC6997473
196. Hauert AB, Martinelli S, Marone C, Niggli V. Differentiated HL-60 cells are a valid model system for the analysis of human neutrophil migration and chemotaxis. *Int J Biochem Cell Biol*. Jul 2002;34(7):838-54. doi:10.1016/s1357-2725(02)00010-9
197. Waithman J, Mintern JD. Dendritic cells and influenza A virus infection. *Virulence*. Nov 15 2012;3(7):603-8. doi:10.4161/viru.21864 PMC3545942
198. Percopo CM, Dyer KD, Ochkur SI, et al. Activated mouse eosinophils protect against lethal respiratory virus infection. *Blood*. Jan 30 2014;123(5):743-52. doi:10.1182/blood-2013-05-502443 PMC3907759
199. Doerschuk CM. Mechanisms of leukocyte sequestration in inflamed lungs. *Microcirculation*. Apr 2001;8(2):71-88.
200. Maas SL, Soehnlein O, Viola JR. Organ-Specific Mechanisms of Transendothelial Neutrophil Migration in the Lung, Liver, Kidney, and Aorta. *Front Immunol*. 2018;9:2739. doi:10.3389/fimmu.2018.02739 PMC6277681
201. Lin WC, Fessler MB. Regulatory mechanisms of neutrophil migration from the circulation to the airspace. *Cell Mol Life Sci*. May 2021;78(9):4095-4124. doi:10.1007/s00018-021-03768-z PMC7863617
202. Evanko SP, Potter-Perigo S, Johnson PY, Wight TN. Organization of hyaluronan and versican in the extracellular matrix of human fibroblasts treated with the viral mimetic poly I:C. *J Histochem Cytochem*. Nov 2009;57(11):1041-60. doi:10.1369/jhc.2009.953802 PMC2762883

203. Kreisel D, Nava RG, Li W, et al. In vivo two-photon imaging reveals monocyte-dependent neutrophil extravasation during pulmonary inflammation. *Proc Natl Acad Sci U S A*. Oct 19 2010;107(42):18073-8. doi:10.1073/pnas.1008737107 PMC2964224
204. Singh B, Doane KJ, Niehaus GD. Ultrastructural and cytochemical evaluation of sepsis-induced changes in the rat pulmonary intravascular mononuclear phagocytes. *J Anat*. Jan 1998;192 (Pt 1)(Pt 1):13-23. doi:10.1046/j.1469-7580.1998.19210013.x PMC1467735
205. Warner AE, Mulina RM, Bellows CF, Brain JD. Endotoxemia enhances pulmonary mononuclear cell uptake of circulating particles and pathogens in a species without pulmonary intravascular macrophages. *Chest*. Mar 1994;105(3 Suppl):50S-51S. doi:10.1378/chest.105.3_supplement.50s
206. Brain JD, Molina RM, DeCamp MM, Warner AE. Pulmonary intravascular macrophages: their contribution to the mononuclear phagocyte system in 13 species. *Am J Physiol*. Jan 1999;276(1):L146-54. doi:10.1152/ajplung.1999.276.1.L146
207. Schneberger D, Aharonson-Raz K, Singh B. Pulmonary intravascular macrophages and lung health: what are we missing? *Am J Physiol Lung Cell Mol Physiol*. Mar 15 2012;302(6):L498-503. doi:10.1152/ajplung.00322.2011
208. Kulkarni HS, Lee JS, Bastarache JA, et al. Update on the Features and Measurements of Experimental Acute Lung Injury in Animals: An Official American Thoracic Society Workshop Report. *Am J Respir Cell Mol Biol*. Feb 2022;66(2):e1-e14. doi:10.1165/rcmb.2021-0531ST PMC8845128
209. George ST, Lai J, Ma J, Stacey HD, Miller MS, Mullarkey CE. Neutrophils and Influenza: A Thin Line between Helpful and Harmful. *Vaccines*. 2021;9(6):597.
210. Arafa EI, Shenoy AT, Barker KA, et al. Recruitment and training of alveolar macrophages after pneumococcal pneumonia. *JCI Insight*. Mar 8 2022;7(5) doi:10.1172/jci.insight.150239 PMC8983128
211. Aggarwal NR, King LS, D'Alessio FR. Diverse macrophage populations mediate acute lung inflammation and resolution. *Am J Physiol Lung Cell Mol Physiol*. Apr 15 2014;306(8):L709-25. doi:10.1152/ajplung.00341.2013 PMC3989724
212. Balamayooran G, Batra S, Fessler MB, Happel KI, Jeyaseelan S. Mechanisms of neutrophil accumulation in the lungs against bacteria. *Am J Respir Cell Mol Biol*. Jul 2010;43(1):5-16. doi:10.1165/rcmb.2009-0047TR PMC2911570

VITA

Jourdan Elizabeth Brune was born and raised in Woodinville, Washington. She attended the University of Washington in Seattle where she earned a Bachelor of Science in Biology in 2011. From 2011-2013, Jourdan worked as a veterinary technician for the Department of Comparative Medicine at the University of Washington during which time she discovered a passion for laboratory animal medicine. She attended the College of Veterinary Medicine at Washington State University in Pullman, Washington and earned her Doctor of Veterinary Medicine in 2017. Immediately, after graduation, Jourdan returned to the Department of Comparative Medicine at the University of Washington to receive specialty training in laboratory animal medicine and biomedical research. At the beginning of her specialty training, Jourdan joined the Frevert laboratory. In 2020, she entered a doctoral program under the guidance of Charles Frevert. Jourdan earned her Doctor of Philosophy in Laboratory Medicine and Pathology from the University of Washington in 2023.